HABILITATION THESIS

Contributions to the Optimal Structures of the Electromechanical Systems and the Electric Power Quality

Assoc. Prof. Sorin MUŞUROI, PhD

– July 2014–

CONTENTS

1. ABSTRACT

1.1. Abstract

The habilitation thesis presents the most important professional and scientific results obtained by the author during 2001-2014. This period follows the public presentation of his doctoral thesis, which took place in 2000.

Three main research areas have been addressed: *The optimal design of AC motors*, *The optimal control of electrical drives with AC motors* and *Single-phase power factor correction converters*.

The activity in the domain of *Optimal design of AC motors* has been oriented towards: (i) the study of the skin effect in the high rectangular bars of the rotors of the three-phase inverter fed induction motors; (ii) the study of the use of ferrite permanent magnets in designing synchronous machines as an alternative to the version with rare earth magnets; (iii) education.

The study of the skin effect in the rotor bars of the three phase induction machines fed by PWM inverters is a continuation of the doctoral activity. The obtained results at the end of the research offers the possibility to calculate the equivalent global factors that change the resistance, respectively the reactance, which characterize the high rectangular rotor bars of the induction motors, under the conditions of the non-sinusoidal regime determined by the inverter supplying. The author has published 14 articles as follows: 4 articles in journals indexed BDI, 3 articles issued in volumes of ISI conferences, 3 articles issued in volumes of BDI indexed conferences, 1 article at an international conference without indexation and 4 articles in national conferences. In recognition of the results obtained, the author was invited to write a chapter entitled *The Behavior in Stationary Regime of an Induction Motor Powered by Static Frequency Converters* of the book entitled *Induction motor. Modeling and control*, published in 2012, at InTech Europe Publishing House under the coordination of Professor Rui Estevez Araujo.

In the domain of designing synchronous machines using ferrite magnets as an economical alternative to the solution of using rare earth magnets, during the research 8 new variants of rotors were conceived, designed, modeled and simulated. Of these, seven variants are with variable reluctance having the rotor flux barriers filled with ferrite magnets and a rotor topology is with flux concentration, also designed to be made with ceramic magnets. All the solutions studied aim a much cheaper alternative to the synchronous motors with rare earth permanent magnets. The research team addressed this direction in 2010, within an international project with Diehl Company from Germany, the author being the manager. The paper section regarding this topic presents the results obtained for three variants of rotor, considered by the author as being representative: a row of flow barriers 1V, with two rows of flux barriers 2V and with flux concentration which have been already executed as a prototype in two variants. The prototypes were made at Electromotor Timişoara, under the author's direct guidance, while the stand tests, whose results are presented in the paper, were performed in Germany. One study was published in the volume of IECON Conference of 2013, from Vienna, under the aegis of IEEE Industrial Electronics Society, an ISI indexed paper. The paper received the Certificate of appreciation for the best work of the section. Three other works are being under review. The author has published three books and one specialty article, in collaboration, on educational topics. It should be highlighted that the author is the project holder from the discipline Electrical motors, taught to the students from Power Engineering.

In the domain of the optimal control of electrical drives with AC motors, the research can be grouped into two categories: (i) electric drives with vector control for induction motors implemented in naval mechanisms, (ii) development of new algorithms for optimal control of AC motors.

In the first domain, the author was part of a joint team consisting of researchers from the Politehnica University of Timişoara, Faculty of Electrical and Power Engineering and from "Mircea cel Bătrân" Naval Academy of Constanţa, Faculty of Marine Military, who collaborated in partnership, approaching the problem of implementing the direct vector control in the torque and flux of the induction machine, for the electric drive systems for naval mechanisms. The theoretical and experimental study was conducted under a national grant in which the author participated as Politehnica University of Timişoara responsible representative. The results were published in 14 articles: 2 in an ISI indexed volume, 1 in a BDI indexed volume, 3 in international conferences and 8 at national conferences. The author collaborated to the publication of three books.

The second domain presents the author's results obtained after his participation in a research developed during 2004-2013 by a joint team consisting of specialists from the German company Diehl and the teachers from Politehnica University of Timişoara. In the theoretical and experimental study the team has developed new algorithms for controlling AC motors. For the present study, three algorithms have been selected to be presented as they have significantly improved the existing control strategies while maintaining the same level of their complexity. 12 articles have been published: 1 article in an ISI indexed journal, 1 in BDI indexed journals, 8 in volumes of ISI indexed conferences and 2 in volumes of BDI conferences. In the educational area, the author taught two subjects, both newly introduced.

The domain of Power factor correction converters was addressed relatively recently, in 2013. The undertaken research has resulted in two international projects in which the author participated as a manager. The first project focused on the segment of single-phase power converters with a power up to 4 [kW] and the second project of the three-phase converters powered up to 10 [kW]. So far, three articles have been written, both under review.

The thesis is structured in five sections.

The first section presents the achievements and results in the author's career.

The second section is devoted to the optimal design of AC motors. The first part of this section presents a selection of results obtained by the author in the study of skin effect that manifests in the high rectangular rotor bars of the induction motor fed by a voltage inverter. This study aims to develop a theory of asynchronous motor, under non-sinusoidal power regime, leading to the optimization of the methodology of the constructive / technologic design, under favorable economic conditions. The second part of this section is devoted to promote a new concept of an economically advantageous design of the synchronous motors. For this purpose, the paper proposes three new topologies of rotors for the synchronous machine. All the solutions studied aim a much cheaper alternative to the synchronous motors with rare earth permanent magnets.

The third section is devoted to the Optimal control of electrical drives with AC motors. The first part of this section presents the results obtained from the implementation of vector control directly in torque and flux for the electric drive systems of marine mechanisms. The second section presents the results of the practical implementation of the algorithms for controlling the AC motors fitting the reversible driving systems, characterized by a wide range of speeds.

The fourth section presents a summary of the research results obtained in the field of single-phase power factor correction converters. The study analyzed the following power factor correction converters: the boost converter, the interleaved boost converter, the bridgeless converter and the bridgeless interleaved converter.

The last section of the habilitation thesis presents perspectives of future development. It presents new possible research directions in the domains mentioned above.

1.2. Rezumat

În cadrul tezei de abilitare sunt prezentate cele mai importante rezultate profesionale şi ştiinţifice pe care autorul le-a obţinut în perioada 2001 – 2014. Această perioadă urmează prezentării publice a tezei de doctorat, care a avut loc în anul 2000.

În această perioadă au fost abordate trei domenii de cercetare principale: *Proiectarea optimală a maşinilor de curent alternativ, Controlul optimal al acţionărilor electrice cu maşini de curent alternativ* şi *Convertoare corectoare de factor de putere monofazate*.

Activitatea în domeniul *Proiectării optimale a maşinilor de curent alternativ* a fost direcţionată către: (i) studiul efectului pelicular din barele dreptunghiulare înalte ale rotoarelor maşinilor de inducţie trifazate alimentate prin invertoare de tensiune; (ii) studiul utilizării magneţilor permanenţi din ferită la proiectarea maşinilor sincrone, ca o alternativă la varianta cu magneţi din pământuri rare; (iii) educaţie.

Studiul efectului pelicular din barele rotorice ale maşinilor de inducţie trifazate alimentate prin invertoare PWM reprezintă o continuare a activităţii doctorale. Rezultatele obţinute la finalul cercetării oferă oportunitatea calculării factorilor globali echivalenţi de modificare a rezistenţei respectiv a reactanţei, ce caracterizează barele rotorice dreptunghiulare înalte ale maşinilor asincrone, în condiţiile regimului neinusoidal datorat alimentării prin invertor. În această temă autorul a publicat 14 articole după cum urmează: 4 articole în reviste indexate BDI, 3 articole in volume ale unor conferinţe indexate ISI, 3 articole în volume ale unor conferinţe indexate BDI, 1 articol la o conferinţă din străinătate fără indexare şi 4 articole în conferinţe naţionale. Ca o recunoaştere a rezultatelor obţinute, autorul a fost invitat să scrie un capitol în cartea intitulată *Induction motor. Modelling and control,* apărută în anul 2012 în Editura InTech Europe, sub coordoonarea Prof. Rui Estevez Araujo. Capitolul este intitulat *The Behavior in Stationary Regime of an Induction Motor Powered by Static Frequency Converters.*

În cadrul cercetărilor întreprinse în domeniul proiectării maşinilor sincrone folosind magneţi din ferită, ca o alternativă economică la soluţia ce utilizează magneţi din pământuri rare, s-au conceput, proiectat, modelat şi simulat 8 variante noi de rotor. Dintre acestea, 7 variante de rotor sunt cu reluctanţă variabilă având barierele de flux umplute cu magneţi din ferită iar o variantă de rotor este cu concentrare de flux, prevăzută de asemenea a fi realizată cu magneţi ceramici. Toate aceste soluţii studiate se doresc a fi o alternativă, mult mai ieftină, la maşinile sincrone cu magneţi permanenţi din pământuri rare. Echipa de cercetare a abordat această direcţie în anul 2010, în cadrul unui proiect internaţional încheiat cu firma Diehl din Germania, avându-l pe autor ca director. În teză sunt prezentate rezultatele obţinute pentru 3 topologii de rotor, considerate de autor ca fiind reprezentative: varianta de rotor cu un rând de bariere de flux 1V respectiv cu două rânduri de bariere de flux 2V şi varianta de rotor cu concentrare de flux, soluţie care a fost executată ca prototip, în două variante constructive. Prototipurile au fost realizate la Electromotor Timişoara, sub directa îndrumare a autorului iar testele de stand, ale căror rezultate sunt prezentate în teză, au fost efectuate la firma parteneră din Germania. A fost publicată o lucrare apărută în Volumul Conferinţei IECON 2013-Vienna, sub egida IEEE Industrial Electronics Society, lucrare indexată ISI. Prezentarea a primit Certificatul de apreciere pentru cea mai bună lucrare din secţiune. Alte trei lucrări elaborate se află sub recenzie.Este de subliniat faptul că au fost publicate 3 cărţi de specialitate pe această temă şi 1 articol în colaborare, pe teme educaţionale. Totodată este important de precizat faptul că autorul a valorificat rezultatele cercetării în activitatea didactică, în cadrul orelor de Proiect de la disciplina Maşini electrice, predată studenţilor de la programul de studiu Inginerie Electroenergetică.

În domeniul Controlul optimal al acţionărilor electrice cu maşini de curent alternativ, activitatea de cercetare poate fi grupată în două subdomenii: (i) Sisteme de acţionare electrică cu control vectorial pentru motoarele de inducţie implementate la mecanismele navale; (ii) Dezvoltarea unor noi algoritmi de conducere optimală a maşinilor de curent alternativ.

În cadrul primului subdomeniu, activitatea autorului a fost desfăşurată în cadrul unui colectiv mixt, format din cercetători de la Facultatea de Electrotehnică şi Electroenergetică, Universitatea Politehnica Timişoara respectiv de la Facultatea de Marină Militară, Academia Mircea cel Batrân Constanţa. Colectivul de cercetare al parteneriatului a abordat problema implementării controlului vectorial direct în cuplu şi flux a maşinii de inducţie, pentru sistemele de acţionare electrică a mecanismelor navale. Studiul teoretic şi experimental a fost realizat în cadrul unui grant naţional la care autorul a participat în calitate de Responsabil al Universităţii Politehnica Timişoara. Rezultatele obţinute au fost publicate în 14 articole: 2 în volume indexate ISI, 1 în volum indexat BDI, 3 la conferinţe din străinătate şi 8 la conferinţe naţionale. Autorul a participat la elaborarea a 3 cărţi de specialitate în domeniu.

Cel de-al doilea subdomeniu prezintă rezultatele obţinute de autor în urma participării la o cercetare realizată în perioada 2004-2013 de o echipă mixtă, formată din specialişti de la firma Diehl din Germania şi cadre didactice de la UPT. În cadrul studiului teoretic şi experimental s-au dezvoltat noi algoritmi de conducere a maşinilor de curent alternativ. Pentru lucrarea realizată au fost prezentaţi 3 algoritmi care au îmbunătăţit semnificativ strategiile de control existente, cu păstrarea nivelului de complexitate al acestora. Rezultatele activităţii s-au materializat în publicarea a 12 articole din care 1 articol într-o revistă indexată ISI, 1 articol în revistă cotată BDI, 8 articole în volume ale unor conferinţe indexate ISI şi 2 articole în volumele unor conferinţe cotate BDI. Pe plan educaţional, autorul a utilizat rezultatele cercetărilor în predarea a două discipline, ambele nou introduse în planul de învăţământ al studiilor de licenţă din domeniu.

Domeniul Convertoarelor corectoare de factor de putere a fost abordat relativ recent, în anul 2013. Cercetările întreprinse s-au concretizat în două proiecte internaţionale la care autorul a participat în calitate de director. Primul proiect a vizat segmentul convertoarelor monofazate cu puteri de pînă la 4 [kW] iar al doilea proiect cel al convertoarelor trifazate cu puteri de până la 10 [kW]. Până în prezent, pe această temă, au fost elaborate 3 articole, toate aflate în recenzie.

În scopul prezentării cercetărilor actuale şi viitoare, aşa cum sunt prezentate anterior, teza este structurată în cinci secţiuni.

Prima secţiune prezintă realizările şi rezultatelor activităţii anterioare.

A doua secţiune este dedicată Proiectării optimale a maşinilor de curent alternativ. În prima parte a acestei secţiuni, se prezintă o selecţie a rezultatelor obţinute de autor în studiul efectului pelicular ce se manifestă în barele rotorice dreprunghiulare înalte ale maşinilor de inducţie alimentate prin invertoare de tensiune. Acest studiu a realizat dezvoltarea unei teorii a maşinii asincrone, în condiţiile regimului nesinusoidal de alimentare, care va conduce la optimizarea metodicii de proiectare constructivă / tehnologică a acesteia, în condiţii economice avantajoase. A doua parte a acestei secţiuni este dedicată dezvoltării şi proiectării economic avantajoasă a maşinilor sincrone. Sunt prezentate trei topologii noi de rotoare care utilizează magneţi din ferită ca alternativă la soluţia cu magneţi din pământuri rare.

Secţiunea a treia este dedicată Controlului optimal al acţionărilor cu maşini de curent alternativ. În prima parte acestei a treia secţiuni, se prezintă rezultatele obţinute în urma implementării controlului vectorial pentru sistemele de acţionare electrică a mecanismelor navale. Partea a doua a secţiunii prezintă rezultatele obţinute în urma implementării practice ale unor algoritmi de conducere a maşinilor de curent alternativ ce echipează sistemele de acţionări reversibile, caracterizate printr-o gamă largă de viteze.

În secţiunea a patra, este prezentată o sinteză a rezultatelor obţinute în cercetările întreprinse în domeniul Convertoarelor monofazate corectoare de factor de putere. În cadrul studiului au fost analizate următoarele convertoare corectoare pentru factorul de putere: convertorul boost, convertorul interleaved boost, convertorul bridgeless şi convertorul bridgeless interleaved.

Ultima secţiune, cea de a cincea a tezei de abilitare, prezintă perspective ale dezvoltării viitoare. Sunt prezentate noi posibile direcţii de cercetare în domeniile specificate anterior.

2. TECHNICAL PRESENTATION

2.1. Overview of Activity and Results, 2001 - 2014

The habilitation thesis presents the most important professional and scientific results obtained by the author during 2001-2014. This period began after I had obtained the Ph.D. degree in Electrical Engineering, with the doctoral thesis, entitled *Analysis of the behavior of low and medium power three-phase squirrel cage induction motors at their power network supplying through a static frequency converter*. The thesis was carried out under the coordination of the Prof. Ph.D. Eng. Ioan Novac.

In the aftermath of supporting the thesis, my activity has been directed towards three area: (i) *research*, (ii) *teaching and professional development activity*, iii) *university management*.

Three main research areas have been addressed in my **research activity**: *The optimal design of AC motors*, *The optimal control of electrical drives with AC motors* and *Single-phase power factor correction converters*.

In the domain of *The optimal design of AC motors*, presented in detail in paragraph 2.2 of the habilitation thesis, two directions were approached: (i) *the study of the skin effect in the high rectangular bars of the rotors of the three-phase inverter fed induction motors*; (ii) *the study of the use of ferrite permanent magnets in designing synchronous machines as an alternative to the version with rare earth magnets.*

The first domain is represented by the study of the skin effect in the rotor bars of the three phase induction machines fed by PWM inverters represents a continuation of the doctoral activity. In the first phase of the study, the electromagnetic field equations in the high rectangular rotor bar were analyzed in the case of the non-sinusoidal regime given by the presence of inverters in powering induction machine. In the second stage, we calculated the particular values of the penetration depth for the two extreme moments of the startup process, corresponding to the zero, respective nominal speed. Finally, the research presented the calculation of the two factors, the changing factor of resistance in alternative current $k_{r(CSF)}$ and the reactance $k_{x(CSF)}$, corresponding to the situation when the motor is fed by PWM inverters under a global form. The geometries of the rotor with the high bar of rectangular form were taken into account. During the research conducted in this area, the research team designed a program for the determination of the two factors, entitled CALCMOT. The research results were presented in 14 articles as follows: 4 articles in journals indexed BDI, references [11], [12], [13], [14] from the thesis bibliography, 3 articles issued in volumes of ISI conferences, references [15], [16], [17], 3 articles issued in volumes of BDI indexed conferences, references [18], [19], [20], 1 article at an international conference without indexation [24] and 4 articles in national conferences, [28], [29], [30], [31]. In recognition of the results obtained, I was invited to write a chapter entitled *The Behavior in Stationary Regime of an Induction Motor Powered by Static Frequency Converters* of the book entitled *Induction motor. Modeling and control*. The book was published in 2012, at InTech Europe Publishing House, under the coordination of Professor Rui Estevez Araujo. During the implementation of the study, I participated as a member of a PNCDI 2 grant (partner P2) entitled, *The Optimizing of Electric Hydro-generators Windings to Increase Energy Efficiency*, manager Prof. Ph.D. Eng. Marius Biriescu. I also published the specialty book *The Induction Motor Fed by Static Frequency Converters,* as a single author.

In the second domain, together with the team whom coordinator I was, we conducted an extensive study on the possibility of designing a synchronous motor using ferrite permanent magnets to replace the current, more expensive technical solution based on rare-earth magnets. After analyzing the characteristics of ferrite magnets, under a large coercive field to about 265 [kA /

m] and a low residual induction up to 0.4 [T], to increase the torque developed by the machine, we adopted as a technical solution a construction in which the rotor presents both permanent ferrite magnets and different magnetic reluctance after the two magnetic axes d and q. The stator of the machine remains unchanged. Basically, we obtained a much cheaper construction of a variable reluctance synchronous motor with ceramic magnets able to develop the same performance as a synchronous motor with permanent rare earth magnets, characterized by a high cost. In the research expanded during a period of two years, 8 new variants of rotors were conceived, designed, modeled and simulated. Of these, seven variants are with variable reluctance having the flux barriers filled with magnets and a rotor topology is with flux concentration. All these designed solutions were designed to be constructed with ferrite magnets. The research team addressed this direction in 2010, within the international project *Contract for research-development and consultancy* with Diehl Company from Germany. I participated in this project as a manager. The 2.2.2 from the thesis presents and analyses the results obtained for three variants of rotor, I have considered representative. The representative topologies are those in which the rotor is: with a row of flow barriers 1V, with two rows of flux barriers 2V and with flux concentration. The last solution has been already executed in two constructive variants. The prototypes were made at Electromotor Timişoara. I made the constructive and technological documentation and I coordinated the main phases of the process and the operations of the technological flux. The stand tests presented in this thesis were performed in Germany, at Diehl Company. The recognition of value and practical applications of the study was proved by the published papers. One study was published in the volume of IECON Conference of 2013, from Vienna, under the aegis of IEEE Industrial Electronics Society, an ISI indexed paper [33]. The paper received the Certificate of Acknowledgment for the best work of the section. Three other works are being under review.

In the domain of the *Optimal control of electrical drives with AC motors*, presented in the paragraph 2.3 of the habilitation thesis, the research can be grouped into two categories: (i) *electric driven systems with vector control for induction motors implemented in naval mechanisms*, (ii) *the development of new algorithms for optimal management of AC motors.*

The first domain regards a theoretical and experimental study developed by a joint team consisting of teachers from the Politehnica University of Timişoara, Faculty of Electrical and Power Engineering and from "Mircea cel Bătrân" Naval Academy of Constanţa, Faculty of Marine Military. The study was conducted within the national grant GR 226 of 2006 entitled *Electric Drives with Vector Control for Induction Motors Implemented in Naval Mechanisms,* project director, Prof. Ph.D. Eng. Dorin Popovici, in which I participated as the responsible representative in charge of the research team staff, on behalf of Politehnica University of Timişoara.

The study aimed to adopt a solution regarding the implementation of the direct vector control in the torque and flux of the induction machine, for the electric drive systems for naval mechanisms. This was intended to replace the current technical variant at the time in which for the operation of the loading equipment 3 speed squirrel cage induction motors were used, which were obtained using three separate stator windings in star connection. The main disadvantages of the variant proposed to be replaced are: large gauge and complicated construction of the control machine; speed change can be achieved only in stages. In order to eliminate these disadvantages, along with the research team which I was part of, we proposed a technical solution that maintains the induction machine as part of the execution, but in which the motion control, which involves speed control and/or position control, respectively torque control, is made by direct vector control in torque and flux. The main advantages that are obtained are obtained are: a quick dznamic response in torque and operation in a wide range of speeds; vector control is robust and relatively simple to implement; does not require current regulators and coordinate transformations; ensures efficient interference rejection; folds very well on numerical control; a normal squirrel cage induction motor with a single stator winding can be used; eliminates the control panel which comprises sense, acceleration, braking contactors and timing relays. The results were published in 14 articles: 2 in an ISI indexed volume, references [63], [64], 1 in a BDI indexed volume, reference [65], 3 in

international conferences [66], [67], [68] and 8 at national conferences [69], [70], [72], [73], [74], [75], [76], [80]. I also collaborated to the publication of three specialty books [6], [61] and [62].

Section 2.3.2, dedicated to the second domain, presents the results obtained after my participation in a research developed during 2004-2013 by a joint team consisting of specialists from the German company Diehl and the teachers from Politehnica University of Timişoara. The theoretical and experimental study mainly aimed the development of new algorithms for the optimal control of AC motors. Three of the proposed algorithms are presents, which have significantly improved the existing control strategies while maintaining the same level of their complexity.

The *first algorithm* is presented in section 2.3.2.1, entitled *Novel Flux Weakening Control Algorithm for PMSM*. It is an algorithm for wide speed range PMSM drives which are fed by PWM-VSI utilizing overmodulation. The PMSM drive system works in generator mode with the proposed algorithm only if the PWM-VSI is equipped with a regenerative unit to the AC power from the mains to DC link. If the PWM-VSI is not equipped with a regenerative unit, the generator mode operation of PMSM should be avoided by limiting the maximum q-axis current. This algorithm allows a smooth transition into and out of the field weakening over the whole speed range. Also the algorithm is not sensitive to the motor parameters; it is relative simple and can be implemented with a 16 [bit] microcontroller. The dynamic and steady-state performance of the PMSM drive are improved by using the VSI in the overmodulation regions but also the switching losses in the power module will be reduced. The control with the proposed algorithm is stable in overmodulation range and it is capable to follow the DC-link variations. The experimental results obtained have shown the benefits of the overmodulation despite know issues that involve this method. The second study, presented in section 2.3.2.2, proposes an enhanced field oriented drive system for PMSMS, where the current sensors are eliminated and only two Hall-effect position sensors are used instead of a high-resolution position sensor. The high performance current control is achieved by use of a state observer for current estimation. The proposed algorithm is capable to generate the optimal d- and q-axes current references in the different operating regions and the limits of the speed controller. This algorithm works in all four quadrants. The experimental results obtained with the proposed speed control drive system of PMSMS, pointed out that the proposed current observer has a good dynamic and also a good dynamic speed response. The proposed algorithm can be implemented with a 16 [bit] MCU. The new algorithm allows to calculate the d- and q-axes current references for the whole speed range, which works in all four quadrants, even the power converter has not a regenerative unit. The third proposed algorithm, presented in section 2.3.2.3, generates the stator flux reference and q-axis current limit in all four quadrants in an induction motor drive systems, which are fed by PWM inverter equipped with diode rectifier front-end and without any extra braking resistors. This algorithm allows a smooth transition into and out of the field weakening mode and also a smooth transition from motor mode to generator mode and inverse over the whole speed range. This algorithm is not sensitive to the motor parameters; it is relative simple and can be implemented with a 16 [bit] DSC. The experimental results obtained have shown that the proposed algorithm has good dynamic performance and good steady-state performance. Optimum torque capabilities can be developed despite significant changes in dc link voltage and motor parameters.

The results of the developed research resulted in 12 articles as follows: 1 article in an ISI indexed journal, reference [102], 1 in BDI indexed journals [95], 8 in volumes of ISI indexed conferences, references [101], [103], [104], [105], [106], [107], [108], [125] and 2 in volumes of BDI conferences [94], [109]. During this period I participated as a member of two national grants completed in 2003, *Testing, Modeling and Monitoring of Electrical Equipment in Machines Using Acquisition Systems and Data Processing,* code CNCSU 2 and *Variable Frequency Drives Using DSP Signal Processors*, code 115/2001. Both grants were led by Prof. Ph.D. Gheorghe Atanasiu.

The domain of the *Power Factor Correction Converters,* presented in paragraph 2.4, was recently approached, in 2013. The undertaken research was conducted in the two international projects in which I participated as a manager along with a team of teachers from Politehnica University of Timişoara: *Analysis and Evaluation of Current Topologies and Solutions for the*

Single Phase Power Factor Correction (PFC) for Grid Tied Inverters, BCI 1/28.01.2013 and *Analysis and Evaluation of Current Topologies and Solutions for three phase Power Factor Correction (PFC) for 400 V mains voltage* BCI 1/24.01.2014. The thesis presents the results obtained in the study conducted in the first project, entirely completed. The aim of the research consists of selecting the four relevant single phase power factor correction (PFC) topologies currently existing for the power range of 1.5 [kW] up to 4 [kW] and to analyse and evaluate them. The evaluation has to be done in regards to electromagnetic compatibility (EMC) requirements, which is very important in the residential ambient. The investigated topologies are the *conventional boost, the basic bridgeless PFC converters, the Boost Interleaved Converters and the Bridgeless Interleaved Converters*. The study deals with the design study of the four topologies selected from a state-of-the-art from literature, then with the implementation of their hardware and control parts in Matlab/Simulink, simulation environment and finally with their performances evaluation and electromagnetic interference EMI analysis using comparison. Loss analysis and efficiency evaluation is also provided. Choosing of the right parameters of the common mode and EMI filters, based on literature, is also provided, as well as their implementation in Matlab/Simulink. Simulation results show that they are compliant with international standards. Nowadays, electrical equipment in Europe must comply with the European EN 61000−3−2, or EN 61000-3-4 Norms. This requirement applies to most electrical appliances. So far three articles have been elaborated, all under review.

The second project is in its early stage, of a theoretical study, and it will be presented in the chapter *Future Directions*, of the thesis.

My teaching and professional activity developed during this period was closely related to the research presented above. I conducted seminar, laboratory, and project classes as an assistant professor from 2000 to 2007 and associate professor from 2007 to the present. I have taught subjects closely related to my research fields: *Electric drives*, *Electromechanical drives*, *Electric drives and converters*, *Advanced driving systems*, *Electric drives design*, *Electric servomotors and the intelligent motion control*, *Electrical machines*, *The technology of producing electrotechnical products, Computer graphics, Matlab and Simulink*. I introduced two new disciplines: *Electrical servomotors and the intelligent motiont control* in the Bachelor's degree programme and Embedded *systems- Industry* for the Master's degree programme.

I coordinated over 60 diploma projects. The topics were closely related to my teaching and research activity, some of the obtained results being routed to be further elaborated in scientific papers or for constructing stands in the *Electric drives* laboratory. I have been permanently dedicated to the goal of updating and raising the scientific level of the content of the material taught in accordance with the latest international achievements, and of exposing the new data in a modern way, accessible to students.

During 2001-2014, I published four specialty books specialist including: one book as single author, see Reference d.1, 3 books in collaboration, see References d.2, d.3 and f.1, 2 books in electronic format as single author, see References e.1 and e.2, and two laboratory guidances, see References f.2 and f.3 from the list of works presented in the References, at the end of the thesis. I also published one chapter in an international monograph, see Reference c.1.

In recognition of my work with students, I was rewarded with the prize *Bologna professor,* in 2009.

My **managerial activity** started in 2008, when I was elected the Scientific Secretary of the Faculty of Electrical and Power Engineering for a period of 4 years. At the same time, I was a member of the Board of the Faculty. In 2012, I was elected Senator of the Politehnica University of Timişoara. From this position, I activated in three committees of the Senate: The Ethics Committee, the Research Committee and The Education Committee. Within the Ethics Committee I was elected chairman, a position that qualified me as a member of the Senate Office of Politehnica University of Timişoara. When the Ethics committee became the Senate Ethics Committee of the University, I continued to hold the position of chairman of the Ethics Committee of the University, according to

the Rector's decision. In the election of 2012, I was elected member of the Department Board of Electrical Engineering of the Faculty of Electrical and Power Engineering. These activities ceased in 2013, as a consequence of the fact that I obtained, through competition, the function of Dean of the Faculty of Electrical and Power Engineering. I currently hold the same position.

The quality of the activity presented above is certified by the following:

- Reviewer in ISI Conferences: Annual IEEE Energy Conversion Congress&Exposition ECCE, 2012, 2013 şi 2014 editions, International Conference on Optimization of Electrical and Electronic Equipment OPTIM 2012

- Member of the editorial board of the following journals: International Journal of Electromagnetic and Applications, since 2010, American Journal of Electrical and Electronic Engineering, since 2011:

- Reviewer in scientific journals indexed in international databases: International Journal of Electromagnetic and Applications, since 2010, American Journal of Electrical and Electronic Engineering, since 2011, International Journal of Engineering and Technology Innovation (IJETI), since 2012;

- Member of professional international associations: Institute of Electrical and Electronics Engineers USA (IEEE), Verein Deutscher Ingenieure Germany (VDI).

During 2001-2014 I published a total of 86 works of which 2 in ISI indexed journals, 7 in BDI indexed journals, 19 in ISI Proceedings, 13 in BDI conferences proceedings, 15 in international conferences proceedings and 30 in volumes of journals, bulletins or national conferences. I participated in two grants as the representative in charge on behalf of Politehnica University of Timişoara, in 3 international projects as a manager, in 5 grants and 3 projects as a member of the research team, of which 1 was international and 2 national.

2.2. Contribution to the optimal design of alternating current electrical machines

2.2.1. Study on the skin effect in the high rectangular bars of the rotors of the three phase induction machine fed by PWM inverter

2.2.1.1. Introduction

Generally, the induction motors are designed for power supply conditions from energy sources to which the voltage is a sinusoidal wave. The parameters and the functional sizes of the electric machines are guaranteed by designers only for this situation. The values of the nominal values of the motors are given in the catalogues of companies producing electric motors for the operational voltage and working nominal frequency engraved on their plate. If the induction machine is powered by a static frequency converter a modification of its parameters and functional dimensions occurs, as compared to the case of the sinusoidal supply due to the presence of high-frequency harmonic in the voltage wave entering the motor. These harmonics, from the voltage and current given by the inverter are of the order $\nu = Jm_f \pm k$, in the case of a classic PWM modulation (ν is odd, different from 3 and the multiples of 3). The harmonics with the sign (+) rotate with the same sequence and those with sign (-) rotate in the opposite sequence as the rotating magnetic field corresponding to the fundamental [1], [2], [3], [4], [5], [7]. They result in a distorted mode of the machine, acting as such. Unfortunately, the deforming regime of the electric motor is also reflected, in the power network that supplies the converter [7].

If *the induction motor* is powered through *a pulse width modulation (PWM) inverter*, due to the presence of high time harmonics in the wave of the input voltage, both its characteristic parameters and functional sizes will be more or less different from those in the case of *sinusoidal supply*. In loading and rotation speed conditions similar to the case of sinusoidal supply, there is an increase of the loss in the motor, of the absorbed electrical power and therefore a reduction in efficiency. It is also noticeable a higher heating of the machine and an electromagnetic torque at a given load is no longer invariable, but pulsating, in relation to the average value corresponding to the load [6], [8], [17].

So far, most of the research conducted both nationally and globally has mainly targeted the inverter. Its force has been examined. Favourable results have been obtained by using IGBT transistors as semiconductor elements of the power, as well as for control, by using various modern control techniques. Regardless of wiring diagrams and of the control strategies taken into account, only alleviation, yet not the elimination of the deforming regime, has been obtained.

This study aims to analyze the skin effect and the consequences it has on the parameters of the rectangular high bar parameters of the rotor of the three-phase induction motor fed by PWM voltage inverters. The *research will highlight the modifications of the parameters of the rotor bars* under the conditions mentioned above, *comparing to the sinusoidal supplying regime*. The *study aims to clarify the behaviour of the induction machine under the condition of non-sinusoidal power*, which will serve *as a starting point for further studies to establish the optimal constructive-technological design measures to be taken to improve the parameters and implicitly the functional sizes of motors*.

The ***skin effect results*** in an uneven current density distribution in the conductors / bars section travelled by the variable (alternative) currents, the current density being higher on their side and top surface. This phenomenon can be interpreted intuitively as the result of the e.m.f. action induced by the variable magnetic flux of the currents in the conductors /bars. The induced eddy currents cause a redistribution of the main current in conductors / bars, which ***increases the resistance*** and ***decreases the reactance*** of the conductors.

In practical calculations, the variation with frequency is highlighted with ***the equivalent global factor of resistance modification in alternative current $k_{r(CSF)}$***, and ***the reactance through the equivalent global factor of reactance change $k_{x(CSF)}$***. In this study the goal is to determine the two global factors, when the three-phase induction machine is fed by PWM inverters. For the non-sinusoidal periodic permanent regime, due to the presence of harmonics in the electromagnetic field of the motor, the analysis of the skin effect must be made for the whole starting process. The two extreme situations of the start-up process, corresponding to zero speed, respectively the nominal speed, will be especially approached as the most significant for analyzing the behaviour of induction machine fed by inverter voltage [28], [29], [30], [31], [32].

The analysis of the induction motor behaviour and the evaluation of its performances in permanent regime under the conditions of supplying through inverters can be done by three methods [8], [21]:

a) **The direct integration of the equations of the machine**. In addition to determining the currents and torque in the permanent regime, this method also allows determining the variations of the rotor speed due to the pulsating torques. The main disadvantage of this method is that, especially for the average power motors, because of the larger time constant of the machine, the stabilization process of the computer integration can take longer, which limits the direct use of this method.

b) **The use of Fourier analysis**. The method is based on the decomposition of the input signal voltage into a sum of sinusoidal harmonics ν, the overall effect being the sum of partial effects. The main advantages of the method are: its simplicity and the possibility of being used in many situations of computing relations in designing electrical machines for the sinusoidal regime, practically tested on tens of thousands of motors. The disadvantage of this method is the decomposition in Fourier series of signals that are not continuous on sections and hence non-sinusoidal, thus involving weakly convergent series, with taking into account a large number of terms. However this disadvantage can be mitigated through the use of computer technology to solve the problem.

c) **The use of state variables**. It is a classical method in the theory of systems that enables the direct, analytical determination of the motor current and torque. The method can be applied in case the analyzed motor is an ideal, unsaturated, isotropic motor with constant parameters and not influenced by the values of voltage, current or frequency (which is generally not the case).

When comparing ***the advantages and disadvantages*** of the three methods described above, they can be synthesized as follows:

1. **Method "a"**. Using method "a" in solving the constructive-technological design problems is difficult, the method being generally disadvantageous because it takes long to stabilize the integration process.

2. **Method "b"**. Despite the limitation mentioned above, whose effects can be reduced by addressing computers, method "b" proves useful in identifying the constructive technological-design features of the induction motor fed by inverter, due to the possibility of using many calculation relations from the classical theory of the induction machines fed in sinusoidal regime, with possible corrections.

3. **Method "c"**. Because of the working assumptions which underpin it, method "c" is recommended to be applied in the study and modelling of automatic control systems with induction motors.

Based on these considerations, for the studies within this research, *the Fourier analysis method* will be considered. Under this method, the non-sinusoidal voltage decomposes in a series of harmonics and the action of each separate harmonics is studied, applying then *the principle of superposition effects*. The machine behavior can be analyzed considering a series of motors with the same shaft, rotating at speed n, fed by different supplies, of voltages $U_{1(v)}$ and frequencies $f_{1(v)}$. To the voltage harmonic of v order, a current harmonic of the same order, $I_{1(v)}$ corresponds. The current harmonics $I_{1(v)}$ will produce fundamental and high harmonics of the current amper spire.

The *following reasoning* will take into account some simplifying assumptions:

a) the phenomenon of current discharge in the rotor slots is neglected;

b) only the fundamental special harmonics of the current amper spire shall be taken into account.

These two hypotheses are added the one mentioned in the preceding paragraph: neglecting the saturation. It is considered that machine parameters (resistance and inductance) are not influenced by the phenomenon of saturation according to the load, so there are no time dimensions through it. The assumption is practically valid for the load changes, within the limit of those usually occurring in the functioning process. This hypothesis does not deform too much the reality as the present study aims specifically to analyze the stationary non-sinusoidal regime of the machine, at a load substantially equal to the nominal one. In this situation, the amount of current that occurs is not much different from the basic sinusoidal current value. This hypothesis is still valid even in the start-up conditions, if the means of reducing the starting current, known from the literature [22], [23], are used.

2.2.1.2. The equations of the electromagnetic field in the high rectangular rotor bars for the induction motor fed by voltage inverters. Penetration depth

In the analyzed situation, in which the three-phase induction machine is fed by a PWM inverter, applying Fourier analysis, in addition to the electromagnetic field corresponding to the fundamental there is one electromagnetic field corresponding to each harmonic of v order.

In the first stage only the fundamental, $v = 1$, is considered present. The equations of the electromagnetic field corresponding to the fundamental in a certain point of the bar from a rotor slot (for generalization, it is assumed a slot of any form) are written as [25]:

$$\Delta \overline{E}_{(1)} - j\omega_{2(1)}\sigma\mu \overline{E}_{(1)} = 0; \quad \Delta \overline{H}_{(1)} - j\omega_{2(1)}\sigma\mu \overline{H}_{(1)} = 0, \tag{2.1}$$

or

$$\Delta \overline{E}_{(1)} - \underline{\gamma}^2_{(1)} \overline{E}_{(1)} = 0; \quad \Delta \overline{H}_{(1)} - \underline{\gamma}^2_{(1)} \overline{H}_{(1)} = 0, \tag{2.2}$$

where: $\overline{E}_{(1)}$ and $\overline{H}_{(1)}$ are the intensity of the electric field, respectively the intensity of the magnetic field, both corresponding to the fundamental; μ, σ - the magnetic permeability, respectively the electrical conductivity of the bar material (material constants); $\gamma_{(1)}$ - is the propagation constant corresponding to the fundamental, with the expression:

$$\underline{\gamma}_{(1)} = \sqrt{j\omega_{2(1)}\sigma\mu} = \sqrt{js_{(1)}\omega_{1(1)}\sigma\mu} = \sqrt{js\omega_1\sigma\mu} \ . \tag{2.3}$$

The propagation constant corresponding to the fundamental can be written as [25]:

$$\underline{\gamma}_{(1)} = \alpha_{(1)} + j\beta_{(1)} = \sqrt{\omega_{2(1)}\sigma\mu} \cdot e^{j\frac{\pi}{4}} = (1+j)\sqrt{\frac{\omega_{2(1)}\sigma\mu}{2}} \tag{2.4}$$

In the relation (2.4):

$\alpha_{(1)}$ - is the attenuation constant corresponding to the fundamental (the real part);

$\beta_{(1)}$ - is the phase constant corresponding to the fundamental (the imaginary part).

It can be noticed that in the considered case, the following relation applies:

$$\alpha_{(1)} = \beta_{(1)} = \sqrt{\frac{\omega_{2(1)}\sigma\mu}{2}} = \sqrt{\frac{s\omega_1\sigma\mu}{2}} = \sqrt{\pi s f_1 \sigma\mu} \ . \tag{2.5}$$

The penetration depth of the fundamental of the electromagnetic field in the bar from the rotor slot of any form is given by the relation [25]:

$$\delta_{(1)} = \sqrt{\frac{2\rho}{\omega_{2(1)}\mu}} = \sqrt{\frac{2\rho}{s\omega_1\mu}} \ , \tag{2.6}$$

where ρ is the electrical resistivity of the bar material.

In the start-up moment, when $s_{(1)} = s = 1$, the relation (2.6) becomes:

$$\delta_{(1)p} = \sqrt{\frac{\rho}{\pi f_1 \mu}} = 0.564\sqrt{\frac{\rho}{\mu f_1}} \ , \tag{2.7}$$

in which $\delta_{(1)p}$ is the penetration depth of the fundamental of the electromagnetic field in a bar placed in a rotor slot at the start-up moment. One considers the value of the frequency voltage $f_1 = 50$ [Hz]. If in the relation (2.7), we consider ρ in [Ωmm^2/m], frequency in [Hz], taking into account that $\mu = \mu_0 \cdot \mu_r$, where $\mu_0 = 4\pi \cdot 10^{-7}$ [H/m] is the void permeability and μ_r is the relative permeability of the cage material, it is obtained:

$$\delta_{(1)p} = 0.564\sqrt{\frac{\rho \cdot 10^{-6}}{4\pi \cdot 10^{-7}\mu_r \cdot f_1}} = 0.503\sqrt{\frac{\rho}{\mu_r \cdot f_1}} \qquad [\text{m}] \ . \tag{2.8}$$

At the end of the start-up process, at the nominal load, the slip is $s_{(1)} = s_n$. For this situation, the relation (2.6) takes the following form:

$$\delta_{(1)n} = \sqrt{\frac{2\rho}{s_n\omega_1\mu}} = 0.503\sqrt{\frac{\rho}{f_1\mu_r s_n}} \ . \tag{2.9}$$

$\delta_{(1)n}$ is the penetration depth of the fundamental in the electromagnetic field of the motor in the bar of the rotor slot, at the nominal load of the induction motor.

If relation (2.8) is divided by (2.9), the following ratio is obtained:

$$k_{\delta(1)n} = \frac{\delta_{(1)p}}{\delta_{(1)n}} = \frac{0.503\sqrt{\dfrac{\rho}{f_1\mu_r}}}{0.503\sqrt{\dfrac{\rho}{f_1\mu_r s_n}}} = \sqrt{s_n} \; . \tag{2.10}$$

The factor $k_{\delta(1)n}$ emphasises the change of the penetration depth corresponding to the fundamental, $\delta_{(1)n}$, during the start-up process. .

Analyzing the relations (2.8), (2.9) and (2.10) the following conclusions can be drawn:

1. The penetration depth of the fundamental of the electromagnetic field in the bar from a rotor slot (of any shape, in the general case) does not depend on the geometric dimensions of the considered rotor bar (slot), but only on the nature of the cage material and on the phenomena frequency.

2. The ratio $k_{\delta(1)n}$ depends only on the nominal slip of the motor.

3. The factor $k_{\delta(1)n}$ emphasises the fact that the penetration depth of the fundamental of the electromagnetic field from the machine in the bar from the rotor slot, at the nominal load of the motor, is much bigger than in the initial start-up point.

Thus, for example, for the nominal slip of the induction machine, $s_n = 0.04$, according to the equation (2.10) it is obtained:

$$k_{\delta(1)n} = \frac{\delta_{(1)p}}{\delta_{(1)n}} = \sqrt{0.04} = 0.2 \, , \text{ namely } \delta_{(1)n} = 5\delta_{(1)p}. \tag{2.11}$$

The relationships (2.9) and (2.10) also allow determining the penetration depth $\delta_{(1)}$ and the factor $k_{\delta(1)}$ for a certain loading of the induction machine. For this, in the relations mentioned above the nominal slip s_n should be replaced with the slip s, corresponding to a certain motor load.

Next, we consider the presence in the supply of the induction motor only of a certain **harmonic ν**. For this, the relations established before get the form:

$$\Delta\overline{\underline{E}}_{(v)} - \underline{\gamma}_{(v)}^2 \overline{\underline{E}}_{(v)} = 0; \quad \Delta\overline{\underline{H}}_{(v)} - \underline{\gamma}_{(v)}^2 \overline{\underline{H}}_{(v)} = 0 \, , \tag{2.12}$$

where $\overline{\underline{E}}_{(v)}$ and $\overline{\underline{H}}_{(v)}$ are the intensity of the electrical field, respectively magnetic field, (both corresponding to the ν order harmonics), and $\gamma_{(v)}$ is the propagation constant correspondent to the same harmonics of the electromagnetic field:

$$\underline{\gamma}_{(v)} = \sqrt{j\omega_{2(v)}\sigma\mu} = \sqrt{js_{(v)}\omega_{1(v)}\sigma\mu} = \sqrt{js_{(v)}\nu\omega_1\sigma\mu} \, , \tag{2.13}$$

in which:

$$s_{(v)} = 1 \mp \frac{1}{\nu} \pm \frac{s}{\nu} \, . \tag{2.14}$$

The pair of signs (-), (+) (above) correspond to the wave which rotates in the direction of the main wave and the pair of signs (+), (-) to the opposite wave.

In this case the following relations are valid:

$$\alpha_{(\nu)} = \beta_{(\nu)} = \sqrt{\frac{\omega_{2(\nu)}\sigma\mu}{2}} = \sqrt{\frac{s_{(\nu)}\nu\omega_1\sigma\mu}{2}} = \sqrt{\pi s_{(\nu)}\nu f_1\sigma\mu} \ . \tag{2.15}$$

The penetration depth of the ν harmonics of the electromagnetic field in the bar from the rotor slot of any shape, can be written as:

$$\delta_{(\nu)} = \sqrt{\frac{2\rho}{s_{(\nu)}\nu\omega_1\mu}} \ . \tag{2.16}$$

In the start-up point $s_{(\nu)} = 1$, in the relation (2.14) $s = 1$, and the relation (2.16) gets the form:

$$\delta_{(\nu)p} = 0.503\sqrt{\frac{\rho}{\nu f_1\mu_r}} \ . \tag{2.17}$$

At the end of the start-up process, considering the induction machine loaded at a nominal load,

$$s_{(\nu)n} = 1 \mp \frac{1}{\nu} \pm \frac{s_n}{\nu}, \tag{2.18}$$

And the relation (2.16) becomes:

$$\delta_{(\nu)n} = 0.503\sqrt{\frac{\rho}{\nu f_1\mu_r s_{(\nu)n}}} \ . \tag{2.19}$$

As in the previous case ($\nu = 1$), the report can be written:

$$k_{\delta(\nu)n} = \frac{\delta_{(\nu)p}}{\delta_{(\nu)n}} = \sqrt{s_{(\nu)n}} \ . \tag{2.20}$$

The conclusions 1 and 2 presented when **analysing the fundamental** remain valid and for the **ν order harmonic**, with the following observations:

1. Frequency at which the phenomena occur n the rotor bar is:

$$f_{2(\nu)} = s_{(\nu)} \cdot f_{1(\nu)} = s_{(\nu)} \cdot \nu \cdot f_1 . \tag{2.21}$$

2. The slip defining the report $k_{\delta(\nu)n}$ for the nominal load is given by the relation (2.18).

3. Similarly, it should be underlined that for the higher ν order harmonics, the penetration depth $\delta_{(\nu)n}$ differs in far less way from $\delta_{(\nu)p,}$ relative to the situation described in fundamental (see also conclusion 3 from the fundamental analysis).

Thus, for example, assuming the same nominal slip as in the case of fundamental analysis, ($s_n = 0.04$), in the case of the 11 order harmonic, of direct succession, according to the equation (2.14), we have $s_{(\nu)n} = 0.912$ (Table 2.1), hence, it results, using the equation (2.20):

$$k_{\delta(\nu)n} = \frac{\delta_{(\nu)p}}{\delta_{(\nu)n}} = \sqrt{0.912} = 0.954, \text{ namely } \delta_{(\nu)n} = 1.047 \cdot \delta_{(\nu)p} . \tag{2.22}$$

In the case of $\nu = 11$ harmonic, yet of inverse succesion, $s_{(\nu)n} = 1.087$, and

$$k_{\delta(v)n} = \frac{\delta_{(v)p}}{\delta_{(v)n}} = \sqrt{1.087} = 1.042 \text{, namely } \delta_{(v)n} = 0.959 \cdot \delta_{(v)p}. \tag{2.23}$$

It can be concluded that, in the case of high time harmonics of v order, the uniformity of the current density on the surface of the bar section is virtually the same in the start-up moment with the one of the nominal load. For ***direct sequence harmonics,*** at nominal load, a slight increase in the penetration depth of the electromagnetic field occurs comparing to the start-up (so there is a slight decrease of the skin effect). In the case of ***the reverse sequence harmonics***, yet of the same order, the penetration depth is slightly lower than the starting regime (there is a slight emphasis on the phenomenon of skin effect).

Further, it will be analysed the pair of measures $\delta_{(1)}$ and $\delta_{(v)}$, also for the two limit points of the start-up process. This way a comparative study is to be developed comparing the penetration depth as a measure of the skin effect, corresponding to the v harmonic of the electromagnetic field, and the penetration depth corresponding to the fundamental electromagnetic field (the electromagnetic field that appears in the motor at its sinusoidal supply). For this it is reported $\delta_{(v)p}$ to $\delta_{(1)p}$ and $\delta_{(v)n}$ to $\delta_{(1)n}$, , obtaining:

$$k_{\delta(v),(1)p} = \frac{\delta_{(v)p}}{\delta_{(1)p}} = \frac{0,503\sqrt{\dfrac{\rho}{vf_1\mu_r}}}{0,503\sqrt{\dfrac{\rho}{f_1\mu_r}}} = \frac{1}{\sqrt{v}} \quad , \tag{2.24}$$

$$k_{\delta(v),(1)n} = \frac{\delta_{(v)n}}{\delta_{(1)n}} = \frac{0,503\sqrt{\dfrac{\rho}{vf_1\mu_r s_{(v)n}}}}{0,503\sqrt{\dfrac{\rho}{f_1\mu_r s_n}}} = \sqrt{\frac{1}{v}\cdot\frac{s_n}{s_{(v)n}}} \quad . \tag{2.25}$$

Analyzing the ratios (2.24) and (2.25), it can be noticed that both at the beginning of the start-up process ($n = 0$) and the end of it ($n = n_n$; the nominal load was considered), the two ratios presented above do not depend on the nature of the material the rotoric cage is made of. At $n = 0$, $k_{\delta(v),(1)p}$ depends only on the order of the harmonic, and at n_n speed, the ratio $k_{\delta(v),(1)n}$ depends not only on the harmonic grade, but also on the nominal slips of the fundamental, respectively the v order harmonics. The material the cage is made of influences the value of the penetration depth for both the fundamental and the v order harmonic, in both key moments of the start-up process ($n = 0$; $n = n_n$).

Given the important role the penetration depth has in the study of the skin effect, it is useful, for information purposes, to know some of its particular values. In this regard, in Table 2.1., some calculated values for the penetration depth $\delta_{(1)}$ and $\delta_{(v)}$ are presented, respectively for the ratios $k_{\delta(1)n}$, $k_{\delta(v)n}$ and $k_{\delta(v),(1)}$, for the two extreme points of the start-up process, corresponding to $n = 0$ and $n = n_n$. The calculations are shown in parallel for the two materials that are currently used to make the rotor cages of the induction motor: ***aluminium*** and ***copper***. In order to investigate the influence of ***the frequency modulation factor m_f*** (defined as the ratio between the switching frequency or the carrier frequency f_r and the frequency of the command/control modulating signals f_c) on the analyzed measures, three particular values were considered for this: $m_f = 9$, $m_f = 15$ and $m_f = 21$. The results obtained are shown in Table 2.1.

It states that:

a. For calculating the measures in Table 2.1, $\delta_{(1)p}$, $\delta_{(\nu)p}$, $\delta_{(1)n}$, $\delta_{(\nu)n}$, $k_{\delta(1)n}$, $k_{\delta(\nu)n}$ and $k_{\delta(\nu),(1)p}$ and $k_{\delta(\nu),(1)n}$ the relations (2.8), (2.17), (2.9), (2.19), (2.10), (2.20), (2.24) and (2.25) were used.

b. The values of the material constants used are: for copper (diamagnetic material) - the electrical resistivity at 20 [°C], $\rho_{Cu20} = 0.01784$ [$\Omega\text{mm}^2/\text{m}$] and the relative permeability $\mu_r = 0.999999$, and for aluminum (paramagnetic material) $\rho_{Al20} = 0.031$ [$\Omega\text{mm}^2/\text{m}$] and $\mu_r = 1.000022$ [25], [26], [27].

c. For the nominal slip it was considered, for example, the value $s_n = 4[\%]$.

d. The phenomena were analyzed for a supplying frequency of the fundamental $f_1 = f_{1n} = 50$ [Hz].

Analyzing the results presented in Table 2.1, we can draw the following conclusions:

1. Upon the initial moment of the start-up process ($n = 0$), when the maximum discharge phenomenon occurs, it should be considered both the contribution of the electromagnetic field corresponding to the fundamental and those of the electromagnetic fields corresponding to the ν order time harmonics. At the end of the starting process (setting motor at the speed $n = n_n$) assuming that the load is the nominal one, in contrast to sinusoidal regime, where it may be considered as first approximation that the electric current density is uniform on the surface of the section bar, at the supplying of the induction motor by a PWM voltage inverter, a skin effect is manifested due to ν order harmonic fields. In the study of the skin effect produced by the ν order electromagnetic fields one must also take into account the percentage these harmonics represent of the fundamental.

2. The increasing of the value of the modulation factor in frequency value m_f by increasing m_f, the ν order of the time harmonic increases) results in decreasing the penetration depth of the ν order harmonic electromagnetic field. Therefore, with the increase of m_f (ν), at a first glance, it would seem that there is an increase in discharge phenomenon. The decreased penetration depth is however compensated by the declining share of the ν order harmonics from the fundamental, as will be seen below.

3. For the direct sequence harmonic fields, $k_{\delta(\nu)n} < 1$, and for those of reverse sequence $k_{\delta(\nu)n} > 1$. For the direct sequence harmonic fields, with increasing the ν order time harmonic, $k_{\delta(\nu)n}$ increases, and for those in reverse sequence, when ν increases a decrease of $k_{\delta(\nu)n}$ is registered. For both sequences, when ν increases, $k_{\delta(\nu),(1)p}$, $k_{\delta(\nu),(1)n}$ decreases (see findings from the fundamental analysis, respectively ν order harmonics).

4. The material the rotor cage is made of only influences the value of the penetration depth $\delta_{(1)p}$, $\delta_{(1)n}$, $\delta_{(\nu)p}$ and $\delta_{(\nu)n}$. The values of the ratios $k_{\delta(1)n}$, $k_{\delta(\nu)n}$ $k_{\delta(\nu),(1)p}$ and $k_{\delta(\nu),(1)n}$ remain constant, regardless of the cage material, for the same ν order and the same sequence (direct or reverse) of the electromagnetic field.

5. For cages made of aluminium an increase in the penetration depth of approx. 31.8% can be observed compared with the cages made of copper, regardless of the harmonic order or sequence. Therefore, for the copper cages the phenomena related to discharging are broader.

Table 2.1. Calculated values for the penetration depths of the electromagnetic field fundamental in the rotoric bar of any shape, $\delta_{(1)p}$, $\delta_{(1)m}$, respectively of the ν order harmonic of the electromagnetic field, $\delta_{(\nu)p}$, $\delta_{(\nu)m}$, under the conditions of a rotoric cage made of aluminium or copper, in the case of supplying the induction motor by a voltage inverter using classical PWM modulation for the particular values of m_f: 9, 15 and 21.

m_f	$\nu = Jm_f \pm k$, $J=1,2,\dots,k\in\mathbf{Z}$, even if $J=1$, odd if $J=2$	ν	$s_{(\nu)n}$	Aluminum								Copper							
				$\delta_{(1)p}$ [mm]	$\delta_{(\nu)p}$ [mm]	$\delta_{(1)n}$ [mm]	$\delta_{(\nu)n}$ [mm]	$k_{\delta(1)n}$	$k_{\delta(\nu)n}$	$k_{\delta(\nu)\Lambda(1)p}$	$k_{\delta(\nu)\Lambda(1)n}$	$\delta_{(1)p}$ [mm]	$\delta_{(\nu)p}$ [mm]	$\delta_{(1)n}$ [mm]	$\delta_{(\nu)n}$ [mm]	$k_{\delta(1)n}$	$k_{\delta(\nu)n}$	$k_{\delta(\nu)\Lambda(1)p}$	$k_{\delta(\nu)\Lambda(1)n}$
	$\nu = 1$		0,04	12,52	-	62,62	-	0,2	-	-	-	9,50	-	47,5	-	0,2	-	-	-
9	1·9±2	11	0.912	-	3.77	-	3.95	-	0.954	0.301	0.063	-	2.86	-	2.99	-	0.954	0.301	0.063
		7	1.137	-	4.73	-	4.43	-	1.066	0.377	0.07	-	3.59	-	3.36	-	1.066	0.377	0.07
9	1·9±4	13	0.926	-	3.47	-	3.60	-	0.962	0.277	0.057	-	2.63	-	2.73	-	0.962	0.277	0.057
		5	1.192	-	5.60	-	5.13	-	1.091	0.447	0.081	-	4.24	-	3.89	-	1.091	0.447	0.081
9	2·9±1	19	0.949	-	2.87	-	2.94	-	0.974	0.229	0.047	-	2.17	-	2.23	-	0.974	0.229	0.047
		17	1.056	-	3.03	-	2.95	-	1.027	0.242	0.047	-	2.30	-	2.24	-	1.027	0.242	0.047
9	2·9±5	23	0.958	-	2.61	-	2.66	-	0.978	0.208	0.042	-	1.98	-	2.02	-	0.978	0.208	0.042
		13	1.073	-	3.47	-	3.35	-	1.035	0.277	0.053	-	2.63	-	2.54	-	1.035	0.277	0.053
9	3·9±2	29	0.966	-	2.32	-	2.36	-	0.982	0.185	0.037	-	1.76	-	1.79	-	0.983	0.185	0.037
		25	1.038	-	2.50	-	2.45	-	1.018	0.20	0.039	-	1.90	-	1.86	-	1.018	0.20	0.039
9	3·9±4	31	0.969	-	2.24	-	2.28	-	0.984	0.179	0.036	-	1.70	-	1.73	-	0.984	0.179	0.036
		23	1.041	-	2.61	-	2.55	-	1.020	0.208	0.04	-	1.98	-	1.94	-	1.020	0.208	0.040
9	4·9±1	37	0.974	-	2.05	-	2.08	-	0.986	0.164	0.033	-	1.56	-	1.58	-	0.986	0.164	0.033
		35	1.027	-	2.11	-	2.08	-	1.013	0.169	0.033	-	1.6	-	1.58	-	1.013	0.169	0.033
9	4·9±5	41	0.976	-	1.95	-	1.97	-	0.987	0.156	0.031	-	1.48	-	1.5	-	0.987	0.156	0.031
		31	1.030	-	2.24	-	2.21	-	1.014	0.179	0.035	-	1.7	-	1.68	-	1.014	0.179	0.035
9	4·9±7	43	0.977	-	1.90	-	1.93	-	0.988	0.152	0.030	-	1.44	-	1.46	-	0.988	0.152	0.030
		29	1.033	-	2.32	-	2.28	-	1.016	0.185	0.036	-	1.76	-	1.73	-	1.016	0.185	0.036
15	1·15±2	17	0.943	-	3.03	-	3.12	-	0.971	0.242	0.049	-	2.3	-	2.37	-	0.971	0.242	0.049
		13	1.073	-	3.47	-	3.35	-	1.035	0.277	0.053	-	2.63	-	2.54	-	1.035	0.277	0.053
15	1·15±4	19	0.949	-	2.87	-	2.94	-	0.974	0.229	0.047	-	2.17	-	2.23	-	0.974	0.229	0.047
		11	1.087	-	3.77	-	3.62	-	1.042	0.301	0.057	-	2.86	-	2.74	-	1.042	0.301	0.057
15	2·15±1	31	0.969	-	2.24	-	2.28	-	0.984	0.179	0.036	-	1.7	-	1.73	-	0.984	0.179	0.036
		29	1.033	-	2.32	-	2.28	-	1.016	0.185	0.036	-	1.76	-	1.73	-	1.016	0.185	0.036
15	2·15±5	35	0.972	-	2.11	-	2.14	-	0.985	0.169	0.034	-	1.6	-	1.62	-	0.985	0.169	0.034
		25	1.038	-	2.50	-	2.45	-	1.018	0.20	0.039	-	1.9	-	1.86	-	1.018	0.20	0.039
5	3·15±2	47	0.979	-	1.82	-	1.84	-	0.989	0.145	0.029	-	1.38	-	1.40	-	0.989	0.145	0.029

m_f	$\nu = Jm_f \pm k$, $J=1,2,...,k\in\mathbf{Z}$, even if $J=1$, odd if $J=2$	$\nu=1$	$s_{(\nu)\pi}$	Aluminum								Copper							
				$\delta_{(1)p}$ [mm]	$\delta_{(\nu)p}$ [mm]	$\delta_{(1)\pi}$ [mm]	$\delta_{(\nu)\pi}$ [mm]	$k_{\delta(1)\pi}$	$k_{\delta(\nu)\pi}$	$k_{\delta(\nu),(1)p}$	$k_{\delta(\nu),(1)\pi}$	$\delta_{(1)p}$ [mm]	$\delta_{(\nu)p}$ [mm]	$\delta_{(1)\pi}$ [mm]	$\delta_{(\nu)\pi}$ [mm]	$k_{\delta(1)\pi}$	$k_{\delta(\nu)\pi}$	$k_{\delta(\nu),(1)p}$	$k_{\delta(\nu),(1)\pi}$
		1	0,04	12,52	-	62,62	-	0,2	-	-	-	9,50	-	47,5	-	0,2	-	-	-
15		43	1.022	-	1.90	-	1.88	-	1.01	0.152	0.030	-	1.44	-	1.43	-	1.01	0.152	0.030
15	3-15±4	49	0.98	-	1.78	-	1.8	-	0.989	0.142	0.028	-	1.35	-	1.37	-	0.989	0.142	0.028
		41	1.023	-	1.95	-	1.93	-	1.011	0.156	0.030	-	1.48	-	1.46	-	1.011	0.156	0.030
15	4-15±1	61	0.984	-	1.60	-	1.61	-	0.991	0.128	0.025	-	1.21	-	1.22	-	0.991	0.128	0.025
		59	1.016	-	1.63	-	1.61	-	1.007	0.130	0.025	-	1.23	-	1.22	-	1.007	0.130	0.025
15	4-15±5	65	0.985	-	1.55	-	1.56	-	0.992	0.124	0.024	-	1.17	-	1.18	-	0.992	0.124	0.024
		55	1.017	-	1.68	-	1.67	-	1.008	0.134	0.026	-	1.28	-	1.27	-	1.008	0.134	0.026
15	4-15±7	67	0.985	-	1.53	-	1.54	-	0.992	0.122	0.024	-	1.16	-	1.17	-	0.992	0.122	0.024
		53	1.018	-	1.72	-	1.70	-	1.008	0.137	0.027	-	1.30	-	1.29	-	1.008	0.137	0.027
21	1-21±2	23	0.958	-	2.61	-	2.66	-	0.978	0.208	0.042	-	1.98	-	2.02	-	0.978	0.208	0.042
		19	1.05	-	2.87	-	2.80	-	1.024	0.229	0.044	-	2.17	-	2.12	-	1.024	0.229	0.044
21	1-21±4	25	0.961	-	2.50	-	2.55	-	0.98	0.20	0.040	-	1.90	-	1.93	-	0.98	0.20	0.040
		17	1.056	-	3.03	-	2.95	-	1.027	0.242	0.047	-	2.30	-	2.24	-	1.027	0.242	0.047
21	2-21±1	43	0.977	-	1.90	-	1.93	-	0.988	0.152	0.030	-	1.44	-	1.46	-	0.988	0.152	0.030
		41	1.023	-	1.95	-	1.93	-	1.011	0.156	0.030	-	1.48	-	1.46	-	1.011	0.156	0.030
21	2-21±5	47	0.979	-	1.82	-	1.84	-	0.989	0.145	0.029	-	1.38	-	1.40	-	0.989	0.145	0.029
		17	1.056	-	3.03	-	2.95	-	1.027	0.242	0.047	-	2.30	-	2.24	-	1.027	0.242	0.047
21	3-21±2	65	0.985	-	1.55	-	1.56	-	0.992	0.124	0.024	-	1.17	-	1.18	-	0.992	0.124	0.024
		61	1.015	-	1.60	-	1.59	-	1.007	0.128	0.025	-	1.21	-	1.20	-	1.007	0.128	0.025
21	3-21±4	67	0.985	-	1.53	-	1.54	-	0.992	0.122	0.024	-	1.16	-	1.17	-	0.992	0.122	0.024
		59	1.016	-	1.63	-	1.61	-	1.007	0.130	0.025	-	1.23	-	1.22	-	1.007	0.130	0.025
21	4-21±1	85	0.988	-	1.35	-	1.36	-	0.993	0.108	0.021	-	1.03	-	1.04	-	0.993	0.108	0.021
		83	1.011	-	1.37	-	1.36	-	1.005	0.109	0.021	-	1.04	-	1.03	-	1.005	0.109	0.021
21	4-21±5	89	0.989	-	1.32	-	1.33	-	0.994	0.105	0.021	-	1.007	-	1.01	-	0.994	0.105	0.021
		79	1.012	-	1.40	-	1.40	-	1.005	0.112	0.022	-	1.06	-	1.07	-	1.005	0.112	0.022
21	4-21±7	91	0.989	-	1.31	-	1.32	-	0.994	0.104	0.021	-	0.99	-	1.001	-	0.994	0.104	0.021
		77	1.012	-	1.42	-	1.41	-	1.005	0.113	0.022	-	1.08	-	1.07	-	1.005	0.113	0.022

2.2.1.3. Determination of equivalent global change factors of the parameters of the high rectangular rotor bar of the three-phase induction motors fed by PWM inverters

Based on the facts analysed in the previous paragraph, the question of determining the ***two changing factors of the resistance in alternative current $k_{r(CSF)}$ and of the reactance $k_{x(CSF)}$***, corresponding to the situation in which the motor is fed by PWM inverters, under a global form. It will be taken into account the geometries of the rotor with high rectangular bars. The study has as starting point the experimental and theoretical results presented extensively in [15], [16], [18], [19], [24].

In the analysis ***the following simplifying assumptions*** are allowed:

a) It is considered that the magnetic core is infinitely large in comparison with that of the air, the lines of the magnetic field being straight lines perpendicular on the axis of slot.

b) Both the ferromagnetic core and rotor cage (bar + shorting rings) are homogeneous and isotropic media.

c) The marginal effect (end) is neglected, the slot being considering very long in the axial direction. The electromagnetic fields, both the fundamental one and those corresponding to the ν order harmonics, are considered in this case as plane-parallel. This hypothesis is accepted for theoretical calculations by most researchers.

d) The skin effect is taken into account in the calculations only in the bars that are in the area of the magnetic transversal field from the slot. For the portions of the bar outside of the slot, in the ventilation channels (where applicable), as well as the shorting rings, the current density is considered constant for the whole cross-section of the bar.

e) The transition from the area with constant density in the one with variable density occurs abruptly.

f) In the real electric machines, the skin effect is often influenced by the degree of saturation (especially at start-up), but the simultaneous coverage of both phenomena in mathematical relationships easily to apply is practically difficult, even uncertain. For this reason, in establishing the relations for the equivalent global factors $k_{r(CSF)}$ and $k_{x(CSF)}$ the simplifying hypothesis of neglecting the saturation effects is admitted.

g) The local variation of the magnetic induction and of the electric current density, both for the fundamental and for each ν harmonic, is considered sinusoidal with respect to time.

In the context of these hypotheses, the ***method of Fourier analysis*** was approached. In this case, this method consists in determining the increasing factors of the resistance, respectively the decreasing one of the reactance for each harmonic, including the ones for the fundamental and then (by applying the effects superposition) in determining the ***two global equivalent factors $k_{r(CSF)}$ and $k_{x(CSF)}$***. As mentioned in the introduction, the following reasoning is valid in the situation of the rectangular high bars from the rotoric slots of the induction machine.

For the start, only one ***fundamental*** is considered present in the supply of the motor to which the supply pulsation $\omega_{1(1)} = \omega_1 = 2\pi f_1$ corresponds.

The apparent power corresponding to the fundamental is [25]:

$$\underline{S}_{(1)} = \int_{\Sigma} \underline{E}_{(1)} \underline{H}^{*}_{(1)} dA = \int_{\Sigma} \sigma \underline{J}_{(1)} \underline{H}^{*}_{(1)} dA \tag{2.26}$$

This power is different from zero just on the surface from the air-gap of the bar and consequently:

$$\underline{S}_{(1)} = \sigma \underline{J}_{(1)}(h)\underline{H}_{(1)}^{*}(h)bl = \sigma(\frac{l}{b})I_{(1)}^2(1+j)\alpha_{(1)}\frac{\text{ch}\alpha_{(1)}(1+j)z}{\text{sh}\alpha_{(1)}(1+j)h}, \tag{2.27}$$

where h and b represent the height, respectively the width of the rectangular slot. By separating the real part from the unreal one it is obtained:

$$\underline{S}_{(1)} = \frac{\rho\, l}{bh}I_{(1)}^2\xi_{(1)}\frac{\text{sh}2\xi_{(1)}+\sin 2\xi_{(1)}}{\text{ch}2\xi_{(1)}-\cos 2\xi_{(1)}} + j\frac{\rho\, l}{bh}I_{(1)}^2\xi_{(1)}\frac{\text{sh}2\xi_{(1)}-\sin 2\xi_{(1)}}{\text{ch}2\xi_{(1)}-\cos 2\xi_{(1)}}, \tag{2.28}$$

where $\xi_{(1)} = \alpha_{(1)}h$ represents the reduced height of the bar corresponding to the fundamental and ρ is the electric resistivity of the material of the bar. The loss in alternative current from the bar corresponding to the fundamental, on a length l is:

$$P_{ca(1)} = \text{Re}\{\underline{S}_{(1)}\} = \frac{\rho\, l}{bh}\xi_{(1)}\frac{\text{sh}2\xi_{(1)}+\sin 2\xi_{(1)}}{\text{ch}2\xi_{(1)}-\cos 2\xi_{(1)}}I_{(1)}^2 \tag{2.29}$$

By reporting this loss to the one without considering the skin effect in a bar of the same dimensions:

$$P_{cc} = RI^2 = \frac{\rho\, l}{bh}I_{(1)}^2 \tag{2.30}$$

The increasing factor of the resistance in alternative, corresponding to the fundamental results in the form:

$$k_{r(1)} = \frac{P_{ca(1)}}{P_{cc}} = \xi_{(1)}\frac{\text{sh}2\xi_{(1)}+\sin 2\xi_{(1)}}{\text{ch}2\xi_{(1)}-\cos 2\xi_{(1)}} \tag{2.31}$$

The reactive power, corresponding to the fundamental has the expression:

$$Q_{ca(1)} = \text{Im}\{\underline{S}_{(1)}\} = \frac{\rho\, l}{bh}\xi_{(1)}\frac{\text{sh}2\xi_{(1)}-\sin 2\xi_{(1)}}{\text{ch}2\xi_{(1)}-\cos 2\xi_{(1)}}I_{(1)}^2 \tag{2.32}$$

By reporting this reactive power to the reactive one in the case of a uniform distribution of the current, it is obtained:

$$Q_{cc} = \frac{1}{3}\omega_2\mu_0 lI_{(1)}^2 \tag{2.33}$$

The reduction factor of the reactance in alternative current, corresponding to the fundamental:

$$k_{x(1)} = \frac{Q_{ca(1)}}{Q_{cc}} = \frac{3}{2\xi_{(1)}}\frac{\text{sh}2\xi_{(1)}-\sin 2\xi_{(1)}}{\text{ch}2\xi_{(1)}-\cos 2\xi_{(1)}} \tag{2.34}$$

When the supply of the motor is considered present just in the harmonic of the **order ν** ($\nu = Jm_f \pm k$, $J = 1, 2, \ldots$; $k \in \mathbf{Z}$, even if J is odd and odd id J is even), to which the supply pulsation $\omega_{1(\nu)} = \nu \cdot \omega_1$ corresponds, the relations $2.26 \div 2.34$ maintaining their validity, with the following observations:

1. "*1*" is replaced by "ν" index;

2. the phenomena in rotor take place with the pulsation $\omega_{2(\nu)}$, given by the relation:

3.
$$\omega_{2(\nu)} = s_{(\nu)} \cdot \omega_{1(\nu)} = \left(1 \mp \frac{1}{\nu} \pm \frac{s}{\nu}\right) \cdot \nu \cdot \omega_1 \quad, \tag{2.35}$$

In the relation (2.35) the signs pair (-) ÷ (+) corresponds to the wave which rotates in the direction of the main wave, while the signs pair (+) ÷ (-) of the opposite direction wave.

Further, the real case will be considered in which both the fundamental and the time harmonics of ν rank are present in the rotoric bar. For this situation, the global equivalent modifying factor of the resistance of the bar in a. c. is calculated through the relation:

$$k_{r(CSF)} = \frac{P_{(CSF)ca}}{P_{(CSF)cc}} \quad, \tag{2.36}$$

where: $P_{(CSF)ca}$ represents the total loss in alternative in rotoric bar, considering the skin effect correspondent to the harmonics and $P_{(CSF)cc}$ the total loss, without considering the skin effect in the rotoric bar. The total loss in alternative in the rotoric bar is obtained applying the principle of the effects superposition, by adding all the loss in alternative from the bar determined by each time harmonic of ν order, including the fundamental. Therefore, it is obtained:

$$P_{(CSF)ca} = \sum_{\nu=1} P_{ca(\nu)} = \sum_{\upsilon=1} \frac{\rho l}{bh} \xi_{(\nu)} \frac{\mathrm{sh}2\xi_{(\nu)} + \sin 2\xi_{(\nu)}}{\mathrm{ch}2\xi_{(\nu)} - \cos 2\xi_{(\nu)}} I^2_{(\upsilon)} = \frac{\rho l}{bh} \sum_{\upsilon=1} \xi_{(\nu)} \frac{\mathrm{sh}2\xi_{(\nu)} + \sin 2\xi_{(\nu)}}{\mathrm{ch}2\xi_{(\nu)} - \cos 2\xi_{(\nu)}} I^2_{(\upsilon)} \tag{2.37}$$

The power in a bar of the same dimensions, in the case the skin effect is not considered, is:

$$P_{(CSF)cc} = \frac{\rho l}{bh} \sum_{\upsilon=1} I^2_{(\upsilon)} \tag{2.38}$$

In these conditions, ***the increasing factor of the resistance in alternative*** has the following formula:

$$k_{r(CSF)} = \frac{\displaystyle\sum_{\upsilon=1} \xi_{(\upsilon)} \frac{\mathrm{sh}2\xi_{(\upsilon)} + \sin 2\xi_{(\upsilon)}}{\mathrm{ch}2\xi_{(\upsilon)} - \cos 2\xi_{(\upsilon)}} I^2_{(\upsilon)}}{\displaystyle\sum_{\upsilon=1} I^2_{(\upsilon)}} = \frac{\displaystyle\sum_{\upsilon=1} \xi_{(\upsilon)} \frac{\mathrm{sh}2\xi_{(\upsilon)} + \sin 2\xi_{(\upsilon)}}{\mathrm{ch}2\xi_{(\upsilon)} - \cos 2\xi_{(\upsilon)}} \frac{I^2_{(\upsilon)}}{I^2_{(1)}}}{\displaystyle\sum_{\upsilon=1} \frac{I^2_{(\upsilon)}}{I^2_{(1)}}} \tag{2.39}$$

Analogically, for the decreasing factor of the reactance in alternative current the following relation is obtained:

$$k_{x(CSF)} = \frac{\displaystyle\sum_{\upsilon=1} \frac{3}{2\xi_{(\upsilon)}} \frac{\mathrm{sh}2\xi_{(\upsilon)} - \sin 2\xi_{(\upsilon)}}{\mathrm{ch}2\xi_{(\upsilon)} - \cos 2\xi_{(\upsilon)}} I^2_{(\upsilon)}}{\displaystyle\sum_{\upsilon=1} I^2_{(\upsilon)}} = \frac{\displaystyle\sum_{\upsilon=1} \frac{3}{2\xi_{(\upsilon)}} \frac{\mathrm{sh}2\xi_{(\upsilon)} - \sin 2\xi_{(\upsilon)}}{\mathrm{ch}2\xi_{(\upsilon)} - \cos 2\xi_{(\upsilon)}} \frac{I^2_{(\upsilon)}}{I^2_{(1)}}}{\displaystyle\sum_{\upsilon=1} \frac{I^2_{(\upsilon)}}{I^2_{(1)}}} \tag{2.40}$$

The ratio $\dfrac{I^2_{(\upsilon)}}{I^2_{(1)}}$ can be also written in the form [18], [19]:

$$\frac{I_{1(v)}}{I_{1(1)}} = \frac{U_{1(v)}}{U_{1(1)}} \cdot \frac{1}{vf_{1r}} \cdot \frac{1}{x_{sc}^*} \quad, \tag{2.41}$$

where: $x_{sc}^* = \dfrac{X_{sc}}{Z_{(1)}}$ - is the reported short circuit impedance, corresponding to the frequency $f_1 = f_{1n}$

(usually $f_{1n} = 50$ [Hz]).

The value of the ratio $\dfrac{U_{1(v)}}{U_{1(1)}}$ depends on the used modulation technique. When the modulation by pulse width PWM is used, the value of this ratio is presented synthetically in Table 2.2.

Table 2.2. – The values of the ratio $U_{1(v)}/U_{1(1)}$ (line tension), for $m_a \leq 1$ and m_f odd and 3 multiple.

ν \ m_a	0.2	0.4	0.6	0.8	1.0
$m_f \pm 2$	0.082	0.151	0.217	0.275	0.318
$m_f \pm 4$	-	-	-	0.01	0.017
$2m_f \pm 1$	0.95	0.816	0.618	0.391	0.181
$2m_f \pm 5$	-	-	-	0.016	0.032
$3m_f \pm 2$	0.221	0.346	0.337	0.22	0.062
$3m_f \pm 4$	-	0.028	0.079	0.13	0.156
$4m_f \pm 1$	0.819	0.392	0.013	0.13	0.068
$4m_f \pm 5$	-	-	0.057	0.104	0.119
$4m_f \pm 7$	-	-	-	0.02	0.049

Notes:

1. The established ratios (2.39) and (2.40) allows determining the two equivalent global factors $k_{r(CSF)}$ and $k_{x(CSF)}$, corresponding to the rotoric cage having high rectangular bars in the situation of taking into account all the time harmonics intervening in the supply. Theoretically the problem is solved.
2. In the case of the sinusoidal regime, the changing factors of resistance, respectively of reactance, depend only on the material of the conductor, on the geometrical shape of the slot and on the frequency of the supply voltage. If the induction machine is fed by PWM inverters, the equivalent global changing factors of the resistance, respectively of the reactance of the high rectangular rotoric bars, depend (in addition to the material of the conductor and the slot shape), on the frequencies of all the harmonics present in the voltage, on their orders, and on the percentage these harmonics represent in the fundamental. This makes the physical meaning (phenomenological) of the two equivalent, global factors to be broader: that of globalization / summation of the effects of the harmonics present in the voltage waveform on the resistance and reactance of the motor.
3. The complex structure of the used algorithm and its component ratios require a very large amount of calculation. This makes the presence of the computer necessary in solving this problem. During the research conducted in this area a program for the determination of the two factors has been designed, entitled CALCMOT.

Based on this computer program, further on it is presented *a quantitative and qualitative analysis of the two factors*. This analysis allows inferring *the quantitatively - qualitatively influence of the supplying the induction motor through PWM inverters on the skin effect*, comparing to the situation of the sinusoidal supply of the machine.

The first stage was analyzing the dependence on the height to be calculated of the rotoric bar corresponding to the fundamental, $\xi_{(1)}$, of the two equivalent global changing factors of the rotoric parameters, situation corresponding to the rectangular rotoric slots. In Figure 2.1 the variations of these factors are set on the basis of the calculated height of the bar $\xi_{(1)}$ (a. $k_{r(CSF)} = f(\xi_{(1)})$, b. $k_{x(CSF)} = f(\xi_{(1)})$). The curves noted with 1 correspond to the sinusoidal supply of the motor for $s = 1$ and $f_1 = 50$ [Hz]. The other two curves correspond to the powering of the machine through the inverter: those noted by 2 for $s_{(1)} = 1$, $f_{1(1)} = 50$ [Hz], $m_a = 0.8$ and $m_f = 21$, and those noted by 3 for $s_{(1)} = 1$, $f_{1(1)} = 50$ [Hz], $m_a = 0.8$ and $m_f = 39$. Figure 2.1 presents the theoretical conclusions regarding the skin effect due to the presence of the time harmonics in the motor supply. Thus, for example, for $\xi_{(1)} = 3$ it is obtained $k_r = 3.01$, $k_{r(CSF)} = 3.345$ (for $m_f = 21$), respectively $k_{r(CSF)} = 3.156$ (for $m_f = 39$); consequently for $m_f = 21$ it results an increasing of the factor changing the resistance with approximately 4.85 [%] comparing to the sinusoidal supply. For the same value of the calculated height of the bar corresponding to the fundamental, $\xi_{(1)}$, $k_x = 0.508$, $k_{x(CSF)} = 0.329$ for $m_f = 21$ and $k_{x(CSF)} = 0.381$ for $m_f = 39$. Thus, it is obtained for $m_f = 21$ a decreasing of the factor changing the inductivity with approximately 35.23 [%], and for $m_f = 39$, a decreasing of the factor changing the inductivity with 25 [%] comparing to the situation of the sinusoidal supply.

It is found that with the increasing of the modulation factor in frequency m_f, the changes of the two factors $k_{r(CSF)}$ and $k_{x(CSF)}$ decrease. This result is normal due to the fact that the filtering of the harmonic spectrum is easier at high frequencies.
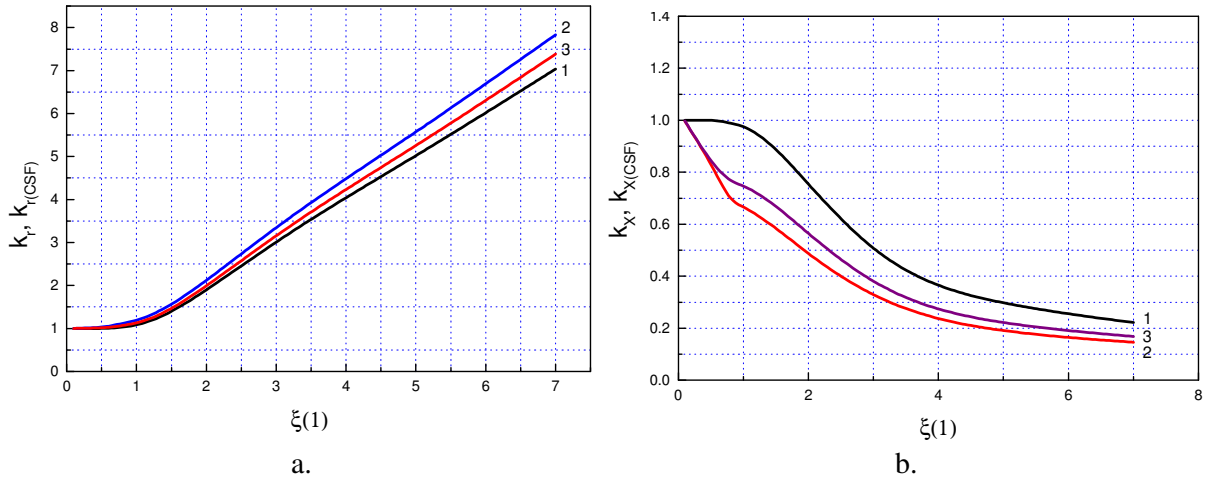
Fig. 2.1. Variation of the equivalent global changing factors of the rotoric parameters with the with the $\xi_{(1)}$ for rectangular high slots: a. $k_{r(CSF)}$ factor versus k_r ;b. $k_{x(CSF)}$ factor versus k_x.

Further on, it is analyzed the influence of the reported short circuit reactance, x^*_{sc} on $k_{r(CSF)}$ and $k_{x(CSF)}$ at the start-up time. To determine this influence, Figure 2.2 displays the variations of the two factors changing the parameters of the machine powered by inverter, in accordance with the reported circuit reactance. Curves 1 reflect the situation of the sinusoidal supply of the motor for $f_1 = 50$ [Hz], $s = 1$; curves 2 correspond to the situation in which the motor is powered by inverter, for $f_{1(!)} = 50$ [Hz], $s_{(1)} = 1$, $m_a = 0.8$ and $m_f = 21$ and curves 3 correspond to the case of the motor fed by inverter, for $f_{1(!)} = 50$ [Hz], $s_{(1)} = 1$, $m_a = 0,8$ and $m_f = 39$. All the 3 curves are valid for the rectangular rotor bars corresponding to $\xi_{(1)} = 3$. From the analysis of Figure 2.2, in the situation of the motor powered by inverter, there is change of the equivalent global factors $k_{r(CSF)}$ and $k_{x(CSF)}$, corresponding to the reported short-circuit reactance ratio x^*_{sc} (if the motors are powered directly from the supply, the reported short-circuit reactance does not have any influence on k_r and k_x , fact

well-known by the literature [27]). The changes are even larger as x^*_{sc} has lower values. Thus, for $x^*_{sc} = 0.05$, at a modulation factor in frequency $m_f = 21$, it is obtained $k_{r(CSF)} = 5.495$, therefore an increase with approx. 82.25 [%] comparing to the situation of the sinusoidal supply, for which $k_r = 3.015$ to $\xi_{(1)} = 3$) and a $k_{x(CSF)} = 0.149$, therefore a reduction of 70.66 [%] comparing to the sinusoidal regime, for which $k_x = 0.508$.

a.   b.
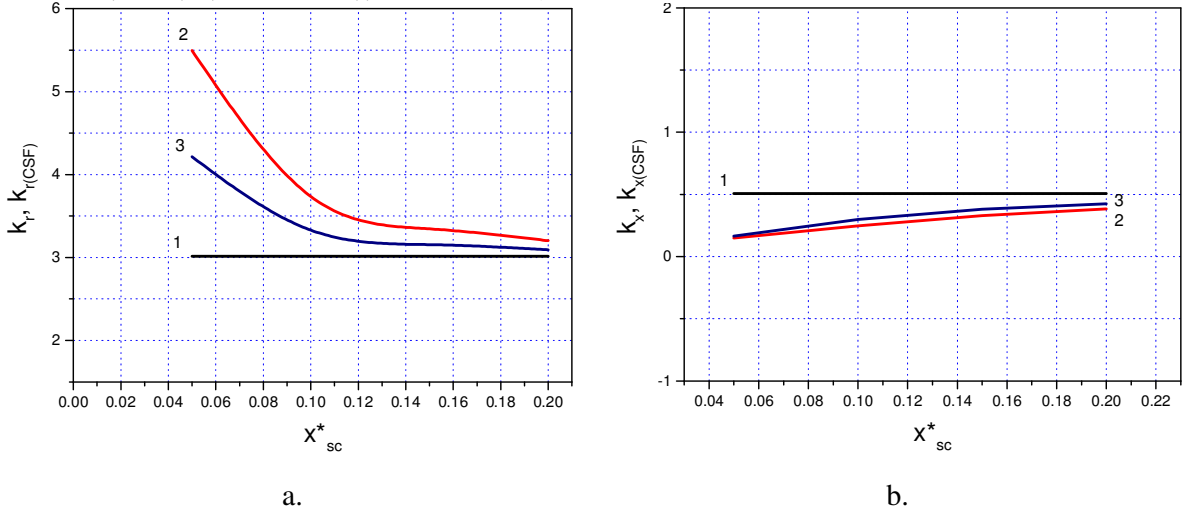
Fig. 2.2. Variation of the equivalent global changing factors of the rotoric parameters with the reported short-circuit reactance of the machine: a. $k_{r(CSF)}$ factor versus k_r; b. $k_{x(CSF)}$ factor versus k_x.

In case of a modulation factor in frequency $m_f = 39$, for the same x^*_{sc}, $k_{r(CSF)} = 4.214$ it results an increase of 39.76 [%] compared to k_r and $k_{x(CSF)} = 0.166$, therefore a reduction of 67.3 [%] in relation to k_x For higher values of the reported short-circuit reactance, the changes of the equivalent global factors $k_{r(CSF)}$ and $k_{x(CSF)}$ are lower. Thus, for $x^*_{sc} = 0.2$ and $m_f = 21$, it is obtained $k_{r(CSF)} = 3.202$, therefore an increase of only 6.2 [%] comparing to the case of sinusoidal supply and $k_{x(CSF)} = 0.384$, which means a decrease of approximately 24.4 [%] comparing to k_x corresponding to the sinusoidal regime. For the same value of x^*_{sc} , but for $m_f = 39$, it is obtained $k_{r(CSF)} = 3.094$, an increase of cu 2.62 [%] comparing to k_r and $k_{x(CSF)} = 0.426$, a decrease of 16.14 [%] comparing to k_x. In conclusion, the higher x^*_s is, the more reduced the modifications of $k_{r(CSF)}$ and $k_{x(CSF)}$ are; for "very" low values of $x^*_{sc,}$ the respective modifications may become substantial.

2.2.1.4. Conclusions

In the present study there are deduced the calculation expressions of the global equivalent increasing factor of the resistance in alternative current and of the global equivalent decreasing factor of the reactance in alternative current in rectangular/high bars when the three phase induction machines are supplied by voltage inverters. The established calculus relations allow to determine the two global equivalent factors $k_{r(CSF)}$ and $k_{x(CSF)}$ in the case that all the time harmonics which interfere in the motor supply are taken into consideration. In the case of the sinusoidal regime, the modifying factors of the resistance, respectively of the reactance depends only on the conductor material, on the geometric shape of the slot and the frequency of supply voltage. In the case when the induction machines are supplied through voltage inverters, the global equivalent modifying factors of the resistance, respectively of the reactance depend, besides on the material of the conductor and the shape of the slot, also on the frequency of all the harmonics present in the supplying voltage, on their orders, as well as on the importance of these harmonics from fundamental. Consequently, this makes the physical significance (phenomenological) of the two global equivalent

factors be greater: the globalization / summing up of the effects of the harmonics present in the wave of the supply voltage of the machine on its resistance and reactance. Parameters of the rotor cage of the machine supplied by the power converter can be calculated with errors less than 10 [%]. The main cause of errors is the assumption of saturation neglect. Even in this case the results can be considered satisfactory, which leads to validate the theoretical study carried out in the study.

2.2.2. Low-Cost Ferrite Permanent Magnet Solutions for Synchronous Motors as an Alternative for Rare Earth Permanent Magnet Synchronous Motors

2.2.2.1. Introduction

The recent developments in power electronics and registered rapid growth in the field of microcontrollers (μCs), digital signal processors (DSPs) and not at least of digital signal controllers (DSCs), which is actually a combination of the first two, makes the use of electric drive systems with variable speed very attractive. More and more companies in the field of power electronics and manufacturing companies of μCs, DSPs and in the last period of time of the DSCs, turn their attention to this segment of drives by the creation of more innovative and cost effective products for this type of applications. So if until recently, the companies in this field currently used as actuators also DC machines, today the induction machines, permanent magnet synchronous machines, synchronous reluctance machines and step by step motors, in various configurations, are used more and more. The reasons for electric drive systems with variable speed for these types of motors are given by the following: the possibility of obtaining a high efficiency of drives; the ability to control the torque, speed or position; improving the transient behavior; the possibility to obtain application-specific drives. *The permanent magnet synchronous motors (**PMSM) variable speed drives** lead to the following advantages: obtaining a high efficiency, eliminating of an additional power supply, the possibility of obtaining high values of electromagnetic torque per volume unit, the possibility of achieving of a high performance control system [33], [34] [35] [36].

The **PMSM** are characterized by a superior power factor and efficiency comparing to other AC machines. PMSM manufacturers choose the using a particular type of permanent magnet (PM) depending on the parameters imposed to the machine, the performances of the PM, the procurement conditions, and, particularly, the cost of the permanent magnet [33]. Now, rare earth permanent magnets and ferrites are mostly uses types. **Rare earth permanent magnets (PM)** are the best technical solution for PMSM. The PM of Samarium-Cobalt has the advantage of a high residual magnetic induction, high energy density, linear demagnetization curve and a very good thermal stability. As a drawback would be the lower maximum operating temperature (~250°C) and the higher price. PM of neodymium-iron-boron have the highest residual magnetic induction, the highest energy density and a high coercive field strength. The drawback is the low maximum working temperature (~ 150°C) and the possibility of oxidation. With their help we can build PMSM with a lower weight due to high energy density [6], [33], [37]. In conclusion, rare-earth magnets (SmCo, NdFeB) are a good alternative for PMSM, but they showing a rapidly rising price trend in the last years, so in the last time in the literature were presented different design solutions for PMSM using ferrites to overcome this problem. **Ferrite PM** is an alternative to the construction of PMSM due to their low price and the fact that they are easy to be produced. Ferrites have a linear magnetization curve, a moderate maximum operating temperature (~350°C), but the residual magnetic flux density is low [6]. The result is a high volume and weight machine.

Synchronous reluctance motors (SynRM) are apparent pole synchronous machines with a large saliency ratio. They are referred in the literature also as reactive synchronous machines and variable reluctance synchronous machines with passive rotor. A large saliency ratio can be achieved by both axially and transversally laminated rotor structures. The process of the electromagnetic torque production in a SynRM is based on the shape anisotropy which characterizes the machine. In the last time transversally laminated rotor structure is preferred, because the axially laminated rotor structure has from the mechanical point of view some drawbacks. The rotor has different construction variants [6], [49]. Generally, all these types aimed at obtaining different magnetic permeances in d and q axes, necessary to produce reluctance torque (reactive). The advantages of these machines are: the simplicity of the technological process, low-cost, low noise and robustness [33], [38], [39], [40], [49]. The main disadvantages are related to the low value of developed electromagnetic torque, low value of power factor and low efficiency.

SynRM electromagnetic characteristics can be improved by creating a rotor having both permanent magnets and variable reluctance, thus obtaining **the permanent magnet assisted synchronous reluctance motor (PMSynRM)**. By this construction is achieved an improvement of magnetic characteristics such as power vs. internal torque angle, power factor vs. mechanical power and efficiency vs. mechanical power [41]. To achieve superior performance with this new topology, a PMSynRM optimization is required. A lot of valuable papers deal with the subject, such as, for example [42], [43], [44], [45], [46], [47] and [48].

In this study research, the author proposes in the first step **two new low-cost ferrite V permanent magnets assisted synchronous reluctance rotor geometries (VPMSynRM)**. The first proposed rotor geometry has **one V flux barrier (1V) and second proposed geometry has two V flux barriers (2V)**. We will add ferrites into these flux barriers to improve the performance of motor. In the extreme case (this is also our case) these flux barriers will be completely filled with ferrites, so this rotor configuration is also known in the literature as **interior inclined V permanent magnet synchronous motor**. In the second step, the author proposes **a new rotor topology with flux concentrators (PMSM-FC) made of ferrite magnets**, as **an alternative to PMSM made with rare earth magnets**, too. **All the solutions studied aim a much cheaper alternative to the synchronous motors with rare earth permanent magnets.**

2.2.2.2. Design Challenge

The main purpose of this research is to study the performance of the new motor obtained by combining the stator of an NdFeB inserted tangential permanent magnet synchronous motor with the proposed rotor geometries. **The proposed rotor structures must be optimal design in such a way that is possible to achieve the same torque per current ratio in the constant torque area and the same torque capability in field weakening are like with the initial PMSM with NdFeB. The main challenge of the rotor design using ferrites is the small space available for the PM and flux barriers, because for the rotor designed with NdFeB a small PM volume is needed, so a compact PMSM can be designed.**

The design is based on existing 12 slot stator with concentrated windings, and 50 mm inner diameter. The stator length is 37 mm. The winding scheme is presented in Figure 2.3.

The new rotor has the same number of poles and the same outer diameter 49.3 mm like the initial rotor. The permanent magnet used for the new proposed rotors is a strontium ferrite FS-4 with following magnetic properties: $B_{r\min} = 0.4$ T $H_C \geq 223$ kA / m and $(BH)_{\max} = 27.2$ kJ/m^3.
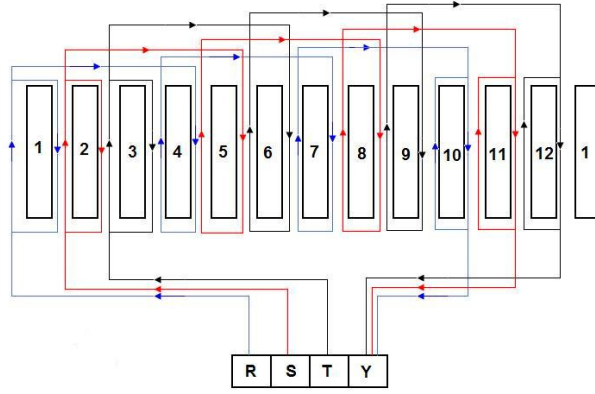
Fig. 2.3. The machine stator winding scheme.

a. Design strategy - PM volume

The required permanent magnet volume was calculated with the following relation:

$$V_{PM} = \frac{2}{\pi^2} \cdot \frac{k_\varphi \cdot k_{ad}(1+\varepsilon)}{f_S \cdot k_{um} \cdot k_{\text{Im}} \cdot B_r \cdot H_c \cdot \eta_m \cdot \cos\phi_m} \cdot k_m \cdot T_{mN} \cdot \Omega_N \ , \tag{2.42}$$

where: k_φ is the form coefficient of the permanent magnet field, $k_{ad,q}$ is the coefficient of the magnetic reaction in the air gap, ε is the degree of excitation of the motor, f_s is the stator frequency, k_{um} is the coefficient of use of permanent magnets, η_m and $\cos\phi_m$ are the efficiency and factor power the motor, T_{mN} is the rated torque, Ω_N is mechanical speed and k_m is the motor overload factor and it can be calculated with the following relation:

$$k_m = \sqrt{1 + \frac{1}{\varepsilon^2} \cdot \left(\frac{k_{ad}}{k_{aq}}\right)^2} \tag{2.43}$$

b. Design Strategy – FEM, L_d, L_q

The design of proposed rotors is carried out using the two-dimensional finite element software Vector Fields OPERA, so it can be considered the nonlinear magnetic behaviors of the materials which play a key role in the motor performance prediction. By the movement of the rotor over the stator slot pitch, the back EMF, cogging torque and the torque ripples caused by permeance variations are taken into account. A standstill method is proposed to simulate the direct *d-* and quadrature *q*-axis inductances with the FEM software. For a nonlinear magnetic material, the inductance is depending on the level of a current.

The Figure 2.4 shows the variation of the *d-* and *q*-axis magnetic flux versus *d-* and *q*-axis current. The inductance in the point "*k*" can be calculated using the following relations:

$$L_{d,qkt}(I_{d,qk}) = \frac{d\Psi_{sd,qk}}{dI_{d,qk}} \ , \tag{2.44}$$

The *d-* and *q*-axis stator flux linkage can be calculated with the following relation:

$$\Psi_{sd,qk} = \int_0^{t_k} (U_{sd,q} - R * i_{d,q}(t)) dt \tag{2.45}$$
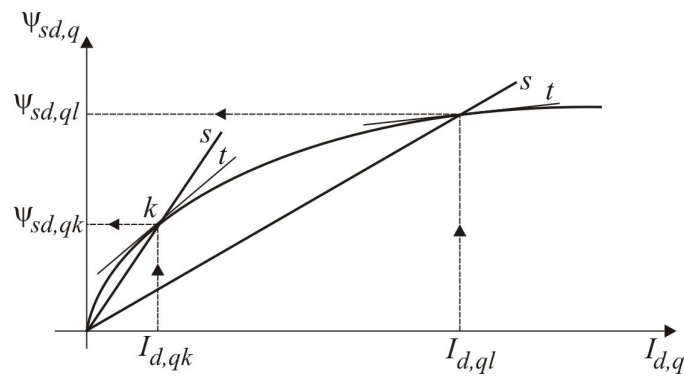
Fig. 2.4. Nonlinearity of *d*- and *q*-axis inductances.

c. Design Strategy – Rotors geometry

To redesign the rotor was studied many rotors geometry patented and already in production. From the very beginning has wanted a new transversal rotor geometry that can be implemented in series production. The 8 proposed variants are presented in Figure 2.5 [49].
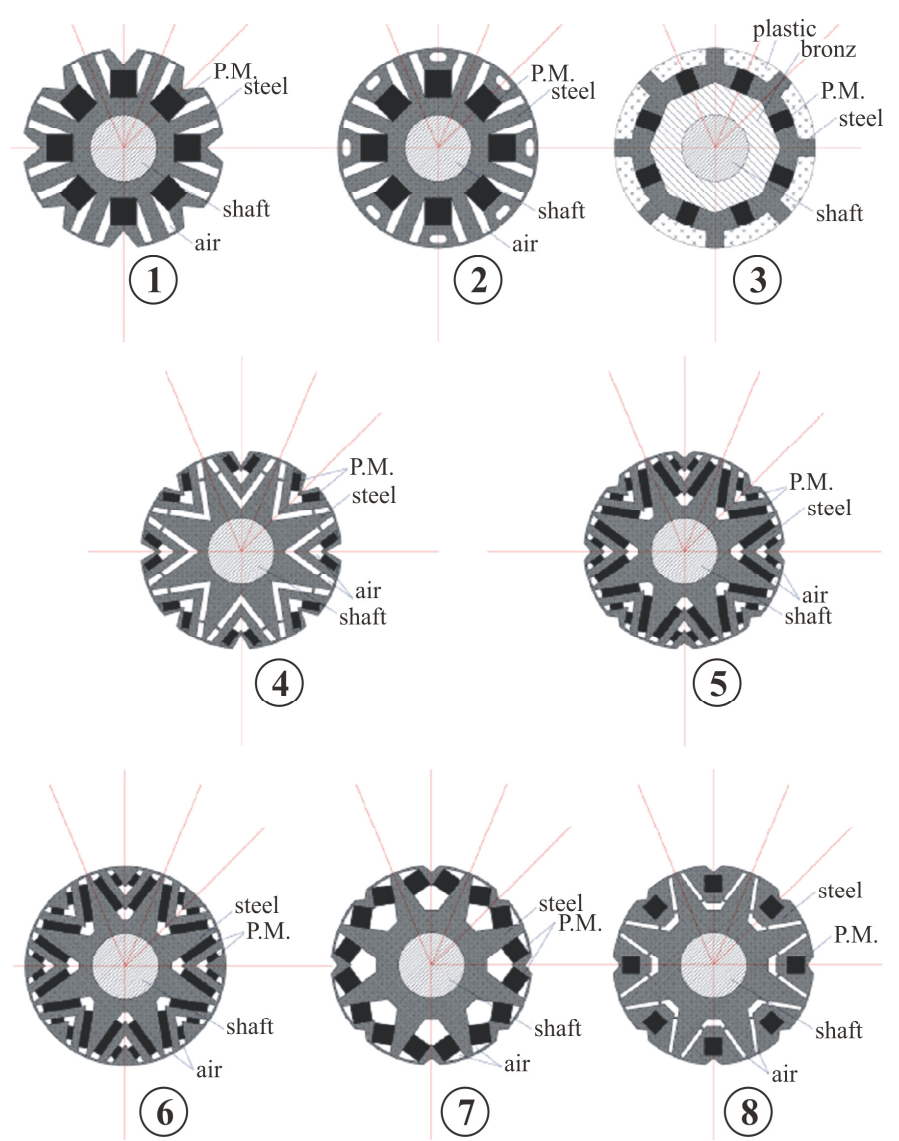
Fig. 2.5. The proposed rotor type variants for PMSynRM .

Can be observed, was proposed 7 variable reluctance rotors assisted by permanents magnets variants (numbers 1, 2, 4, 5, 6, 7, 8) and one rotor variant with flux concentration (number 3).

In conclusion, ***has to be shown the fact that during this research were designed all the rotor geometries presented in Figure 2.5 from which was retained to a deep analyze the variant with one V flux barrier (1V), with two V flux barriers (2V) and a variant with flux concentrators (PMSM-FC) made of ferrite magnets, as an alternative to PMSM made with rare earth magnets.***

2.2.2.3. VPMSynRM with One V Flux Barrier - 1 V

The ***first proposed VPMSynRM-1V rotor geometry*** is shown in Figure 2.6. The permanent magnet volume V_{PM} = 39587.37 [mm^3] was determined by relations (2.42) and (2.43). As can be seen from Figure 2.6 the required volume of ferrite is high so the flux barrier is adapted at the magnet volume. In this case ***there are no many possibilities to optimize the shape of the flux barrier***. The width of the flux barrier is 5.7 [mm]. In the Figure 2.6 can be seen also the *d*-axis and *q*-axis flux plots of the permanent magnet. The simulated distribution of the PM flux density in air gap is shown in Figure 2.7.

a.   b.
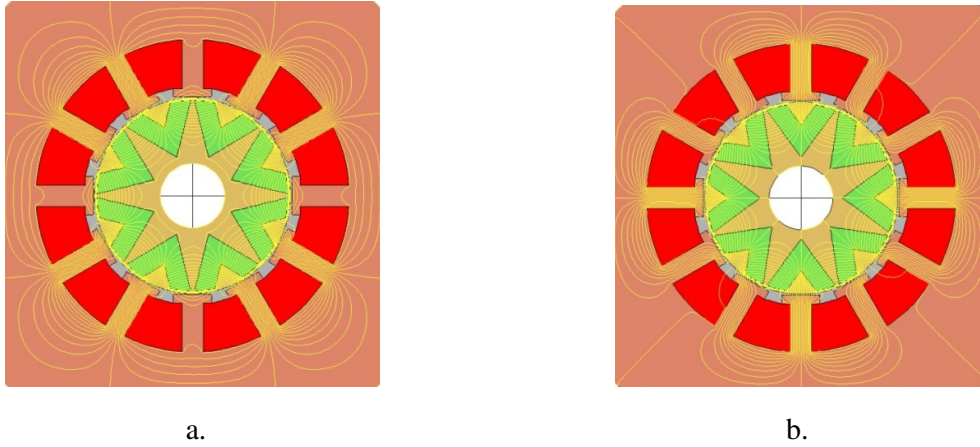
Fig. 2.6. One V flux barrier rotor geometry: *d*-axis PM flux plots, b. *q*-axis PM flux plots.

a.   b.
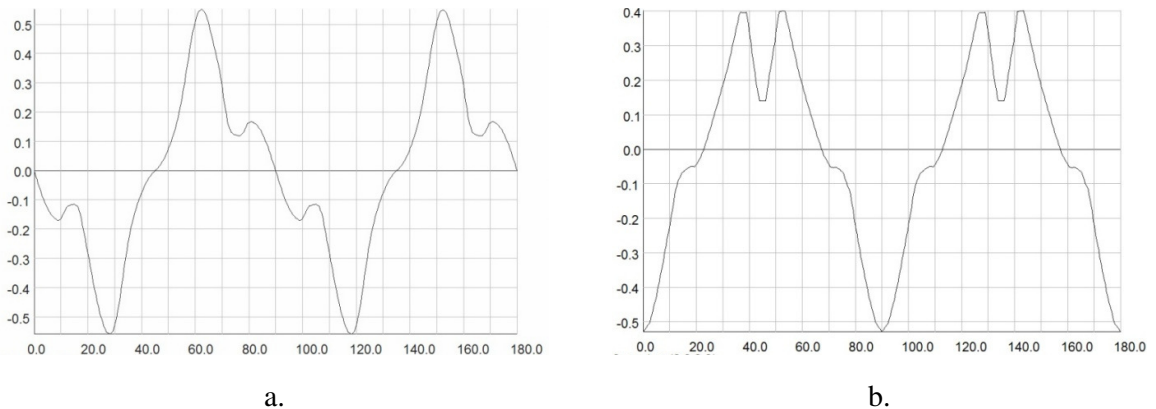
Fig. 2.7. Flux density distribution: a *d*-axis, b *q*-axis.

The peak values of the simulated *d*- and *q*-axis magnetic flux density in the air gap are 0.55 [T], respectively 0.4 [T]. Figure 2.8 shows the shape of the back-EMF and the shape of the cogging torque at 750 [rpm]. From this figure, we can determine the peak value of the back-EMF (E_{pk} = 16 [V]) and the peak value of the cogging torque (T_{cogg} = 0.045 [Nm]). The permanent magnet flux linkage has the value ψ_{PM} = 0.051 [Wb]. The curves of the simulated inductances L_d and L_q versus currents

I_d and I_q are shown in the Figure 2.9. The curves of inductance were simulated using the FEM and the method described above using the relations (2.44), and (2.45). For *d*- and *q*-axis inductance following values were obtained: $L_d(4A) = 23.80$ [mH], $L_q(4A) = 12.1$ [mH] and the saliency ratio $L_d/L_q = 1.96$. Figure 2.10 presents the variation of torque caused by the permeance variations at 5 [A] in the constant torque area. In this case for the proposed VPMSynRM-1V rotor at 5 [A] the average torque is $T_{av} = 2.3$ [Nm] and the torque ripple is $T_{ripple} = 26$ [%].
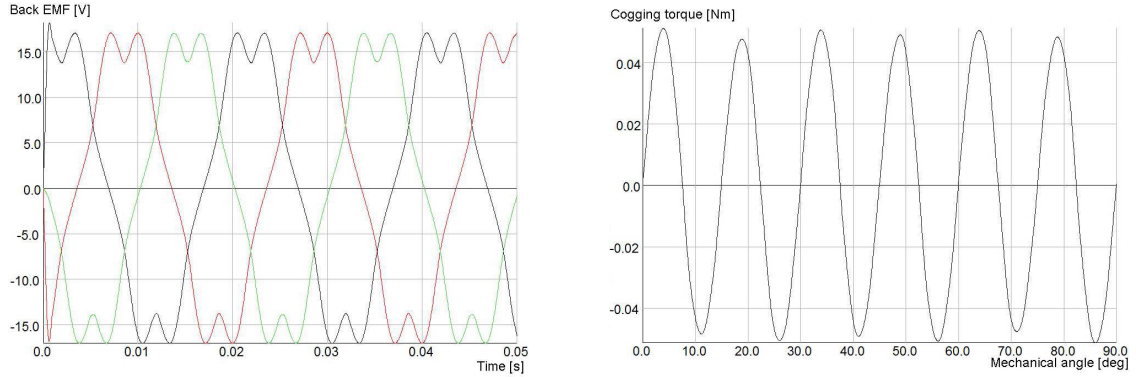
a.   b.

Fig. 2.8. a. Back-EMF, b. Cogging torque.
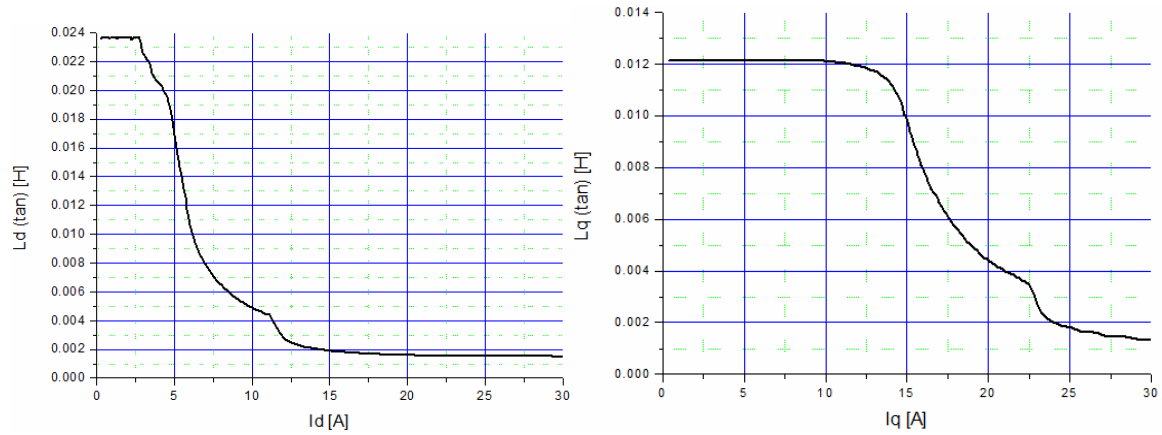
a.   b.

Fig. 2.9. a. *Ld* and b. *Lq* inductivities curves vs. currents.
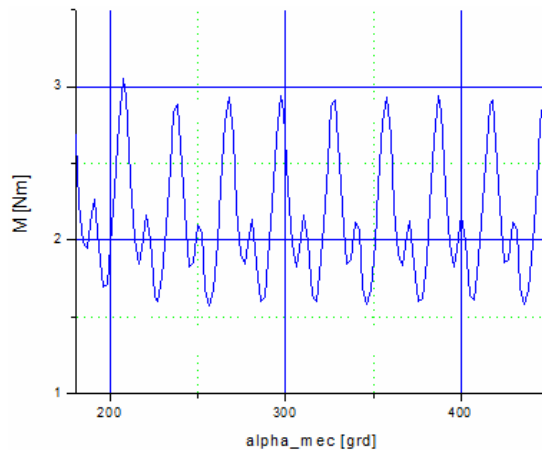
Fig. 2.10. Torque variation at 5 [A].

2.2.2.4. VPMSynRM with Two V Flux Barriers - 2V

The *second proposed VPMSynRM-2V rotor geometry two flux barriers* which are filled with ferrite. The stator remains unchanged as topology and geometric dimensions and the characteristics of material used are the same like in the first proposed version. In this case of the proposed rotor with two flux barriers are proposed actually two different variants (see Figure 2.11 a. and b.):

- the first variant (2V) has two flux barriers with the same width (2 [mm]), and the volume of the permanent magnet is V_{PM} = 29325.04 [mm^3];
- the second variant (2VU) has also two flux barriers but the width of these two flux barriers is different (2.2 [mm] and 1.27 [mm]), and the volume of the permanent magnet is V_{PM} = 24339.78 [mm^3] (17 [%] less volume than in the first variant).

In both variants with 2 flux barriers we get at least 26 [%] less magnet compared to the previous version 1V. In this case the simulated distribution of the PM magnetic flux density (*d*-axis and *q*-axis) in air gap isn't shown, but the shape of the magnetic flux density is the same (see Figure 2.7). The peak values of the simulated *d*- and *q*-axis magnetic flux density in the air gap are in this case with about 25 [%] higher than in the case of 1V rotor geometry.

a.   b.
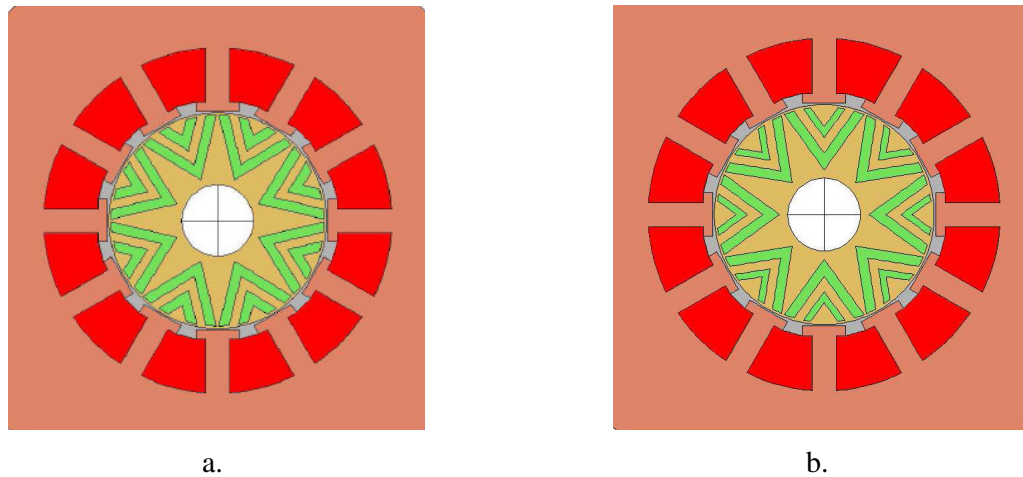
Fig. 2.11. Two V flux barriers rotor geometry: a. with same width of flux barriers 2V; b. with different widths of the flux barriers 2VU.

a.   b.
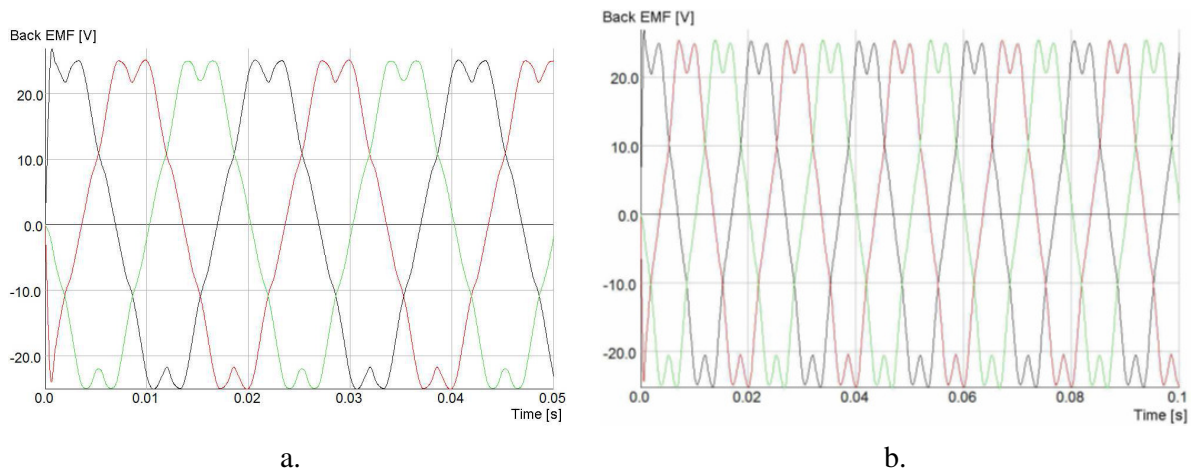
Fig. 2.12. Back-EMF a. 2V; b. 2VU.

a.   b.
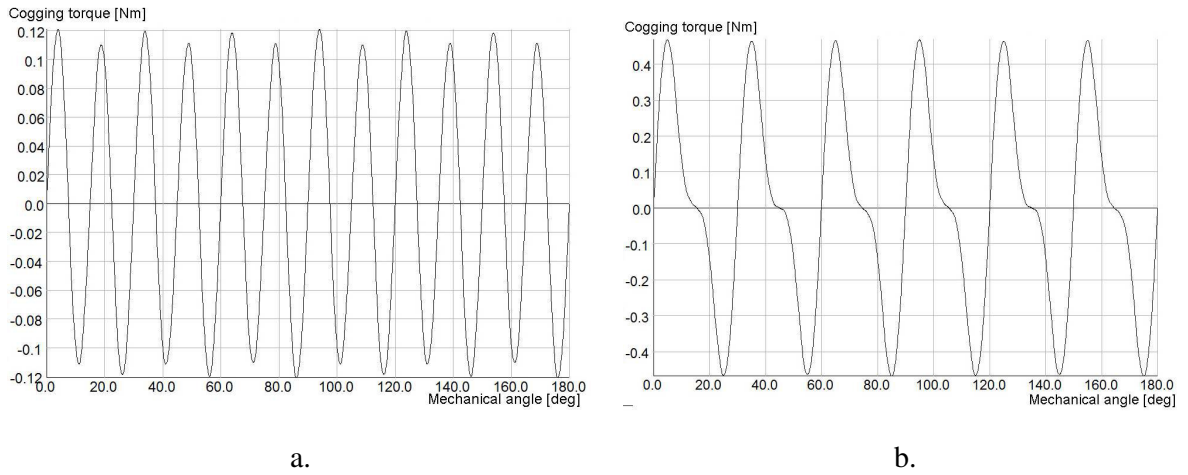
Fig. 2.13. Cogging torque 2V; b. 2VU.

Further, the curves obtained by simulation for back-EMF and cogging torque, shown in Figure 2.12 and Figure 2.13, will be analyzed. The variant with two equal width barriers 2V is characterized by a peak of E_{pk2v} = 24 [V] back-EMF so an increase of 33 [%] from 1V variant and the variant 2VU has the peak value of the back-EMF E_{pk2vu} = 22 [V]. The permanent magnet flux linkage has the following values ψ_{PM2v} = 0.076 [Wb], respectively ψ_{PM2v} = 0.070 [Wb]. The peak value of the cogging torque for the two proposed variants with two flux barriers are T_{cogg2v} = 0.012 [Nm] respectively $T_{cogg2vu}$ = 0.045 [Nm]. Figure 2.14 presents the curves of inductance L_d and L_q versus currents I_d and I_q for variant with 2 flux barriers 2V. The curves of inductance L_d and L_q versus currents I_d and I_q for the variant 2VU is not presented in this section but the variation is near the same. For *d*- and *q*-axis inductance following values were obtained: L_d(4A) = 23.75 [mH], L_q(4A) = 15.8 [mH] and the saliency ratio L_d/L_q = 1.50.

a.   b.
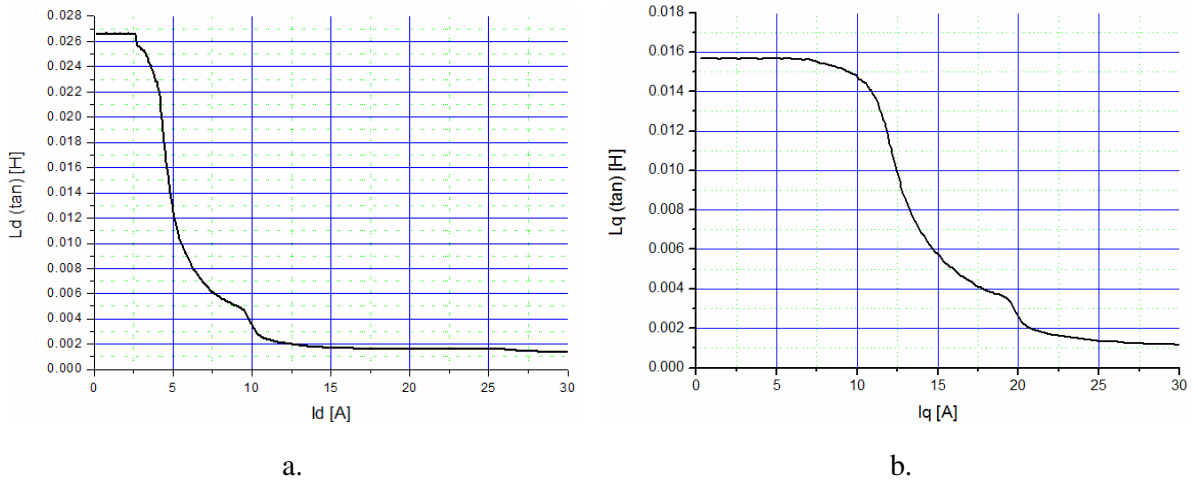
Fig. 2.14. The a. *Ld* and b. *Lq* inductivities curves vs. current for version 2V.

Figure 2.15 presents the variation of torque caused by the permeance variations at 3.6 [A] in the constant torque area for the rotor variant 2V. In this case for the proposed VPMSynRM-2V rotor at 3.45 [A] the average torque is T_{av2v} = 1.9 [Nm] and the torque ripple is $T_{ripple2v}$ = 26.3 [%].
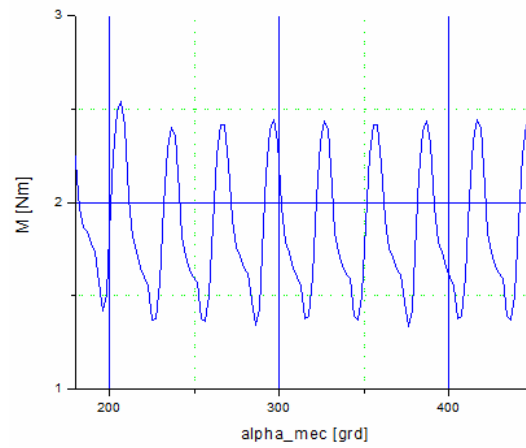
Fig. 2.15. Torque variation at 3.45 [A].

2.2.2.5. PMSM with Flux Concentrator Rotor (PMSM-FC)

The third optimized *new variant introduced by this research is with flux concentration*. This variant, which uses also ferrite PM, wants to be an alternate solution to the PMSM realized with rare earth PMs. So, in this case also, the stator remains unchanged in terms of dimensions and material characteristics. The proposed geometry is presented in Figure 2.16. The volume of the permanent magnet VPM = 26481.72 [mm^3] has been calculated using relations (2.42) and (2.43). It can observe a volume reduction of 9.7 [%] comparing to the variant VPMSynRM-2V and an increase of 8 [%] comparing to the variant VPMSynRM-2VU. The simulated distribution of the PM flux density in air gap is shown in Figure 2.17. The peak values of the simulated *d-* and *q*-axis magnetic flux density in the air gap are greater than 0.6 [T]. Figure 2.18 shows the shape of the back-EMF and the shape of the cogging torque at 750 [rpm]. From Figure 2.18 a., we can determine the peak value of the back-EMF (E_{pk} = 22 [V]) and the peak value of the cogging torque (T_{cogg} = 0.021 [Nm]). It can observe a decrease of the back-EMF of 8.33 [%] comparing to the variant VPMSynRM-2V and the same value comparing to the variant VPMSynRM-2VU. For the peak values of the cogging torque, the variant with flux concentration rotor PMSM-FC has an increased value of 75 [%] comparing to the variant VPMSynRM-2V and a diminution of 114 [%] comparing to the variant VPMSynRM-2VU.
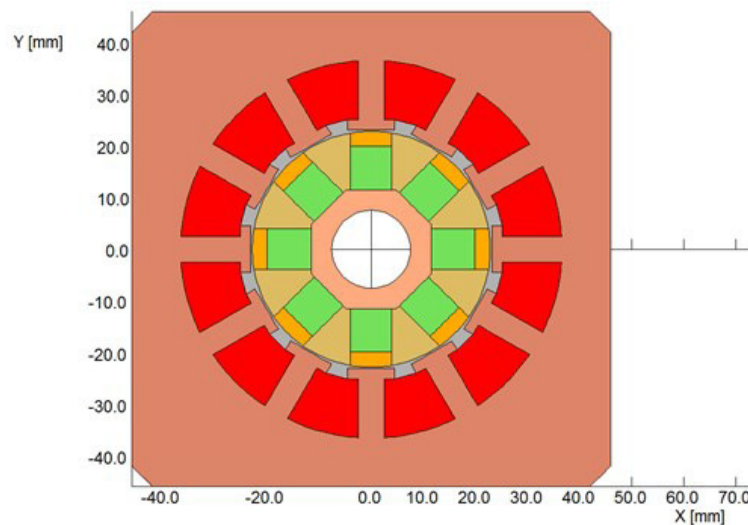
Fig. 2.16. PMSM wit flux concentrator (PMSM-FC).
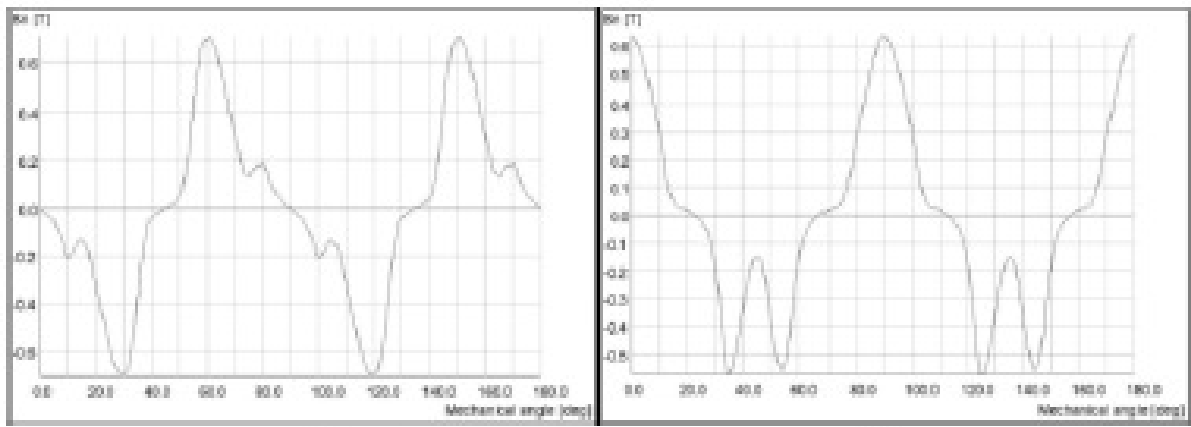
a.   b.

Fig. 2.17. Flux density distribution: a *d*-axis, b *q*-axis.
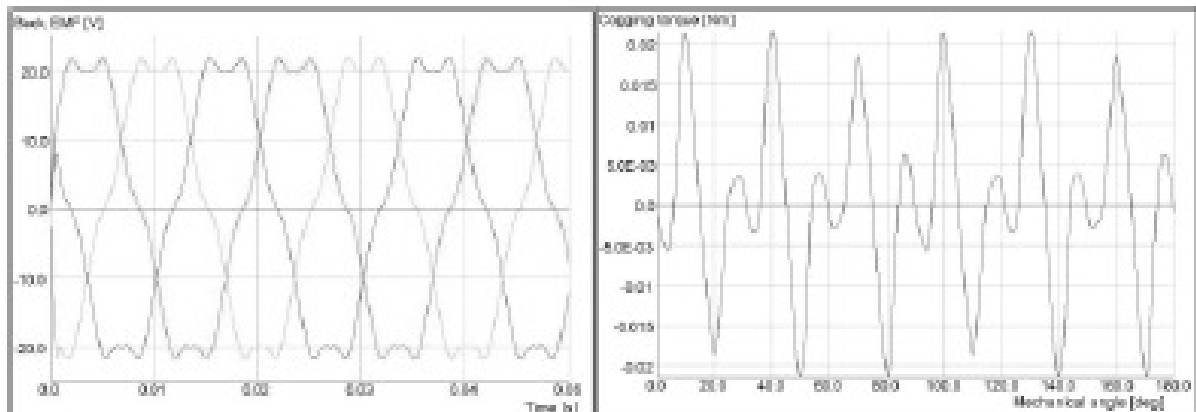
a.   b.

Fig. 2.18. . a. Back-EMF, b. Cogging torque.

The curves of the simulated inductances *Ld* and *Lq* versus currents *Id* and *Iq* are shown in the Figure 2.19.
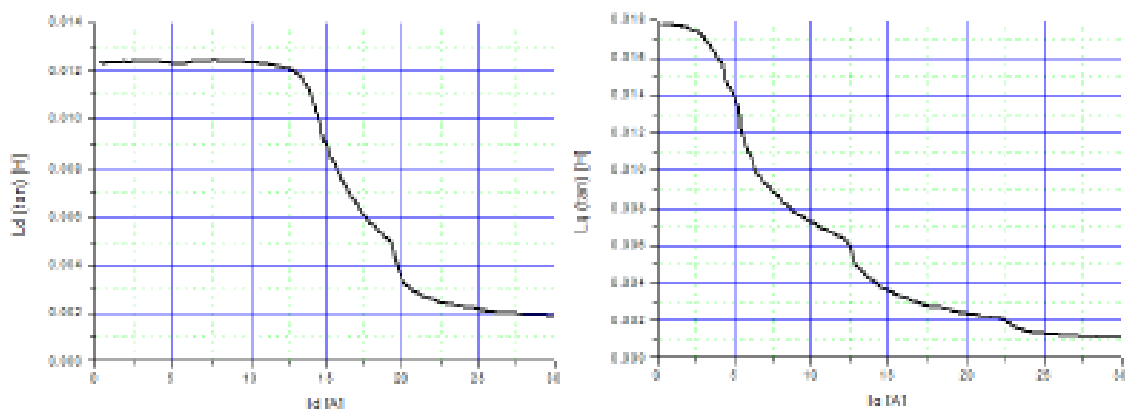
a.   b.

Fig. 2.19. a. Ld and b. Lq inductivities curves vs. currents.

The curves of inductance were simulated using the FEM and the method described above using the relations (2.44) and (2.45). For *d*- and *q*-axis inductance following values were obtained:

Ld(4A) = 12.76 [mH], Lq(4A) = 15.91 [mH]. Figure 2.20 presents the variation of torque caused by the permeance variations at 5 [A] in the constant torque area. In this case for the proposed PMSM with concentration flux rotor at 5 [A] the average torque is $T_{av\ PMSM\text{-}FC}$ = 2.2 [Nm] and the torque ripple is $T_{ripple\ PMSM\text{-}FC}$ = 26.3 [%].
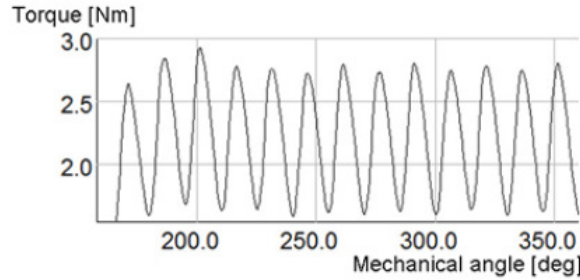
Fig. 2.20. Torque variation at 5.0 [A].

In Table 2.3 are listed the simulation results of the proposed solutions for the rotor geometry.

Table 2.3. Simulation results.

	Rotor Type			
	Conc. flux	**2V**	**2VU**	**1V**
V_{PM} [mm^3]	26481.72	29325.04	24339.78	39587.37
L_d(4A) [mH]	12.76	23.75	~23.75	23.80
L_q(4A) [mH]	15.91	15.8	~15.8	12.1
L_d/L_q	0.8	1.50	~1.50	1.96
ψ_{PM} [Wb]	0.070	0.076	0.070	0,051
T_{av}/I [Nm/Apk]	2.2/4.5	1.9/3,45	~1.9/3.45	2,3/5
T_{ripple} [%]	26.3	26.3	~26.3	26

2.2.2.6. Experimental results

The PMSM-FC rotor (see Figure 2.21) was manufactured to Electromotor Timişoara and the experimental results were compared with the simulated results.

In the Table 2.4 are listed the measured motor parameters of the PMSM-FC.

Table 2.4. Measured motor parameters of the PMSM-FC.

Rs [Ω]	Ld [mH]	Lq [mH]	ψ_{PM} [mWb]
2.65	14.98	19.12	68.0

Fig. 2.21. PMSM with flux concentrator rotor PMSM-FC.

The measured values of the *d*- and *q*-axis inductance are different from the simulated values and the ratio *Lq/Ld* is better in the case of the measured values. This difference can be explained by the fact that the pole geometry was modified for a better fixation of the magnets. The difference between the simulated and the measured PM flux linkage is small, so we can say that simulated results have been validated by the experimental results. The obtained prototype was also tested on the dyno. The electromechanical performance (motor current vs. torque and efficiency vs. torque) of the PMSM-FC are presented in Figure 2.22 and Figure 2.23.
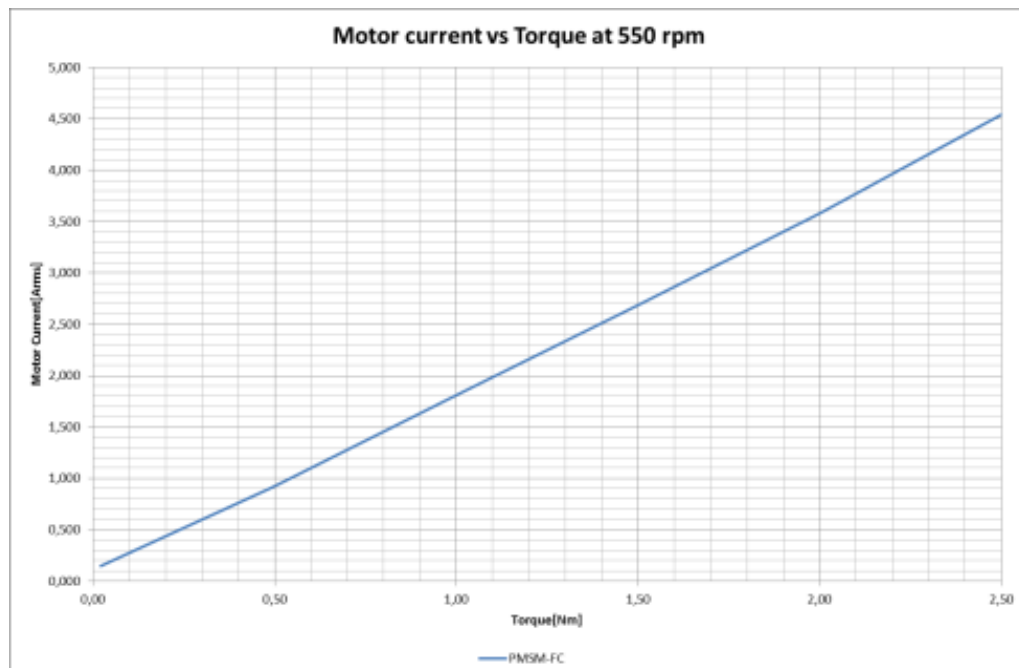
Fig. 2.22. Measured motor performance – Motor current vs. torque.
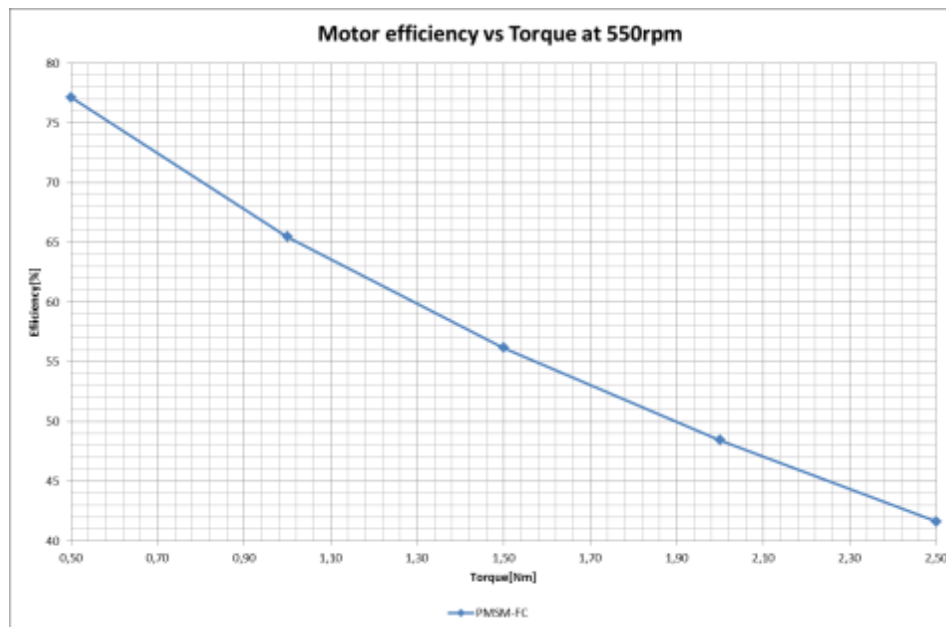
Fig. 2.23. Measured motor performance – Motor efficiency vs. torque.

2.2.2.7. Conclusions

This research proposes two different low-cost ferrite solutions: first two V permanent magnet assisted synchronous reluctance rotor (VPMSynRM) and the second a permanent magnet synchronous with rotor flux concentrator PMSM-FC as an alternative solution to the rare earth inserted tangential permanent magnet synchronous motor (PMSM). Finite element (FEM) approach has been utilized to show the performance of the proposed rotors. The PMSM-FC rotor was manufactured and the simulated results have been validated by the experimental results. ***All these proposed rotor geometries with the flux barriers or flux concentrator and ferrites are attractive alternative solutions to reduce the cost of the rotor by changing the type of PM***.

2.3. Contributions to the optimal control of electric drives with alternative current machines

2.3.1. Electrical drive systems with vector control for the induction motors implemented on naval mechanisms

2.3.1.1. Introduction

In this research, our team studied and proposed the adoption of a solution for implementing the ***direct vectorial torque and flux control of the induction motor with squirrel-cage rotor for the electric drive systems of naval mechanisms***. The aim of this study is intended to replace the current technical variant for which the operation of the loading systems uses asynchronous motors with squirrel cage rotor, with three speed steps, obtained by using three statoric distinct windings in star connection. The main disadvantages of the current versions are: big building and complicated construction of the operating machine, speed change can be achieved only in steps.

In order *to eliminate these disadvantages*, *the research team proposed a technical solution that preserves the induction machine as part of the execution, but in which the control, which involves speed control and / or position control, respective the torque control is done by direct vector torque and flux control*. The main advantages obtained are:

- a fast dynamic response in torque and an operating in a wide range of speeds;

- a vectorial control is robust and relatively simple to be implemented;

- does not require current regulators and coordinate transformations;

- requires neither a decoupling circuit of the stator voltage equations nor a separated vectorial modulator for controlling the PWM inverter;

- ensures an efficient rejection of disturbances;

- very good adjustment to numeric control;

- can use an normal induction motor with rotor cage, with a single stator winding, the speed change being achieved by vectorial control;

- eliminates the control panel which comprises sense contactors, acceleration, braking and timing relays [6], [61], [62], [63], [64], [65].

2.3.1.2. Presentation of the current technical solutions existing on ships

Loading-unloading mechanisms are characterized by a large number of operating modes and functions with loads and speeds that are repeated cyclically. The cycle consists of periods in which the mechanism works and of brakes. The brakes duration depends on the speed of load lifting and lowering and varies very widely. The speed range of these mechanisms must be very broad because, on the one hand, the high speeds shorten the cycle, and the low speeds allow the smooth load placement. Based on the data regarding the operating modes of loading-unloading mechanisms one can determine the optimal speed characteristics and the parameters of the regimes to which the electric drive must correspond [79].

The loading system, located in the bow consists of the following main elements: *derricks, column, hatches, ropes and load hook, load winches and cranes.*

The modern naval mechanisms designed for loading and unloading operations must provide: high productivity, economy, small weight and dimensions, installation simplicity.

Currently, the electric drive systems for loading faculties are done both with DC and AC machines [7].

The operation with *continuous current motors with derivation or separate excitation is practically* used more because of its good opportunities for speed change and control, for starting, reversing and economic electric braking and automatic driving. Despite all the clear advantages that these types of motor present, their use in operating systems is somewhat limited by some drawbacks. Therefore, for DC motors the power is transmitted to the rotor by brush form sliding contacts - collector, which limits (superiorly) the nominal power at lower values. The nominal voltage and thereby the speed are limited by the maximum permissible voltage between the two collector blades may not exceed 20 to 24 [V] (because of commutation). The presence of the

collector also leads to the increasing of the motor cost, reducing its reliability compared to the asynchronous motors with short-circuit rotor. Also, due to the existence of mobile contact brushes – collector, the collector and brushes wear out n time. .

Asynchronous motors have seen a rapid spread in the electric drives for naval hosting units on the following bases:

a. The electricity distribution on modern ships is in alternative three-phase system, which is the most economic system;
b. The asynchronous motors, particularly with short-circuit rotor, are characterized by a simple and robust construction, recognized as the most reliable electrical motors.

Compared to DC motors, the induction cage motors have many advantages that make their use in driving systems to be tempting. Thus, by removing the sensitive components (collector system - brushes), induction motors with short-circuit rotor are reliable in operation, having a practically constant rotational speed at given load, while having moments of inertia inferior to those of direct current. They can operate at high speeds for long periods of time without maintenance, requiring only a source of alternative current. The value of the stator voltage is limited by the commutation phenomenon. The advantage of induction motors comparing to those with direct current appears also from the point of view of economic considerations. The price of the squirrel cage induction motors is much smaller (the rapport power / kg is almost double comparing to that of DC motors).

Due *to technical and economic advantages* aforementioned, the asynchronous motor is currently used in the vast majority of electric drives systems for the modern loading - unloading facilities of ships.

Currently, both for *cargo winches with derricks and for cranes*, *the squirrel cage induction motors with three speed stages obtained using three separate stator windings in star connection* are mostly used.. Basic step is the third step. The existing automatic control electric diagram does not allow the direct change from position 0 directly on the based position III. Also, the time relays from this scheme require switching to the 3rd step speed successively through the inferior 1st and 2nd stages through an energy recovery braking system.

The disadvantages of the solution are given by the big dimensions and the more complicated construction the machine, plus the fact that it can only change the speed in steps.

2.3.1.3. The implementation of the vectorial control for the electric drive systems with induction machines serving naval mechanisms

In order to eliminate these disadvantages, during the research a technical solution was analyzed and proposed that keeps the induction machine as element of execution, because of the above considerations, but on which the movement control, which involves speed and/or position control, respectively torque control is done by direct torque control.

Electric drive systems for naval mechanisms must meet the following requirements:

- to have an appropriate class of protection systems for naval applications;
- to be equipped with mechanical brakes to allow blocking duties in the event of an accidental fall in the supply voltage of the inverter;
- take into account the limited power sources supply ships.

Direct torque and flux vectorial control (Direct Tourque Control - DTC) provides direct control of the stator flux and electromagnetic torque by selecting the best commutation mode of transistors of the PWM inverter. Commutation is designed so that the flux error and torque should be within a hysteresis band with the well-determined goal to get a torque fast response and also to reduce the commutation frequency of the inverter. Classic DTC combines the vectorial control theory with the direct control theory [74], [75], [76]. This vectorial control strategy is suitable for controlling the position or velocity, leading to a stable regulation to about 0.1 [r / h].

The *basic structure of a direct vector control system in classic torque and flux with induction motor and PWM voltage inverter* is shown in Figure 2.24. The machine orientation is made according to the stator flux, this classic scheme being proposed by Takahashi and Noguchi.
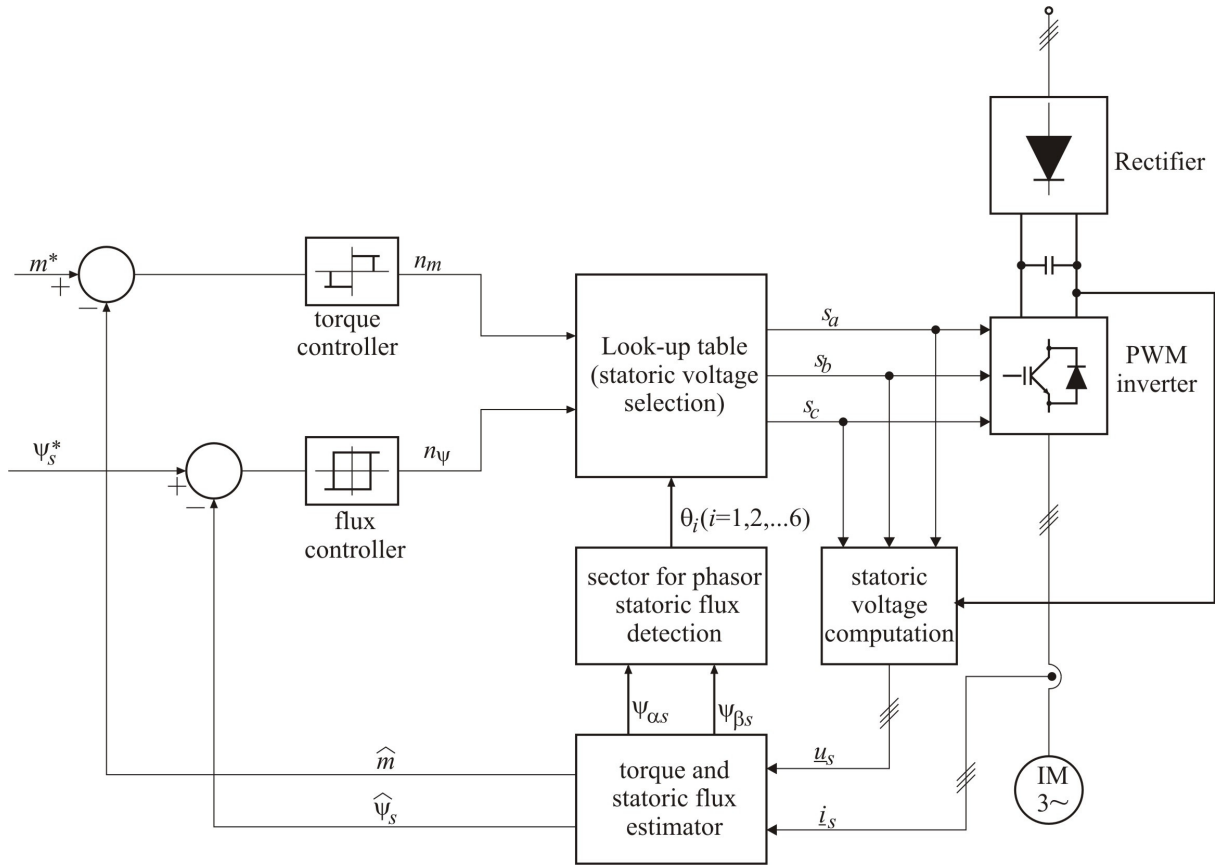
Fig. 2.24. Classic DTC stator-flux-oriented induction motor fed by a PWM voltage inverter

Classic DTC involves direct control of the machine after the two key measures: electromagnetic torque m and flux ψ_s. These are two independent control loops, one for the torque, the other for the flux, working in parallel. For the control of the PWM voltage inverter a table of optimum commutations s used, the stator voltage vectors, being controlled directly by the two controllers with hysteresis.

The input values for the two regulators are electromagnetic torque errors $m^* - \hat{m}$, respectively stator flux errors $\psi_s^* - \hat{\psi}_s$. The torque controller is a comparator with three-positional hysteresis (three levels) while the flux regulator is a comparator with bipositional hysteresis (two levels). At the output of the two regulators numeric signals are obtained, n_m respectively n_ψ, which are defined as follows:

- for ***the torque regulator***,

$$n_m = \begin{cases} 1, & \text{for } m^* \rangle \ \hat{m} + \dfrac{h_m}{2}, \\ 0, & \text{for } m^* = \hat{m} \\ -1, & \text{for } m^* \langle \ \hat{m} - \dfrac{h_m}{2}. \end{cases} \qquad (2.46)$$

- for ***the flux regulator***,

$$n_\psi = \begin{cases} 1, \text{for } \psi_s^* \rangle \ \hat{\psi}_s + \dfrac{h_\psi}{2}, \\ 0, \text{for } \psi_s^* \langle \ \hat{\psi}_s - \dfrac{h_\psi}{2}. \end{cases} \qquad (2.47)$$

In the above relations, h_m and h_ψ, represent the width of the hysteresis band of the two controllers. The measures $\hat{m}$ and $\hat{\psi}_S$ are estimated based on the measured stator voltage and stator currents.

The operation of the voltage inverter, controlled with elements of rapid static commutation (e.g. IGBT), is further analyzed based on the model shown in Figure 2.25.
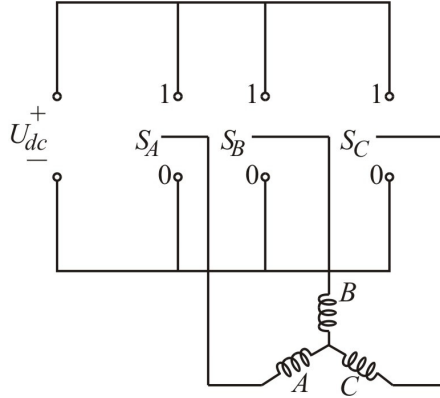
Fig. 2.25. Model of voltage inverter

The model of the inverter has been obtained by introducing three binary commutation function S_A, S_B, S_C. The binary function $S_A \in \{0,1\}$, corresponding to phase A is defined as follows:

$$S_A = \begin{cases} 1, & \text{if phase } A \text{ is connected to the plus voltage source } U_{dc} ; \\ 0, & \text{if phase } A \text{ is connected to the minus.} \end{cases}$$

Similarly, the functions S_B and S_C are defined.

The states of the three functions can generate in the referential $\alpha\beta$ ***eight discrete stator voltage vectors***, $\underline{u}_s = \underline{V}_v(S_A, S_B, S_C), v = 0,1,...,7,$ of which six are non-null and two are null. Non-null vectors $\underline{V}_1(1,0,0), \underline{V}_2(1,1,0), \underline{V}_3(0,1,0), \underline{V}_4(0,1,1), \underline{V}_5(0,0,1), \underline{V}_6(1,0,1)$ have a constant modulus, their position being successively fixed with 60° electric in the plane $\alpha\beta$ (see Figure 2.26). The two

null vectors are $\underline{V}_0\left(0,0,0\right)$ şi $\underline{V}_7\left(1,1,1,\right)$. By applying the null vectors, the phases of the motor are short-circuited (see Figure 2.25).

The vector components $\underline{u}_s$ can be written according to the states of the three functions and the source voltage U_{dc}.

Thus, in the coordinates of the phases (natural), it is obtained:

$$
\begin{aligned}
U_{S_A} &= \frac{U_{dc}}{3}\left(2S_A - S_B - S_C\right), \\
U_{S_B} &= \frac{U_{dc}}{3}\left(-S_A + 2S_B - S_C\right), \\
U_{S_C} &= \frac{U_{dc}}{3}\left(-S_A - S_B + 2S_C\right).
\end{aligned}
\tag{2.48}
$$

and in the *referential* $\alpha\beta$:

$$
\begin{aligned}
U_{\alpha s} &= \frac{U_{dc}}{3}\left(2S_A - S_B - S_C\right), \\
U_{\beta s} &= \frac{\sqrt{3}U_{dc}}{3}\left(S_B - S_C\right).
\end{aligned}
\tag{2.49}
$$

The question is still to select the corresponding voltage vectors, so as to ensure the required stator flux and electromagnetic torque. For this, we start from the vectorial equation of the stator voltage in the reference system $\alpha\beta$, in which the stator resistance R_s is neglected:

$$
d\underline{\psi}_s \approx \underline{u}_s \cdot dt,
\tag{2.50}
$$

from where it is obtained:

$$
\underline{\Psi}_s = \underline{\Psi}_{so} + \int_0^t \underline{u}_s dt \;,
\tag{2.51}
$$

relation that emphasizes the evolution of the stator flux vector $\underline{\psi}_s$ based on the stator voltage vector.

In the time interval [0, t_c) between two successive switching $\underline{u}_s\left(S_A, S_B, S_C\right)$ it is constant in magnitude and direction. Under these conditions, (2.51) can be written as:

$$
\underline{\Psi}_s = \underline{\Psi}_{s0} + \underline{u}_s\left(S_A, S_B, S_C\right)\cdot t \quad \text{with } t\in\left[0, t_c\right) \;,
\tag{2.52}
$$

or

$$
\Delta\underline{\Psi}_s = \underline{\Psi}_s - \underline{\Psi}_{s0} = \underline{u}_s\left(S_A, S_B, S_C\right)\cdot t \quad \text{with } t\in\left[0, t_c\right).
\tag{2.53}
$$

The relations presented above model the evolution of the stator flux depending on the state of three binary functions. It is noted that the variations of the flux are made along the stator voltage vector by which the inverter voltage is controlled.

To see how to select the voltage vectors needed to control the stator flux, the plan $\alpha\beta$ is divided into six sectors, each having 60° electric and the vector corresponding to $\underline{V}_i$ as a bisector (see Figure 2.26). For reasons of computational algorithms, the sectors separation is done by

bisecting. In order to maintain the flux vector trajectory within the hysteresis band h_ψ the optimum voltage vector must be selected $\underline{u}_s = \underline{V}_i(S_A, S_B, S_C)$, which may be applied. This vector depends on the initial position of the stator flux phasor $\underline{\Psi}_{s0}$ which is reduced in this case to the factual knowledge of the sector θ_i in which $\underline{\psi}_{s0}$, is found, information that can be obtained from simple comparison.
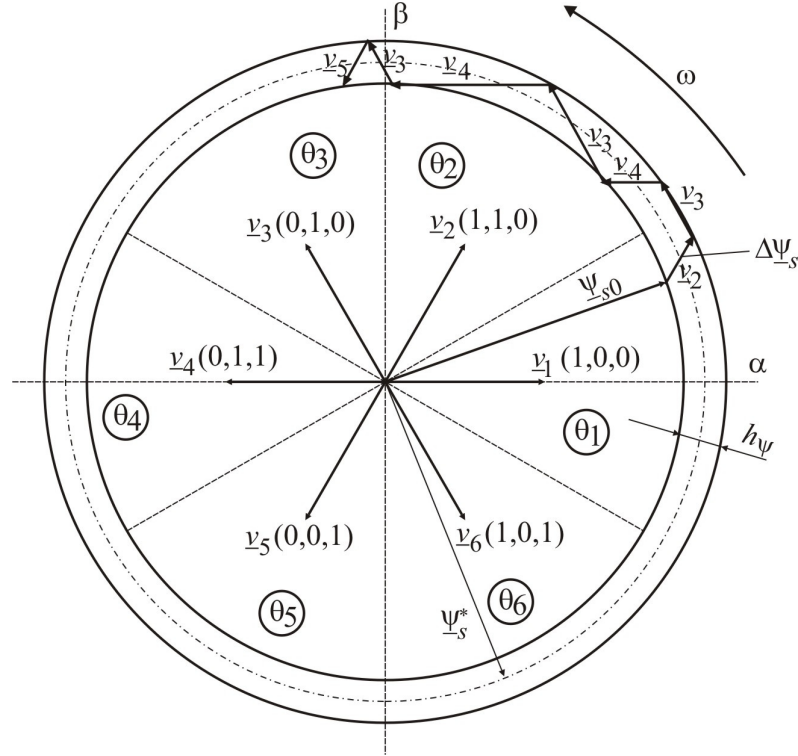
Fig. 2.26. Discrete stator voltage vectors $\underline{V}_i(S_A, S_B, S_C)$ and the evolution of the stator flux trajectory within the hysteresis band h_ψ.

The control of the voltage inverter is achieved by the optimum choosing of the triplet (S_A, S_B, S_C) based on the torque error $\varepsilon_m = m^* - \hat{m}$ and flow error $\varepsilon_\psi = \psi_s^* - \hat{\psi}_s$ translated by the two controllers in the numerical variables n_m and n_ψ, as well as on the sector θ_i in which the flux vector is found.

The control system transposes the necessary in torque and flux for the controlled machine in synthetic values chosen by convention as follows:

- for the torque: - $n_m = 1$, where the torque grows;

                   - $n_m = 0$, if the torque does not change;

                   - $n_m = -1$, when the torque decreases.

- for flux: - $n_\psi = 1$, if the flux increases;

                   - $n_\psi = 0$ if the flux decreases.

The selection of the optimal voltage vector according to the sign and size of the flux and torque errors and their effects on the evolution of the electromagnetic torque and stator flux are shown in Figure 2.27.
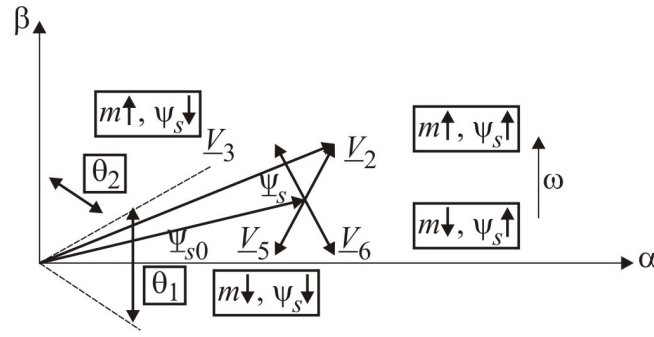
Fig. 2.27. Selection of the optimum voltage vector and the effects on the evolution
of the electromagnetic torque and stator flux.

From the analysis of Figure 2.27 the following conclusions can be synthesized:

1. If you select one of the two null stator voltage vectors, the stator flux stops its rotation remaining constant. The null torque command is obtained. It should be noted the observation that in reality, due to the stator resistance which has been neglected, the flux module slowly decreases and the dynamic torque response slows.

2. The acceleration of the stator flux, which basically means increasing the stator frequency and implicitly the slip and the electromagnetic torque, is achieved by selecting the voltage vectors found in the immediate vicinity of the sector θ_i in which the stator flux vector $\underline{\psi}_{s0}$ is found. If the voltage vectors more distanced from the sector θ_i are chosen, a decrease in the stator flux is obtained.

3. In order to produce a positive torque, the flux vector is accelerated. A negative torque results from the deceleration of the stator flux vector.

4. The acceleration of the torque in the rotation direction is obtained by the choosing the voltage vectors corresponding to the first two sectors which succeed θ_i in this respect. For deceleration, the voltage vectors in the two sectors joined to θ_i are selected, but in the opposite direction. The numerical variables n_m, n_ψ and the sector θ_i in which the stator flux vector forms a binary word by accessing the address of a memory EPROM, select the optimal voltage vector (see Table 2.5).

Table 2.5. Table of optimal commutation.

$n_{\psi_1} n_m$ \ θ_i		θ_1	θ_2	θ_3	θ_4	θ_5	θ_6
$n_\psi = 1$	$n_m = 1$	$\underline{V}_2(1,1,0)$	$\underline{V}_3(0,1,0)$	$\underline{V}_4(0,1,1)$	$\underline{V}_5(0,01)$	$\underline{V}_6(1,0,1)$	$\underline{V}_1(1,0,0)$
	$n_{m=0}$	$\underline{V}_0(0,0,0)$	$\underline{V}_7(1,1,1)$	$\underline{V}_0(0,0,0)$	$\underline{V}_7(1,1,1)$	$\underline{V}_0(0,0,0)$	$\underline{V}_7(1,1,1)$
	$n_m = -1$	$\underline{V}_6(1,0,1)$	$\underline{V}_1(1,0,0)$	$\underline{V}_2(1,1,0)$	$\underline{V}_3(0,1,0)$	$\underline{V}_4(0,1,1)$	$\underline{V}_5(0,0,1)$
$n_\psi = 0$	$n_m = 1$	$\underline{V}_3(0,1,0)$	$\underline{V}_4(0,1,1)$	$\underline{V}_5(0,0,1)$	$\underline{V}_6(1,0,1)$	$\underline{V}_1(1,0,0)$	$\underline{V}_2(1,1,0)$
	$n_m = 0$	$\underline{V}_7(1,1,1)$	$\underline{V}_0(0,0,0)$	$\underline{V}_7(1,1,1)$	$\underline{V}_0(0,0,0)$	$\underline{V}_7(1,1,1)$	$\underline{V}_0(0,0,0)$
	$n_m = -1$	$\underline{V}_5(0,0,1)$	$\underline{V}_6(1,0,1)$	$\underline{V}_1(1,0,0)$	$\underline{V}_2(1,1,0)$	$\underline{V}_3(0,1,0)$	$\underline{V}_4(0,1,1)$

Note: To get a finer control of the stator flux vector $\underline{\psi}_s$ the number of sectors can be increased to 12, situation in which each sector is of electrical 30°.

The duration of the voltage vector can be obtained either by setting the commutation frequency or by imposing the width h_ψ of the hysteresis band in which to produce the variation of the amplitude of the stator flux. The classic system CVDCF in Figure 2.24 allows the regenerative braking by simply reducing the reference value of the torque which leads to a limitation of the electromagnetic torque m^* of opposite sign.

The direct classic torque and flux vector control has the following advantages:

- ensures a fast dynamic torque response and the operation in a wide range of speeds;

- is robust and relatively simple to implement;

- does not require current regulators and coordinates transformations;

- does not require either a stator voltage equations decoupling circuit or a separate vector modulator for the control of the PWM inverter;

- provides an efficient rejection of disturbances;

- can be successfully applied in the case of resonant inverters.

- folds very well on numeric control.

It should be emphasized that by ***the implementation of the torque and flux control vector*** for the electric drive systems with asynchronous motors of the naval mechanisms, to the characteristic advantages of this type of control strategy listed above, the following two must be added:

- through the proposed solution, an induction motor can be used with the rotor in normal short-circuit, with a single stator winding, the modification of the speed being achieved by vector control. This eliminates the existing version that uses as execution elements the asynchronous motors with three-speed stages obtained using three separate windings in star connection;

- the proposed solution also removes the control panel that comprises direction contactors, acceleration, braking and timing relays.

2.3.1.4. Experimental determinations

The implementation of the vectorial torque and flux control for the electric drive systems with induction machines serving naval mechanisms was made in two stages. In the first phase, the implementation was conducted in a model of laboratory developed at the Faculty of Electrical and Power Systems Engineering of Timişoara and then on an experimental stand provided by the Naval Academy of Constanţa. The main experimental results obtained from the measurements made on this stand are shown in the following [63], [70], [71], [72], [73], [74], [79]. On the designed test stand the two ABB inverters acquired in the research were implemented. Thus during the experiments conducted at the Faculty of Electrical and Power Systems Engineering of Timişoara, the ACS800 inverter, of 4 [kW] was used. The measurements were performed on the stand of the Naval Academy of Constanta. The ACS800 frequency converter of 11 [kW] was used, executed by naval standards. The used electric drive machine was an asynchronous squirrel cage of 11 {kW] type.

In order to highlight the conversion and control processes in the present operation three signals have been acquired: ***the supply voltage of the motor*** (inverter output), ***the motor supply current*** (the output current of the inverter) and ***the speed***. For this, two data **acquisition systems** have been used in accordance with the diagram in Figure 2.28.
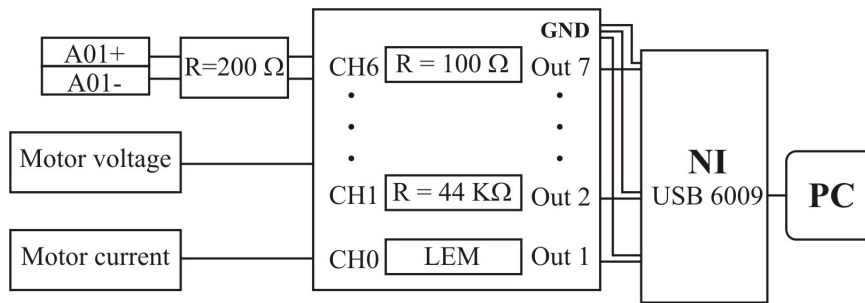
Fig. 2.28. The block diagram of the data acquisition system.

From the output terminals of the inverter one of the motor phases was taken and passed through the LEM. Its role is of current transducer as at the output of the acquisition board there is voltage proportional to the current. In either of the two phases of the output voltage of the inverter the acquisition of the voltage signal can be made. It is used in parallel to a resistor of 44 [kΩ], at its output the voltage is proportional to the input one, but of much smaller value to be supported by the second acquisition board. The converter has two current outputs proportional to the speed and torque of the operating motor. The measuring range of the two outputs is from 0 to 20 [mA] corresponding to the speed from zero up to the nominal speed, inscribed as a parameter in the ABB equipment. Since acquisition board does not measure currents that are so small, a great precision resistance of 200 [Ω] it is placed in parallel with its output. Thus, the voltage is applied at the input of the acquisition board on a resistance of 1.8 [k Ω]. At the exit of the first acquisition board voltage proportional to the speed results [68], [69].
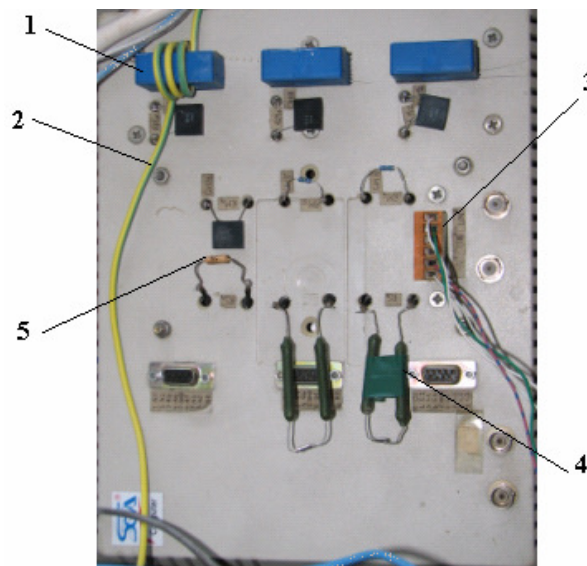
Fig. 2.29. The signal conversion plate received from inverter 1, MEL, current transducer; 2-phase used for current aquisition at the inverter output; 3 - the output used for voltage acquisition; 4- resistance of 44 [kΩ] corresponding to the motor voltage; 5-resistance of 1.8 [kΩ] corresponding to speed signal.

From the schema of the acquisition board shown in Figure 2.30, it is observed what the channel corresponds to each measured captured. Thus, the supply current of the motor enters channel 0 and the output signal is acquired on the pins 1-11. The motor voltage enters channel 6 having an output signal on pins 7-11. Speed enters as voltage on channel 1 and is output from the acquisition board is on pins 2-11.
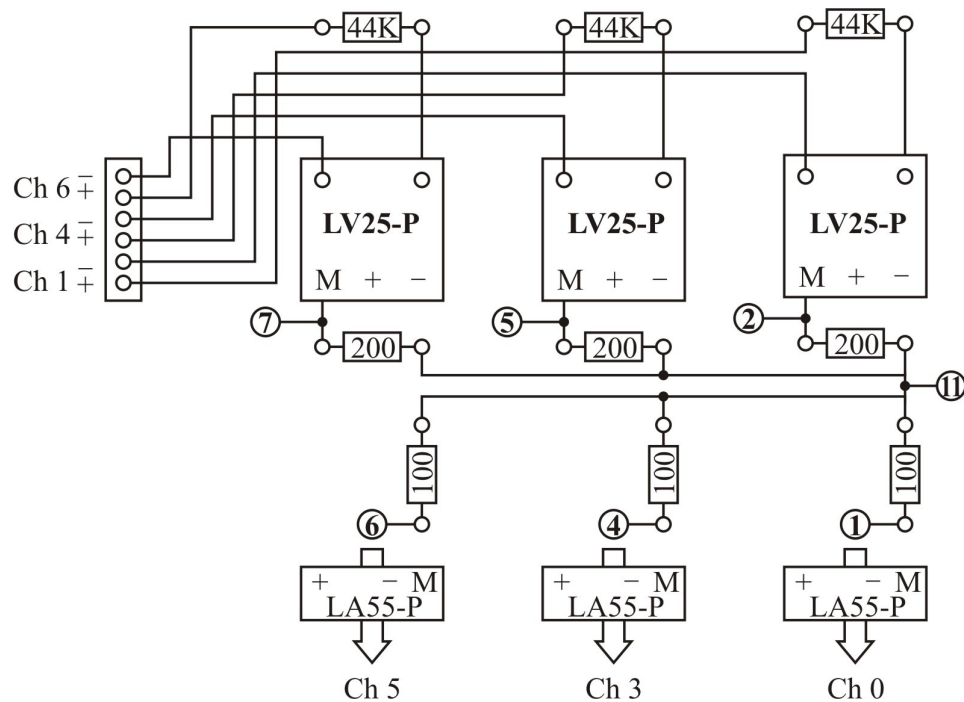
Fig. 2.30. The acquisition board scheme.

The second acquisition board (see Figure 2.31) is produced by National Instruments. It is a low-cost, poor precision board, designed more for laboratory applications for teaching purposes. The benefit of this board is that it connects via USB to the computer; it has 12 digital inputs. The connectors can be changed very easily. The transfer speed can be up to 48 [Kbits / sec]. The input voltage range is of ± 1 up to 20 [V] and the output voltage between 0 and 5 [V].

Fig. 2.31. National Instruments 6009 acquisition board.

To process the data sent by the second acquisition board a Matlab program was used, designed by the research team to view the signals. The simultaneous display of the three signals is obtained in real time. The maximum length of time that can make the acquisition is 1 [s]. This restriction is given by the construction of the NI 6009 acquisition board. For the speed signal in normal operating regime a filtering is performed. In the dynamic regime, the filtration was eliminated in order to better observe the rise and fall of the speed. In Figures 2.32, the waveforms obtained at different speeds of the machine are presented.

On the third chart the frequency of the voltage signal of the motor can be observed. Also on this signal can be observed how results after the "cutting" the continuous voltage from the intermediate circuit. The signal corresponding to the speed, the chart in the centre, is filtered through the realized Matlab program. An arithmetic average is made of all of the acquired values on the signal of the speed, thus a straight line is obtained that is parallel with the time axis. In the first chart the signal corresponding to the current on a feeding phase of the motor.
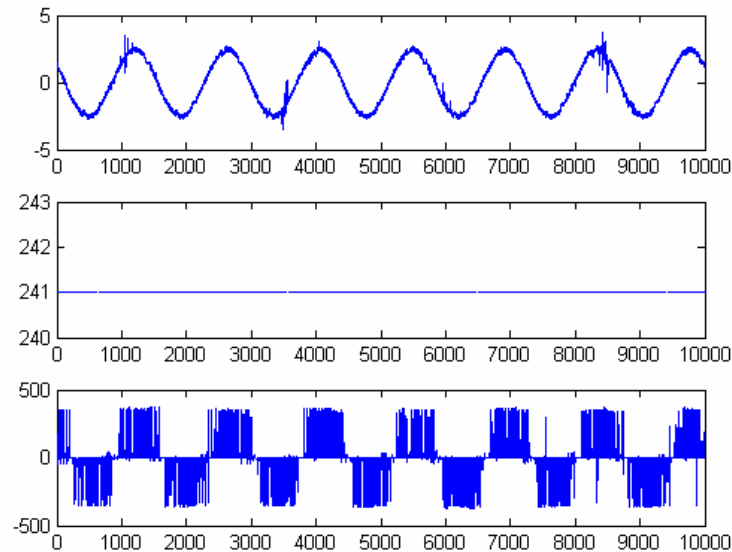
Fig. 2.32. The normal functioning regime at 20 % of the prescribed speed: phase current, speed, voltage.
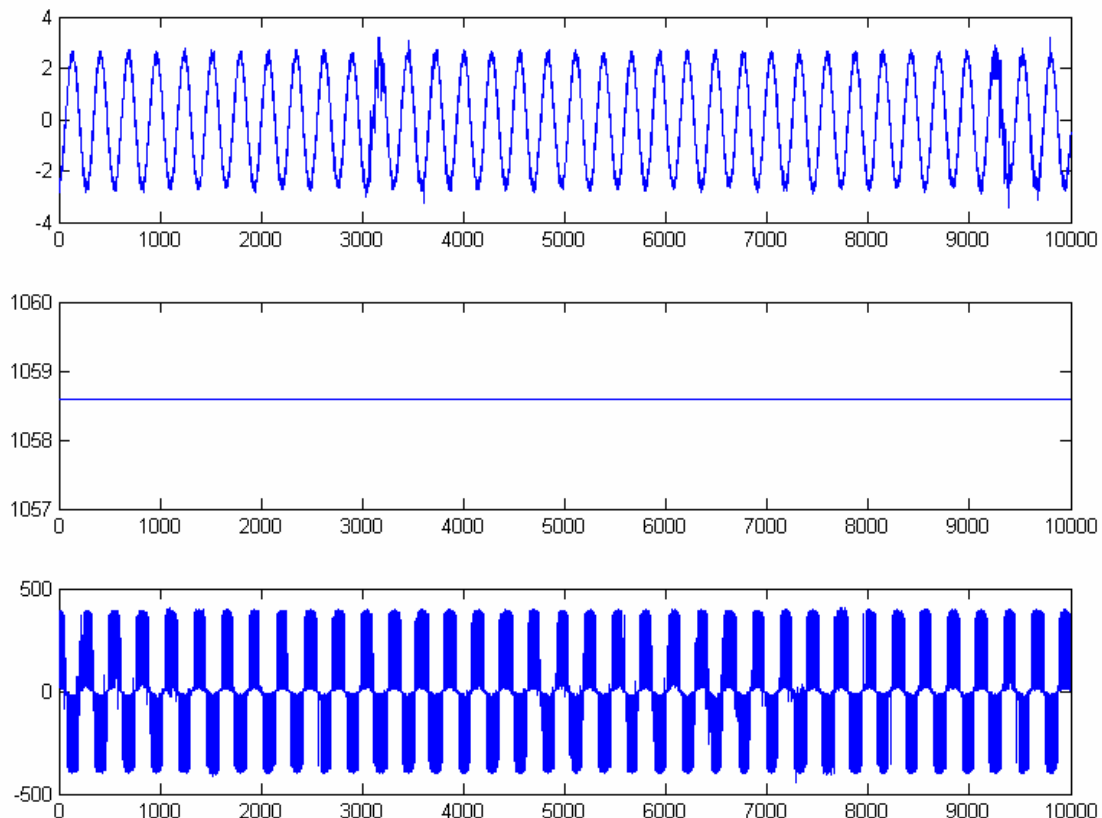
Fig. 2. 33. The normal functioning regime at 90 % of the prescribed speed.
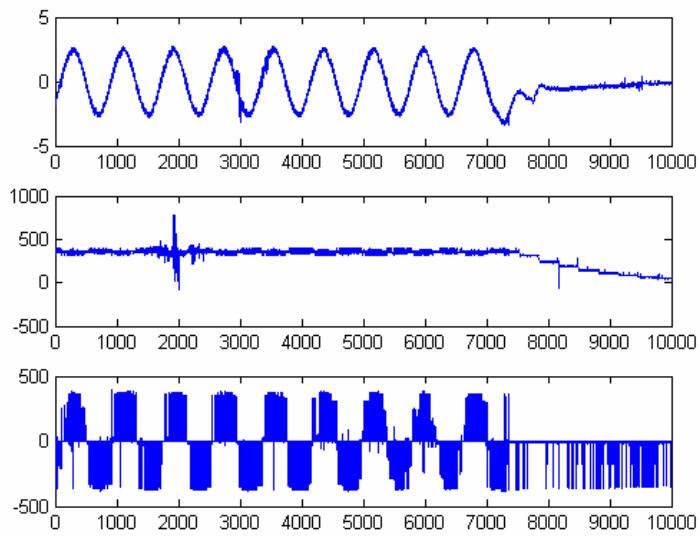
Fig. 2. 34. Stopping at 40 % of the prescribed speed.
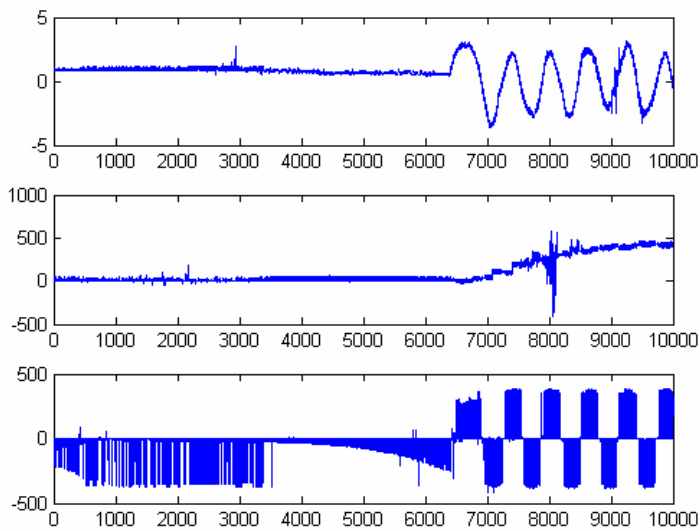
Fig. 2. 35. Starting regime until 40 % of the prescribed speed.
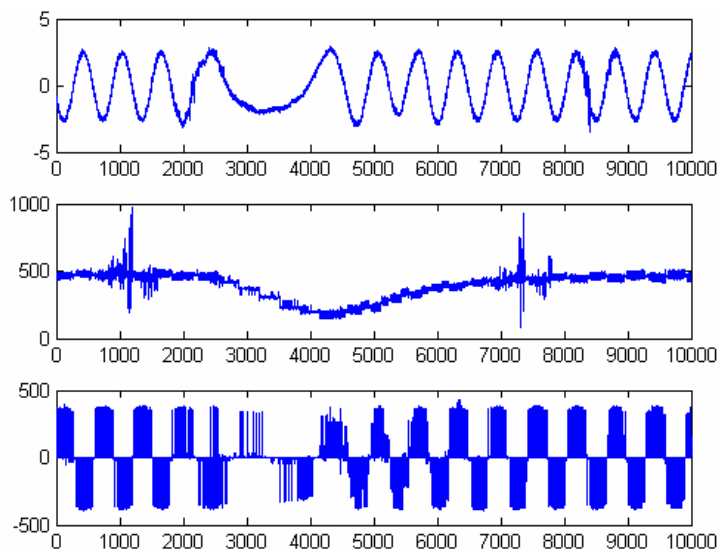
Fig. 2. 36. Speed reversing diagrams.

2.3.1.5. Conclusions

The practical implementation of the purposed solution highlights the following advantages:

- there is the possibility of the adjustment of the speed of the motor at predefined values before the starting;

- the steps of the speed are commanded through the closing or opening of some contacts;

- the potentiometer mounted on the controller is not used;

- the command being external, can be mounted in separate command room or in a place where the operator is protected;

- the usage of the converter commanded in voltage reduces the power consumption. More than this, presents visible advantages regarding the safety of the operations. Also, the compact form of this devices optimizes the used space in the distribution panel;

- has a high degree of precision and very good dynamic in the conditions of a variable load and speed;

- there is the possibility of a permanent display of the output parameters from the frequency converter.

2.3.2. Contributions to the development of algorithms for optimal control of alternative current machines

2.3.2.1. Novel Flux Weakening Control Algorithm for PMSM

2.3.2.1.1. Introduction

In the last years **permanent magnet synchronous motors (PMSM)** are receiving increased attention for drive systems instead of induction motors because of their high controllability, high efficiency, high torque to inertia ratio and high power density. Wide speed range drives are required in applications like traction, spindle and home appliances. As the price for digital signal processors (DSP), digital signal controllers (DSC), ARM processors and complex instruction set microcontrollers (CISC) for motor control applications tend to decrease and the performances of these microcontrollers tend to increase, the choice of a sensored / sensorless field oriented PMSM drive system becomes more attractive for low power applications. Using variable speed PMSM drives for low power applications the energy efficiency and the performance of the system will increase and may further eliminate the need of a gearbox.

In the literature have been investigated *a lot of interesting algorithms to generate the d- and q-axis reference currents* (in the constant torque area and flux-weakening area) (e.g. [82], [83], [84], [85]. [86], [87], [88], [89], [90], [91]). In the [82], [83] the mathematical model of PMSM is used to generate the *d*-axis reference current which is affected by the variation of the motor parameters (due to temperature and saturation effect). The flux-weakening methods proposed in [84], [85], [86], [87] are not parameters sensitive. In [84] the *d*-axis current is adjusted according to the current error in *q*-axis. In [85] the *q*-axis voltage error is used to adjust the *d*-axis current and in

[86] the voltage error is used to adjust the *d*-axis and *q*-axis current. A voltage regulation method is proposed in [87], to generate the *d*-axis current. In [88], [89], [90], [91] a look-up table method is presented which is motor dependent. Different methods of carrier-based pulse width-modulated (PWM) in overmodulation region are investigated in [92], [93].

In this research, ***our team proposed an algorithm, starting from the mathematical model of PMSM in per-unit, used to calculate the optimal d- and q-axis reference currents, in the constant torque region and field weakening region taking into account the PMSM with salient-pole or nonsalient-pole***. ***The existing constraints for the operation in field weakening region are the maximum output voltage of the VSI and the maximum current of the VSI or the maximum permitted current of PMSM*** [94], [95].

By using the overmodulation method the installed capacity of the voltage source inverter (VSI) is used better and dynamic and steady-state performance of the control system will be improved. However in the overmodulation region the motor current will have lower order harmonics but also the switching losses in the power module will be reduced.

The ***proposed control has the following advantages***:

- easy to control the motor, with no need of tables for *d*- and *q*-axis reference currents;

- direct limitation of the maximum *q*-axis current for the whole speed range;

- the flux-weakening area is well exploited;

- the control is stable in the overmodulation region.

2.3.2.1.2. System Limitation

a. Dynamic model of PMSM

In this study all variables are in per-unit. The mathematical model in per-unit of the PMSM in d-q rotor reference frame can be written as follows:

$$\begin{bmatrix} v_{dpu} \\ v_{qpu} \end{bmatrix} = \begin{bmatrix} r_{pu} + pl_{dpu} & -\omega_{rpu}l_{qpu} \\ \omega_{rpu}l_{dpu} & r_{pu} + pl_{qpu} \end{bmatrix} \begin{bmatrix} i_{dpu} \\ i_{qpu} \end{bmatrix} + \begin{bmatrix} 0 \\ \omega_{rpu}\psi_{PMpu} \end{bmatrix} \tag{2.54}$$

$$t_{dqelmpu} = \psi_{PMpu}i_{qpu} + \left(l_{dpu} - l_{qpu} \right) i_{qpu}i_{dpu} \tag{2.55}$$

where: ω_{rpu} is electrical angular velocity in per-unit, i_{dpu}, i_{qpu} are the d- and q-axes armature currents in per-unit, v_{dpu}, v_{qpu} are the d- and q-axes terminal voltages in per-unit, r_{pu} is the armature resistance in per-unit, l_{dpu}, l_{qpu} are the d- and q-axes inductances in per-unit, ψ_{PMpu} is the permanent magnet flux linkage, $t_{dqelmpu}$ is the developed electric torque in per-unit and *p* is the differential operator in per-unit.

In the case of ***nonsalient-pole PMSM*** the relation between *d*- and *q*-axes inductances is $l_{dpu} = l_{qpu}$, while in the case of ***salient-pole PMSM*** the relation between *d*- and *q*-axes inductances is $l_{dpu} \neq l_{qpu}$.

b. Voltage and current limitation

The maximum current of the inverter or the maximum current of the PMSM must be restricted to limiting the torque producing component *q*-axis current while the *d*-axis current must be unaffected. The maximum voltage is dependent from the dc link voltage of the inverter. The condition for the maximum current limiting and the limit condition of the voltage are:

$$i_{qpu} \le \sqrt{I_{\max\,pu}^2 - i_{dpu}^2} \tag{2.56}$$

$$\sqrt{v_{dpu}^2 + v_{qpu}^2} \le V_{\max\,pu} \tag{2.57}$$

where: $V_{\max pu}$ is the maximum voltage magnitude in per-unit, $I_{\max pu}$ is the maximum current magnitude in per-unit, i_{dpu}, i_{qpu} are the *d*-axis and *q*-axis armature currents in per-unit and v_{dpu}, v_{qpu} are the *d*-axis and *q*-axis terminal voltages in per-unit.

c. Operating conditions of PMSM

The analysis of PMSM in different operation regions can be carried out using the circle diagram in the I_d-I_q plane (see Figure 2.37). The current limit in the I_d-I_q plane is a circle, centered in origin, and the voltage limit in the I_d-I_q plane is an ellipse, centered in $(-i_{carpu}$ (F, or U), 0) , if we neglect the stator resistance of PMSM.
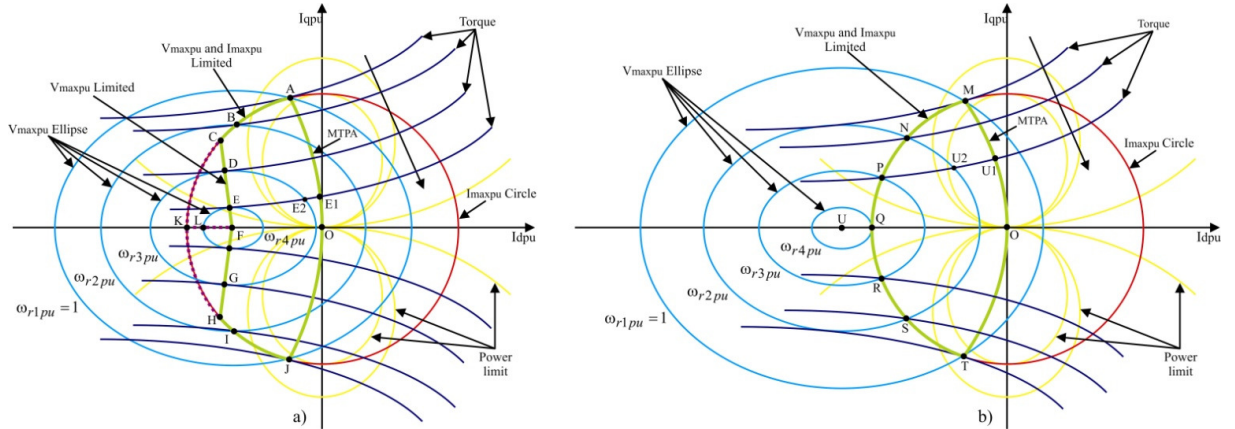
Fig. 2.37. Cycle diagrams of PMSM drive.

In the constant torque region, the *d*-axis reference current in per-unit can be generated using the maximum torque-per-ampere control method (MTPA) (see relation (2.58)). In this case the operating points are on the curve AOJ or curve MOT (see Figure 2.37).

In the flux-weakening there are two operating regions [81] (see Figure 2.37):

- ***flux-weakening region I***, where the operation is limited by $V_{\max pu}$ and $I_{\max pu}$, (area OACFHJ Figure 2.37 a), or OMQT see Figure 2.37 b));

- ***flux-weakening region II***, where the operation is limited by the $V_{\max pu}$ (CFH see Figure 2.37 a)).

The operation of the PMSM drive system in the flux-weakening region II is only possible if the characteristic current $i_{carpu} = (\psi_{PMpu}/l_{dpu})$ is less than $I_{\max pu}$ (the center of the voltage ellipse (F see Figure 2.37 a)) is inside of the current limit). In this case there is no theoretical upper speed

limit and the control needs a maximum torque per voltage control strategy. An example of flux-weakening control trajectory in region II is presented in Figure 2.37 a) line CFH.

d. Current reference calculator

The block of the proposed algorithm scheme is presented in Figure 2.39. In this proposed speed control drive system, the output of the PI speed controller is the amplitude of q-axis current (see Figure 2.38) in per-unit (i^*_{qpu}). Depending on this value (i^*_{qpu}) and depending on the speed region (constant-torque region or flux-weakening region) can be calculated the d-axis current and the limit for the q-axis current. Using the maximum torque-per-ampere (MTPA) control method, in the constant-torque region, the d-axis reference current in per-unit can be calculated using the following relation:

$$i^*_{dpu} = -\frac{\Psi_{PMpu}}{2\left(l_{dpu} - l_{qpu}\right)} - \sqrt{\left(\frac{\Psi_{PMpu}}{2\left(l_{dpu} - l_{qpu}\right)}\right)^2 + i^{*2}_{qpu}} \qquad (2.58)$$

The d-axis reference current can be calculated in the case of nonsalient-pole PMSM using the following relation:

$$i^*_{dpu} = 0 \qquad (2.59)$$

The limit for the q-axis reference current can be calculated with the following relation:

$$i^*_{qpu} = \sqrt{I^{*2}_{\max pu} - i^{*2}_{dpu}} \qquad (2.60)$$
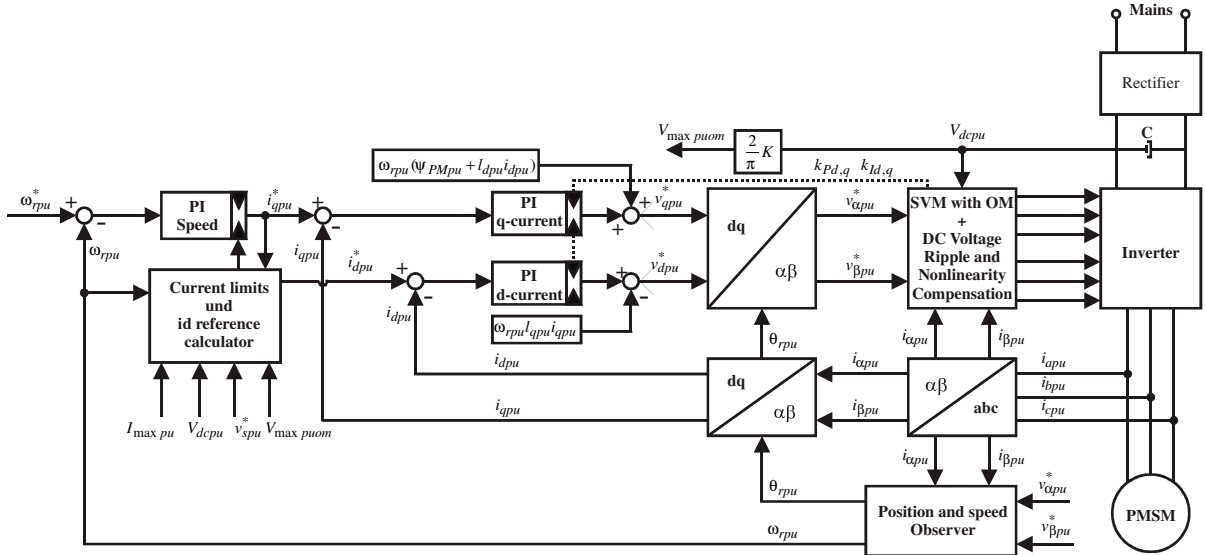
Fig. 2.38. Block diagram of the proposed rotor field oriented control.

The MTPA control trajectory can be implemented in a lookup table that associates the correct d-axis reference current with the q-axis required current, or it can be calculated using relation (2.58) or (2.59). In the flux-weakening region I, the d-axis reference current in per-unit can be calculated using the following relation ($r_{pu} = 0$):

$$i^*_{dpu} = -\frac{\Psi_{PMpu}}{l_{dpu}} + \frac{1}{l_{dpu}}\sqrt{\left(\frac{V_{\max pu}}{\omega_{rpu}}\right)^2 - l^2_{qpu} i^{*2}_{qpu}} \qquad (2.61)$$

In this region I the *d*-axis reference current can be calculated in the case of nonsalient-pole PMSM using the following relation ($r_{pu} = 0$):

$$i^*_{dpu} = -\frac{\Psi_{PMpu}}{l_{dpu}} + \sqrt{\left(\frac{V_{\max pu}}{l_{dpu}\omega_{rpu}}\right)^2 - i^{*2}_{qpu}} \tag{2.62}$$

The limit for the *q*-axis reference current can be calculated in the flux-weakening region I using the same relation (2.60). In the flux-weakening region II, the *d*-axis current reference in per-unit can be calculated using the following relation ($r_{pu} = 0$):

$$i^*_{dpu} = -\frac{\Psi_{PMpu}}{4\left(l_{dpu} - l_{qpu}\right)l_{dpu}}\left(4l_{dpu} - 3l_{qpu} - \sqrt{l^2_{qpu} + \frac{8V^2_{\max pu}\left(l_{dpu} - l_{qpu}\right)^2}{\omega^2_{rpu}\Psi^2_{PMpu}}}\right) \tag{2.63}$$

The *d*-axis current reference can be calculated in the flux-weakening region II, in the case of nonsalient-pole PMSM using the following relation:

$$i^*_{dpu} = -\frac{\Psi_{PMpu}}{l_{dpu}} \tag{2.64}$$

The *q*-axis reference current in flux-weakening region II can be calculated using relation ($r_{pu} = 0$):

$$i^*_{qpu} = \pm\frac{1}{l_{qpu}}\sqrt{\left(\frac{V_{\max pu}}{\omega_{rpu}}\right)^2 - \left(l_{dpu}i^*_{dpu} + \Psi_{PMpu}\right)^2} \tag{2.65}$$

If you want a more accurate calculation of the d- and q-axis reference currents using the above relations the saturation and cross-saturation must be considered.

2.3.2.1.3. Description of the proposed algorithm

The *proposed algorithm, for the wide speed range PMSM drives, can be easy integrated in a well-known rotor field oriented control* (see Figure 2.38), where the *d*-axis and the *q*-axis currents are the main control variables.

The *d*-axis reference current for the whole speed range and the limits of the speed controller are generated using the proposed algorithm from the block *"Current limit and i_d reference calculator"* (see Figure 2.38 and Figure 2.39). With this algorithm, the optimum reference current and current limits can be generated for the whole speed range. This algorithm is suitable for PWM-VSI which works in the *overmodulation region*. In the constant torque region the **"PIIdCor" controller** is not active (the positive limit of the controller is zero) and the *d*-axis reference current is calculated using the relation (2.58) or (2.59) (see Figure 2.38) according to the required *q*-axis current. In the flux-weakening area, the *d*-axis reference current will be adjusted using a PI voltage controller, **"PIIdCor"**. The limits of the PI voltage controller are (0, -$I_{\max pu}$). Using in parallel the PI controller and the relation (2.58) or (2.59) a fast dynamic response and smooth transitions between operating regions can be achieved. The d- and *q*-axis reference currents and the limits in d- and *q*-axis are dependent of the operating regions and of the value of I_{carpu}. The minimum *d*-axis reference current can be calculated using the following relation:

$$I_{d\min pu} = \begin{cases} -I_{\max pu} & i_{qpu}\omega_{rpu} < 0 \\ -I_{\max pu} & i_{qpu}\omega_{rpu} \geq 0 \quad I_{carpu} \geq I_{\max pu} \\ (2.63) \text{ or } (2.64) & i_{qpu}\omega_{rpu} \geq 0 \quad I_{carpu} < I_{\max pu} \end{cases} \tag{2.66}$$

If the current $I_{carpu} = \Psi_{PMpu}/l_{dpu}$ is bigger than the $I_{\max pu}$ the PMSM works just in the flux-weakening region I (see Figure 2.37 b)) and the maximum d-axis current and the maximum q-axis current can be calculated simple in the motor mode and generator mode. If the current $I_{\max pu}$ is bigger than the I_{carpu} the PMSM works in the flux-weakening region I and the flux-weakening region II (see Figure 2.37 a)). In this case the limit for d-axis current can be calculated using the relation (2.63) or (2.64) or using a lookup table that associates the maximum d-axis current with the motor speed. The values in the lookup table can be either evaluated analytically (2.63) or, in the case the model is not accurately known, on the field. In this case a series of tests can be performed with different values and speeds with the aim to get the fastest speed acceleration.
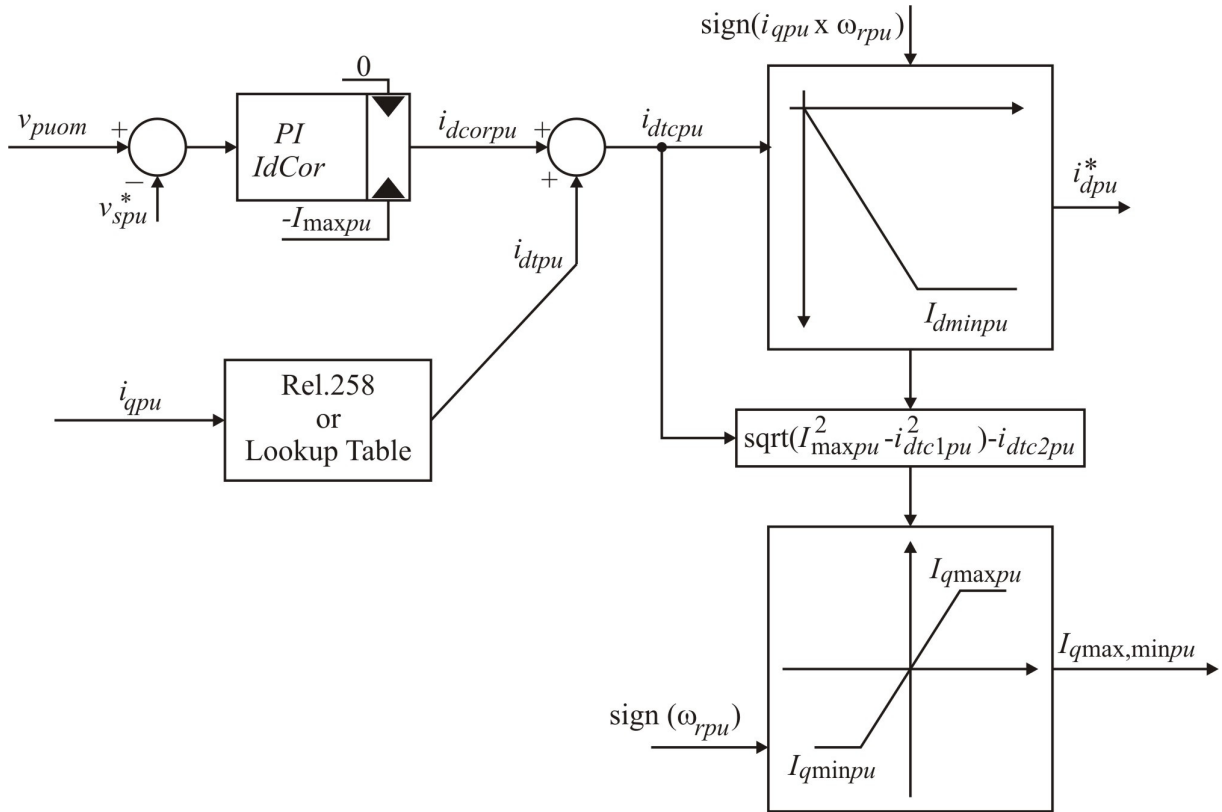
Fig. 2.39. Block diagram of the proposed algorithm.

If the i_{dtcpu} is less than $I_{d\min pu}$ the d-axis current is limited at this value, and the q-axis current will be reduced using the relation (2.67). The limits of the speed controller can be calculated using the following relation:

$$I_{q\min,\max pu} = sign(\omega_{rpu}) \times \left(\pm\sqrt{I_{\max pu}^2 - i_{dtc1pu}^2} - i_{dtc2pu} \right) \tag{2.67}$$

In the above relation (2.67) i_{dtc1pu} and i_{dtc2pu} can be calculated using the following relation:

$$
\begin{array}{ccc}
i_{dtc1\,pu} & i_{dtc2\,pu} & \\
\left| i_{dtcpu} \right| & 0 & i_{dtcpu} \geq I_{d\,min\,pu} - \text{region I} \\
\left| I_{d\,min\,pu} \right| & \left| i_{dtcpu} \right| - \left| I_{d\,min\,pu} \right| & i_{dtcpu} < I_{d\,min\,pu} - \text{region II}
\end{array}
\tag{2.68}
$$

The degree of the overmodulation can be determined by the relationship:

$$
V_{\max\,puom} = \frac{2}{\pi} K V_{dcpu}
\tag{2.69}
$$

We can say that the *d*-axis reference current and the *q*-axis current limit are influenced by the modulation index. ***The proposed control algorithm is relatively simple and it is easy to implement.***

2.3.2.1.3. Carrier-based PWM-VSI Overmodulation for SVM

The PWM-VSI goes into the overmodulation region when the reference voltage is located outside the inner circle. The overmodulation region is subdivided into two regions: the overmodulation region I where (0.907≤ *K* < 0.952) and the overmodulation region II where (0.951≤ *K* ≤ 1.00) [92]. In the overmodulation region I (see Figure 2.40 a)), the preprocessor manipulates the magnitude of the reference voltage vector, while the angle of the reference voltage vector is not changed and in the over-modulation region II (see Figure 2.40 b)) the preprocessor manipulates the magnitude and the angle of the reference voltage vector.

a) Overmodulation Region I

b) Overmodulation Region II
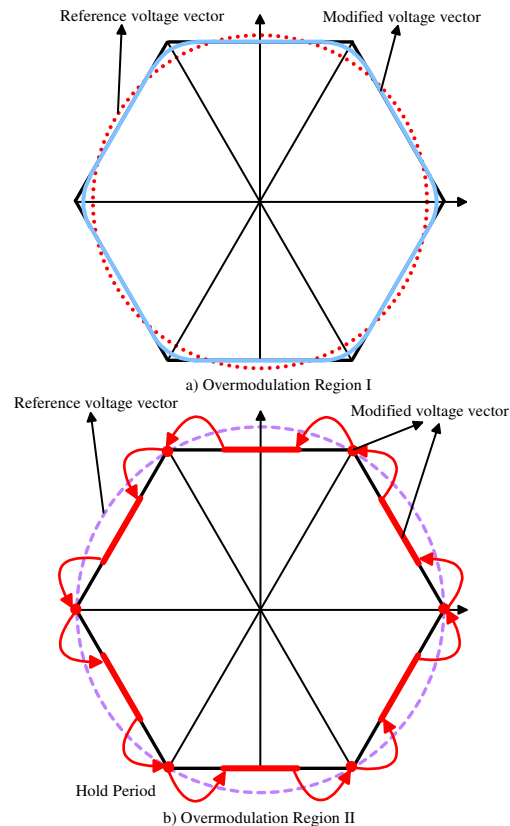
Fig. 2.40. Trajectory of voltage vector in:
a) Overmodulation Region I; b) Overmodulation Region II.

A method for calculating the on-times of the switching state vectors is presented in [93]. The same overmodulation technique is used also in this study. It is known that in the overmodulation region the motor currents will have lower order harmonics and the settings of the PI current controllers used in the linear region will work against overmodulation. A simple way to avoid this effect is to reduce the bandwidth of the current controller (see Figure 2.38). The dynamic and steady-state performance of the PMSM drive are improved by using the VSI in the overmodulation regions.

2.3.2.1.4. Experimental results of the proposed algorithm

The experimental performance of the proposed algorithm is presented using the sensorless rotor field oriented control PMSM drive presented in Figure 2.38. The motor control algorithm was implemented using a 16 [bit] DSC. The used PMSM has 1 [kW] and the performance of the system was tested with a dynamometer. To simulate the same inertia as for the real application of the drive system and additional weight is added to the motor shaft. To verify the advantages of the proposed algorithm with the PWM-VSI in the overmodulation region, different acceleration, braking and steady-state tests are performed on the dynamometer. The experimental results of the proposed algorithm in constant-torque region and flux-weakening region, are shown in Figure 2.41, Figure 2.42, Figure 2.43 and Figure 2.44.

Acceleration performances are shown in the Figure 2.41. Figure 2.41 a) shows the d-and q-axes reference currents generated with proposed algorithm, at 0.03 pu accelerating gradient, in the constant-torque region and also in the field weakening region I and II. Figure 2.41 b) shows the armature voltage reference V^*_{spu} and the maximum terminal voltage of the inverter V_{maxpu}.

Because the used inverter has no regenerative unit, in the case of regenerative brake it is possible to limit the dc-link voltage with the proposed algorithm if the regenerative energy is dissipated in the PMSM.

If the deceleration gradient is too big, the rotor speed of PMSM can't follow the reference speed. In this case the *decelerating performance* of the proposed algorithm is shown in Figure 2.42.

The *regenerative brake performance* is limited due to the possibility to dissipate the regenerative energy in the PMSMS stator resistance. Figure 2.42 a) shows the generated *d*-axis reference current and *q*-axis reference current in the regenerative mode. In the regenerative mode the *d*-axis reference current is kept at maximum value and the *q*-axis reference value is reduced because of dc link voltage limitation V_{dcpu}.

The Figure 2.43 a) shows the *performance of the current controllers in the overmodulation region and the maximum generated voltage according to the dc-link voltage for the proposed algorithm*. The *overmodulation benefits* are shown in Figure 2.43 b). In this case the motor is accelerated using the VSI in overmodulation region (n_{puom}, P_{dcpuom}) and then using the VSI in the linear region (n_{pu}, P_{dcpu}) under the same power limitation (see Figure 2.43 b). We achieve better acceleration performance in the case of the VSI with overmodulation region.

The *advantages of the overmodulation in steady-state* are presented in Figure 2.44. The exploitation of the overmodulation range shows that the required motor current and the power consumption (i_{spuom}, P_{dcpuom}) is lower than the required motor current and power consumption (i_{spu}, P_{dcpu}) of the motor in linear modulation range at the same load. Both tests confirm that the overmodulation range is effectively, so we can see that, the dynamic and steady-state performances

of the system are improved. ***By using the proposed algorithm in the overmodulation range, the stability of the system is not compromised***.
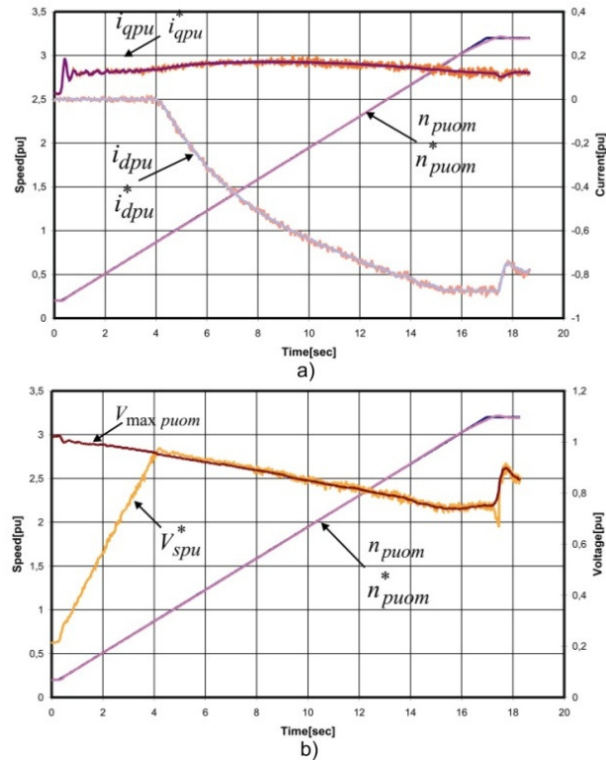
Fig. 2.41. Accelerating performance showing, at 0.03 pu accelerating gradient: a) the speed (n^*_{puom}, n_{puom}), d-axis current (i^*_{dpu}, i_{dpu}) and q-axis current (i^*_{qpu}, i_{qpu}), b) the speed (n^*_{puom}, n_{puom}), the regulated stator voltage (V^*_{spu}) and the maximum terminal voltage (V_{maxpu}).
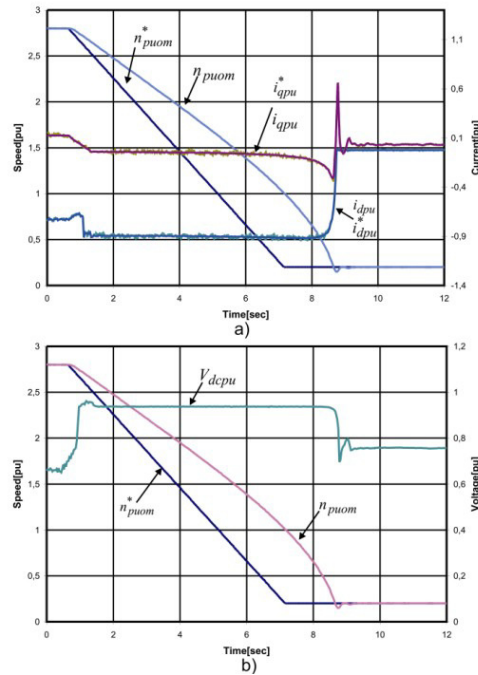
Fig. 2.42. Braking performances showing the speed ($n^*_{puom, npuom}$), d-axis current ($i^*_{dpu, idpu}$) and q-axis current ($i^*_{qpu, iqpu}$) gradient 0.2 pu a), b) the speed ($n^*_{puom, npuom}$), regulated dc link voltage (V_{dcpu}) braking gradient 0.02 pu.
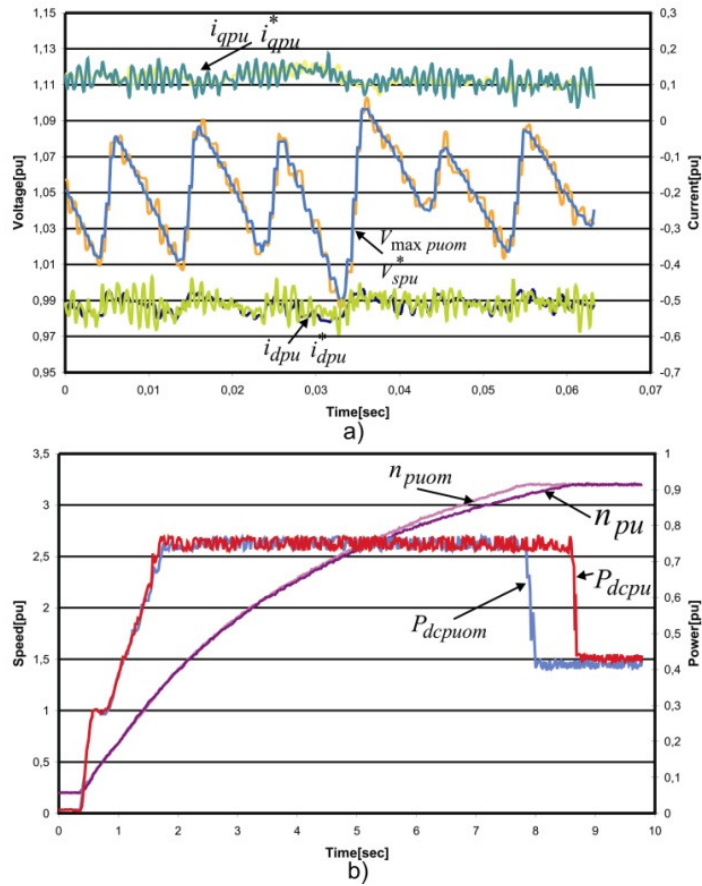
Fig. 2.43. Overmodulation benefits showing the voltage:
a) ($V_{\max puom}$, V^*_{spu}), *d*-axis current (i^*_{dpu}, i_{dpu}) and *q*-axis current (i^*_{qpu}, i_{qpu}) ,
b) the motor speed (n_{puom}, n_{pu}) and regulated dc link power (P_{dcpuom}, P_{dcpu}).
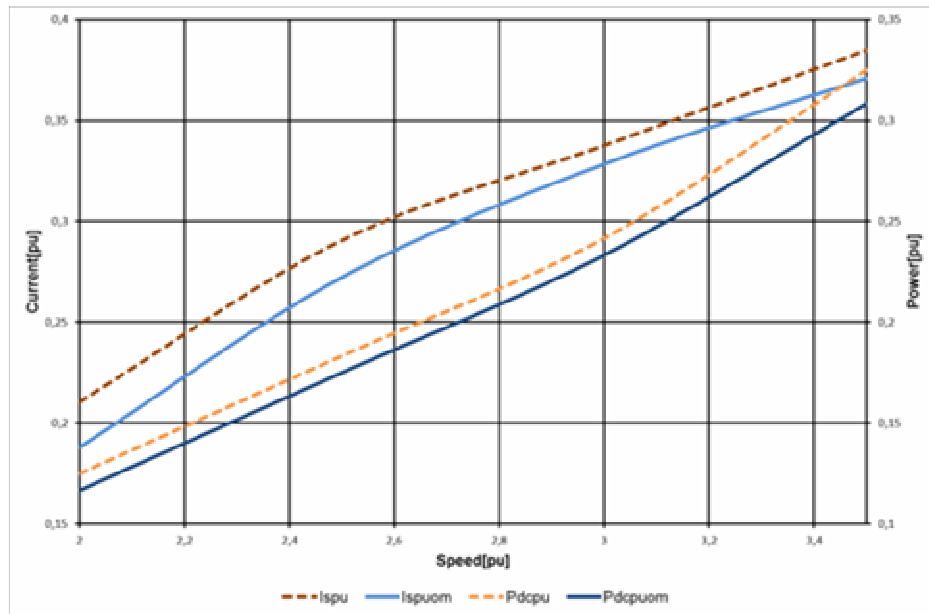
Fig. 2.44. Overmodulation benefits in steady-state showing motor current (i_{spuom}, i_{spu}), and dc link power (P_{dcpuom}, P_{dcpu}) with or without overmodulation versus motor speed.

The carrier-based PWM voltage in the overmodulation range is shown in Figure 2.45 (in this case *K* = 0.98 see (2.69)).
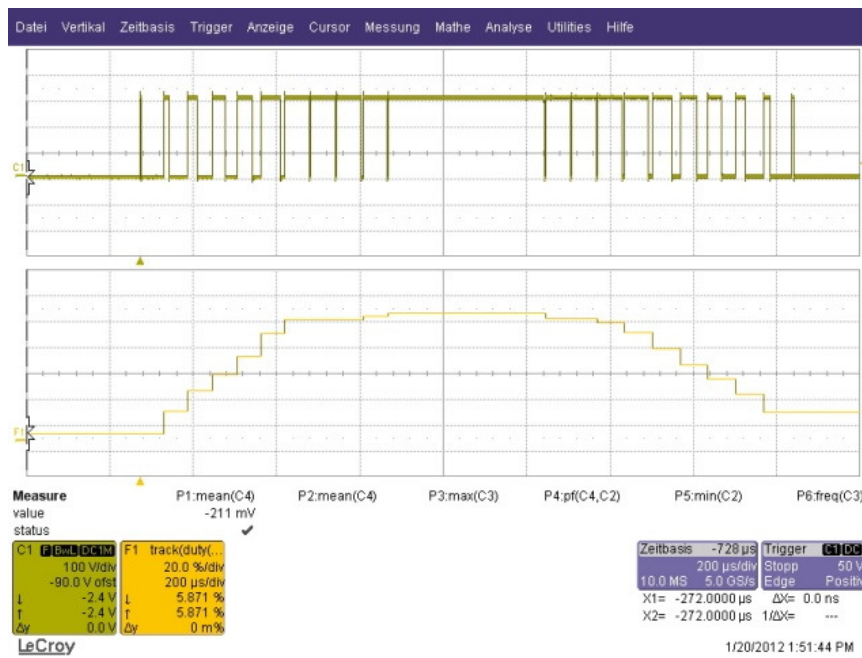
Fig. 2.45. Carrier-based pulse width-modulated voltage with overmodulation.

2.3.2.1.5. Conclusions

This study has presented an algorithm for wide speed range PMSM drives which are fed by PWM-VSI utilizing overmodulation. The PMSM drive system works in generator mode with the proposed algorithm only if the PWM-VSI is equipped with a regenerative unit to supply to supply the ac power from the mains to dc link. If the PWM-VSI is not equipped with a regenerative unit, the generator mode operation of PMSM should be avoided by limiting the maximum *q*-axis current. This algorithm allows a smooth transition into and out of the field weakening over the whole speed range. Also the algorithm is not sensitive to the motor parameters; it is relative simple and can be implemented with a 16 [bit] microcontroller. The dynamic and steady-state performance of the PMSM drive are improved by using the VSI in the overmodulation regions but also the switching losses in the power module will be reduced. The control with the proposed algorithm is stable in overmodulation range and it is capable to follow the dc-link variations. The experimental results obtained have shown the benefits of the overmodulation despite know issues that involve this method.

2.3.2.2. Optimum Current Reference Generation Algorithm for FourQuadrant Operation of PMSMS Drive System

2.3.2.2.1. Introduction

Permanent magnet synchronous motors (PMSM) are receiving increased attention for drive systems instead of induction motor because of *their high controllability, high efficiency, high torque to inertia ratio, high power density and high power factor operation*. As the price of permanent magnet tends to decrease and the price of iron and the price of copper tends to increase, the choice of PMSM for drive systems becomes more attractive. Using PMSM may further eliminate the need of a gearbox. The proposed control scheme may be used with traction applications and home appliances. In the field oriented drive system, it is important to control the current vector appropriately according to the operating conditions and the type of PMSM. An ordinary drive system requires current sensors and high-resolution position sensor such as a rotary encoder or a resolver, which are expensive. The rotor position sensor presents several disadvantages from the standpoint of the drive cost, machine

size, reliability and noise immunity. However, there has been an increased interest in techniques for eliminating the rotor position sensor, to improve the reliability and reduce the cost of the drive.

In the literature have been investigated a lot of position sensorless drive systems for synchronous motors, but there is just some study of the current-sensorless drive system for synchronous motors [96]-[99]. The position sensorless drive system needs current sensors in order to estimate the rotor position and speed. The current-sensorless drive systems proposed in [96]-[98] use high-resolution position sensors. In the current sensorless drive systems [97], [99] the PMSMS currents are estimated using the mathematical motor model and thus become inaccurate with parameter drift due to temperature and saturation effects.

In this ***study, our research team proposes an enhanced field oriented drive system for PMSMS, where the current sensors are eliminated and only two Hall-effect position sensors are used instead of a high-resolution position sensor***. ***The high performance current control is achieved by use of a state observer for current estimation***. In this research **is** *also proposed a new algorithm to generate the optimal d- and q-axes current references in the different operating regions and the limits of the speed controller ($I_{spu\,max}$, $I_{spu\,min}$), algorithm which works in all four quadrants*.

2.3.2.2.2. Drive system design

a. Speed control system description

The block diagram of the proposed speed control drive system of PMSMS is shown in Figure 2.46. For the proposed speed control algorithm the mathematical model of PMSMS in per-unit is used. The speed control and current control are implemented using a 16 MCU. For the speed control a PI controller is used, and the output of the controller is the amplitude of armature current (i^*_{spu}).

The different blocks used in the proposed speed control algorithm are presented below.
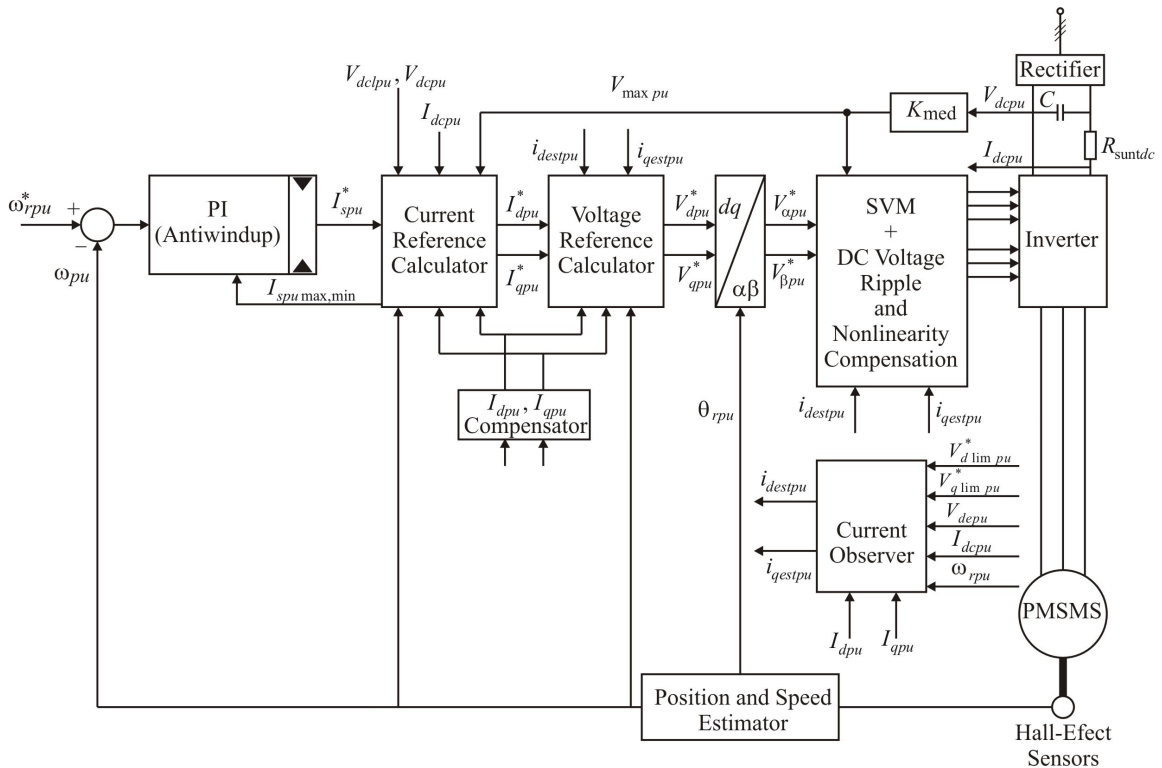
Fig. 2.46. Block diagram of proposal speed control drive system using a state observer for the current estimation and two Hall-effect sensors.

b. Dynamic model of PMSMS

From electrical model in per-unit of PMSMS in rotor reference frame, by choosing as state variables the d- and *q*-axis currents in per-unit, the PMSMS dynamic model can be written as follows:

$$\frac{di_{pu}}{dt_b} = Ai_{pu} + Bv_{pu} + K_{PMpu}$$

$$i_{pu} = \begin{bmatrix} i_{dpu} \\ i_{qpu} \end{bmatrix} \qquad v_{pu} = \begin{bmatrix} v_{dpu} \\ v_{qpu} \end{bmatrix}$$

$$B = \begin{bmatrix} \dfrac{1}{l_{dpu}} \\ \dfrac{1}{l_{qpu}} \end{bmatrix} \qquad K_{PMpu} = \begin{bmatrix} 0 \\ -\dfrac{\omega_{rpu}\psi_{PMpu}}{l_{qpu}} \end{bmatrix} \tag{2.70}$$

$$A = \begin{bmatrix} -\dfrac{r_{pu}}{l_{dpu}} & \dfrac{\omega_{rpu}l_{qpu}}{l_{dpu}} \\ -\dfrac{\omega_{rpu}l_{dpu}}{l_{qpu}} & -\dfrac{r_{pu}}{l_{qpu}} \end{bmatrix}$$

and: ω_{rpu} is electrical angular velocity in per-unit, i_{dpu}, i_{qpu}, are the *d*- and *q*-axes armature currents in per-unit, u_{dpu}, u_{qpu}, are the *d*- and *q*-axes terminal voltages in per-unit, r_{pu} is the armature resistance in per-unit, l_{dpu}, are the *d*- and *q*-axes inductances in per-unit and ψ_{PMpu} is the permanent magnet flux linkage. In the case of nonsalient-pole PMSMS the relation between *d*- and *q*-axes inductances is $l_{dpu} = l_{qpu}$, while in the case of salient-pole PMSMS the relation between *d*- and *q*-axes inductances is $l_{dpu} \neq l_{qpu}$.

c. Current observer

We assume that the inverter is an ideal power converter, i.e. the output power of the inverter is equal with the input power of the inverter, and thus it can be written:

$$p_{dcpu} = V_{dcpu}I_{dcpu} \approx \frac{3}{2}p_{dqpu} = \frac{3}{2}\left(v_{dpu}i_{dpu} + v_{qpu}i_{qpu}\right) \tag{2.71}$$

V_{dcpu} is the DC-link voltage in per-unit and I_{dcpu} is the DC-link current. The relation (2.71) can be rewritten as:

$$I_{dcpu} = Ci_{pu}, \tag{2.72}$$

where:

$$C = \frac{2}{3}\begin{bmatrix} \dfrac{v_{dpu}}{V_{dcpu}} & \dfrac{v_{qpu}}{V_{qcpu}} \end{bmatrix}. \tag{2.73}$$

By considering the relations (2.70), (2.71) we can build *a typical Luenberger state observer* as follows:

$$\frac{d\hat{i}_{pu}}{dt_b} = A\hat{i}_{pu} + Bv_{pu} + K_{PMpu} + L\left(I_{dcpu} - \hat{I}_{dcpu}\right), \tag{2.74}$$

where: $\hat{i}_{pu}$ is the matrix of the *d-* and *q*-axes estimated armature currents in per-unit, $\hat{I}_{dcpu}$ is the estimated DC-link current and L is the matrix of observer gain. The unknown observer gains of the matrix *L* (I_1, I_2) can be calculated using the relation:

$$\left| sI - \left(A - LC^T \right) \right| = 0 \qquad (2.75)$$

where: *I* is the identity matrix.

The characteristic equation (2.75) can be expressed as:

$$(s - p_1)(s - p_2) = s^2 + \alpha_1 d + \alpha 2 \qquad (2.76)$$

where: $p_{1,2}$ are the poles of characteristic equation.

The desired pole location are given by relation:

$$p_{1,2} = \sigma \pm j\omega_d = \xi\omega_n + j\omega_n\sqrt{1-\xi^2} \qquad (2.77)$$

where: ξ is damping ratio, and ω_n natural frequency.

In the choice of values ξ and ω_n we choose desired rise time, settling time and the maximum overshoot as follow:

$$t_r = \frac{1.8}{\omega_n} \approx 0.6 \sec ; \qquad\qquad t_s = \frac{4.6}{\xi\omega_n} \approx 2.6 \sec$$

$$M_p = e^{-\frac{\xi\pi}{\sqrt{1-\xi^2}}} \approx 10 \% \qquad (2.78)$$

The coefficients of gain matrix can be determined from relations (2.75) and (2.76). Finally, the d- and q-axes estimated currents in per-unit, using the state observer, can be calculated using the following discrete equations:

$$\hat{i}_{dpuk} = \left(1 - \frac{r_{pu}}{l_{dpu}}t_b\right)\hat{i}_{dpuk-1} + \frac{l_{qpu}}{l_{dpu}}t_b\omega_{rpuk}\hat{i}_{qpuk-1} + \frac{t_b}{l_{dpu}}v_{dpuk} + l_1 t_b\left(I_{dcpuk} - \hat{I}_{dcpuk}\right), \qquad (2.79)$$

$$\hat{i}_{qpuk} = \left(1 - \frac{r_{pu}}{l_{qpu}}t_b\right)\hat{i}_{qpuk-1} - \frac{l_{dpu}}{l_{qpu}}t_b\omega_{rpuk}\hat{i}_{qpuk-1} - \frac{\Psi_{PMpu}}{l_{qpu}}\omega_{rpuk} + \frac{t_b}{l_{qpu}}v_{qpuk} + l_1 t_b\left(I_{dcpuk} - \hat{I}_{dcpuk}\right). \qquad (2.80)$$

where: t_b is the base time.

The DC-link current $\hat{I}_{dcpu}$ is deduced from the estimated *d-* and *q*-axes armature currents using relation (2.71).

d. Current reference calculator

In the proposed speed control drive system the PI speed controller output is the amplitude of armature current in per-unit (i^*_{spu}). Depending on this value (i^*_{spu}) and depending on the speed region (constant-torque region or flux-weakening region) can be calculated the d- and q-axes current references. Using the maximum torque-per-ampere control method, in the constant-torque

region, the *d-* and *q*-axes current references in per-unit can be calculated using the following relations:

$$i_{dpu}^* = -\frac{\Psi_{PMpu}}{4(l_{dpu} - l_{qpu})} - \sqrt{\left(\frac{\Psi_{PMpu}}{4(l_{dpu} - l_{qpu})}\right)^2 + \frac{i_{spu}^{*2}}{2}} \quad , \tag{2.81}$$

or,

if $\qquad\qquad\qquad\qquad\qquad (l_{dpu} = l_{qpu}): i_{dpu}^* = 0 , \tag{2.82}$

$$i_{qpu}^* = \sqrt{i_{spu}^{*2} - i_{dpu}^{*2}} . \tag{2.83}$$

In field-weakening, armature voltage in per-unit and armature current in per-unit are limited by the inverter:

$$V_{spu} = \sqrt{V_{dpu}^2 + V_{qpu}^2} \leq V_{\max pu} , \tag{2.84}$$

$$I_{spu} = \sqrt{I_{dpu}^2 + I_{qpu}^2} \leq I_{\max pu} , \tag{2.85}$$

where: $V_{\max pu}$ is the maximum voltage magnitude in per-unit and $I_{\max pu}$ is the maximum current magnitude in per-unit.

In the flux-weakening there are two operating regions [95]:

- ***flux-weakening region I***, where the operation is limited by $V_{\max pu}$ and $I_{\max pu}$;

- ***flux-weakening region II***, where the operation is limited by the $V_{\max pu}$.

The operation of the PMSMS drive system in the flux-weakening region II is only possible if the characteristic current $I_{carpu} = \Psi_{PMpu} / l_{dpu} < I_{\max pu}$ (the center of the voltage ellipse is inside of the current limit). In the flux-weakening region I, the *d-* and *q*-axes current references in per-unit can be calculated using the following relations:

$$i_{dpu}^* = -\frac{\Psi_{PMpu} I_{dpu}}{4(l_{dpu}^2 - l_{qpu}^2)} - \sqrt{\left(\frac{\Psi_{PMpu} I_{dpu}}{(l_{dpu}^2 - l_{qpu}^2)}\right)^2 - \frac{\Psi_{PMpu}^2 - \left(\dfrac{V'_{\max pu}}{\omega_{rpu}}\right) + l_{qpu}^2 i_{spu}^{*2}}{(l_{dpu}^2 - l_{qpu}^2)}} \tag{2.86}$$

or

if $(l_{dpu} = l_{qpu}) :$ $\qquad\qquad i_{dpu}^* = \dfrac{\Psi_{PMpu}^2 - \left(\dfrac{V'_{\max pu}}{\omega_{rpu}}\right) + l_{qpu}^2 i_{spu}^{*2}}{2\Psi_{PMpu} l_{dpu}} \tag{2.87}$

$$i_{qpu}^* = \sqrt{i_{spu}^{*2} - i_{dpu}^{*2}} \tag{2.88}$$

In the flux-weakening region II, the d- and q-axes current references in per-unit can be calculated using the following relations:

$$i^{*}_{dpu} = -\frac{\Psi_{PMpu}}{4\left(l_{dpu} - l_{qpu}\right)l_{dpu}}\left(4l_{dpu} - 3l_{qpu} - \sqrt{l^{2}_{qpu} + \frac{8V'^{2}_{\max pu}\left(l_{dpu} - l_{qpu}\right)^{2}}{\omega^{2}_{rpu}\Psi^{2}_{PMpu}}}\right)$$ (2.89)

or,

(if: $l_{dpu} = l_{qpu}$):
$$i^{*}_{dpu} = -\frac{\Psi_{PMpu}}{l_{dpu}}$$ (2.90)

$$i^{*}_{qpu} = \pm\frac{1}{l_{qpu}}\sqrt{\left(\frac{V'_{\max pu}}{\omega_{rpu}}\right)^{2} - \left(l_{dpu}i^{*}_{dpu} + \Psi_{PMpu}\right)^{2}}$$ (2.91)

In the relations (2.86), (2.88), (2.89) and (2.91) the $V'_{\max pu}$ can be calculated with one of the following relations:

$$V'_{\max pu} = V_{\max pu} - r_{pu}I_{spu},$$ (2.92)

$$V'^{2}_{\max pu} = V^{2}_{\max pu} - 2r_{pu}p_{dqpu} + r^{2}_{pu}I^{2}_{spu}.$$ (2.93)

where: $p_{dq\,pu}$ is the electrical output power of the inverter in per-unit.

Starting from the above considerations there are (see e.g. [94], [95]) interesting algorithms to generate the *d-* and *q*-axes current references in the different operating regions. In this study is proposed a new algorithm to generate the d- and q-axes current references in the different operating regions and the limits of the speed controller ($I_{spu\,max}$, $I_{spu\,min}$), algorithm which works in all four quadrants (see Figure 2.47). In constant-torque region the *d*-axis current reference is calculated using relation (2.81), and the output of the ***voltage PI controller, "PI_IdCor"*** is zero. In the flux-weakening region the output of the ***voltage PI controller, "PI_IdCor"*** is added to the *d*-axis current reference calculated with relation (2.81).

The inputs of the ***voltage PI controller "PI_IdCor"*** are $V_{\max pu}$ and V^{*}_{spu}.

There are power converters which haven't the regenerative unit for cost reasons. In this case, in the proposed algorithm, a voltage PI controller "PI_SVCor" is designed to increase the *d*-axis current reference and decrease *q*-axis reference current if $V'_{dclpu} < V_{dcpu}$ (regenerative brake). V'_{dclpu} is the maximum allowed DC link voltage.

e. Voltage reference calculator

In the rotor reference frame the d-and q-axes currents become DC values in the steady state. For the *d-* and *q*-axes current control two PI controllers can be used. ***These PI controllers can control the d- and q-axes independently by decoupling the cross coupling in rotor***. The block for voltage reference calculator, using two PI controllers and decoupling control, is shown in Figure 2.48.

f. l_{dpu}, l_{qpu} compensator

In the proposed algorithm the values of l_{dpu}, l_{qpu} , inductances are established experimental considering the saturation effect. These values are implemented in a table as function of *d-* and *q*-axes current.
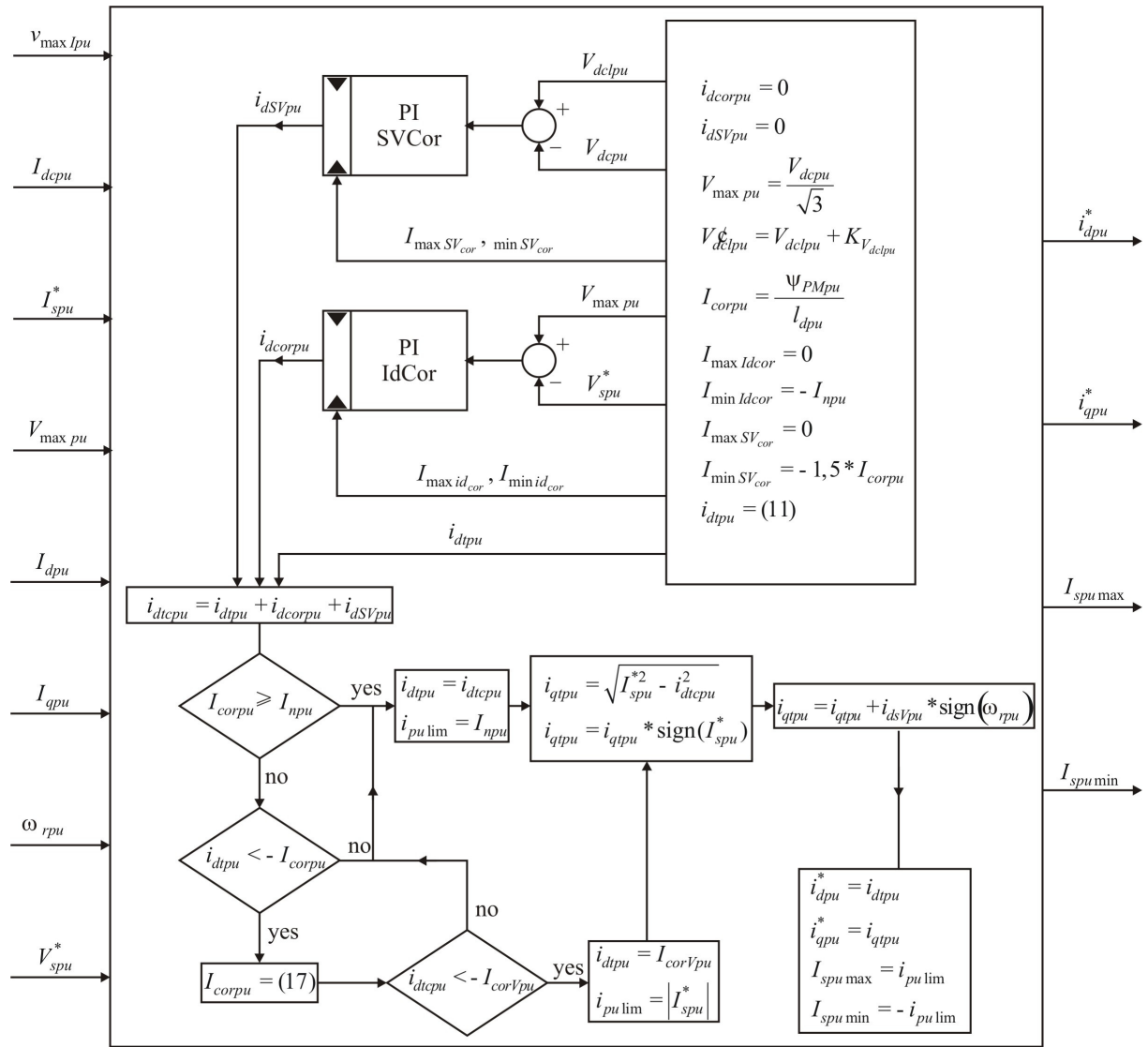
Fig. 2.47. Block diagram of the proposed current reference calculator.
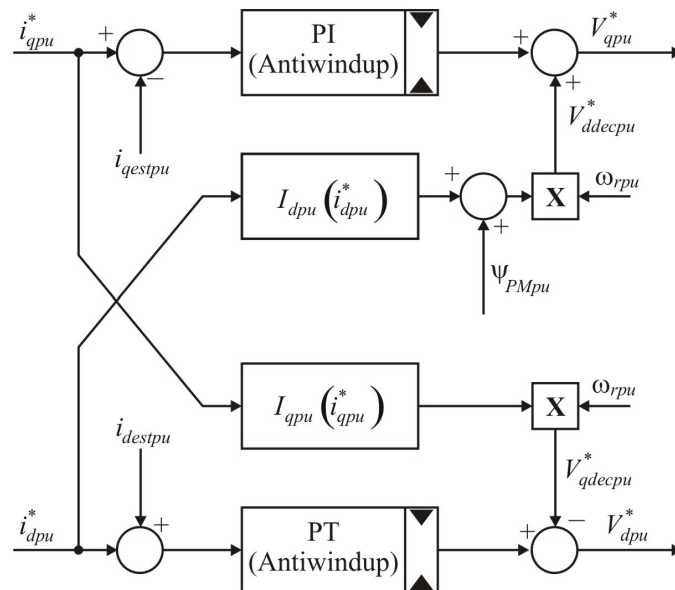
Fig. 2.48. Voltage reference calculator block in the rotor reference frame

g. DC Voltage ripple and Nonlinearity compensation

Due to the rectifier, the DC-link voltage is not constant. The variation of DC-link voltage will cause undesirable voltage variations in stator voltage. An algorithm (in stator reference frame) to overcome this problem is proposed in Figure 2.49.
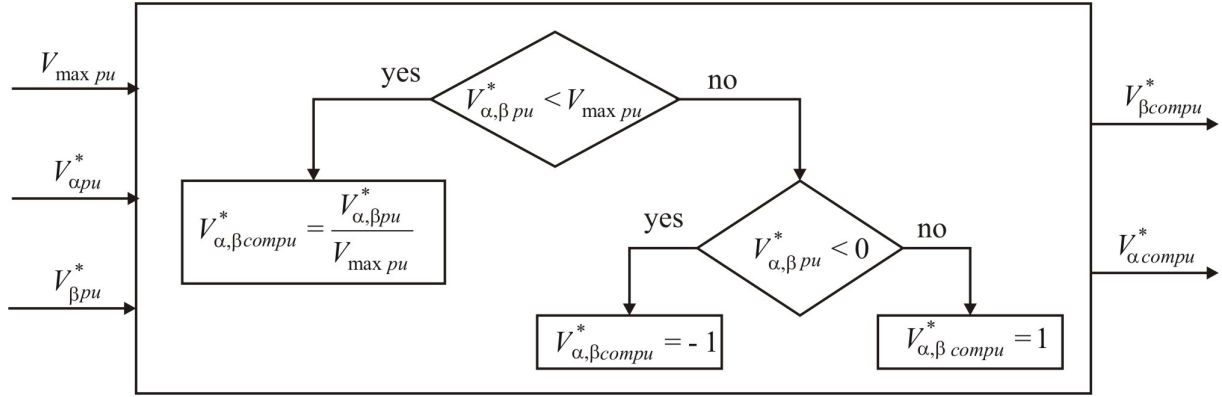
Fig. 2.49. DC-link voltage ripple compensation.

The inverter nonlinearities caused by dead-time, diodes drop voltage and IGBT drop voltage are compensated using the following relation [5]:

$$\Delta u^*_{cna,b,cpu} = \begin{cases} -\dfrac{1}{T_c}\left(V_{dcpu}t_m - \dfrac{V^2_{dcpu}C_T Z_b}{2i_{a,b,cspu}}\right), & i_{a,b,cspu} < -\dfrac{V_{dcpu}C_T Z_b}{t_m} \\[3mm] \dfrac{t_m^2}{2C_T Z_b T_c}i_{a,b,cspu}, & \left|i_{a,b,cspu}\right| < -\dfrac{V_{dcpu}C_T Z_b}{t_m} \\[3mm] \dfrac{1}{T_c}\left(V_{dcpu}t_m - \dfrac{V^2_{dcpu}C_T Z_b}{2i_{a,b,cspu}}\right), & i_{a,b,cspu} > -\dfrac{V_{dcpu}C_T Z_b}{t_m} \end{cases} \tag{2.93}$$

where: $\Delta u^*_{cna,b,cpu}$ is corrected voltage for phase *a, b, c* in per-unit, t_m is the dead-time, C_T is the capacity of IGBT and T_c is the SVM period.

h. Position and speed estimation

In the proposed speed control drive system of PMSMS, for the position and speed estimation, two Hall-effect sensors are used. The resolution of the position sensor is only 90 electrical degrees. The signals obtained from the Hall-effect sensors are shown in Figure 2.50.

The average speed between two Hall-effect sensors signal can be calculated with the following relation:

$$\omega_{ravpu} = \omega_{rpu} = \omega_{rmpu} = \frac{f_{timer}}{2f_b V_{ctimer}} \tag{2.94}$$

where: f_{timer} is the timer frequency, V_{ctimer} is the counted value.

Between two Hall-effect sensors signal the rotor position can be estimated using the following relation:

$$\theta_{rpuk} = \theta_{rpuk-1} + \omega_{rpu}t_s \tag{2.95}$$

where: t_s is the sampling time.
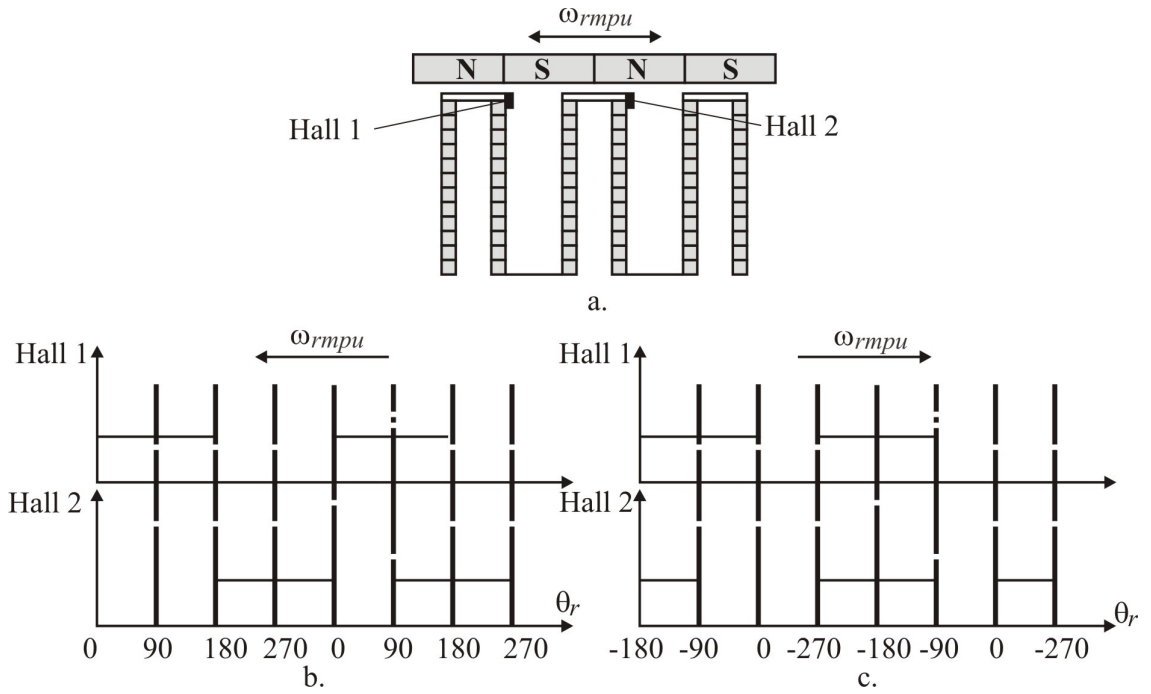
Fig. 2.50. Hall-effect position sensor signals.

The relation (2.95) used to estimate the rotor position corresponds to the actual rotor position when the rotor speed is constant. In order to improve the estimated rotor position between two Hall-effect signals the rotor speed can be calculated with the following relation:

$$\omega_{rpuk} = \omega_{rpuk-1} + K_{cu}I_{spu}t_s \tag{2.96}$$

where: K_{cu} is an experimental value.

2.3.2.2.3. Experimental results of proposed drive system of PMSMS

The proposed speed control drive system was implemented using a 16 [bit] MCU and a motor a 2 [kW] PMSMS. The speed control drive system of PMSMS was tested with a dynamometer. The performance of the proposed system, in the constant-torque region, is shown in Figure 2.51 and Figure 2.52. Figure 2.51 a) shows the speed regulation performance, when load torque has a variation from 0 [Nm] to 28 [Nm] in 1 [sec]. The corresponding electrical power variation P_{el}, mechanical power variation P_{mec} and the amplitude armature current variation I_s are shown in the Figure 2.51 b). The estimated currents corresponding to the load variation from Figure 2.51 are shown in Figure 2.52. Small estimation error appears in the d- and q-axes currents i_{dest}, i_{qest} and DC-link current I_{dcest}. i_d, i_q, I_{dc} are the measured currents using current sensors. Performance of the proposed drive system in constant-torque region and flux-weakening is shown in Figure 2.53, Figure 2.54 and Figure 2.55. Acceleration performances are shown in the Figure 2.53. The speed regulation is very good, with the proposed drive system. Figure 2.53 a) shows the d-and q-axes current references generated with proposed algorithm. Figure 2.53 b) shows the armature voltage reference V^*_s and the maximum terminal voltage of the inverter V_{max}. The used inverter has no a regenerative unit. With the proposed current references algorithm it is possible to limit the DC-link voltage in case of regenerative brake. The decelerating performance of the drive system is shown in the Figure 2.54 and Figure 2.55.
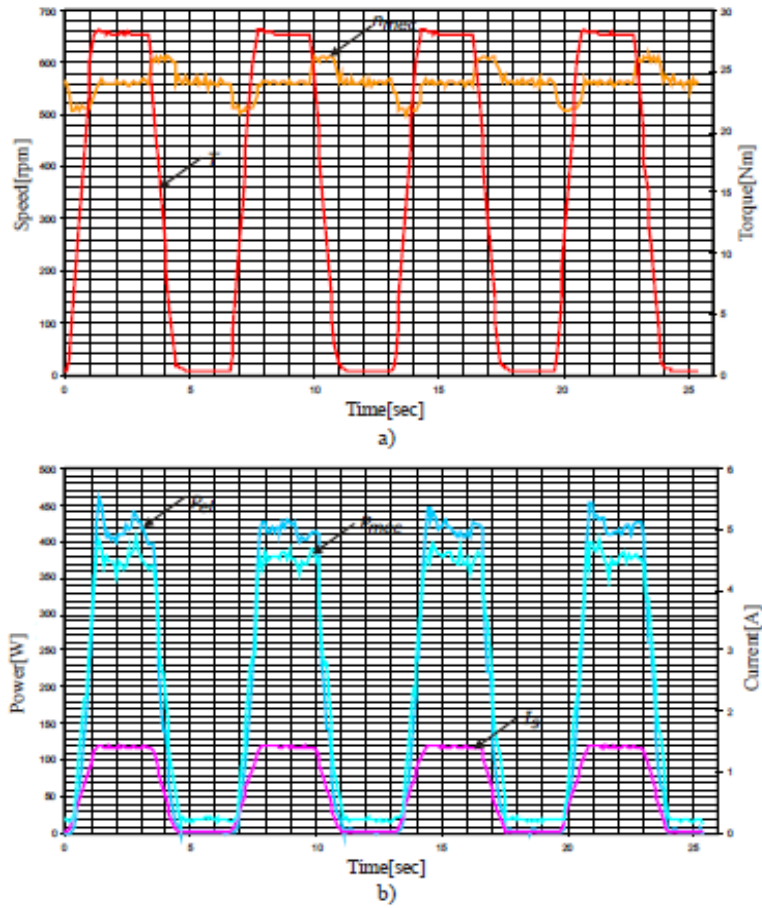
Fig. 2.51. Experimental speed regulation performance in the constant-torque region.
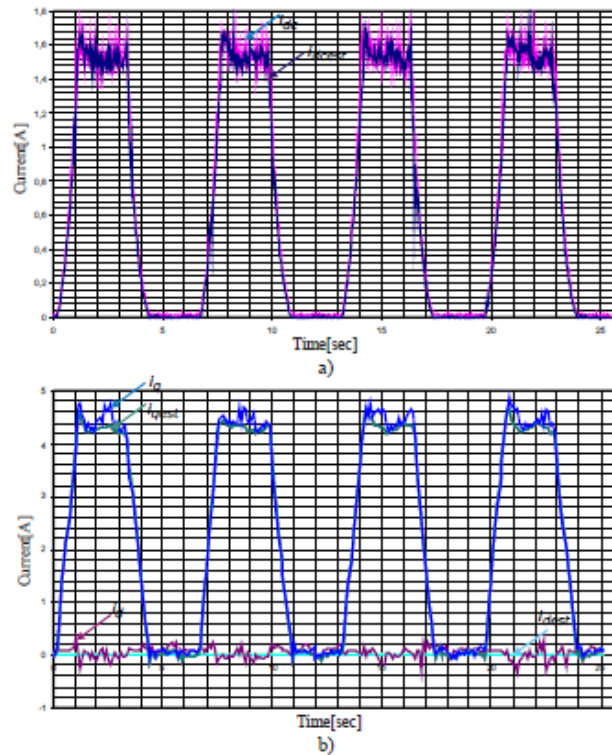
Fig. 2.52. Current estimation performance in the constant-torque region.
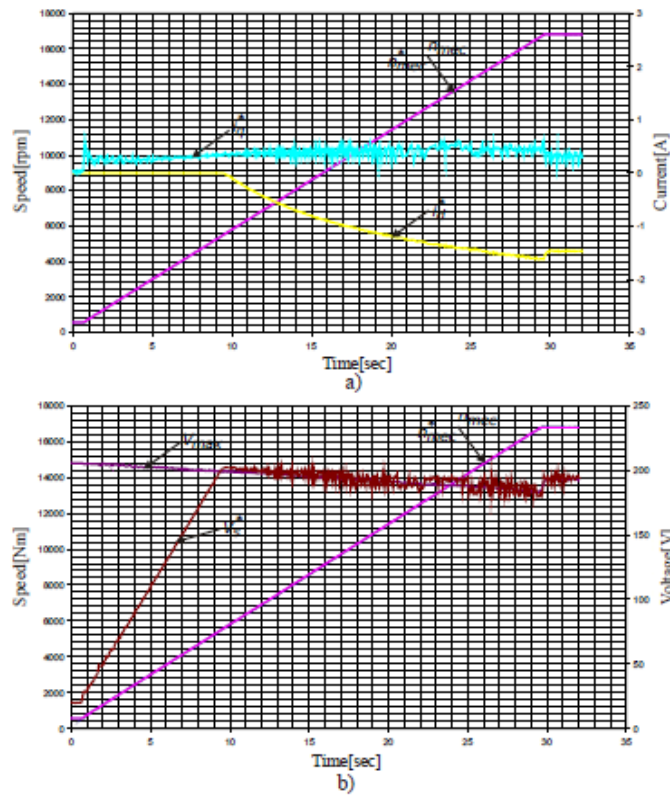
Fig. 2.53. Accelerating performance of the proposed speed regulation drive system of MSMPS.
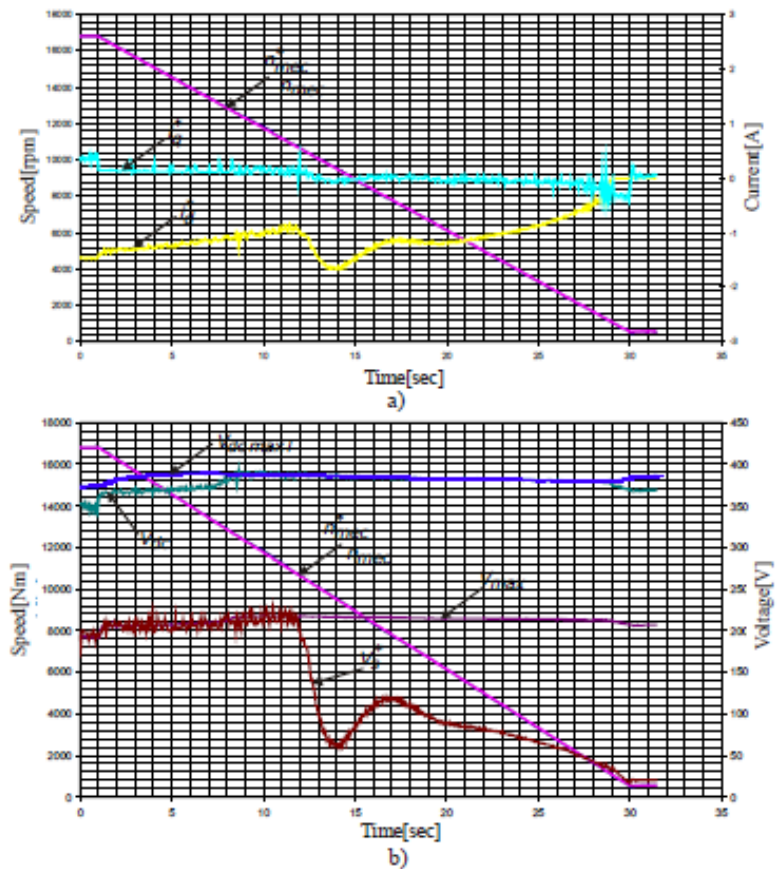
Fig. 2.54. Decelerating performance of the proposed speed regulation drive system of MSMPS.
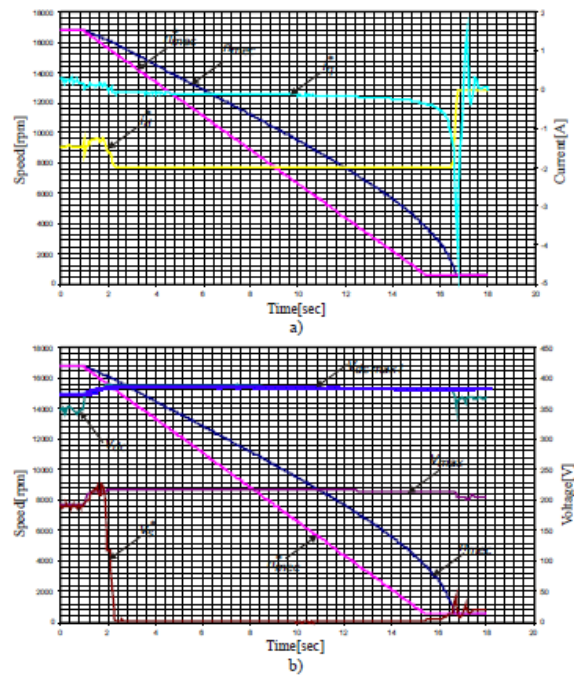
Fig. 2.55. Decelerating performance of the proposed speed regulation drive system of MSMPS.

If the deceleration gradient is too big, the rotor speed of PMSMS can not follow the reference speed (see Figure 2.55). The regenerative brake performance is limited due to DC-link voltage limitation. With the proposed algorithm the DC-link voltage is limited at the maximum value $V_{dc\,maxl}$ (see Figure 2.54 b) and Figure 2.55 b)).

2.3.2.2.3. Conclusions

The experimental results obtained with the proposed speed control drive system of PMSMS, pointed out that the proposed current observer has a good dynamic and also a good dynamic speed response. In the proposed research to estimate the *d-* and *q*-axes armature currents it is necessary to measure the DC-link voltage, and DC-link current. To measure the DC-link current it is not necessary a fast AD converter and can be use also a comparator instead of an operational amplifier. The proposed algorithm can be implemented with a 16 [bit] MCU. In the proposed speed regulation drive system the current sensors are eliminated and, moreover, only two Hall-effect sensors for position and speed estimation are used, thus the cost of drive is reduced. In the proposed drive system the influences of inverter nonlinearities, DC-link voltage and saturation effect are eliminated. Also, in this paper is presented a new algorithm to calculate the *d-* and *q*-axes current references for the whole speed range, which works in all four quadrants, even the power converter has not a regenerative unit.

2.3.2.3. Optimum Torque Control Algorithm for Wide Speed Range of Stator Flux Oriented Induction Motors

2.3.2.3.1. Introduction

As the price for digital signal processors (DSP), digital signal controllers (DSC), ARM processors and complex instruction set microcontrollers (CISC) for motor control applications tend to decrease and the performances of these microcontrollers tend to increase, the choice of a sensorless field oriented IM drive system becomes more attractive for low power applications.

Using variable speed IM drives for low power applications the energy efficiency and the performance of the system will increase and may further eliminate the need of a gearbox. In the literature, there are two well-known field oriented control methods for sensored or sensorless IM drives: *the rotor flux oriented control (RFO)* and *stator flux oriented control (SFO).* The SFO system has better performance than the RFO system (the RFO control, with the rotor flux estimated from terminal quantities is sensitive to variations in leakage and magnetizing inductances) [111], [112]. In the field weakening area the control of IM can be classified in three categories. The most applied method is the adjustment of the stator flux or rotor flux in inverse proportion to the speed [112] and [113]. The feed-forward stator flux or rotor flux control is based on machine equations [114], [115], and [116]. In these proposed algorithms the performance of the drive system is limited by the parameter variation of the IM associated with temperature or saturation effects. The close loop algorithm of the stator voltage used the maximum voltage capabilities of the inverter [118], [119] and [120]. In these papers the *q*-axis current is limited if the phase-shift between the stator flux vector and rotor flux vector is greater than 45°. In the generator mode a braking resistor in parallel to the dc link capacitor [121] can be used for dissipating the regenerated braking power. This solution increases the price and size of the drive and it is avoided in low-power applications. In the low-power applications the power dissipation in the motor is very effective due to their large phase resistances. In the paper [122] an efficient braking method for a RFO IM drive equipped with the diode rectifier front-end is proposed. To increase the power losses in the motor a square-wave current component is superimposed on the flux current component. Another efficient braking method for a RFO IM drive is presented in [123]. In this case the power losses are increased by increasing the rotor flux. With the proposed algorithm the regenerated power is also dissipated in the IM.

There is less *attention given* **for** *the SFO control of the IM drive for the whole speed range and four quadrant operation of the drive without regenerative unit*. *In this study the proposed algorithm will be described starting from the mathematical model in per -unit of the IM in a synchronous reference frame oriented to the stator flux. The existing constraints for the proposed algorithm in motor mode and generator mode are the maximum output voltage of the inverter, the maximum current of the inverter or the maximum permitted current of IM and the relationship between the regenerated power and the dissipated power in the IM*.

2.3.2.3.2. System description

a. Mathematical model of SFO IM

In this research all variables are in per-unit. The SFO machine model in per-unit of IM in synchronous reference frame oriented to the stator flux can be written as follows:

$$
\begin{cases}
\overline{v}_{pu} = r_{spu}\overline{i}_{pu} + \dfrac{d\overline{\psi}_{spu}}{dt_b} + j\omega_{epu}\overline{\psi}_{spu} \\[4mm]
0 = r_{rpu}\overline{i}_{rpu} + \dfrac{d\overline{\psi}_{rpu}}{dt_b} + j\omega_{rpu}\overline{\psi}_{rpu}
\end{cases}, \tag{2.97}
$$

$$
\begin{cases}
\overline{\psi}_{spu} = L_{spu}\overline{i}_{pu} + L_{mpu}\overline{i}_{rpu} \qquad \overline{\psi}_{spu} = \psi_{sdpu} = \psi_{spu} \\[2mm]
\overline{\psi}_{rpu} = L_{mpu}\overline{i}_{pu} + L_{rpu}\overline{i}_{rpu} \qquad \overline{\psi}_{rpu} = \psi_{rdpu} = j\psi_{rqpu}
\end{cases}, \tag{2.98}
$$

where: ω_{epu} is the electrical frequency in per-unit, ω_{rpu} is the rotor (slip) frequency in per-unit and:

$$\overline{v}_{pu} = v_{dpu} + jv_{qpu}\;; \qquad \overline{i}_{pu} = i_{dpu} + ji_{qpu}\;; \qquad \overline{i}_{rpu} = i_{rdpu} + ji_{rqpu}\,. \tag{2.99}$$

We can get also the following relations [2]:

$$\left(i_{qpu} + \sigma T_{rpu}\frac{di_{qpu}}{dt_b}\right)L_{spu} = \omega_{rpu}T_{rpu}\left(\psi_{sdpu} - \sigma L_{spu}i_{dpu}\right), \tag{2.100}$$

$$\psi_{sdpu} + T_{rpu}\frac{d\psi_{spu}}{dt_b} = L_{spu}\left(i_{dpu} + \sigma T_{rpu}\frac{di_{dpu}}{dt_b}\right) - \omega_{rpu}T_{rpu}\sigma L_{spu}i_{sqpu}, \tag{2.101}$$

$$T_{epu} = \psi_{sdpu}i_{qpu}\,, \tag{2.102}$$

where: σ is the total leakage factor, T_{rpu} is the rotor time constants in per-unit and p is the number of pole pairs.

b. Voltage, Current and Power Limitation

The maximum current of the inverter must be restricted by limiting the torque producing component q-axis current while the d-axis current must be unaffected. The maximum voltage is dependent from the dc link voltage of the inverter. The condition for the maximum current limiting and the limit condition of the voltage are:

$$i_{qpu} \le \sqrt{I_{\max pu}^2 - i_{dpu}^2}\,, \qquad \sqrt{v_{dpu}^2 + v_{qpu}^2} \le V_{\max pu}\,, \tag{2.103}$$

where: $V_{\max pu}$ is the maximum voltage magnitude in per-unit, $I_{\max pu}$ is the maximum current magnitude in per-unit, i_{dpu}, i_{qpu} are the d-axis and q-axis armature currents in per-unit and v_{dpu}, v_{qpu} are the d-axis and q-axis terminal voltages in perunit. In generator mode the dissipated power in the motor has to be larger than the regenerated power and can be expressed in the steady-state operation by following relation:

$$p_{mpu} + p_{cupu} + p_{Fepu} \ge 0\,, \tag{2.104}$$

where: p_{mpu} is the regenerated mechanical power in per-unit, p_{cupu} is the copper losses in the stator and in the rotor in perunit, p_{Fepu} is the stator core losses in per-unit.

c. Operating conditions of IM

The d-axis stator flux reference and the q-axis reference current are dependent of the operating region. With reference to maximum torque there are three different operating regions: *region I, constant torque region*, within the base speed characterized by utilizing of maximum current, but the output voltage is lower than the maximum available voltage; *region II, constant-power region*, characterized by utilizing both maximum current and maximum available voltage; *region III decreasing-power region* characterized by utilizing of maximum available voltage, the motor current is lower than the maximum value, the stator flux is so low that the maximum torque is the pull-out torque.

d. Maximum torque per current strategy (MTPC)

The MTPC strategy means that for a given torque and speed, the rotor frequency is adjusted so that the stator current is minimized. It was shown [124], that for RFO control strategy the MTPC

can be reached when $i_{dpu} = i_{qpu} = I_{\max pu}/\sqrt{2}$. In this case the relations for the rotor frequency and for the electromagnetic torque are:

$$\omega_{r \max puT=ct.} = \frac{1}{T_{rpu}} , \qquad (2.105)$$

$$T_{e \max puT=ct.} = L_{spu} \frac{1-\sigma}{2} I_{m \max pu}^2 . \qquad (2.106)$$

We can choose the same maximum rotor frequency (2.105) also for the SFO control strategy. Taking into account the relations (2.100), (2.101) in steady-state and (2.105), we can obtain the following relation for the stator flux in steady-state:

$$\psi_{spuT=ct.} = L_{spu} \frac{1+\sigma^2}{1-\sigma} i_{qpu} . \qquad (2.107)$$

Finally, we obtain for the electromagnetic torque the same relation as (2.106).
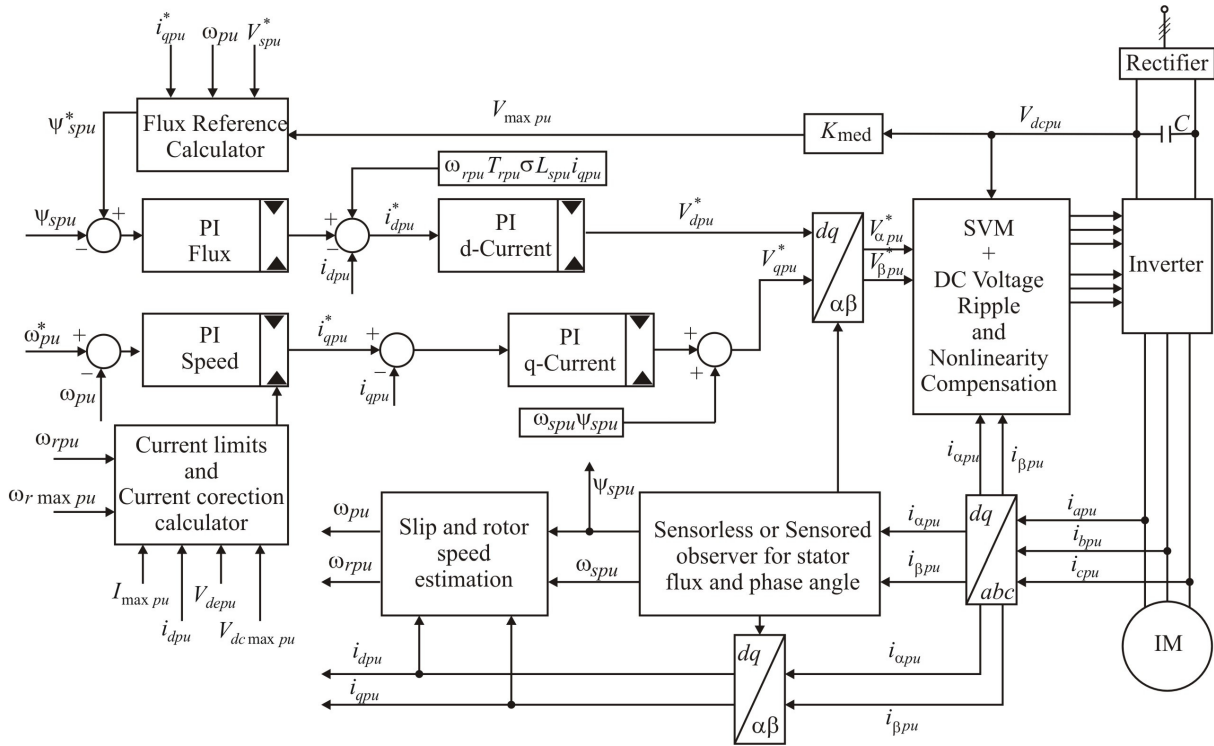
Fig. 2.56. Block diagram of the proposed stator flux oriented control for IM.

The stator reference flux, in the region I, can be chosen using the relation (2.107) (see Figure 2.57a)). Of course, we must not forget the saturation effect (we have to limit the stator flux reference).

e. The pull-out torque

The pull-out torque and the rotor frequency for the pullout torque are defined by the same relations for the SFO control strategy or RFO control strategy [111], [112]:

$$T_{e \max puV \max} = \frac{1-\sigma}{2\sigma L_{spu}} \psi_{m \max pu}^2 , \qquad (2.108)$$

$$\omega_{r\max pu} = \frac{1}{\sigma T_{rpu}}. \tag{2.109}$$

The above relation (2.109) is used to calculate the maximum admissible rotor frequency, in region III, with the proposed algorithm (see Figure 2.57 b)). If the estimated rotor frequency is higher than maximum admissible rotor frequency, the *q*-axis current will be reduced (see Figure 2.57 b *"PI Current Correction" controller*).
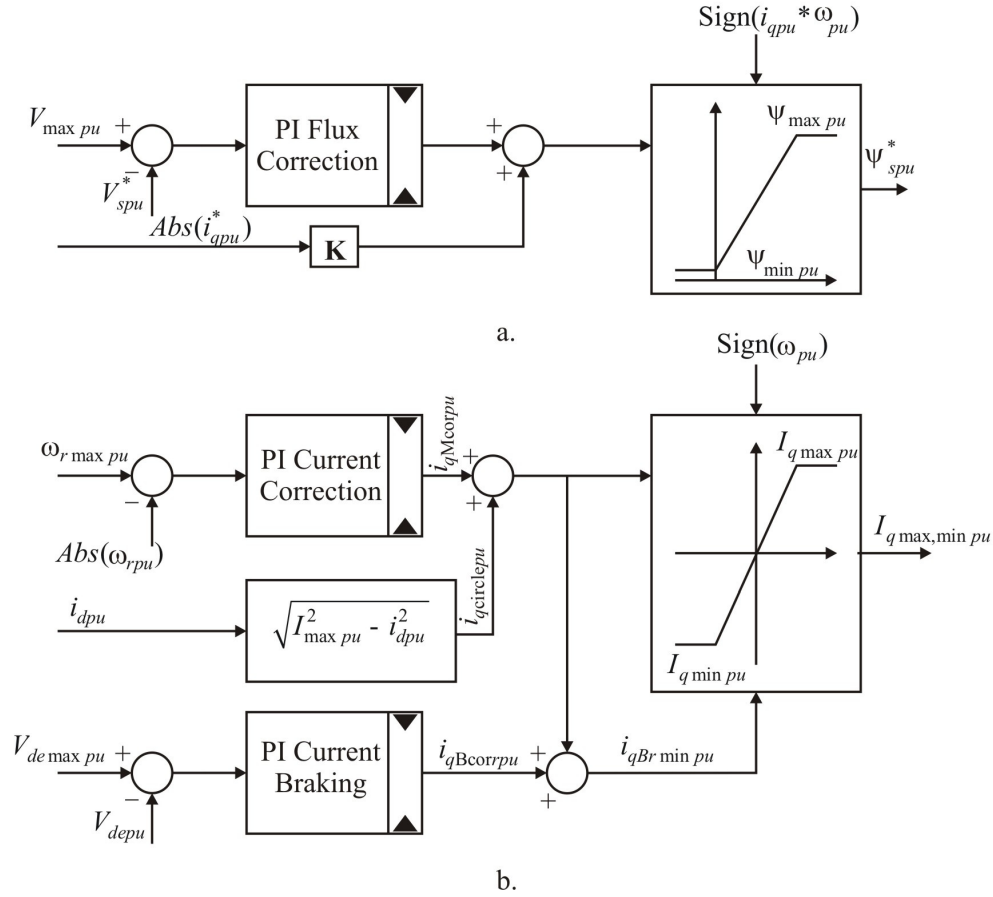
Fig. 2. 57. a) Block diagram of proposed "Flux reference calculator";
b) Block diagram of proposed "Current limits and current correction calculator.

2.3.2.3.3. Description of the proposed algorithm

The proposed algorithm can be easy integrated in the well-known SFO, where the stator flux and the *q*-axis current are the main control variables (see Figure 2.56). The stator flux reference for the whole speed range is generated using the proposed algorithm from the block *"Flux reference calculator"* (see Figure 2.56 and Figure 2.57 a)). In the region I the *"PI flux correction"* controller is not active (the positive limit of the controller is zero see Figure 2.57 a) and the reference flux can be calculated using the relation (2.107):

$$\psi_{spu}^* = K\left|i_{qpu}^*\right|, \quad K = L_{spu}\frac{1+\sigma^2}{1-\sigma}, \tag{2.110}$$

If we would like maximum dynamic performance, then we would keep the stator flux reference constant to the maximum value $\psi_{s\max pu}$. Using relation (2.110) the stator flux reference can be adjusted with the required electromagnetic torque, thus the system has not the best dynamic

performance but the efficiency of the system is better. This type of regulation worsens the electromagnetic torque response of the IM drive, but we get a better efficiency of the drive. The maximum stator reference flux (due to saturation) can be calculated using the following relation:

$$\begin{cases} \psi_{s\max pu} = L_s i_{d\max pu} & \omega_{pu} i_{qpu} \geq 0 \\ \psi_{s\max pu} = \psi_{\max brakepu} & \omega_{pu} i_{qpu} < 0 \end{cases}. \tag{2.111}$$

The minimum stator reference flux $\psi_{s\min pu}$ (Figure 2.57 a) can be chosen taking into account the observability of the sensorless control and reasonable torque response. In the region II and III the controller integrate the difference $V_{\max pu}$ - V^*_{spu} and the stator flux reference will be reduced. The q-axis current limit for the whole speed range is generated using the proposed algorithm from the block *"Current limits and current correction calculator"* (see Figure 2.56 and Figure 2.57 b)). In the region I and II the rotor frequency is lower than the rotor frequency for the pull-out torque ($\omega_{rpu} < \omega_{r\max pu}$ see relation (2.105)) and the q-axis current limit can be calculated using relation (2.102). In the region III the operating point reaches the pull-out location in which it needs to decrease the q-axis current limit. In this region the operation point at pull-out torque is obtained when the displacement between the stator flux linkage and rotor flux linkage is ±45°. The *"PI Current Correction"* works in region III and the operation at the pullout torque is obtained. The controller adjusts the q-axis reference current. In all three regions, in generator mode, the *"PI Current Braking"* controller works when the dc link voltage is higher than the maximum admissible value $V_{dcmaxpu}$ (condition (2.104) is not satisfied).

2.3.2.3.4. Experimental results of the proposed algorithm

The experimental performance of the proposed algorithm is presented using the sensorless SFO IM drive system from Figure 2.56. This drive system was implemented using a 16 [bit] DSC. The used IM has 1.4 [kW]. The performance of the proposed algorithm was tested with a dynamometer. Acceleration performances are shown in the Figure 2.58 and Figure 2.59. Figure 2.58 a) shows the q-axis reference currents generated and the measured q-axis current with proposed algorithm, at 0.06 pu accelerating gradient, in the region I, region II and III. Figure 2.58 b) shows the generated stator flux reference and the estimated stator flux in all three regions. In region III the accelerating gradient is too big and the rotor speed can't follow the reference speed. The value of the estimated rotor frequency using the relation (2.100), in steady-state conditions, is shown in the Figure 2.59 a. In the region III the rotor frequency is limited at the maximum value rotor frequency (2.109). In this way the operation at the pull-out torque is obtained. Figure 2.59 b) shows the armature voltage reference V^*_{spu} and the maximum terminal voltage of the inverter $V_{\max pu}$. The used inverter has no a regenerative unit. With the proposed reference currents algorithm it is possible to limit the dc-link voltage in case of regenerative brake. The decelerating performances of the proposed algorithm are shown in Figure 2.60 and Figure 2.61. If the deceleration gradient is too big, the rotor speed of IM can't follow the reference speed. The regenerative brake performance is limited due to dc link voltage limitation $V_{dc} = V_{dc\max pu}$ (the q-axis reference current is limited) and due to the possibility to dissipate the regenerative energy in the IM stator resistance. Figure 2.60 a) shows the q-axis reference current in generator mode. In the generator mode the stator flux reference is kept at maximum value (see Figure 2.60 b) and the q-axis reference value is reduced because of dc link voltage limitation V_{dcpu}. The value of the estimated rotor frequency in generator mode is shown in the Figure 2.61 a) while Figure 2.61 b) shows the armature voltage reference V^*_{spu} and the maximum terminal voltage of the inverter $V_{\max pu}$. The experimental results show the effectiveness of the proposed algorithm.
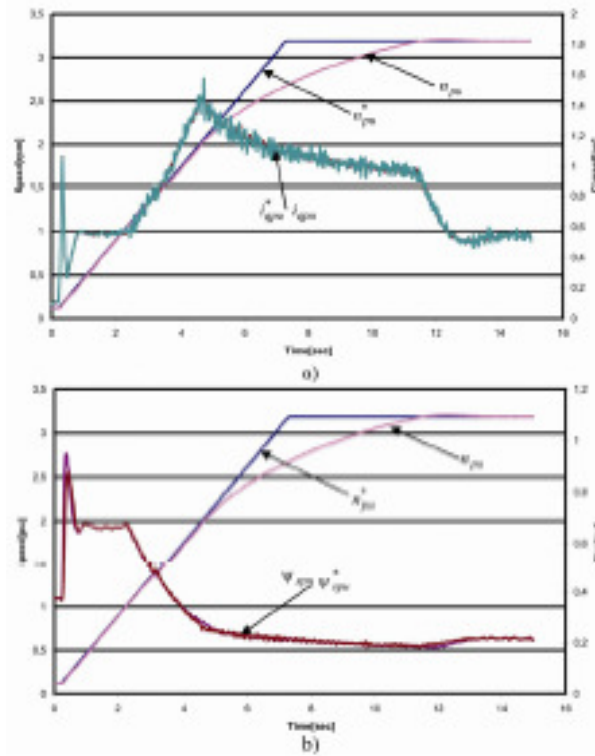
Fig. 2. 58. Acceleration performance showing, at 0.06 pu accelerating gradient: a) the speed (n^{*}_{pu}, n_{pu}), q-axis stator current (i^{*}_{qpu}, i_{qpu}); b) the speed (n^{*}_{pu}, n_{pu}), the stator flux (ψ^{*}_{spu}, ψ_{spu}).
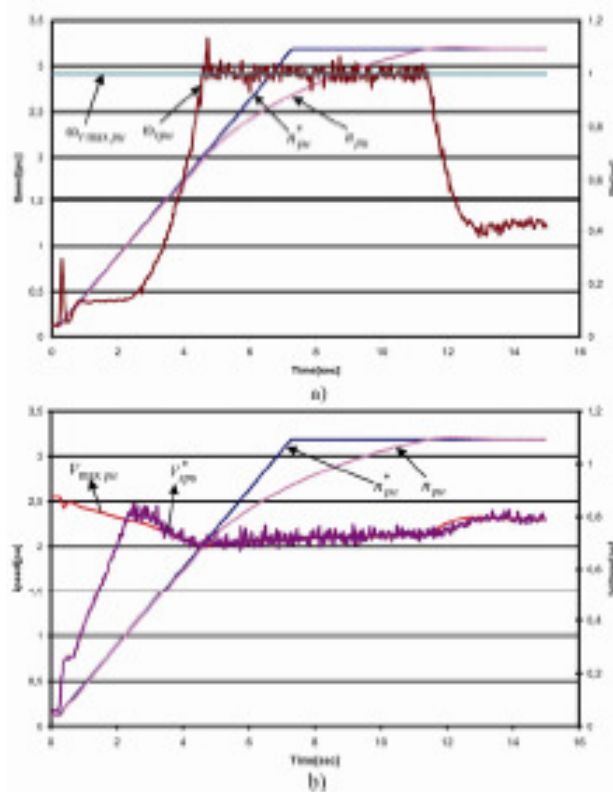
Fig. 2.59. Acceleration performance showing, at 0.06pu accelerating gradient: a) the speed (n^{*}_{pu}, n_{pu}), rotor angular frequency ($\omega_{rmax\,pu}$, ω_{rpu}); b) the speed (n^{*}_{pu}, n_{pu}), the regulated stator voltage (V^{*}_{spu}) and the maximum terminal voltage ($V_{max\,pu}$).
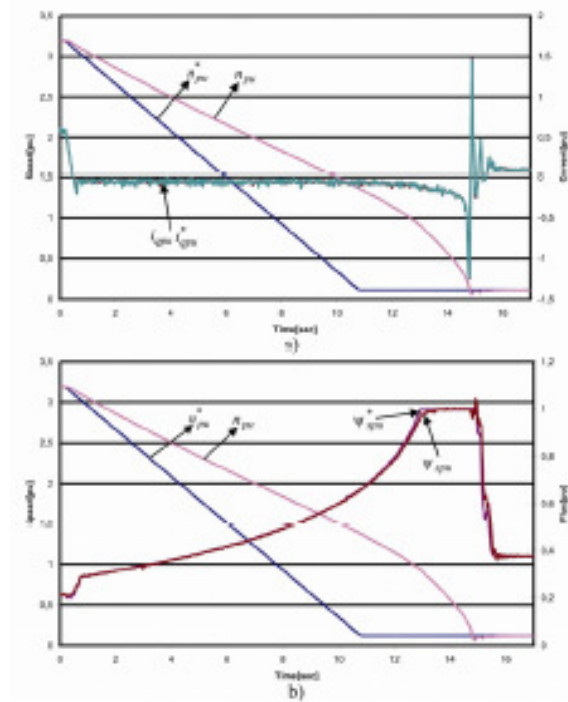
Fig. 2.60. Decelerating performance showing, at 0.06pu accelerating gradient: a) the speed
(n^*_{pu}, n_{pu}), q-axis stator current (i^*_{qpu}, i_{qpu}); b) the speed (n^*_{pu}, n_{pu}), the stator flux (ψ^*_{spu}, ψ_{spu}).
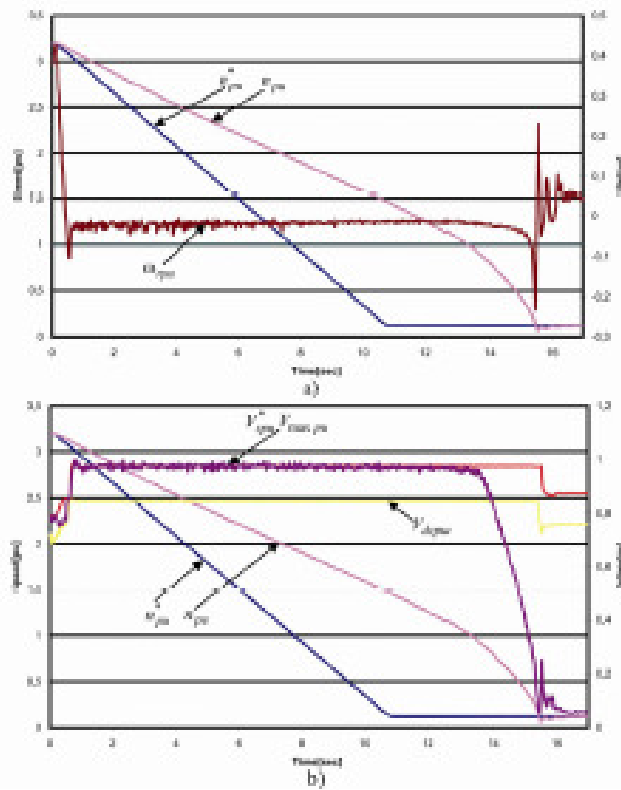
Fig. 2.61. Decelerating performance showing, at 0.04 pu accelerating gradient:
a) the speed (n^*_{pu}, n_{pu}), rotor angular frequency (ω_{rpu}); b) the speed (n^*_{pu}, n_{pu}), the regulated
stator voltage (V^*_{spu}), the maximum terminal voltage ($V_{\max pu}$) and the dc link voltage (V_{dcpu}).

2.3.2.3.4. Conclusions

The proposed algorithm generates the stator flux reference and q-axis current limit in all four quadrants in an IM drive systems, which are fed by PWM inverter equipped with diode rectifier front-end and without any extra braking resistors. This algorithm allows a smooth transition into and out of the field weakening mode and also a smooth transition from motor mode to generator mode and inverse over the whole speed range. This algorithm is not sensitive to the motor parameters; it is relative simple and can be implemented with a 16 [bit] DSC. The experimental results obtained have shown that the proposed algorithm has good dynamic performance and good steady-state performance. Optimum torque capabilities can be developed despite significant changes in dc link voltage and motor parameters.

2.4. Contribution to Single Phase Power Factor Correction (PFC) for grid Tied Inverters

Power factor correction shapes the input current of various non-linear loads, to ***maximize the real power available from the mains***. Ideally, the electrical appliance should present a load that emulates a pure resistor, in which case the reactive power drawn by the device is zero. The current is a perfect replica of the input voltage (usually a sine wave) and is exactly in phase with it. In this case, the current drawn from the mains is at a minimum for the real power required to perform the needed work, and this minimizes losses and costs associated not only with the distribution of the power, but also with the generation of the power and the capital equipment involved in the process.

For single-phase low power applications, Power Factor Correction (PFC) converters are designed in order to ensure a high power factor at the mains side, and to emulate a purely resistive operation of the diode bridge-based front-end rectifier [129]. Another reason to employ PFC in many of today's power supplies is to comply with regulatory requirements. Nowadays, electrical equipment in Europe must comply with the European EN 61000−3−2, or EN 61000-3-4 standards. These requirements specify the maximum amplitude of line−frequency harmonics up to and including the 39th harmonic [130], [136], [137].

One major drawback, related to the PFC circuits, is that they involve additional losses, thus reducing the overall efficiency. They also increase the EMI, due to the high-frequency content of the input current [132].

The PFC solutions can be categorized as *passive* or *active*, [129]-[132]:

- ***Passive PFC***: only passive elements are used in addition to the diode bridge rectifier, to improve the shape of the line current. Obviously, the output voltage is not controllable.

- ***Active PFC***: active switches are used in conjunction with reactive elements in order to increase the effectiveness of the line current shaping and to obtain controllable output voltage. The switching frequency further differentiates the active PFC solutions into two classes: ***In low-frequency*** active PFC, switching takes place at low-order harmonics of the line-frequency and it is synchronized with the line voltage. ***In high-frequency*** active PFC, the switching frequency is much higher than the line frequency.

Even though the passive PFC converters are simple, do not generate high frequency EMI and do not have high frequency switching losses, their disadvantages make them not being suitable

for industrial applications: reactive components are heavy and bulky due to line frequency operation, they demonstrate poor dynamic response, lack of voltage regulation, the shape of input current depend on the load, thus the power factor is reduced.

To overcome the disadvantages of the passive PFC converters, a new concepts of quasi-active PFC are proposed in [134]. In [135], a comparison between conventional boost converter and quasi-active PFC converter in terms of circuit construction and performance is presented. It may be seen, that the proposed converter presents a high quality input current with **THD<10% and high efficiency**. However, the proposed converter has an additional winding, but small in size since it operates at the converter switching frequency.

An active PFC is using active switches in conjunction with reactive elements in order to increase the effectiveness of the line current shaping and to obtain controllable output voltage. Because active PFC uses a circuit to correct power factor, active PFC is able to generate a theoretical power factor of over 95%, up to 99%, but they are expensive [165].

In the last two decades, a great deal of research in the power electronics area has been devoted to find methods of improving the input current waveform while simultaneously avoiding phase displacement. The aim of the research consists of selecting the four relevant single phase power factor correction (PFC) topologies currently existing for the power range of 1.5 [kW] up to 4 [kW] and to analyse and evaluate them. The evaluation has to be done in regards to electromagnetic compatibility (EMC) requirements, which is very important in the residential ambient. The investigated topologies by our team are the **conventional boost, the basic bridgeless PFC converters, the Boost Interleaved Converters and the Bridgeless Interleaved Converters**. Performances of these converters are simulated in Matlab/Simulink and it is shown that both of them are compliant with European EN 61000−3−2, or EN 61000-3-4 standards. Loss analysis and efficiency evaluation is also provided.

2.4.1. Boost versus Bridgeless Converter Performances and EMI Analysis

2.4.1.1. Introduction

Today two topologies can be considered as attractive for industry [129], [131], [132], [134], [135], 166]: **the bridgeless PFC boost rectifier with the bidirectional switch** and **the bridgeless PFC boost rectifier with two dc/dc boost circuits**. **The last one was selected as a representative member of the bridgeless PFC boost rectifier family for performances and electromagnetic interference EMI evaluation comparison with the conventional PFC boost rectifier**.

The **boost PFC topology** is an active PFC converter topology, suitable for a low to medium power range up to approximately 1 [kW] due to the diode bridge losses which significantly degrade the efficiency by dissipating heat in a limited area. For power levels above 1 [kW], typically, parallel semiconductors are being used in order to deliver greater output power. The **inductor volume** also becomes a critical design issue at high power. As a result, in recent years, significant efforts have been made to improve the performance of high-power boost converters [131].

For applications above 1 [kW], where power density and efficiency are important, the bridgeless converter is an attractive solution. It also solves the problem of heat management in the

input rectifier diode bridge, but it introduces increased EMI. Based on the theoretical analysis, 1 [%] efficiency improvement is expected from this active PFC topology. The efficiency improvement comes at the cost of increased complexity for input voltage and current sensing.

For a bridgeless PFC, the output voltage ground is always floating relative to the AC line input. Thus, all parasitic capacitance including MOSFET drain to earth and the output terminals to the earth ground contribute to common mode (CM) noise [166].

To solve the EMI noise issue, an EMI noise reduction circuit should be introduced. Information about EMI model building of boost and bridgeless PFC circuits are also given in [139]. Based on these methods and requirement, proper models common mode and EMI filters are then implemented.

The general aim of this research study was to evaluate the performances as well as the EMI emissions f the two PFC topologies: the conventional PFC boost rectifier and the representative member of the bridgeless PFC boost rectifier family, e.g. the bridgeless PFC rectifier with two dc/dc boost circuits.

2.3.1.2. Boost PFC Converter Topology

The boost PFC converter topology is presented in Figure 2.62. It uses a dedicated diode bridge to rectify the AC input voltage to DC, which is then followed by the boost section. It has a step-up conversion ratio; hence, the output voltage V_o is always higher than the amplitude V_{AC} of the input voltage.

The hardware implementation for the boost PFC converter topology as well as its controller design *was done by our research team in Matlab/Simulink* environment as depicted in Figure 2.63. The resonant filters used to diminish the common-mode EMI noises are also employed in here (the filters inductances are all equal to 60 [μH], while the capacitances are all equal to 22.7 [nF]). Its functionality is described below.

The measured DC bus voltage is compared with set reference voltage. The resulting voltage error is then fed to the PI voltage controller for zero error DC bus voltage regulation and distortion free current reference. The output of the controller is taken as amplitude of the reference supply current and is fed to the inner controller.

In addition, in order to emulate a pure resistor behavior, the current reference must have the same shape as the rectified source voltage V_{DC}, with an adjustable magnitude.

An analog multiplier is used for this purpose. The sensed inductance current is then subtracted from the reference current. The inner controller is chosen to be a hysteresis control type with a 0.1 [A] width.

According to this control technique, the switch is turned on when the inductor current decreases below the lower reference and is turned off when the inductor current increases above the upper reference, giving rise to a variable frequency control.

To achieve smaller ripple in the input current, a narrow hysteresis band must be desired. However, the narrower the hysteresis band, the higher the switching frequency. The hysteresis control scheme provides excellent dynamic performance because it acts quickly. To ensure high stability of the control system, the outer loop is designed to be enough slower than the inner one.
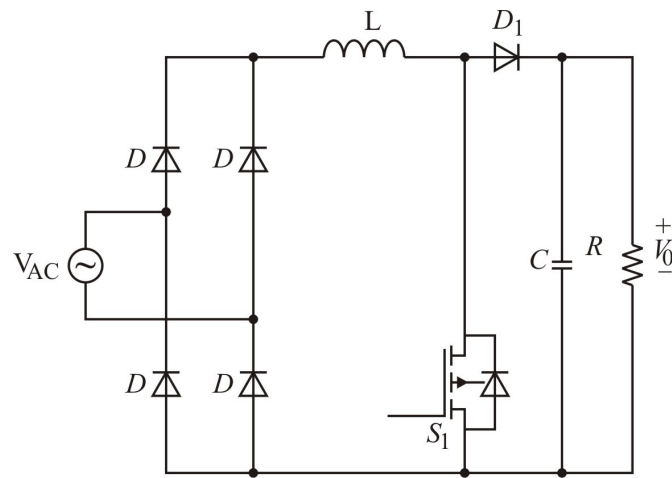
Fig. 2.62. Boost PFC converter topology.
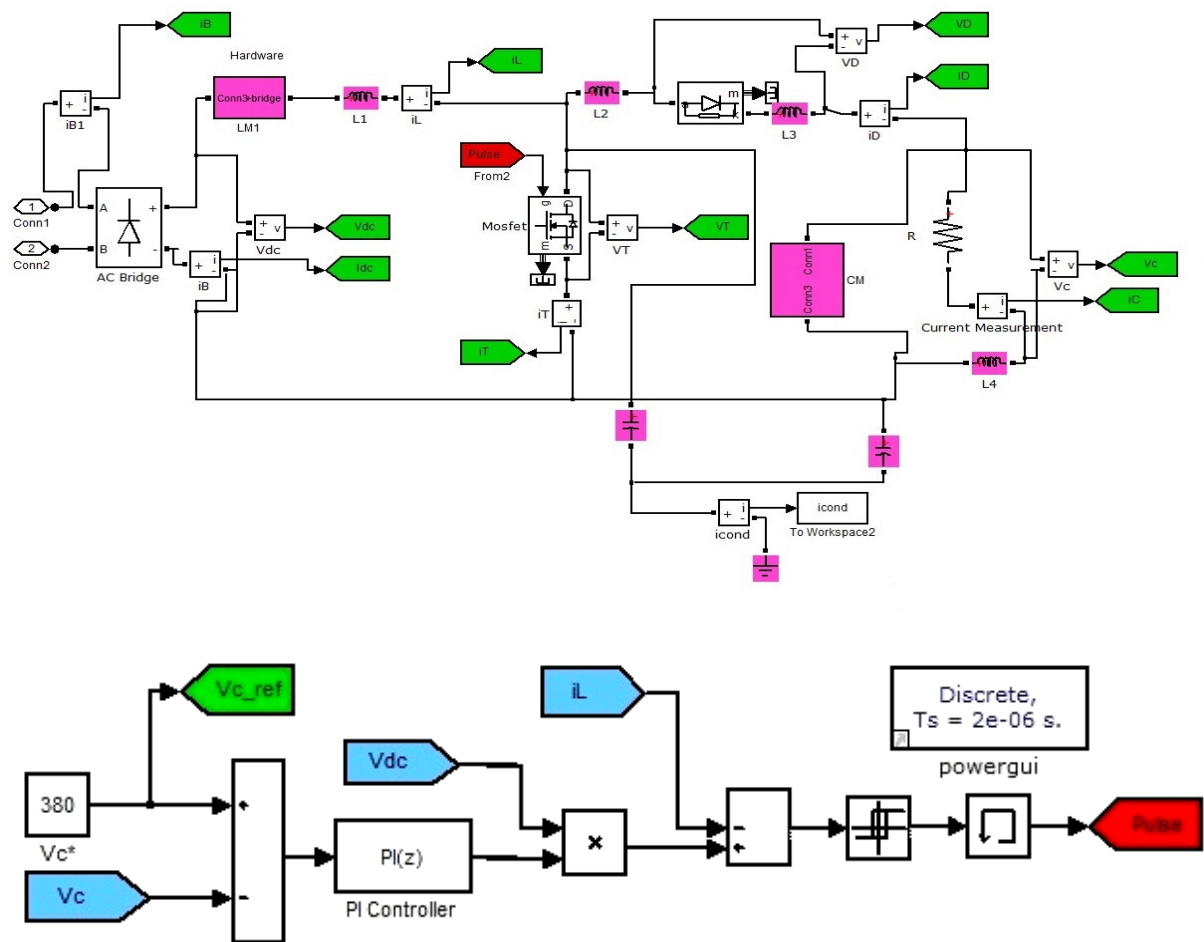
Fig. 2.63. Boost PFC converter model implementation in Matlab/Simulink.

2.4.1.2. Bridgeless PFC Converter Topology

In the bridgeless configuration topology, the need for the rectifier input bridge is avoided, yet the classic boost topology is maintained. This is done by making use of the intrinsic body diode connected between drain and source of MOSFET switches. A simplified schematic of the bridgeless

PFC configuration is shown in Figure 2.64, while ***its implementation in Matlab/Simulink, by our team,*** is depicted in Figure 2.65. As for the boost PFC case implementation, in here also resonant filters are being used to suppress the common-mode EMI noises (the filters inductances are all equal to 60 [µH], while the capacitances are all equal to 22.7 [nF]).
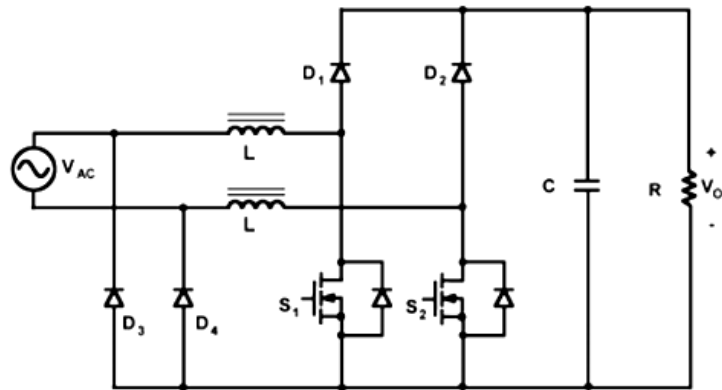
Fig. 2.64. Bridgeless PFC converter topology.
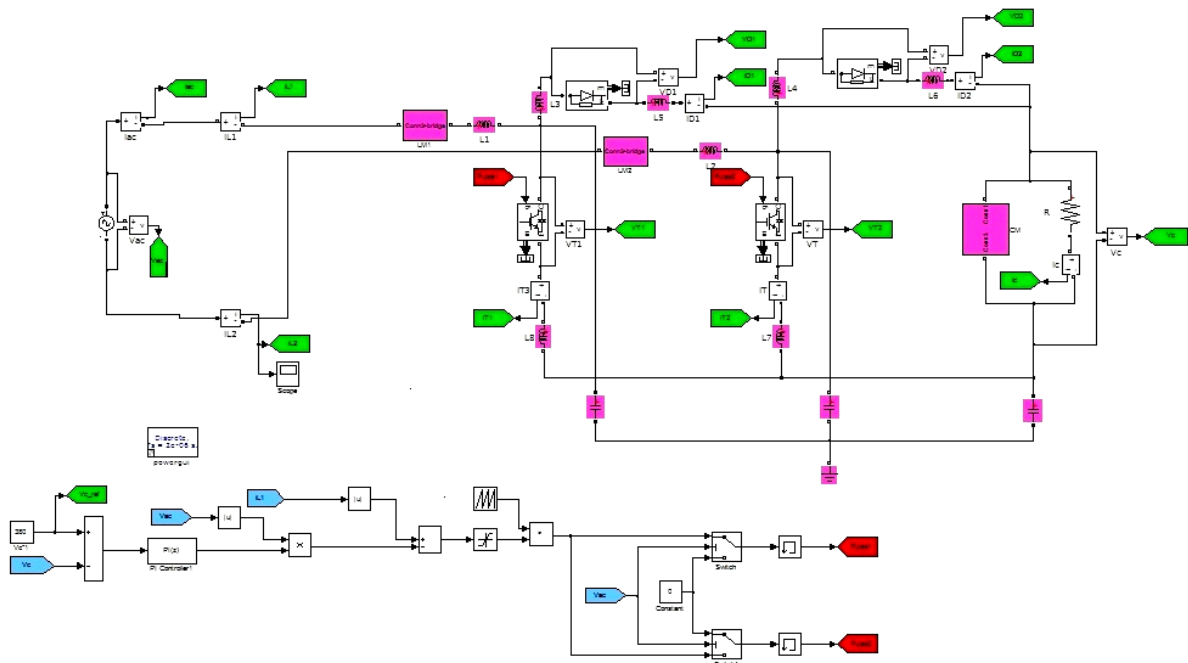
Fig. 2.65. Bridgeless PFC converter model implemntation in Matlab/Simulink.

In the traditional boost PFC topology, current flows through two of the bridge diodes in series. In the bridgeless PFC configuration, current flows through only one diode with the MOSFET switches providing the return path.

The gate commands for the two switches are guided by the logic signals which are generated by comparing the current error signal with a triangular carrier of 48 [kHz]. The 180° phase-shift is obtained by comparing the former resulted signal with the measured AC voltage signal.

Compared to a conventional boost PFC topology, the losses due to the bridge rectifier are eliminated, but the diode of the inactive MOSFET must be taken into account for the bridgeless configuration.

Thus, overall there are only the conduction losses from one diode for a bridgeless PFC converter compared to conduction losses from two diodes in a boost PFC converter. So, there is some efficiency gain for this topology by eliminating the voltage drop of one diode in the line-current path.

2.4.1.3. EMI Filters

Even though, the bridgeless PFC is one of the most attractive PFC topologies, being able to achieve high efficiency by eliminating the line-voltage bridge rectifier, this topology emits much higher conducted common mode (CM) EMI noise than conventional boost PFC converters. Thus, significantly larger CM chokes are needed in order to meet the Electromagnetic Compatibility (EMC) standards.

The study presented in [136] has investigated the effects of boost inductors on the DM noise of boost PFC converters. The results shown that the impedance of boost inductor significantly affects the DM noise of boost PFC. The higher the impedance is, the lower the DM noise is. As a result, the impedance of the boost inductor is determined by the converter design at low frequencies.

At high frequencies, the parasitic, such as the winding capacitance of the inductor, determine the impedance of the inductor. Reducing the effects of parasitic so as to increase the impedance of the inductor is a key to reduce HF DM noise. EMI filters are designed taken into consideration three requirements as presented below [137], [153]:

- *First requirement*:

The first requirement for the EMI filter is to provide the required attenuation, in order to ensure compliance with the EMI standards.

- *Second requirement*:

The second requirement for the EMI filter is that the displacement angle Φ between the line input current and the line input voltage, must be kept low, in order not to degrade power factor.

- *Third requirement:*

The third requirement is related to the overall stability of the system. It is known that unstable operation may occur due to the interaction between the EMI filter and the power stage.

Based on the above mentioned requirements and methods met in the literature, the EMI filters for the simulation models of boost PFC converter and of bridgeless PFC converter were developed by our team. The schematic of the PFC converter including the common mode and EMI filters is depicted in Figure 2.66 and the parameters used for modeling the filters are presented in Table 2.6.

Table 2.6. CM & EMI Filters Parameters

CM Filter Parameters		*EMI Filter Parameters*	
R	50 Ω	C_1	1.5 μF
R_1	50 Ω	C_2	1.5 μF
R_2	50 Ω	C_3	0.47 μF
R_3	50 Ω	C_4	4.7 nF

CM Filter Parameters		EMI Filter Parameters	
C	10 µF	C_5	4.7 nF
C_1	0.1 µF	L_1	3.3 mH
C_2	10 µF	L_2	3.3 mH
C_3	0.1 µF	L_3	3.3 mH
$L_1 = L_2$	50 mH	L_4	3.3 mH

a)   b)
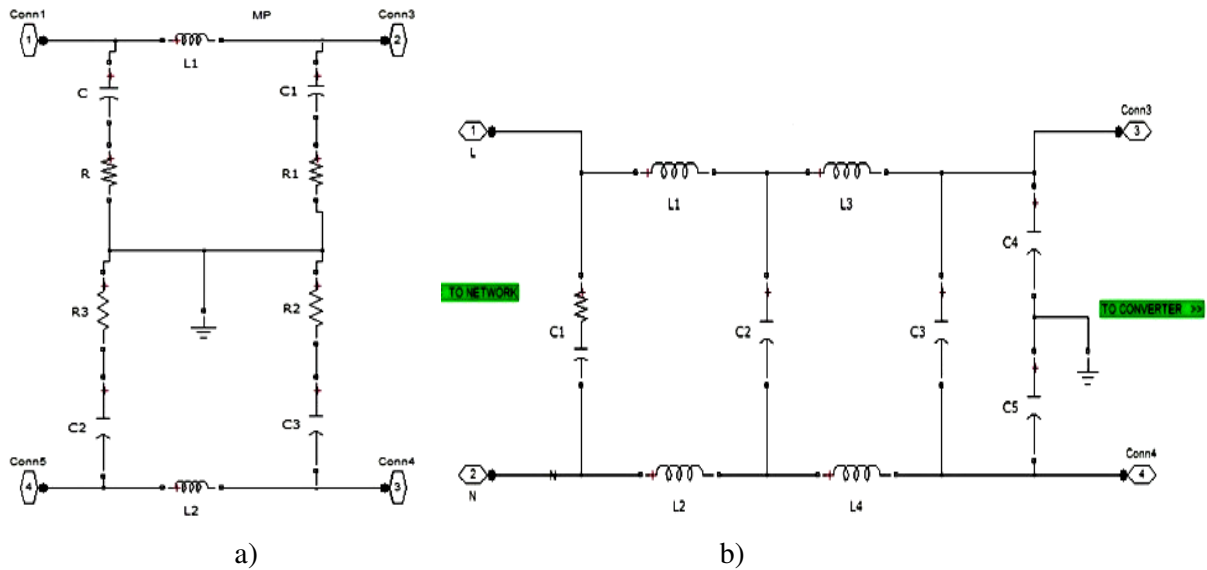
Fig. 2.66. Matlab/Simulink Implementation of the Common Mode (a) and EMI filters (b).

2.4.1.4. Simulation Results

a. Simulation results for the Boost Power Factor Correction Converter

The following assumptions were made before proceeding with the performances analysis of the two converters topologies:

- Unity power factor achievement, i.e. the line current is in phase with the input line voltage, and has a sinusoidal waveform;

- The PFC output voltage regulation, with minimum ripple.

The simulation results in this paragraph were obtained by our team in the next operation conditions and parameters: input AC voltage set to 230 [V] (RMS), a 48 [kHz] switching frequency, the DC-link capacitor voltage controlled to around 380 [V] by a PI type controller, the dc capacitance C around at 780 [µF], the magnetically coupled inductances L = 100 [µH] and the resistive load set to 57.76 [Ω]. The parameters of PI controller are: $kp = 0.545e-3$, $ki = 0.0073$ and the hysteresis band is ± 0.1.

The simulation of the boost PFC converter is carried out for different loading conditions at 48 [kHz] switching frequency, in order for the efficiency curve to be drawn, as shown in Figure 2.73.

The simulation results showing the boost PFC converter performances are next presented (see Figure 2.67 – Figure 2.72). They were obtained for operation at P = 2.5 [kW].

A Fast Fourier analysis of the input current waveform, respectively of the input voltage waveform is done, as presented in Figure 2.73- Figure 2.77. The current between the DC capacitor C and ground is also analyzed and its Fast Fourier analysis is depicted in Figure 2.78, respectively in Figure 2.79. The analysis was done for 25 cycles of the selected signal and for two frequency ranges: from 0 to 1 [kHz], respectively from 1 [kHz] to 150 [kHz].

Table 2.7 presents the RMS and average values for the MOSFET (I_{mosfet}), diode (I_{diode}) and inductance (I_{ac}).

The losses for the simulated boost converter model, as per Table 2.8, were computed based on the catalogue parameters for the MOSFET, diode and inductance devices, as follows: $R_{mosfet} = 0.38$ [Ω], $R_{diode} = 0.118$ [Ω] and $R_{cu} = 0.075$ [Ω]. P_{mosfet} COND and P_{mosfet} SW stand for the conducting losses, respectively for the switching losses.

Table 2.7. Rms & Avg Values [A]

	RMS	*AVG*
I_{mosfet} **[A]**	7.063	4.201
I_{diode} **[A]**	9.546	6.263
I_{ac}**[A]**	11.76	0.009468

Table 2.8. Breakdown of Losses at Nominal Load [W]

P_{diode} [W]	P_{mosfet} COND [W]	P_{mosfet} SW [W]	P_{cu} [W]	P_{out} [W]	P_{in} [W]
10.75	18.95	2.743	10.55	2438	2702
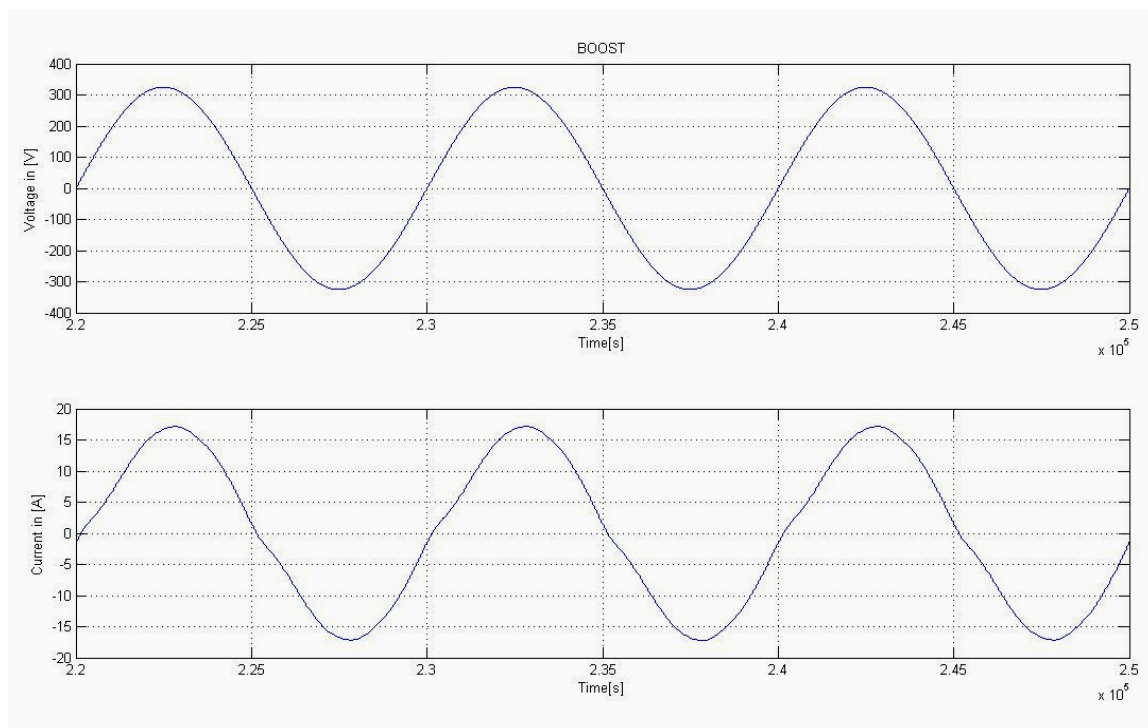
Fig. 2.67. Zoom on input voltage & input current for the Boost topology.
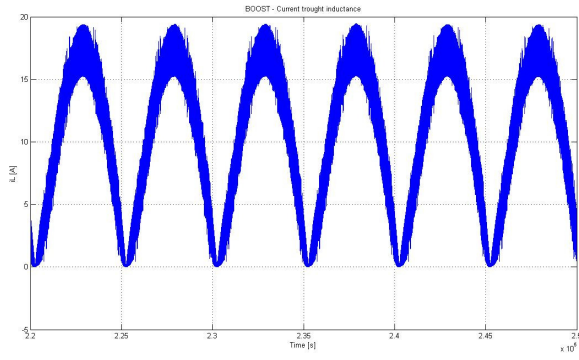
Fig. 2.68. Zoom on inductance current for the Boost topology.
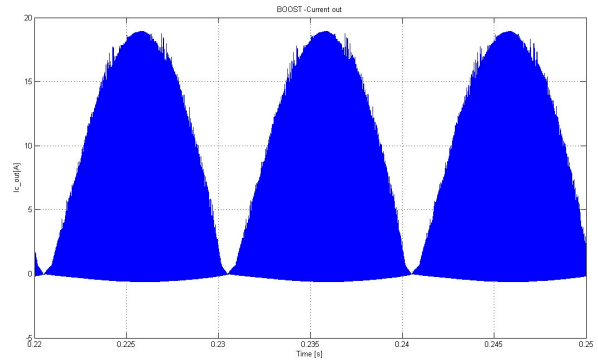
Fig. 2.69. Zoom on capacitor current for the Boost topology.
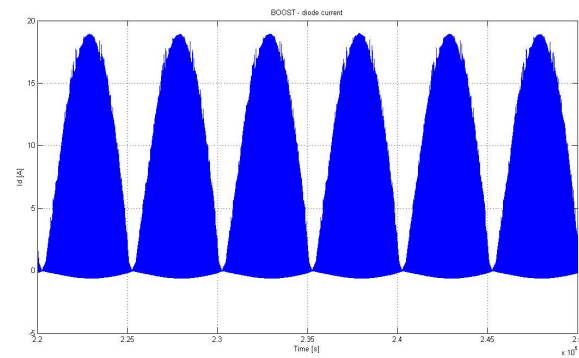
Fig. 2.70. Zoom on diode current for the Boost topology.
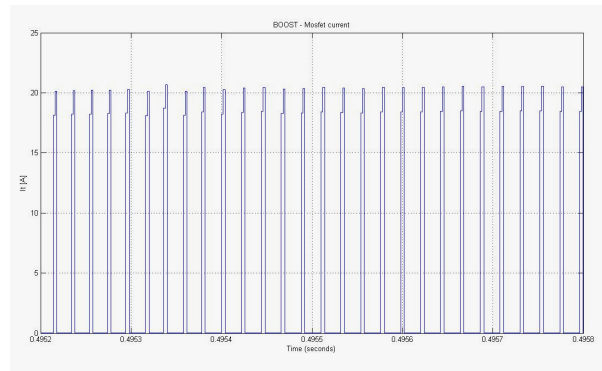
Fig. 2.71. Zoom on Mosfet current for the Boost topology.
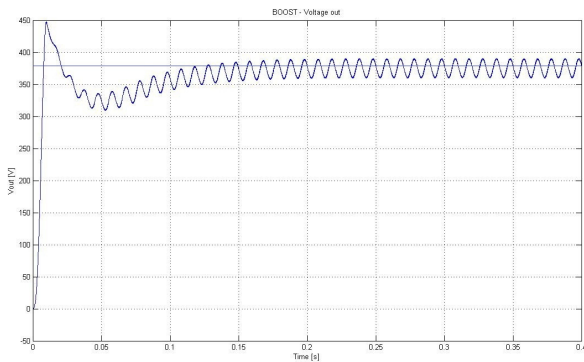
Fig. 2.72. Voltage output for the Boost topology
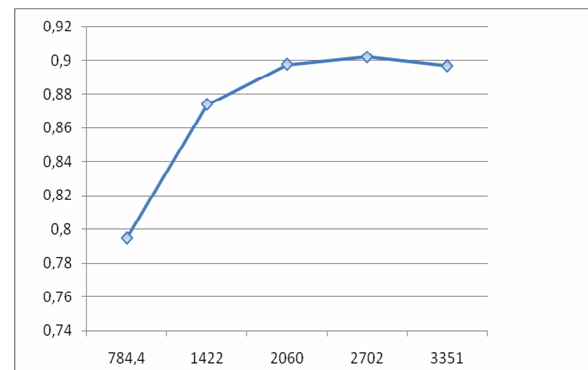
Fig. 2.73. Efficiency versus power curve for the Boost topology.
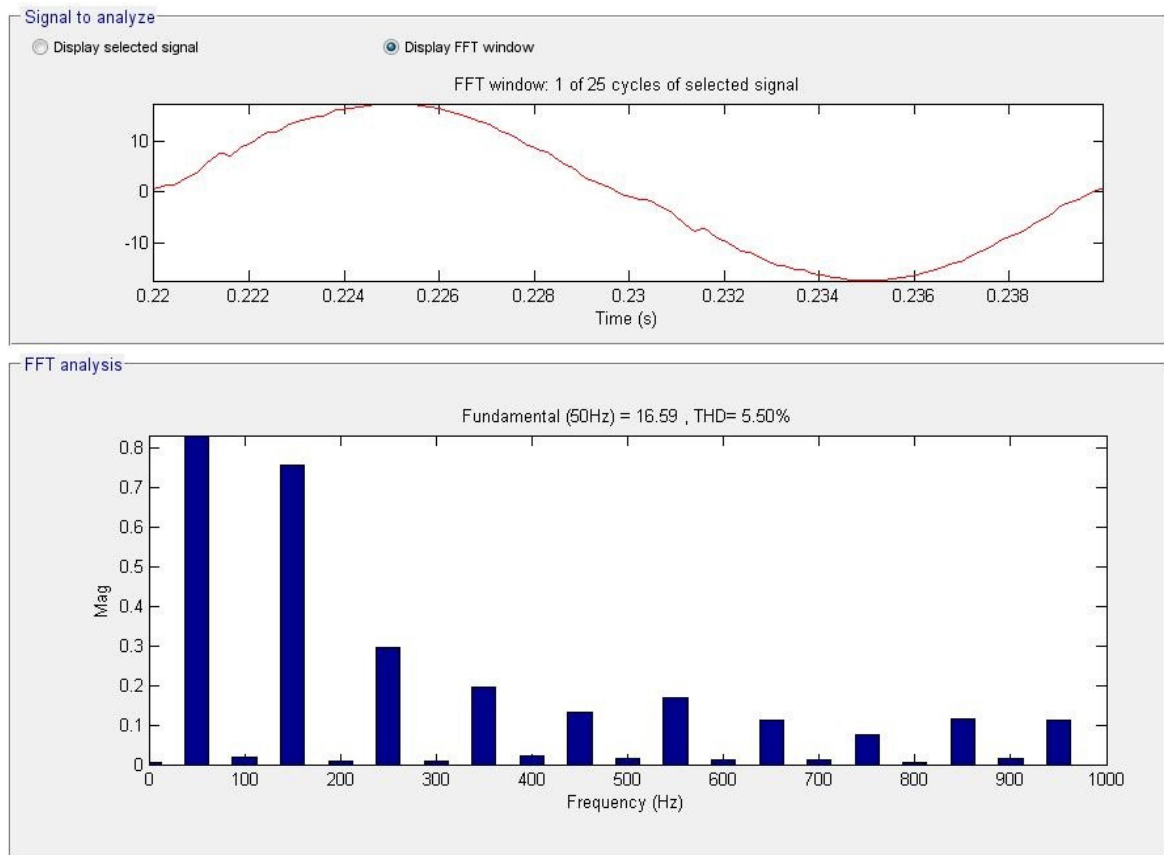
Fig. 2.74. FFT for input current range from 0 to 1kHz for Boost **t**opology.
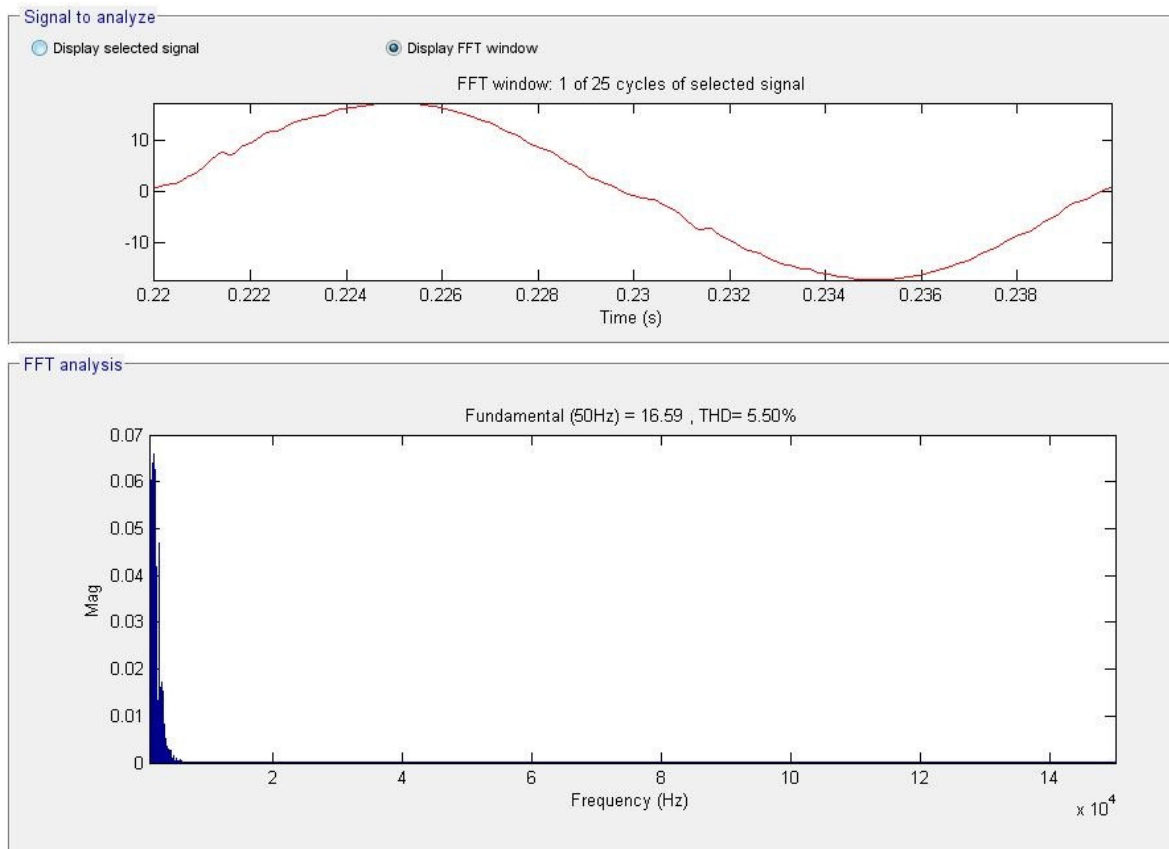
Fig. 2.75. FFT for input current range from 1 to 150kHz for Boost topology.
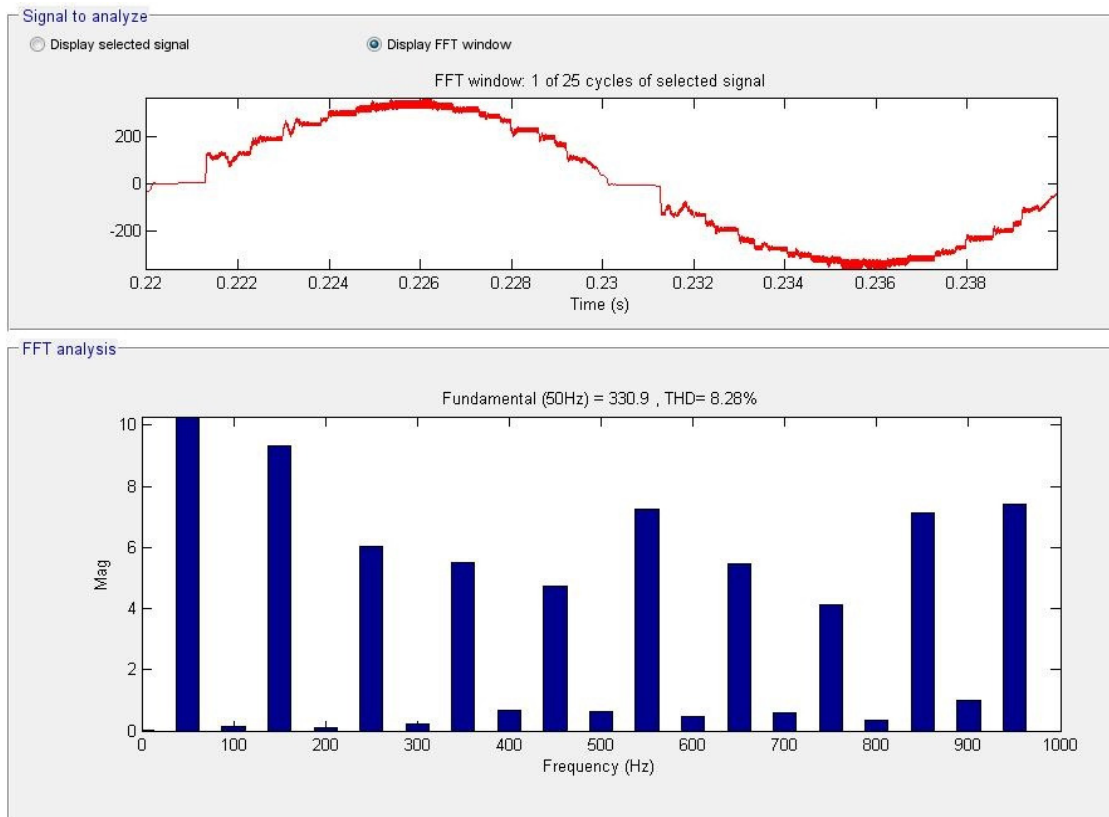
Fig. 2.76. FFT for voltage measured after EMI filter within 0 to 1kHz range
for the Boost topology.
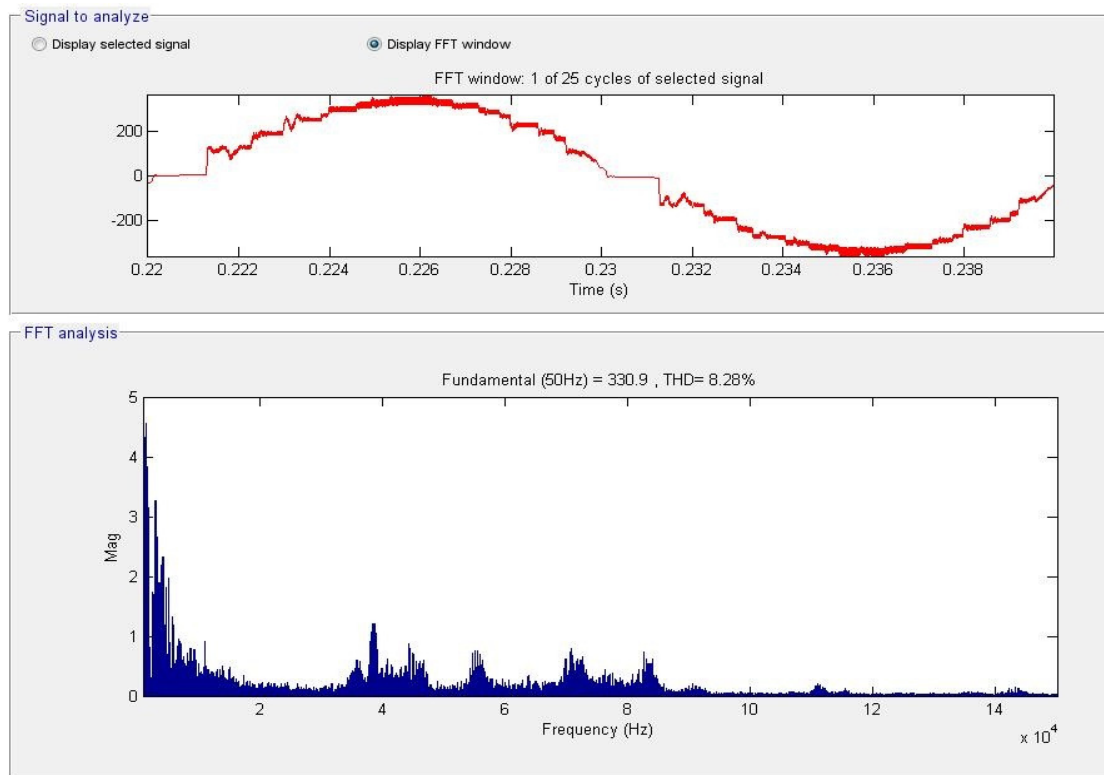
Fig. 2.77. FFT for voltage measured after EMI filter within 1 to 150kHz range
for the Boost topology.
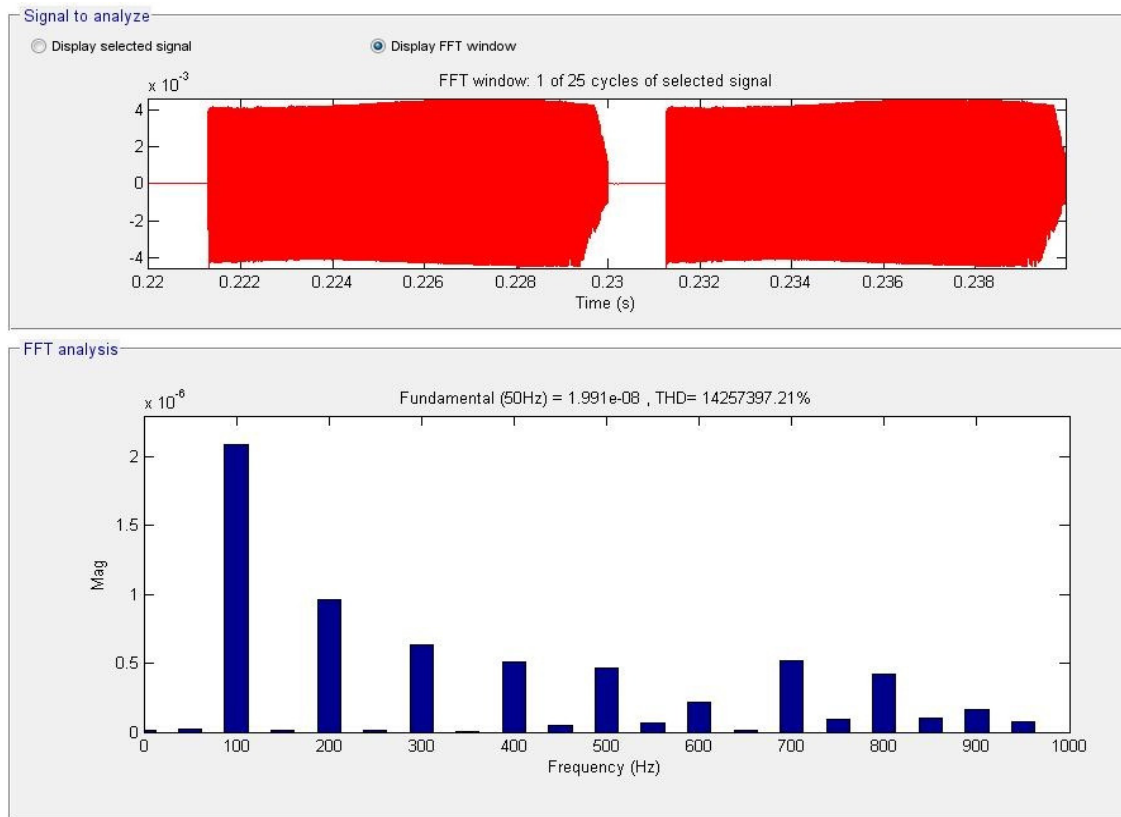
Fig. 2.78. FFT current between C and ground within 0 to 1kHz range for the Boost topology.
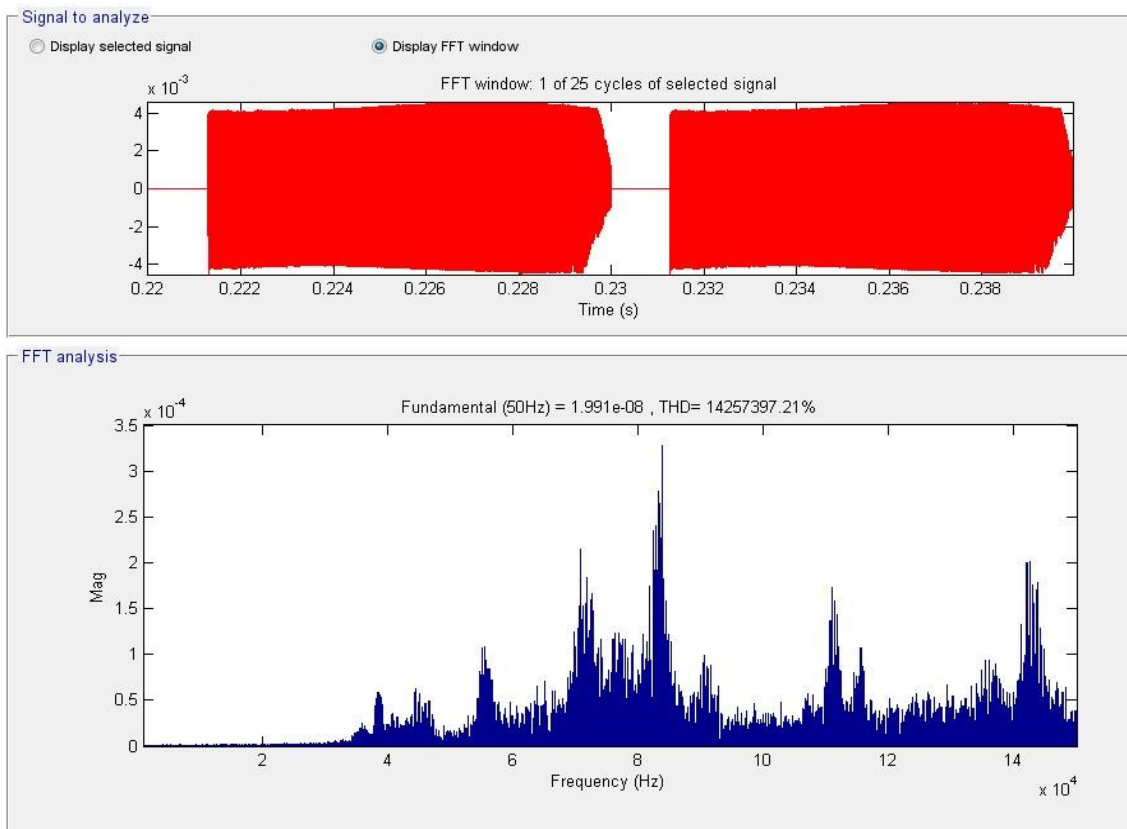
Fig. 2.79. FFT current between C and ground within 1 to 150kHz range for the Boost topology.

b. Simulation results for the Bridgeless Power Factor Correction Converter

Similar operation conditions and parameters as for the boost PFC converter case are assumed in here also, with the only mention that now the inductances L_1, respectively L_2 are 300 [μH] each. Therefore, a comparison between the two converter topologies could be done.

The parameters of PI controller are: $kp = 0.05e\text{-}3$, $ki = 0.01$.

Waveforms of the input voltage, input current through one inductor (I_{mosfet}), boost current through one diode (I_{diode}), sensed current through one MOSFET device (I_{ac}) and PFC bus voltage of the converter are provided in Figure 2.80 – Figure 2.86. The reference and the regulated DC voltage is shown in Figure 2.85. The efficiency of the simulated model of the boost converter is depicted in Figure 2.86.

A Fast Fourier analysis of the input current waveform, input voltage waveform and of the current between the DC capacitor C and ground is provided as depicted in Figure 2.87 - Figure 2. 92. Similar conditions for the FFT were employed: 25 cycles of the selected signal and two frequency ranges: from 0 to 1 [kHz], respectively from 1 [kHz] to 150 [kHz] were taken into consideration.

Table 2.9 presents the RMS and average values for the MOSFET, diode and inductance.

The losses for the bridgeless converter model, as per Table 2.10, were computed based on the same catalogue parameters for the MOSFET, diode and inductance devices, as used in the previous paragraph: $R_{mosfet} = 0.38$ [Ω], $R_{diode} = 0.118$ [Ω] and $R_{cu} = 0.075$ [Ω].
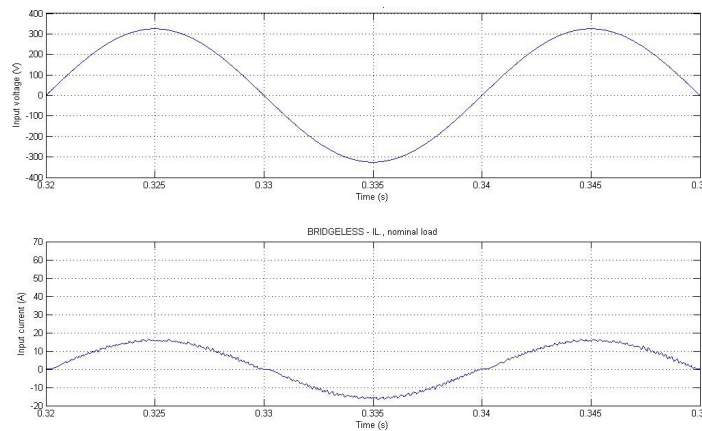
Fig. 2.80. Zoom on input voltage & input current for the Bridgeless topology.
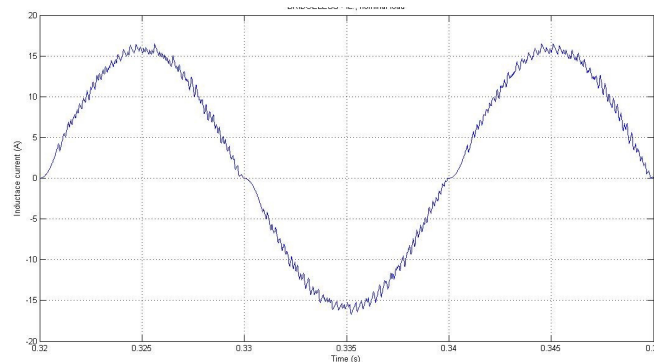
Fig. 2.81. Zoom on inductance current for the Bridgeless topology.
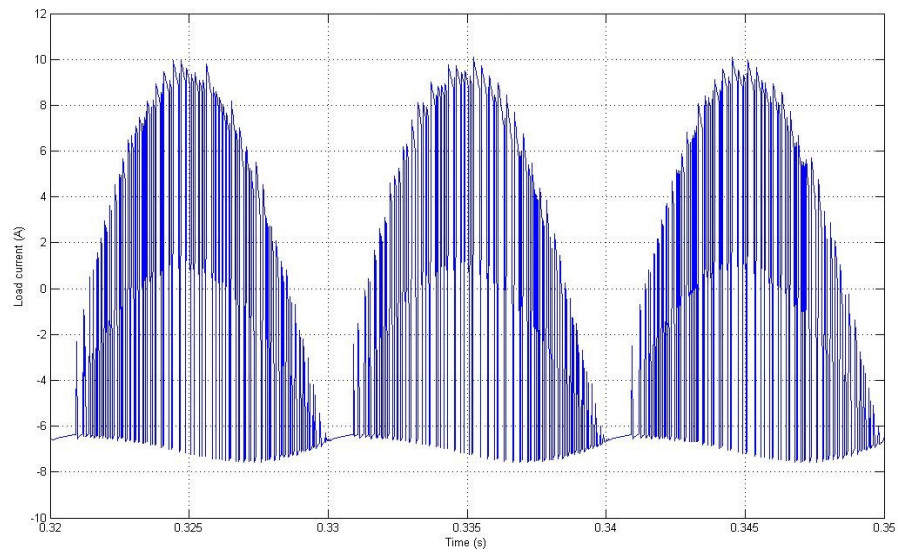
Fig. 2.82. Zoom on capacitor current for the Bridgeless topology.
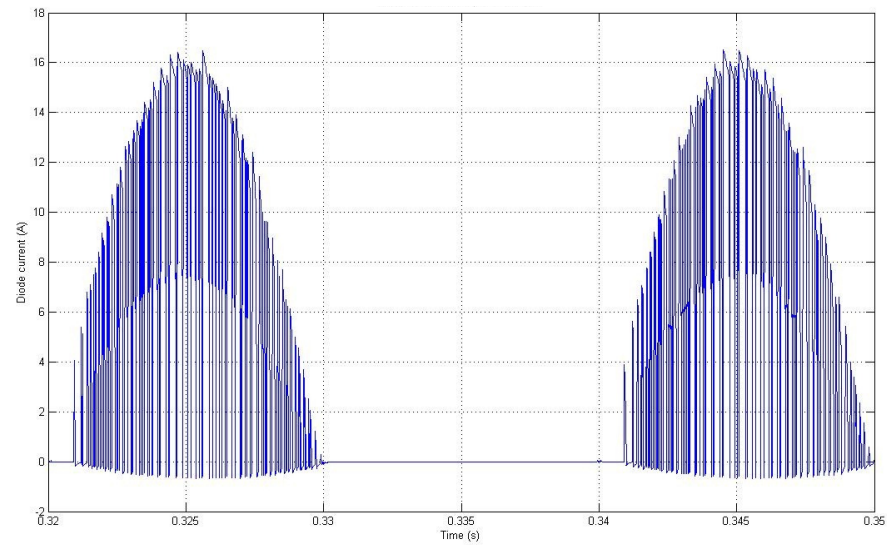
Fig. 2.83. Zoom on diode current for the Bridgeless topology.
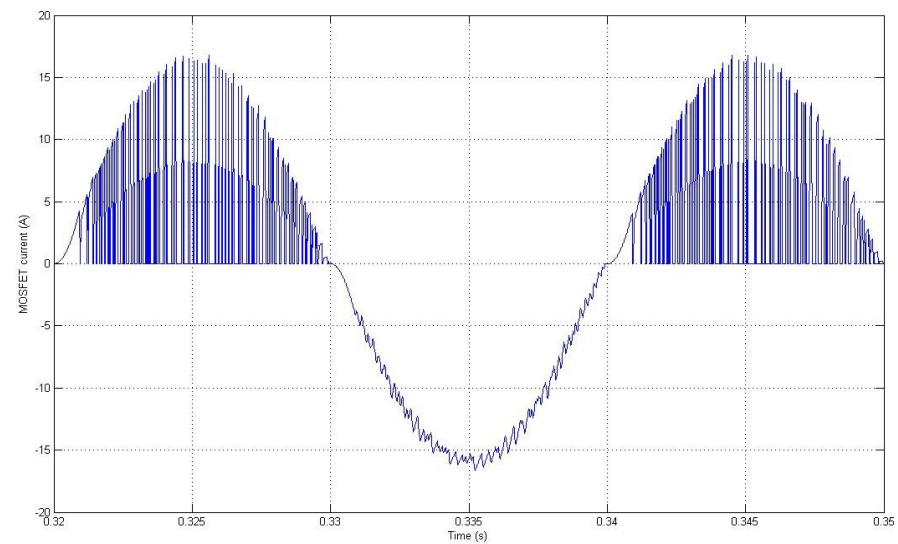
Fig. 2.84. Zoom on Mosfet current for the Bridgeless topology.
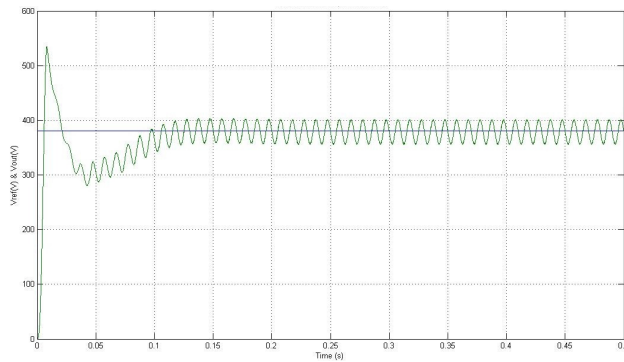
Fig. 2.85. Voltage output for the Bridgeless topology.
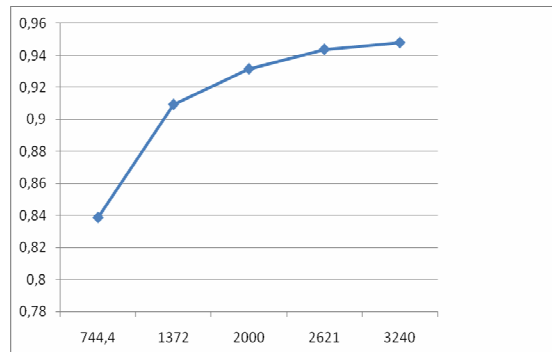
Fig. 2.86. Efficiency versus power curve for the Bridgeless topology.
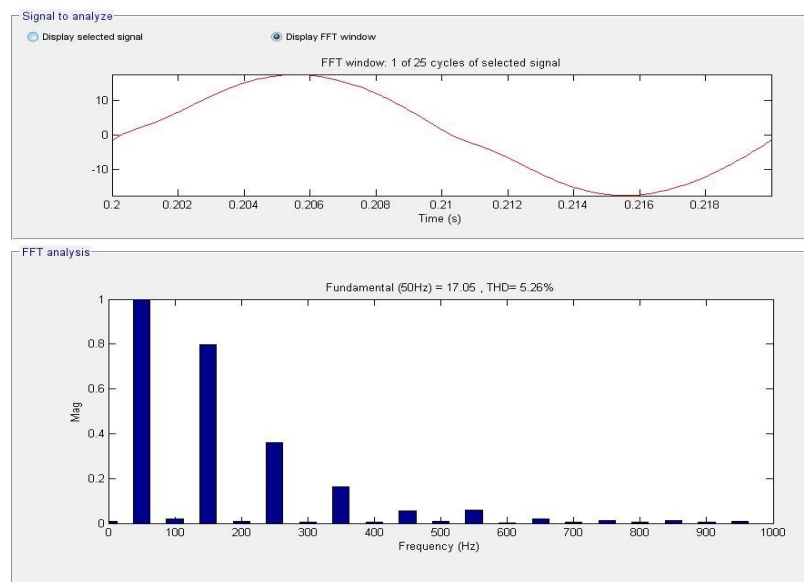
Fig. 2.87. FFT for input current range from 0 to 1kHz for Bridgeless topology
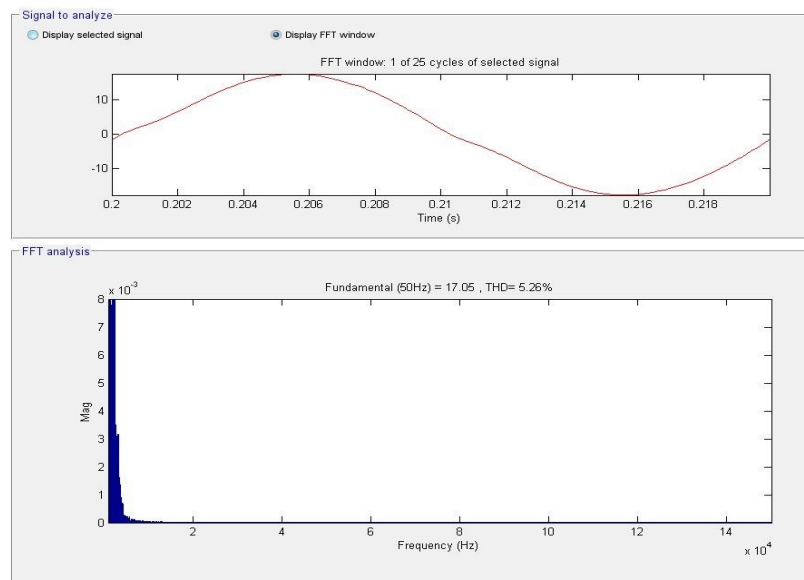
Fig. 2.88. FFT for input current range from 1 to 150kHz for Bridgeless topology.
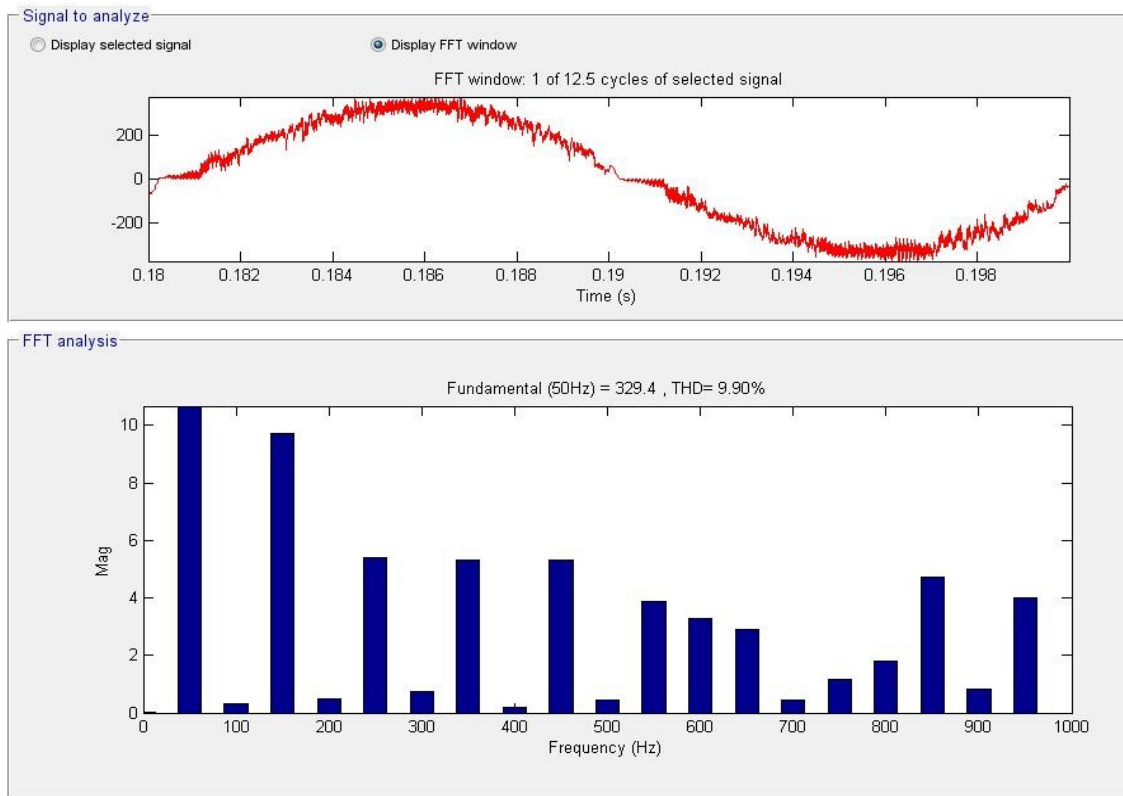
Fig. 2.89. FFT for voltage measured after EMI filter within 0 to 1kHz range for the Bridgeless topology.
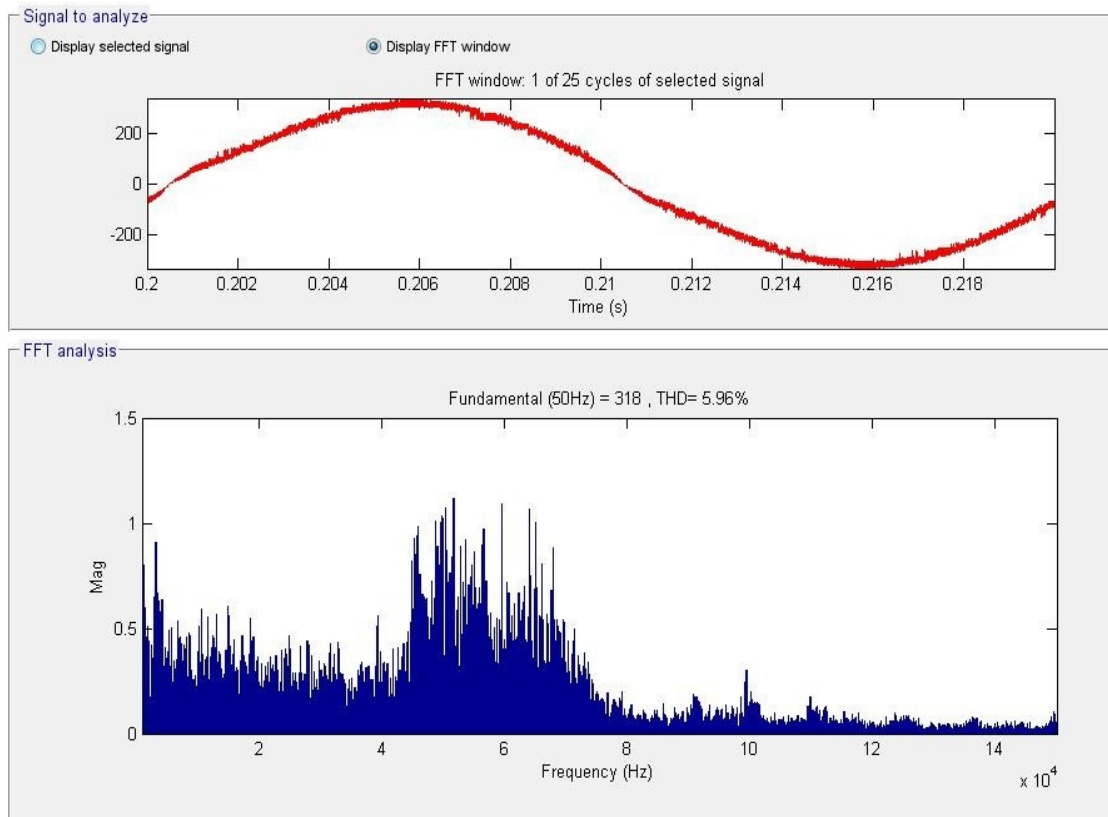
Fig. 2.90. FFT for voltage measured after EMI filter within 1 to 150kHz range for the Bridgeless topology.
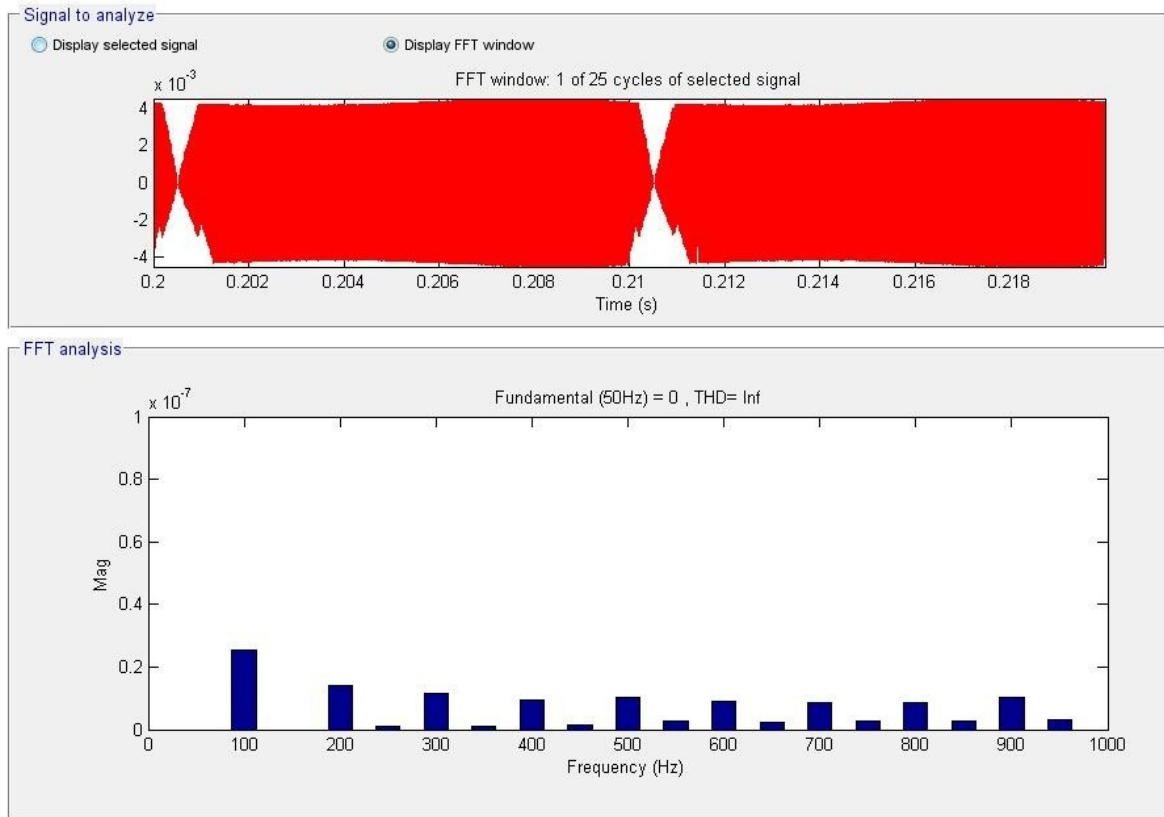
Fig. 2.91. FFT current between C and ground within 0 to 1kHz range for the Bridgeless topology.
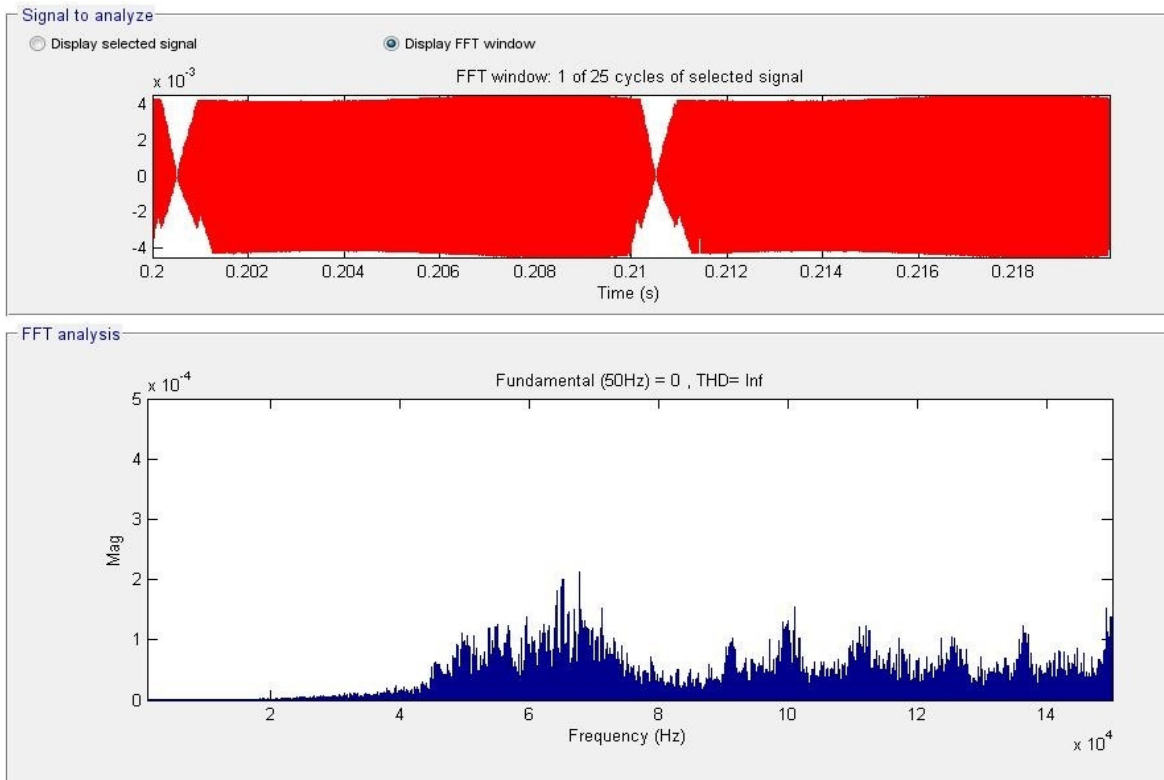
Fig. 2.92. FFT current between C and ground within 1 to 150kHz range for the Bridgeless topology.

Table 2.9. Rms & Avg Values [A]

	RMS	**AVG**
I_{mosfet} **[A]**	5.258	0.26
I_{diode} **[A]**	6.956	3.447
I_{ac} **[A]**	11.91	0.01249

Table 2.10. Breakdown of Losses at Nominal Load [W]

P_{diode} **[W]**	$P_{mosfet}\,COND$ **[W]**	$P_{mosfet}\,SW$ **[W]**	P_{cu} **[W]**	P_{out} **[W]**	P_{in} **[W]**
5.715	10.5	2.341	5.61	2576	2737

2.4.1.5. Conclusion

In this study research, the topologies which are chosen by our team to be investigated are: the conventional boost PFC and the bridgeless PFC converters. In the last two decades, both topologies have competed to become the topology of choice for the PFC front-end in industrial applications.

The study deals with the design study of the two topologies selected from a state-of-the-art from literature, then with the implementation of their hardware and control parts in Matlab/Simulink simulation environment and finally with their performances evaluation and EMI analysis using comparison.

In terms of control principle and implementation, the bridgeless PFC is equivalent to the conventional boost PFC.

Simulation results run for the same operation mode, show that the input current is in phase with the input voltage, and its shape is nearly perfectly sinusoidal, as expected, for both topologies.

It also can be seen that the RMS and AVG values for current through the output capacitor is constant—independent of topology (either for the boost or bridgeless configuration). Loss analysis and efficiency evaluation are also provided.

It can be noted that in the bridgeless topology, a new loss has been introduced in the intrinsic body diodes of the MOSFETs, but since input bridge rectifiers were eliminated, there is some efficiency gain for this topology. This feature makes the bridgeless PFC more useful in high power applications.

The freedom from harmonics also minimizes electromagnetic interference (EMI) with other devices being powered from the same source. Another reason to employ PFC in many of today's power supplies is to comply with regulatory requirements.

Nowadays, electrical equipment in Europe must comply with the European EN 61000−3−2, or EN 61000-3-4 Norms. This requirement applies to most electrical appliances.

Choosing of the right parameters of the common mode and EMI filters, based on literature, is also provided, as well as their implementation in Matlab/Simulink. Simulation results show that they are compliant with international standards. Compared to the conventional boost PFC converter (at equal power), the reduced ripple in the input current for the bridgeless PFC converter decreases the conducted-EMI noise and helps reducing the EMI filter size.

Further experimental results from the two prototypes studied in here will be developed by our team in a next-future research.

2.4.2. Interleaved Boost versus Bridgeless Interleaved Converter Performances Analysis

2.4.2.1. Introduction

The boost PFC topology is an active PFC converter topology, suitable for a low to medium power range up to approximately 1 [kW] due to the diode bridge losses which significantly degrade the efficiency by dissipating heat in a limited area.

Compared with the classic boost PFC converter, *the interleaved (IL) boost converter has the advantage of paralleled semiconductors*. *It also reduces output capacitor high frequency ripple, but it still has the problem of heat management for the input diode bridge rectifiers* [130].

Interleaving, if is done correctly, could decrease the size of the EMI filter without increasing the size of the boost inductor volume compared to a single stage pre-regulator approach. A common design practice is to select the switching frequency of the power converter below the EMI lower limit of 150 [kHz] [136], [135].

The family of bridgeless converters has been widely used since it allows considerable reduction in conduction losses providing increased global efficiency of the converter structure.

Compared to the interleaved boost PFC converter, *the bridgeless interleaved (BLIL) PFC converter introduces two more FETs and two more fast diodes in place of four slow diodes used in input bridge for the former converter. In this case the application of the interleaving of multiple converters cells technique is interesting because allows the division of the current stresses in the semiconductors* [137].

Based on literature studies, efficiency improvement is expected for the bridgeless interleaved PFC topology compared with the interleaved boost PFC topology [129]-[132].

To solve the EMI noise issue, an EMI noise reduction circuit should be introduced. Information about EMI model building of boost and bridgeless PFC circuits are also given in [165]. Based on these methods and requirement, proper models common mode and EMI filters are then implemented.

The general aim of this study is to investigate the performances and EMI emissions of the two PFC topologies: the interleaved boost PFC converter and the bridgeless interleaved PFC converter. Loss analysis and efficiency evaluation of the two above mentioned converters is also provided.

2.4.2.2. Interleaved Boost PFC Converter Topology

The interleaved boost converter, illustrated in Figure 2.93, consists of two boost converters in parallel, operating 180° out of phase. The input current is the sum of two inductor currents.
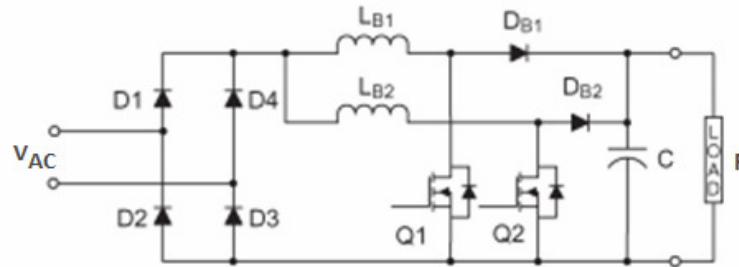
Fig. 2.93. Boost IL PFC converter topology.

The interleaved boost converter has the advantage of paralleled semiconductors. It also reduces output capacitor high frequency ripple, but it still has the problem of heat management for the input diode bridge rectifiers.

To evaluate some of the benefits of interleaving a two phase, interleaved boost PFC was implemented by our team in Matlab/Simulink environment, as given by Figure 2.94. The resonant filters used to diminish the common-mode EMI noises are also employed in here (the filters inductances are all equal to 60 [μH], while the capacitances are all equal to 22.7 [nF]).

Its control consists of: measured DC bus voltage is compared with set reference voltage. The resulting voltage error is then fed to the PI voltage controller for zero error DC bus voltage regulation and distortion free current reference. A multiplier is used to adjust its magnitude with the DC voltage V_{DC}. From the resulted signal, the reference current is then subtracted and by its comparison with two triangular carriers of 48 [kHz] (180° phase-shifted from each other), gate commands for Q_1, respectively for Q_2 MOSFET devices are generated.

2.4.2.3. Bridgeless Interleaved PFC Converter Topology

The bridgeless interleaved (BLIL) PFC topology for application in the front-end ac–dc converter is shown in Figure 2.95. Two more MOSFETs and two more fast diodes are introduced in place of four slow diodes used in the input bridge of the interleaved boost PFC converter. It retains the same semiconductor device count as the interleaved boost PFC converter presented in the precedent paragraph.

It control consists in two loops. A slow outer control loop is used to regulate the output voltage V_o to a constant reference voltage and to generate a reference current signal for the fast inner current control loop with similar waveform shape of the rectified input voltage, as it is shown by its implementation by our team in Matlab/Simulink in Figure 2.96. As for the interleaved boost PFC case implementation, in here also resonant filters are being used to suppress the common-mode EMI noises (the filters inductances are all equal to 60 [μH], while the capacitances are all equal to 22.7 [nF]).
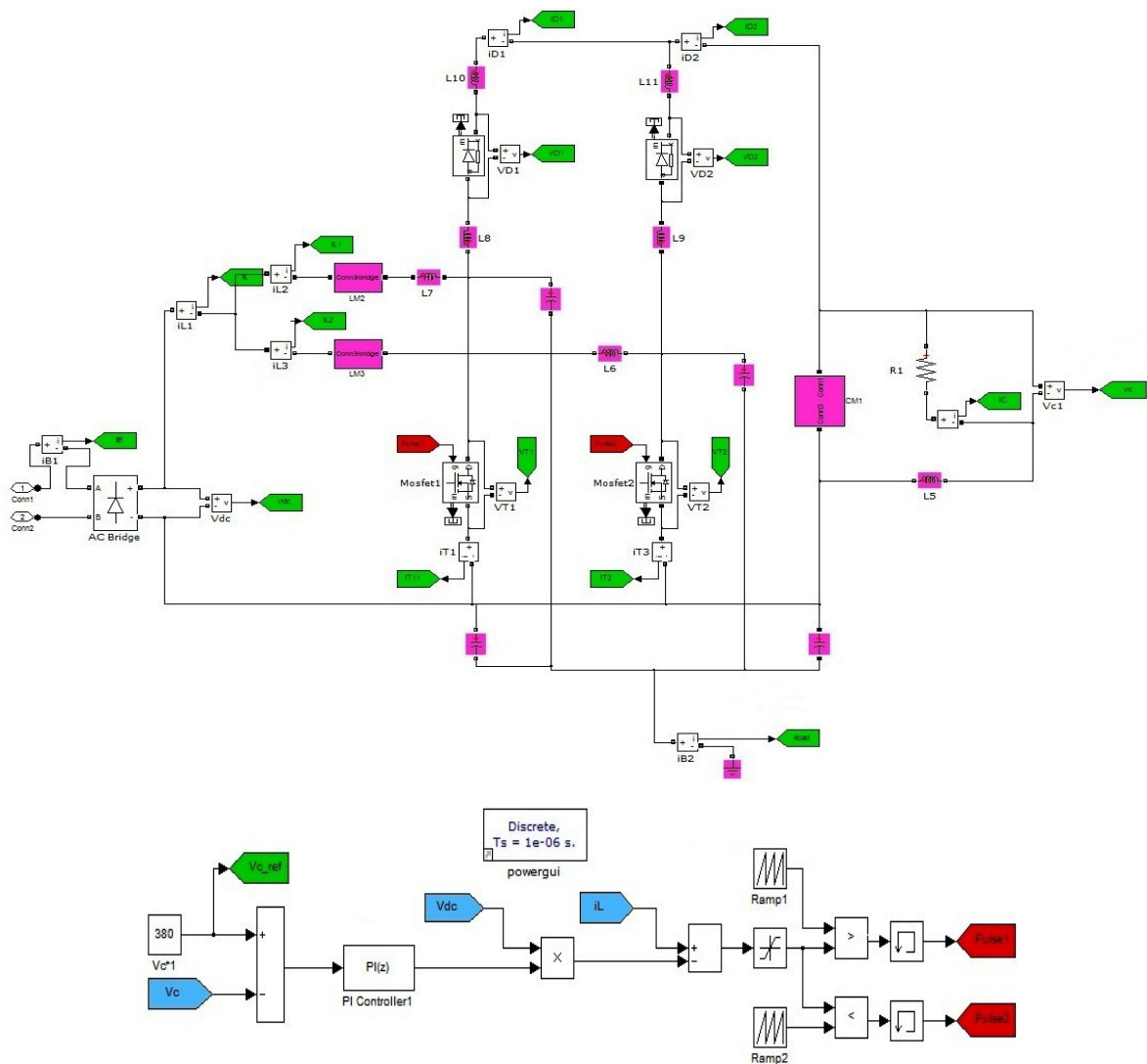
Fig. 2.94. Boost IL PFC converter model implementation in Matlab/Simulink.

Further, the current error signal is compared with a triangular carrier of 48 [kHz] and the resulted signal is then compared with the AC voltage signal, providing the gate commands for Q_1 and Q_3 MOSFET devices. The gate commands for the other two switches Q_2, respectively for Q_4 are generated by comparing the current error signal with a second triangular carrier of 48 [kHz], which is 180° phase-shift from the first one.
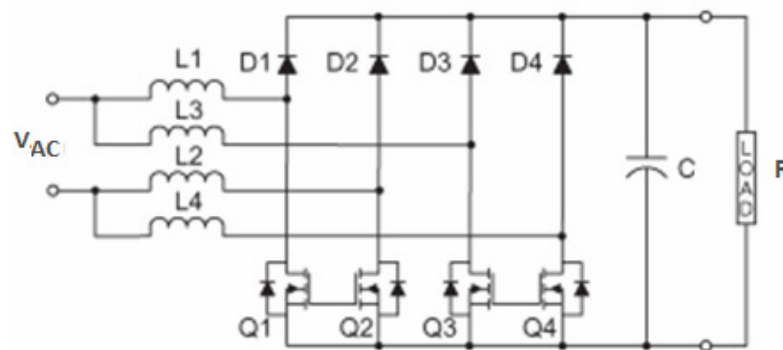
Fig. 2.95. Bridgeless IL PFC converter topology.
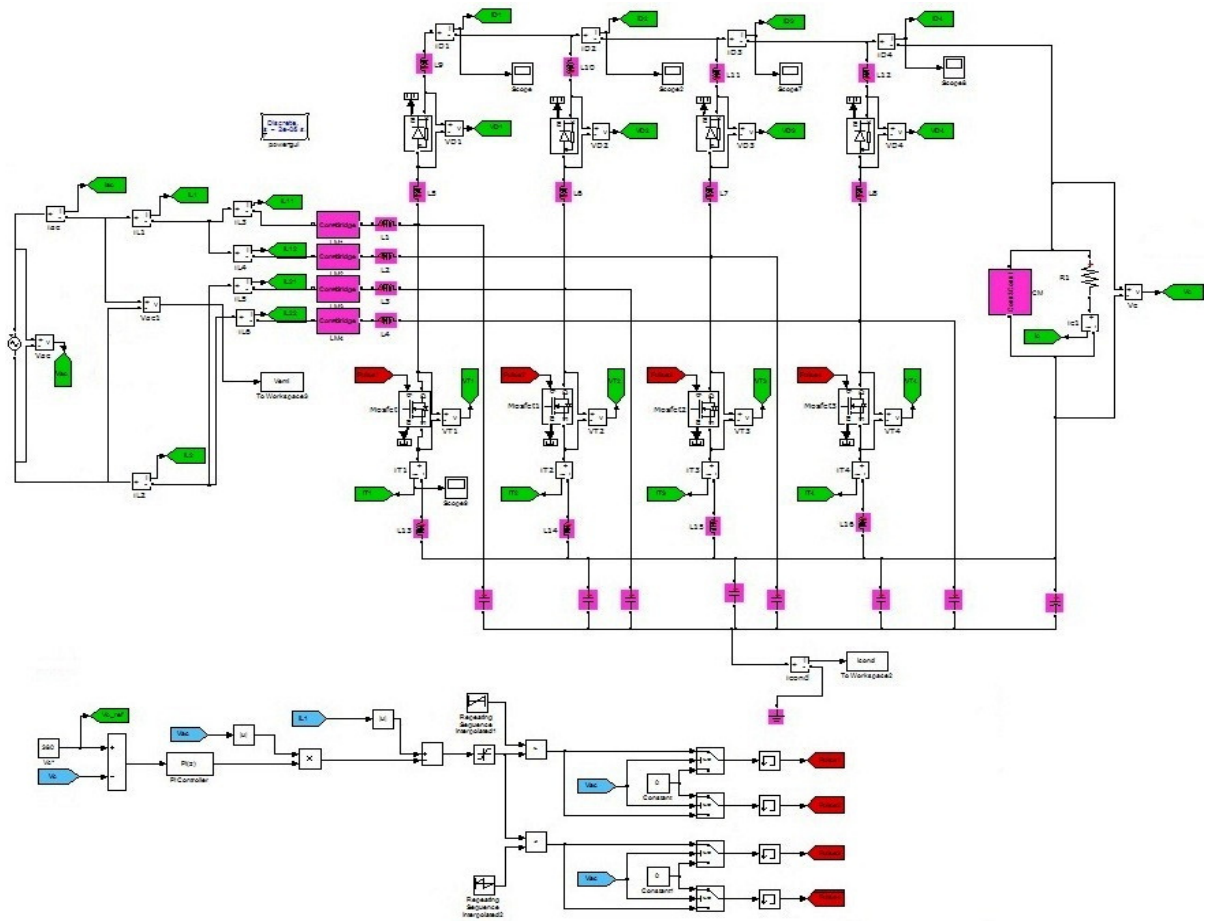
Fig. 2.96. Bridgeless IL PFC converter model implemntation in Matlab/Simulink

2.4.2.4. Simulation Results

a. Simulation results for the Interleaved Boost Power Factor Correction Converter

The following assumptions were made before proceeding with the performances analysis of the two converters topologies:

- Unity power factor achievement, i.e. the line current is in phase with the input line voltage, and has a sinusoidal waveform;

- The PFC output voltage regulation, with minimum ripple.

The simulation results in this paragraph were obtained in the next operation conditions and parameters: input AC voltage set to 230 [V] (RMS), a 48 [kHz] switching frequency, the DC-link capacitor voltage controlled to around 380 [V] by a PI type controller, the dc capacitance C around at 780 [μF], the two inductances $L_{B1} = L_{B2} = 150$ [μH] and the resistive load set to 57.76 [Ω]. The parameters of PI controller are: $k_p = 0.05e\text{-}3$, $k_i = 0.01$ and the hysteresis band is ± 0.8.

The simulation results showing the boost PFC converter performances are next presented (see Figure 2.97 – Figure 2.103). They were obtained for operation at $P = 2.5$ [kW].

The simulation of the boost PFC converter is carried out for different loading conditions at 48 [kHz] switching frequency, in order for the efficiency curve to be drawn, as shown in Figure 2.103.

A Fast Fourier analysis of the input current waveform, respectively of the input voltage waveform is done, as presented in Figure 2.104 – Figure 2.107. The current between the DC capacitor C and ground is also analyzed and its Fast Fourier analysis is depicted in Figure 2.108, respectively in Figure 2.109. The analysis was done for 25 cycles of the selected signal and for two frequency ranges: from 0 to 1 [kHz], respectively from 1 [kHz] to 150 [kHz].

Table 2.11 presents the RMS and average values for one MOSFET (I_{mosfet}), one diode (I_{diode}) and one inductance (I_{ac}).

The losses for the simulated boost converter model, as per Table 2.12, were computed based on the catalogue parameters for the MOSFET, diode and inductance devices, as follows: R_{mosfet} = 0.38 [Ω], R_{diode} = 0.118 [Ω] and R_{cu} = 0.075 [Ω]. P_{mosfet} COND and P_{mosfet} SW stand for the conducting losses, respectively for the switching losses.
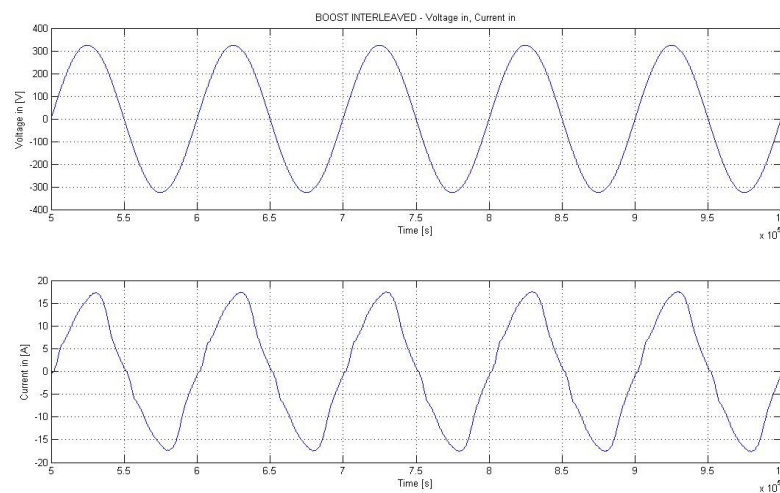
Fig. 2.97. Zoom on input voltage & input current for the Boost IL topology.
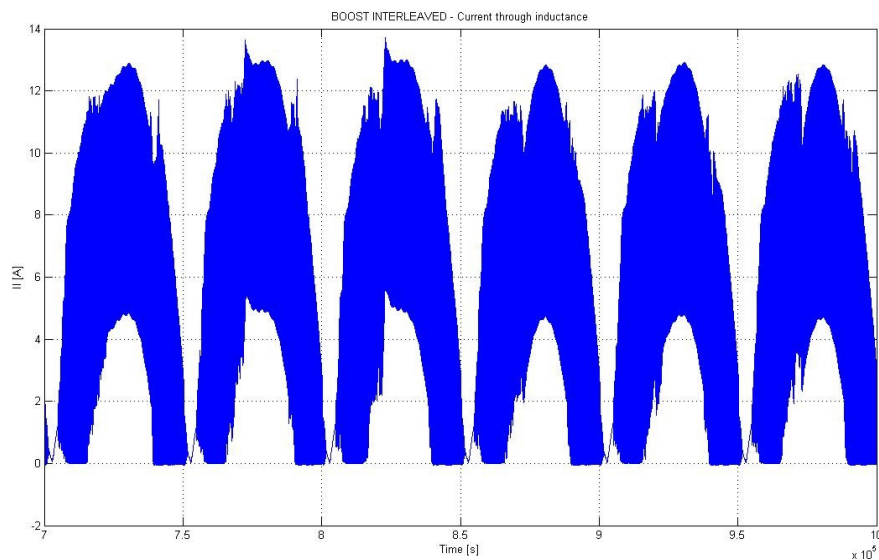
Fig. 2.98. Zoom on inductance current for the Boost IL topology.
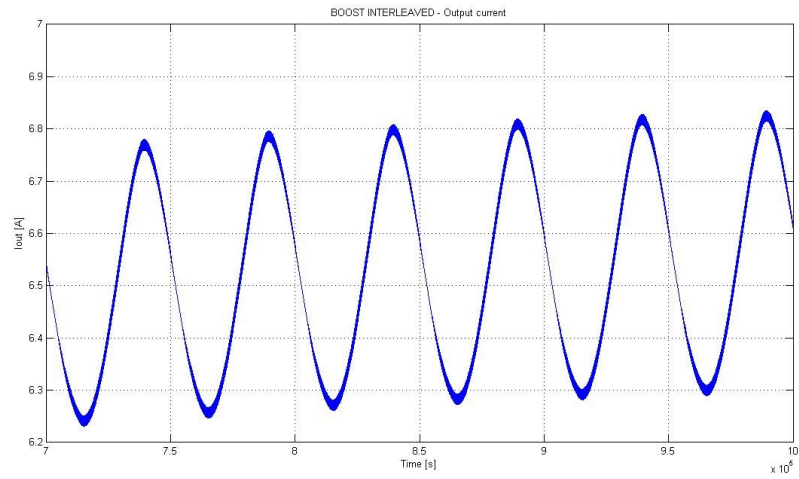
Fig. 2.99. Zoom on capacitor current for the Boost IL topology.
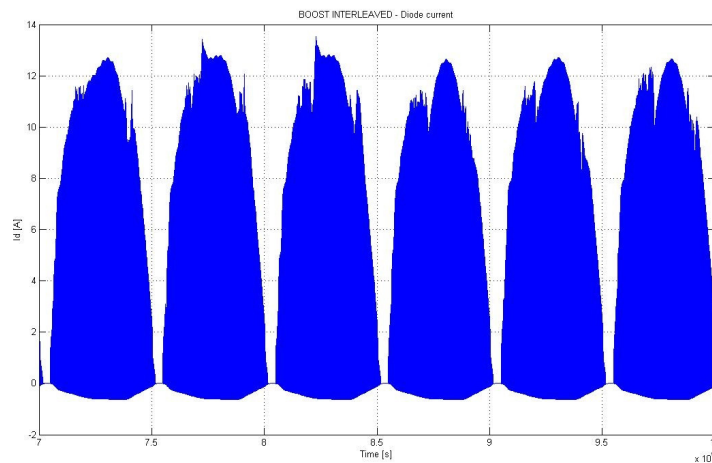
Fig. 2.100. Zoom on diode current for the Boost IL topology.
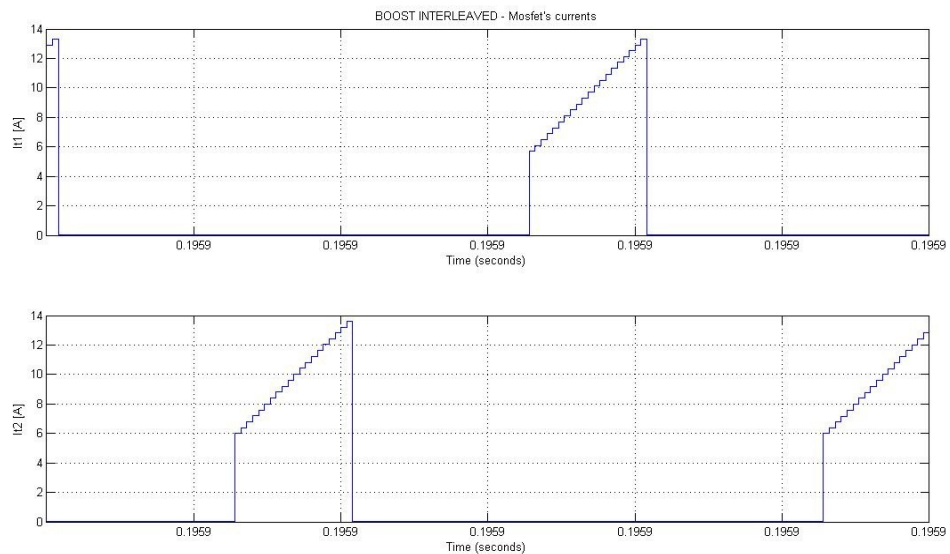
Fig. 2.101. Zoom on Mosfet currents for the Boost IL topology.
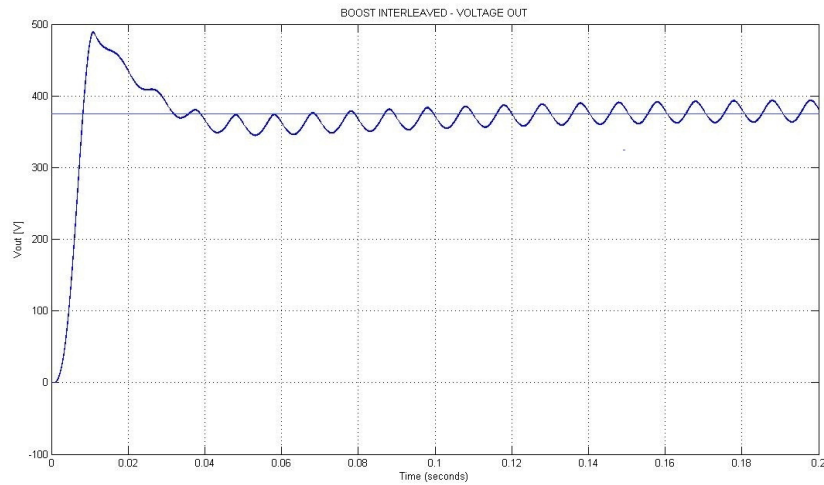
Fig. 2.102. Voltage output for the Boost IL topology.
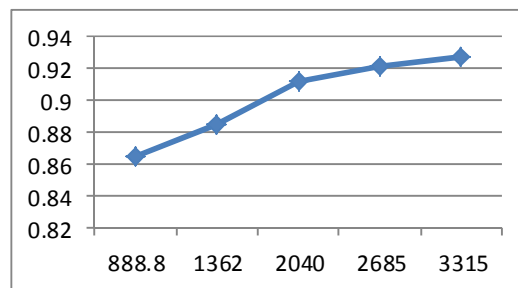
Fig. 2.103. Efficiency versus power curve for the Boost IL topology.
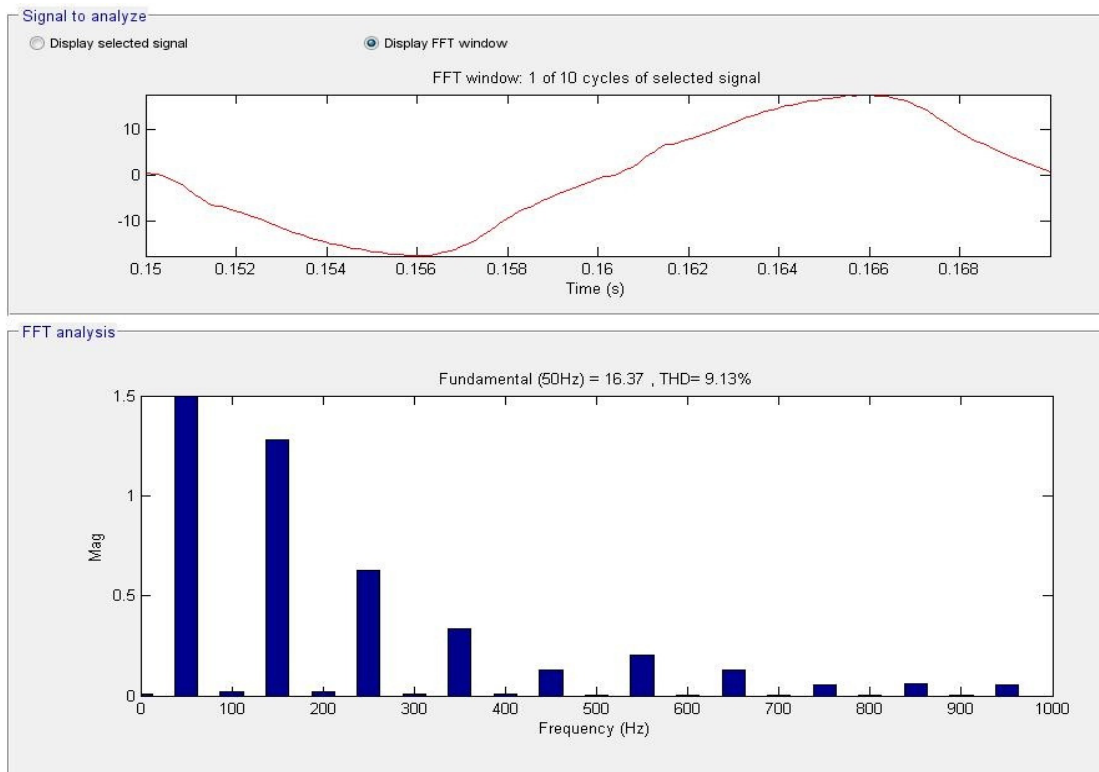
Fig. 2.104. FFT for input current range from 0 to 1 [kHz] for Boost IL topology.
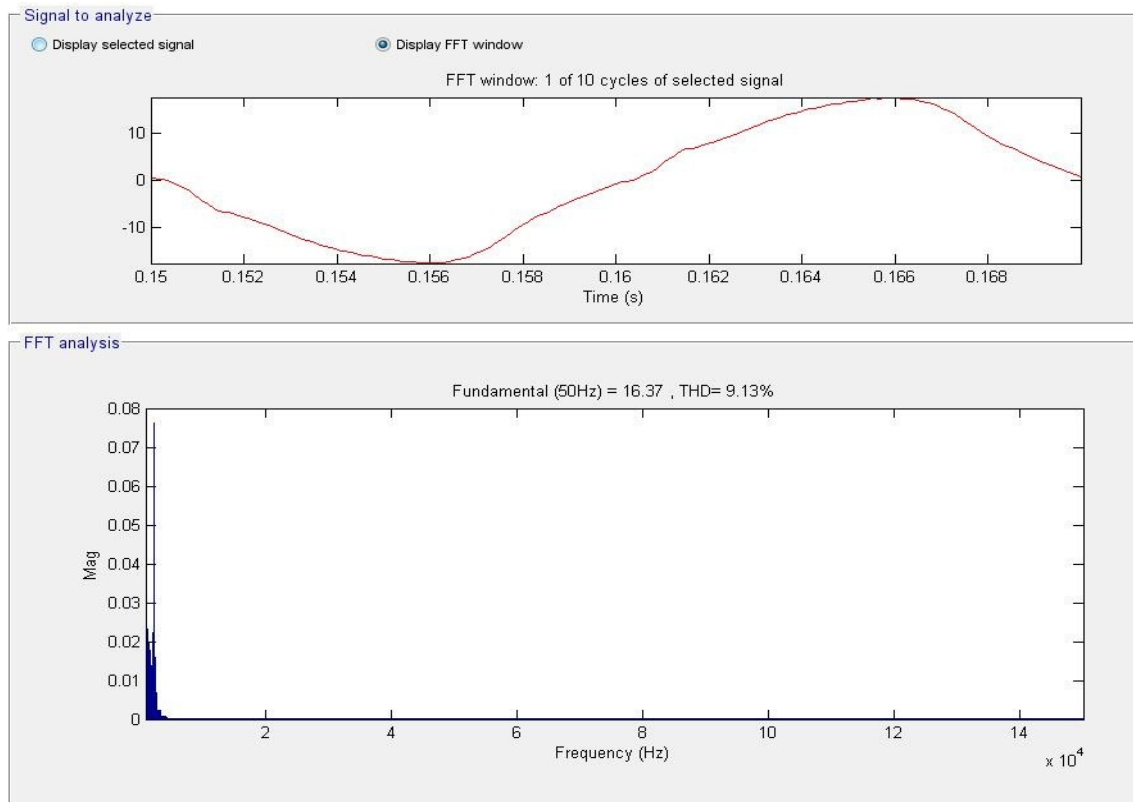
Fig. 2.105. FFT for input current range from 1 to 150 [kHz] for Boost IL topology.
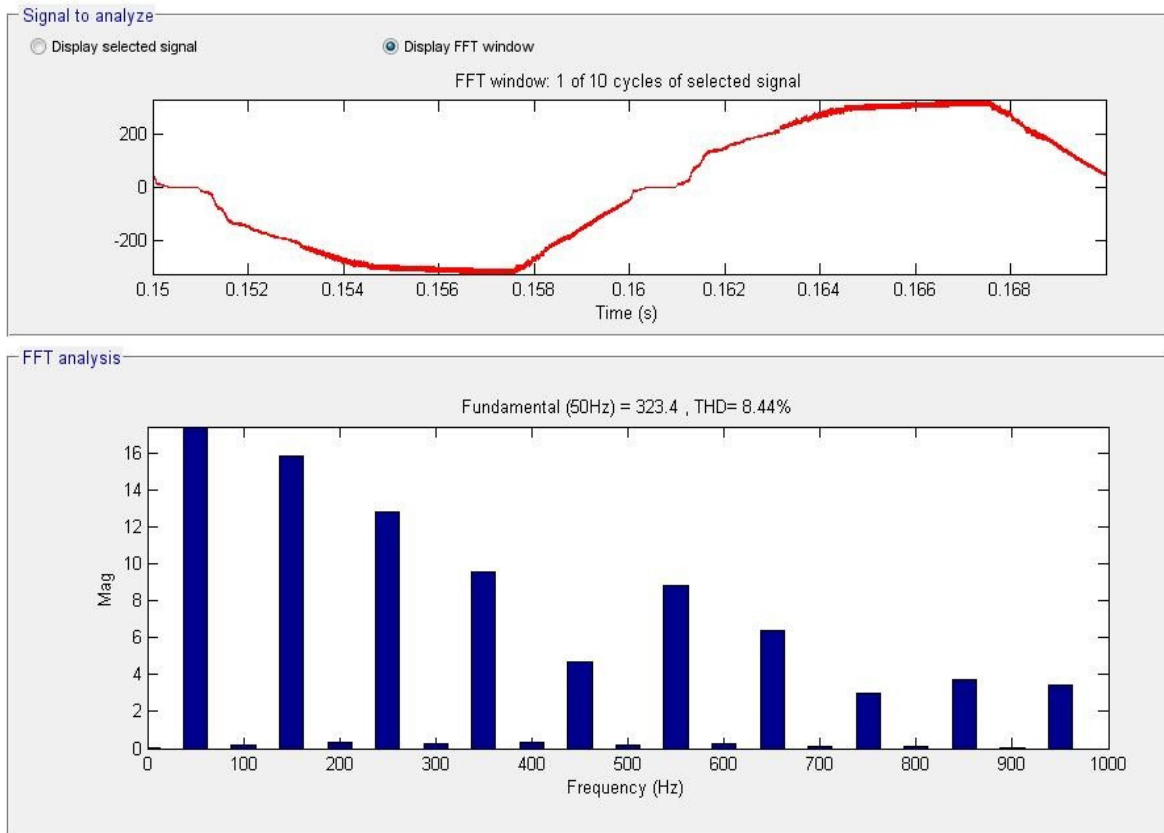
Fig. 2.106. FFT for voltage measured after EMI filter within 0 to 1 [kHz] range
for the Boost IL topology.
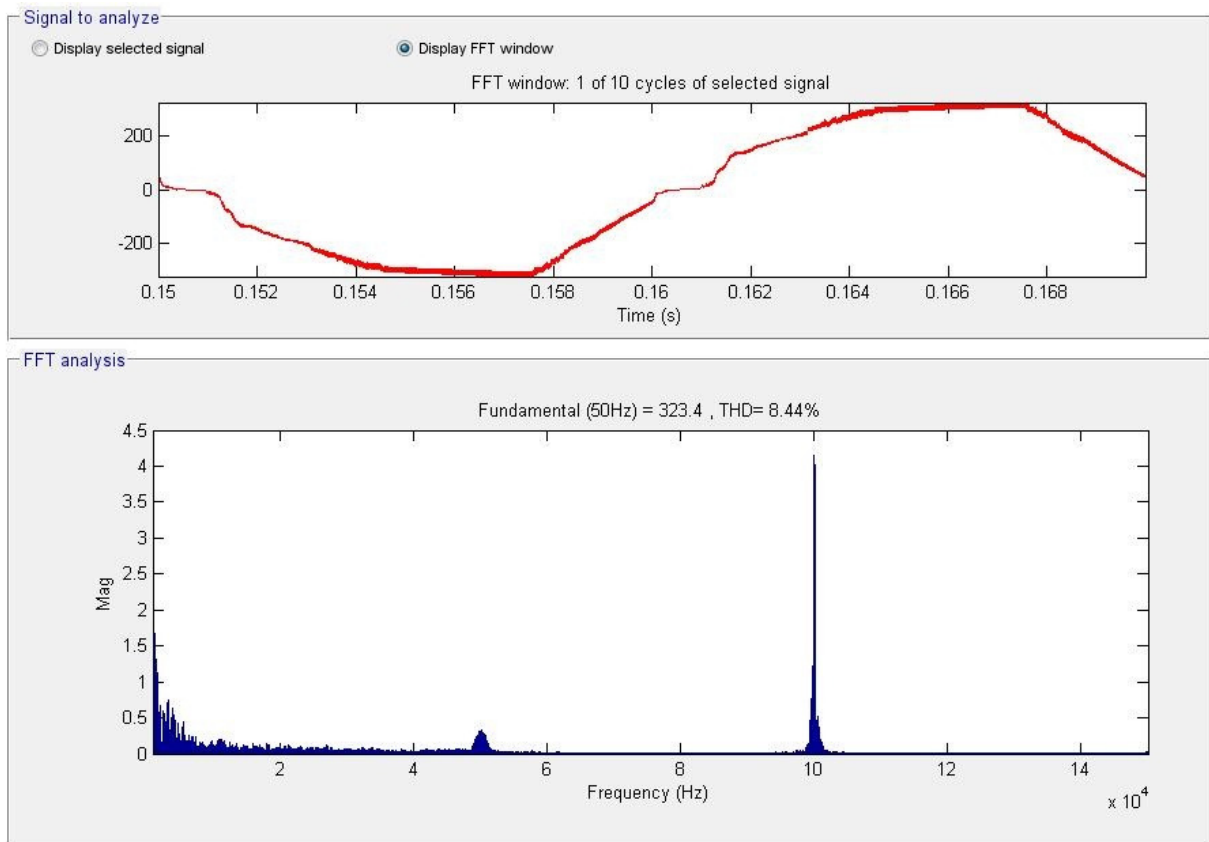
Fig. 2.107. FFT for voltage measured after EMI filter within 1 to 150kHz range
for the Boost IL topology.
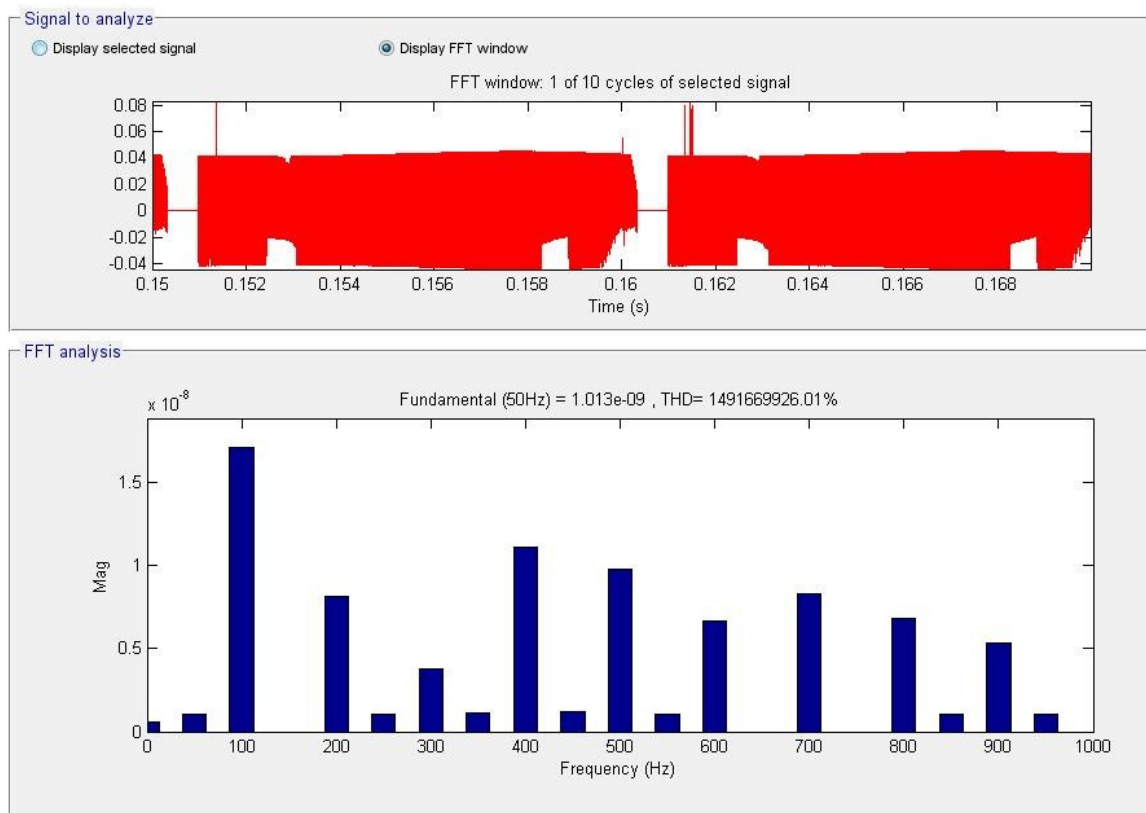
Fig. 2.108. FFT current between C and ground within 0 to 1kHz range for the Boost IL topology.
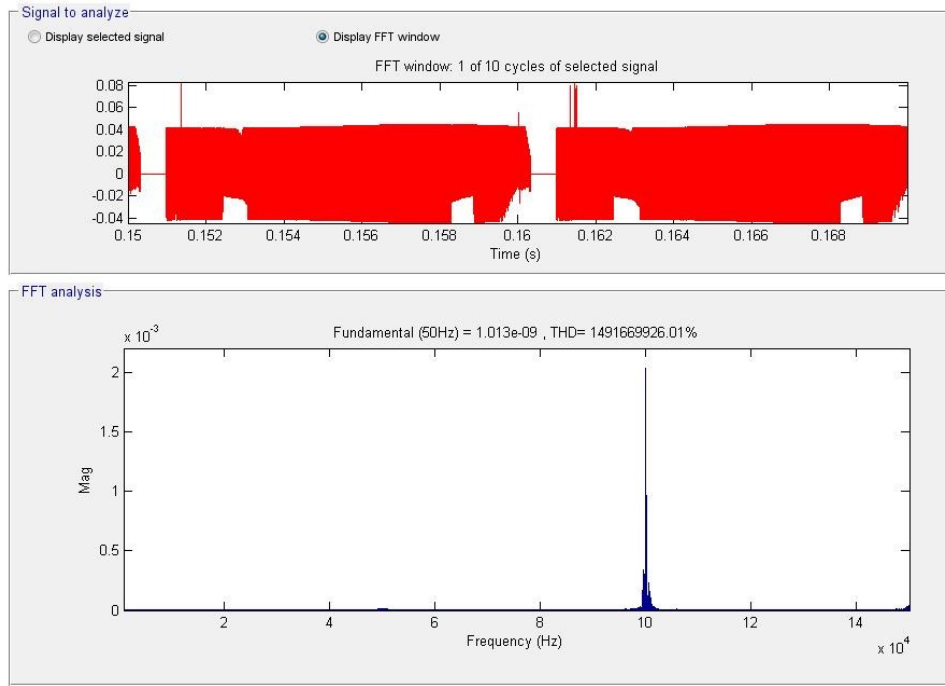
Fig. 2.109. FFT current between C and ground within 1 to 150kHz range for the Boost IL topology.

Table 2.11. Rms & Avg Values [A]

	RMS	**AVG**
I_{mosfet} **[A]**	4.088	9.226
I_{diode} **[A]**	0.4393	0.3881
I_{ac} **[A]**	11.68	0.007998

Table 2.12. Breakdown of Losses at Nominal Load [W]

P_{diode}/1device [W]	P_{mosfet} COND/1device [W]	P_{mosfet} SW/1device [W]	P_{cu}/1device [W]	P_{out} [W]	P_{in} [W]
0.02277	6.349	2.07	6.85	2474	2705

b. Simulation results for the Bridgeless Interleaved Power Factor Correction Converter

Similar operation conditions and parameters as for the interleaved boost PFC converter case are assumed in here also, with the only mention that now the four inductances $L_1 = L_2 = L_3 = L_4 = 300$ [µH]. Therefore, a comparison between the two converter topologies could be done. The parameters of PI controller are: $k_p = 0.05e-3$, $k_i = 0.01$.

Waveforms of the input voltage, input current, current through one inductor, current per one diode, sensed current per one MOSFET device and PFC bus voltage of the converter are provided in Figure 2.110 – Figure 2.116.

The reference and the regulated DC voltage is shown in Figure 2.115.

The efficiency of the simulated model of the interleaved boost converter is depicted in Figure 2.116.

A Fast Fourier analysis of the input current waveform, input voltage waveform and of the current between the DC capacitor C and ground is provided as depicted in Figure 2.117 – Figure 2.122. Similar conditions for the FFT were employed: 25 cycles of the selected signal and two frequency ranges: from 0 to 1 [kHz], respectively from 1 [kHz] to 150 [kHz] were taken into consideration.

Table 2.13 presents the RMS and average values for the MOSFET, diode and inductance. The losses for the bridgeless interleaved converter model, as per Table 2.14, were computed based on the same catalogue parameters for the MOSFET, diode and inductance devices, as used in the previous paragraph: $R_{mosfet} = 0.38$ [Ω], $R_{diode} = 0.118$ [Ω] and $R_{cu} = 0.075$ [Ω].

Table 2.13. Rms & Avg Values [A]

	RMS	**AVG**
I_{mosfet} **[A]**	5.535	1.482
I_{diode} **[A]**	6.229	2.539
I_{ac} **[A]**	11.88	0.0202

Table 2.14. Breakdown of Losses at Nominal Load [W]

P_{diode}/**1device** [W]	P_{mosfet} **COND/1device** [W]	P_{mosfet} **SW/1device** [W]	P_{cu}/**1device** [W]	P_{out} [W]	P_{in} [W]
4.578	11.64	2.412	5.178	2538	2730
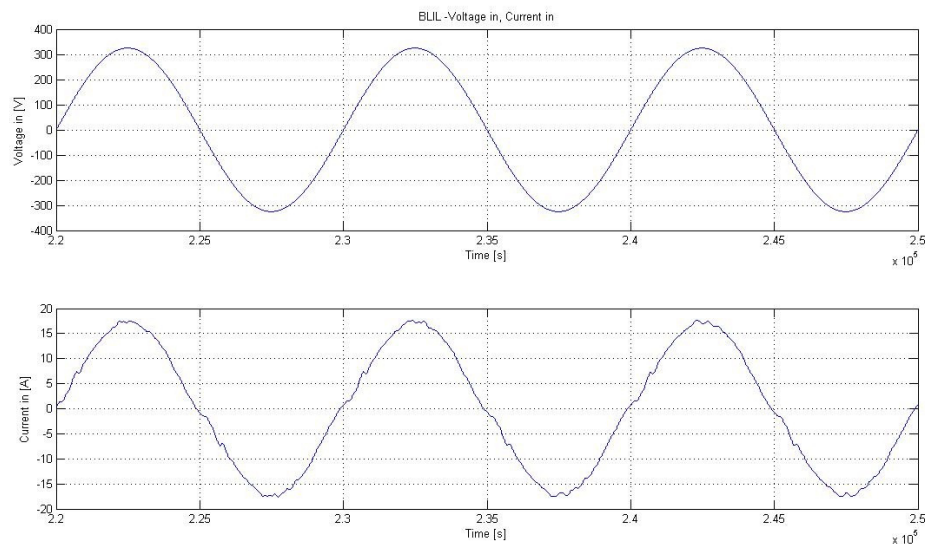
Fig. 2.110. Zoom on input voltage & input current for the Bridgeless IL topology.
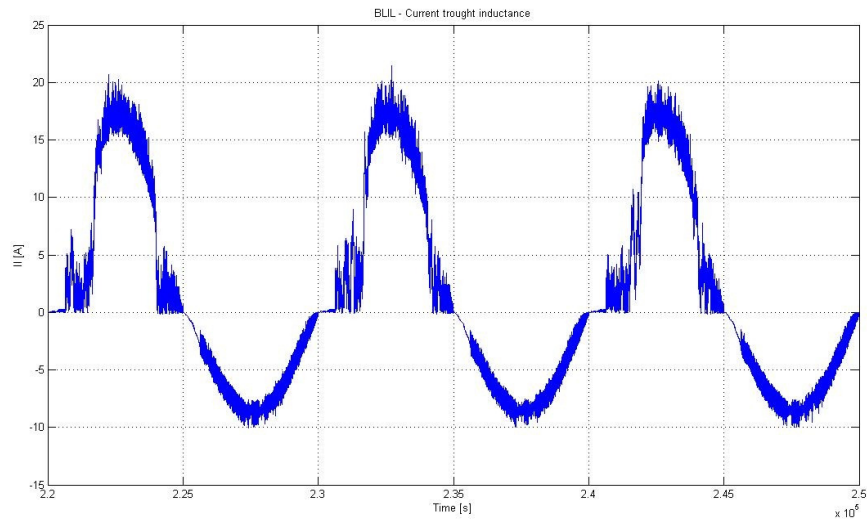
Fig. 2.111. Zoom on inductance current for the Bridgeless IL topology.
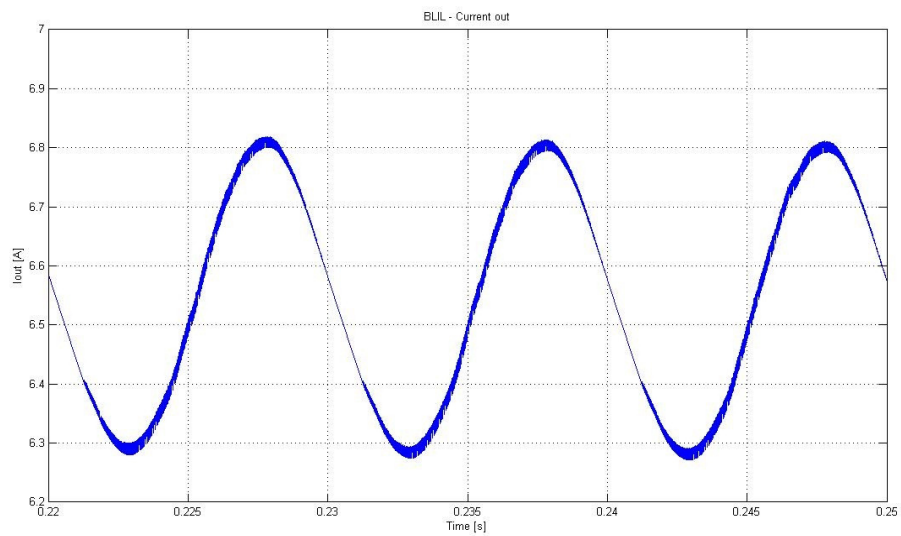
Fig. 2.112. Zoom on capacitor current for the Bridgeless IL topology.
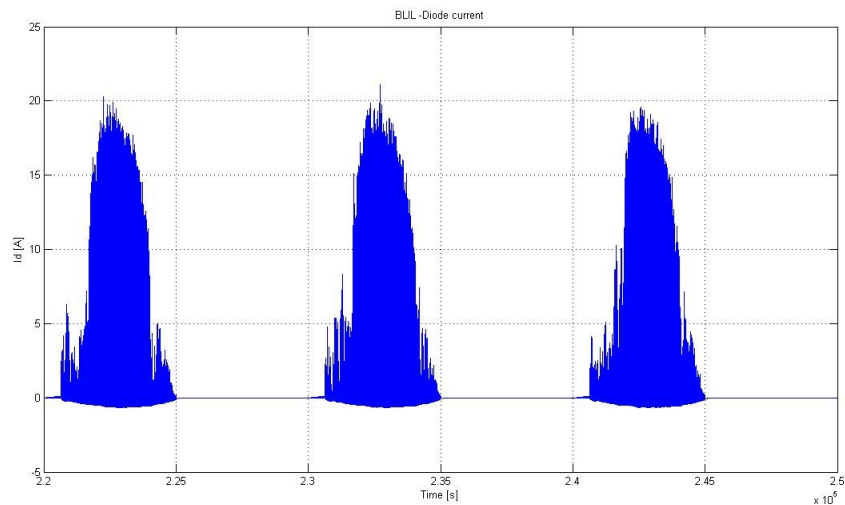
Fig. 2.113. Zoom on diode current for the Bridgeless IL topology.
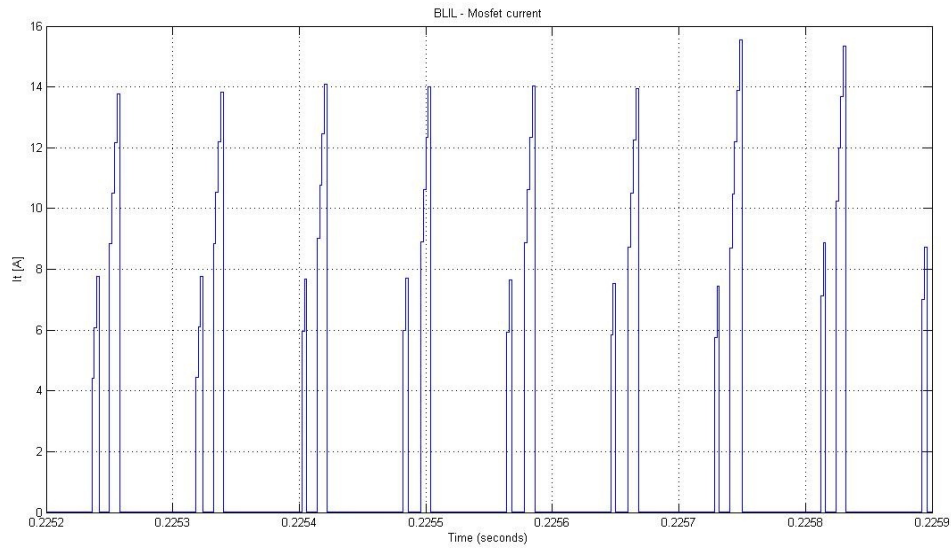
Fig. 2.114. Zoom on Mosfet current for the Bridgeless IL topology.
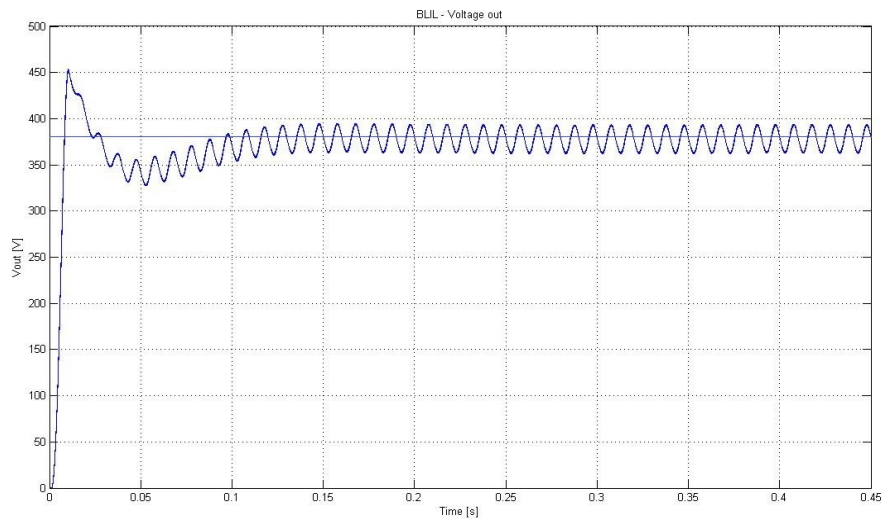
Fig. 2.115. Voltage output for the Bridgeless IL topology.
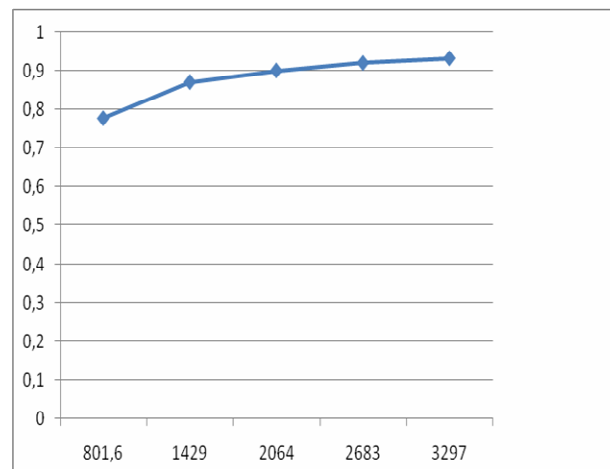
Fig. 2.116. Efficiency versus power curve for the Bridgeless IL topology.
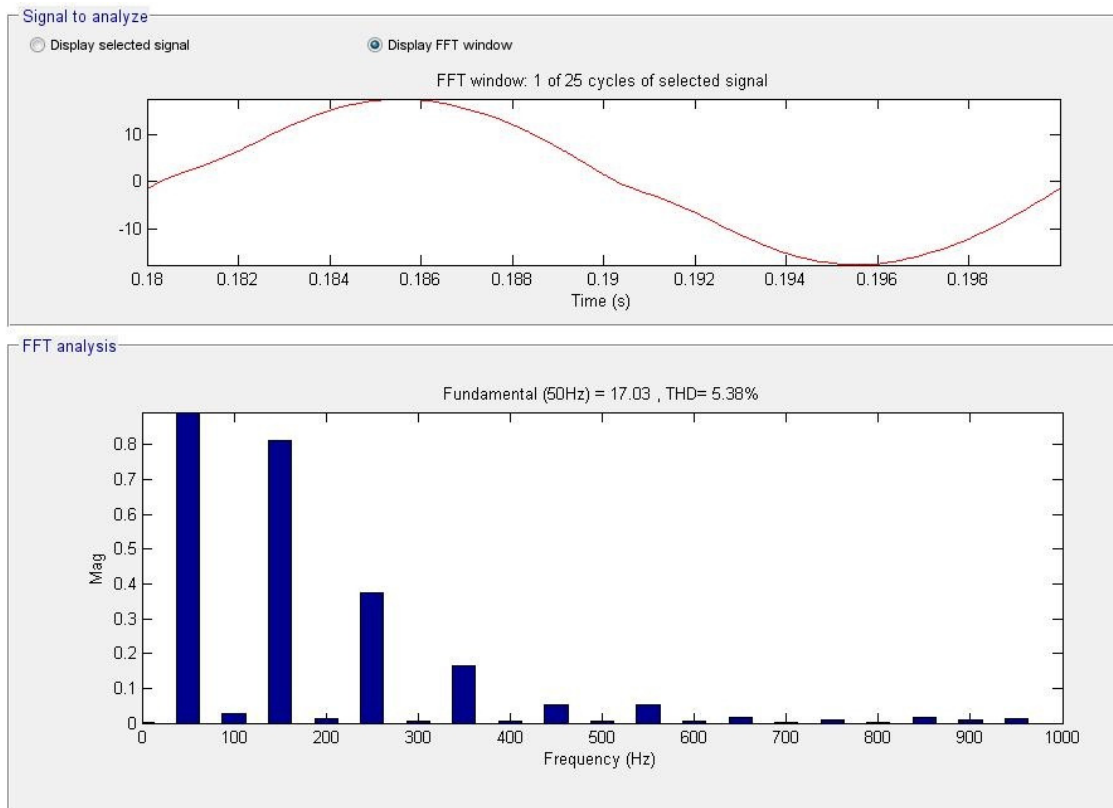
Fig. 2.117. FFT for input current range from 0 to 1kHz for Bridgeless IL topology.
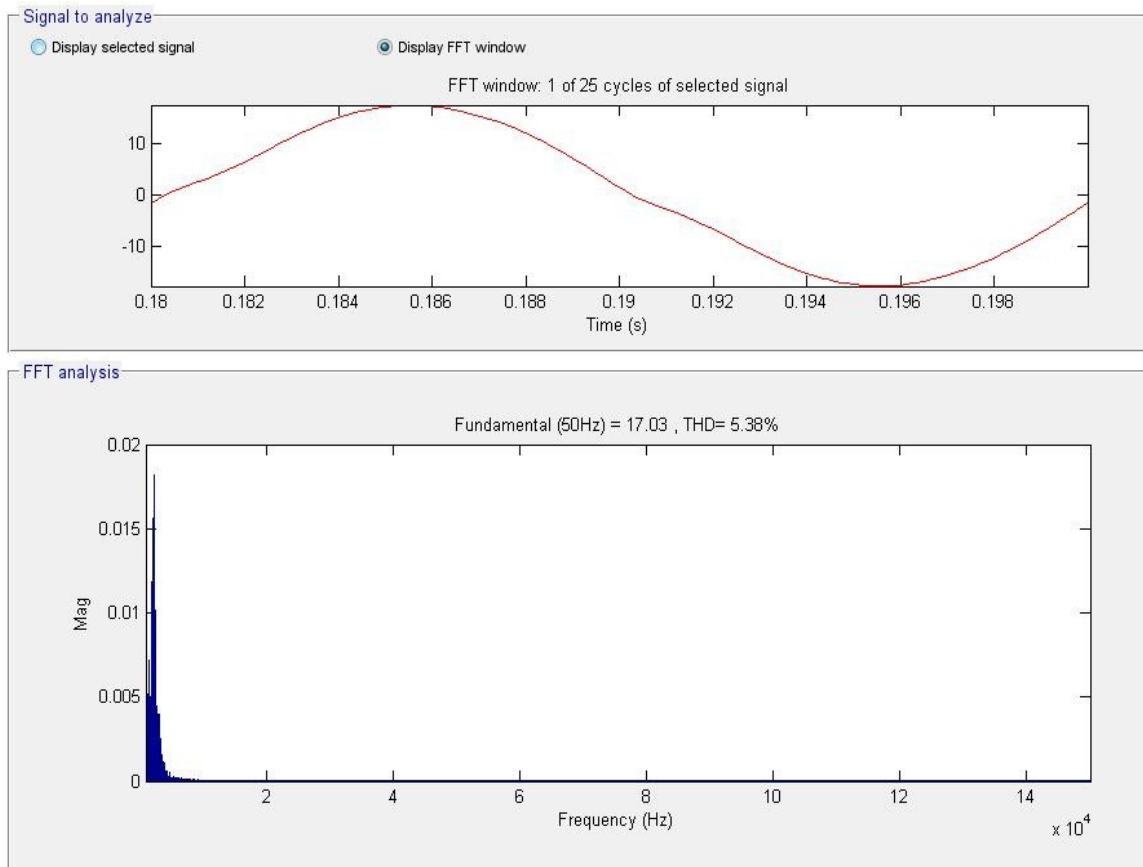
Fig. 2.118. FFT for input current range from 1 to 150kHz for Bridgeless IL topology.
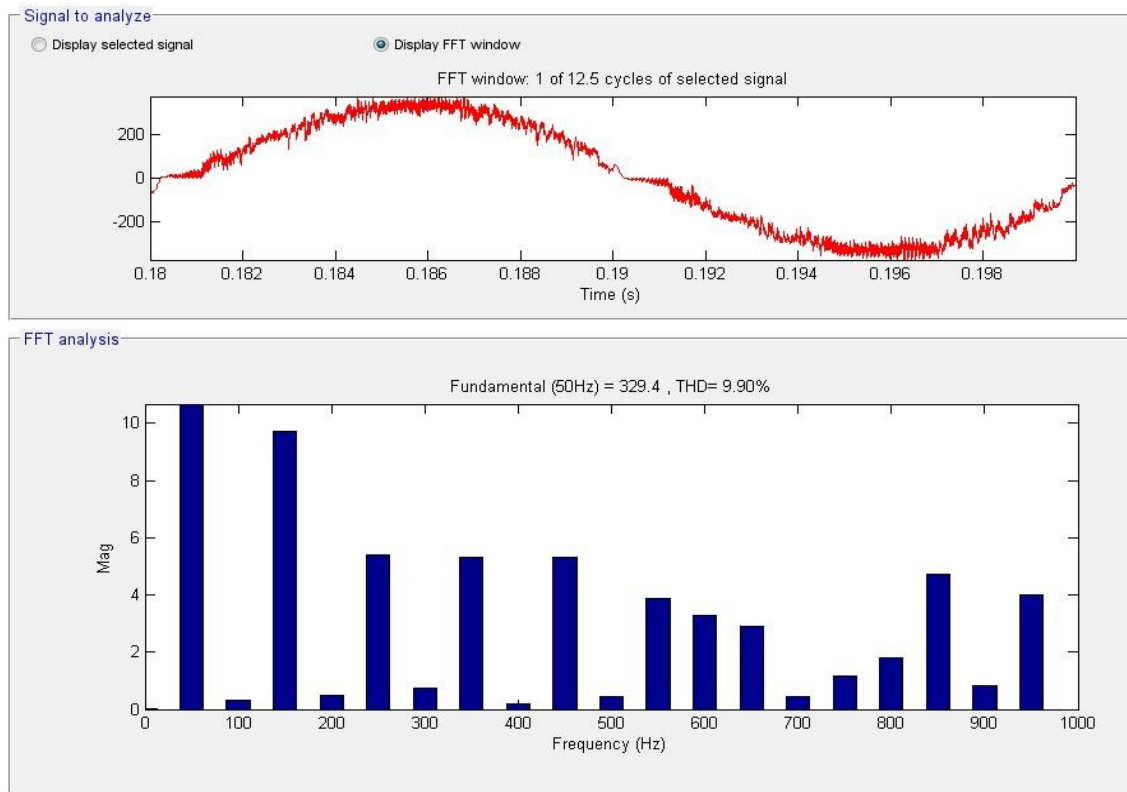
Fig. 2.119. FFT for voltage measured after EMI filter within 0 to 1kHz range
for the Bridgeless IL topology.
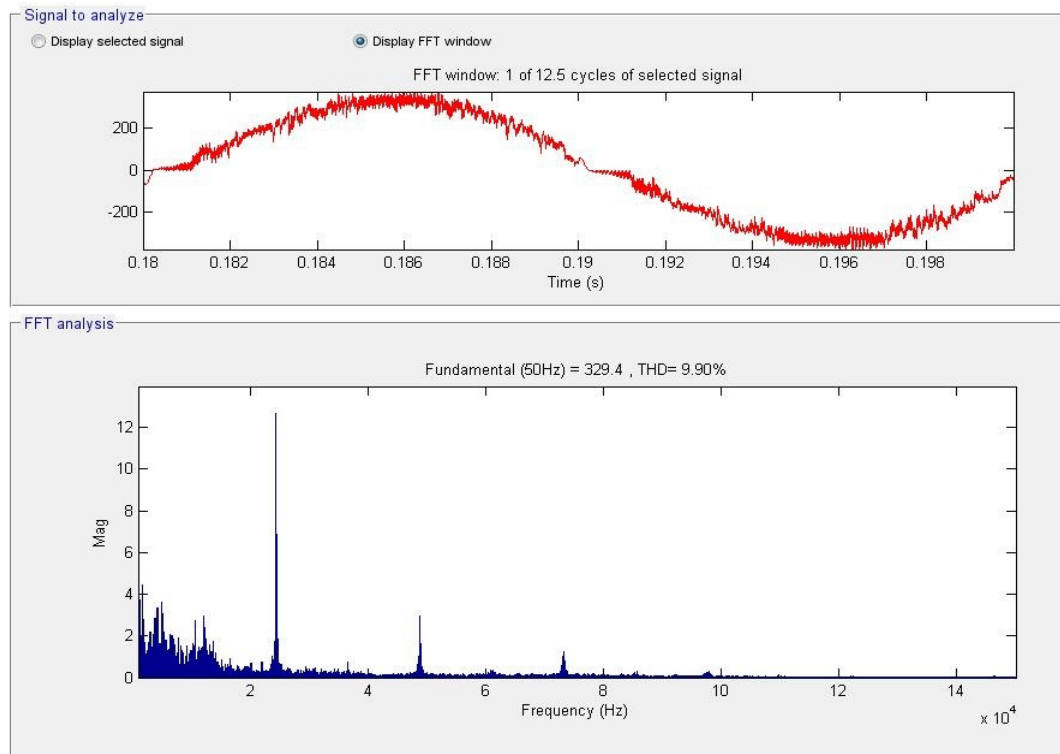
Fig. 2.120. FFT for voltage measured after EMI filter within 1 to 150kHz range
for the Bridgeless IL topology.

114
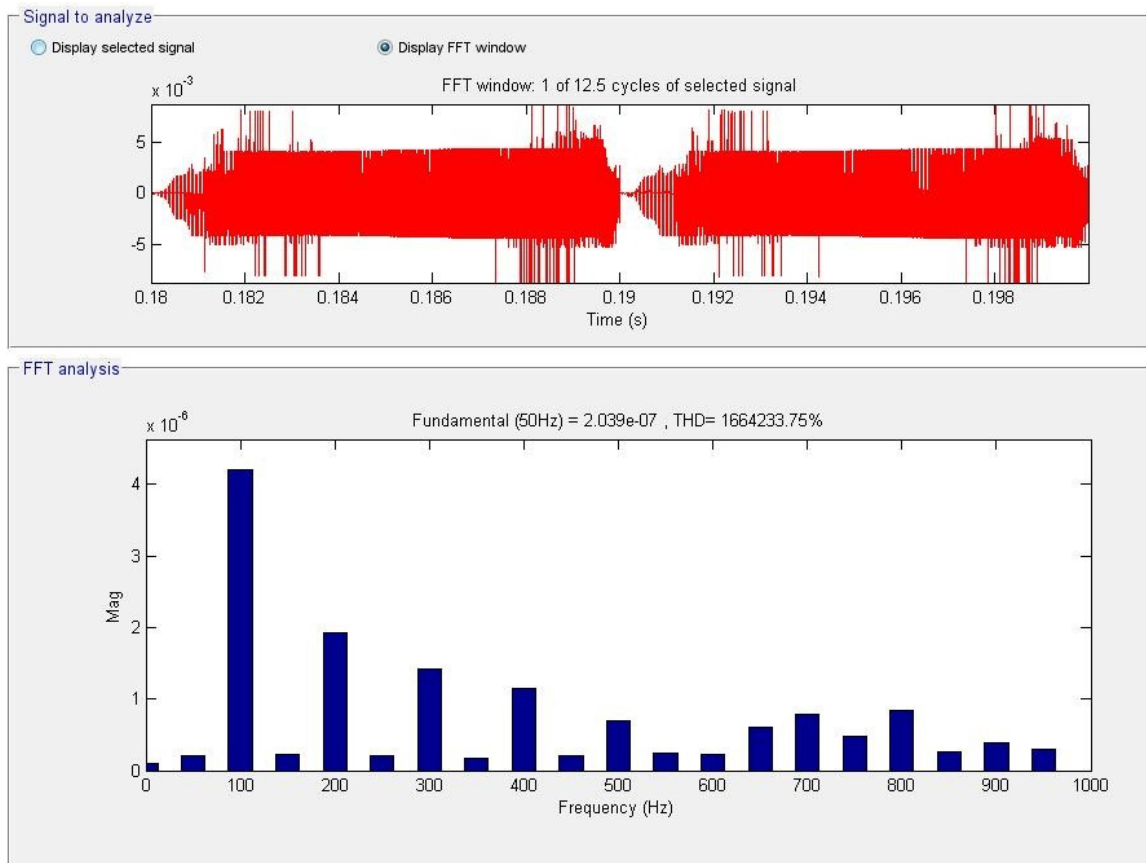
Fig. 2.121. FFT current between C and ground within 0 to 1kHz range
for the Bridgeless IL topology.
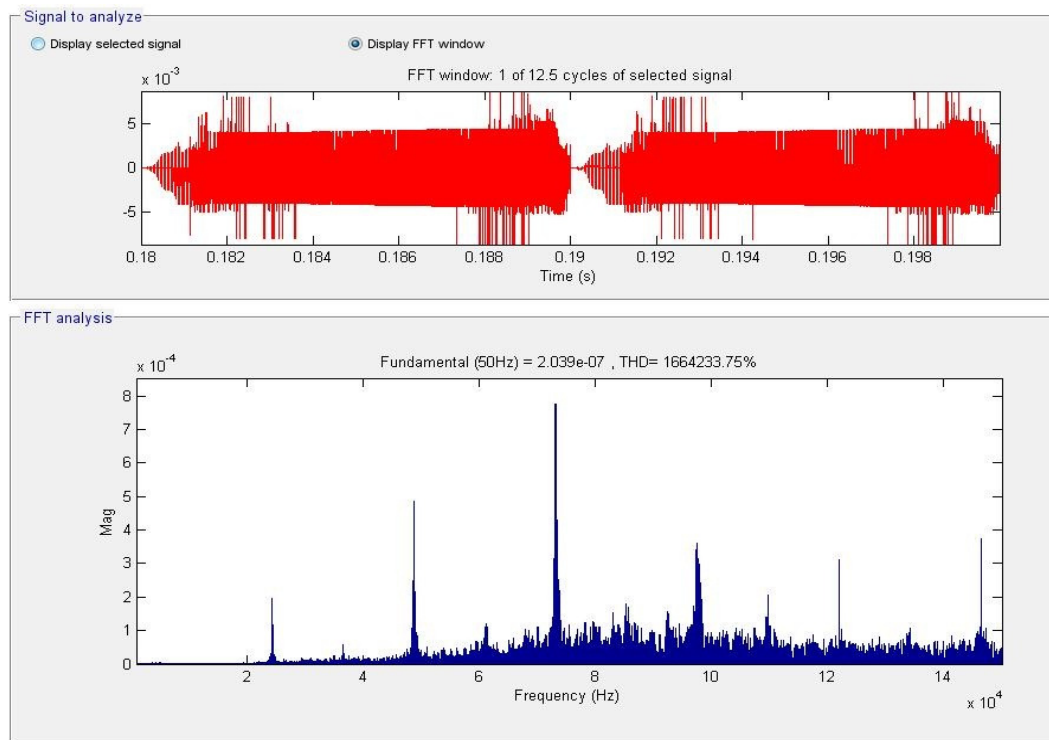
Fig. 2.122. FFT current between C and ground within 1 to 150kHz range
for the Bridgeless IL topology.

2.4.2.5. Conclusion

In this paper, firstly, a study of the PFC topologies existent in the literature has be done by our team. Thus, it was simple to choose which topologies have to be investigated for power application ranges up to 4 [kW]. As result, the interleaved boost PFC and the bridgeless interleaved PFC converters seemed to be the suitable ones.

The research deals with their *design implementation of both hardware and control parts in Matlab/Simulink simulation environment and finally with their performances evaluation and EMI Fast Fourier analysis by comparison*.

Simulation results, run for the same operation mode, show that the input current is in phase with the input voltage, and its shape is nearly perfectly sinusoidal, as expected, for both topologies.

In the interleaved boost PFC topology, the input current is the sum of the two inductor currents. It can be noted, that for interleaved topology, the currents flowing through the two inductors are 180° phase-shifted. Thus, the total input current has smaller ripple than in each individual inductor.

Comparing the two efficiency curves versus power for both topologies, it results that for the bridgeless interleaved topology there is a slightly gain in efficiency. So, in conclusion, interleaving and paralleling power converters can increase the efficiency of the power converter; as long as, the inductor ripple currents are kept within reason. The semiconductor switching losses will remain roughly the same.

The freedom from harmonics also minimizes electromagnetic interference (EMI) with other devices being powered from the same source. Another reason to employ PFC in many of today's power supplies is to comply with regulatory requirements.

Nowadays, electrical equipment in Europe must comply with the European EN 61000−3−2, or EN 61000-3-4 Norms. This requirement applies to most electrical appliances.

Choosing of the right parameters of the common mode and EMI filters, based on literature, is also provided, as well as their implementation in Matlab/Simulink. Simulation results show that they are compliant with international standards. Compared to the interleaved boost PFC converter (at equal power), the reduced ripple in the input current for the bridgeless interleaved PFC converter decreases the conducted-EMI noise and helps reducing the EMI filter size.

Further experimental results from the two prototypes studied in here will be presented by our team in a next-future research study.

2.5. Development

In the next period, my activity will focus on the three consecrated directions presented above: *research activity, teaching and professional development, university management activities.*

My future **research activity** will follow three main study areas: *The optimal design of AC motors, The optimal control of electrical drives and* the *Three-phase power factor correction converters.*

In the domain of the *Optimal design of AC motors*, I shall address two areas: *(i) the optimal design of induction machines fed by PWM voltage inverters; (ii) the optimal design of ferrite magnets-assisted variable reluctance synchronous machines.*

The studies in the first area, (i*) Optimal design of induction machines fed by PWM voltage inverters*, will be based on the theoretical and experimental studies conducted so far. They were commenced in the doctoral thesis and continued by the subsequent studies undertaken together with my research team and presented in detail in Section 2.2.1 of the habilitation thesis. I mainly aimed to achieve a substantial theoretical and experimental foundation for the definition and analysis of the three-phase induction machine fed by PWM inverters as follows: we determined the expressions of calculating the two factors, the changing factor of resistance in alternative current $k_{r(CSF)}$ and the reactance $k_{x(CSF)}$, corresponding to the situation when the motor is fed by PWM inverters under a global form. The relations of stator and rotor windings parameters were calculated in the context of considering the real repression that occurs in the presence of non-sinusoidal regime. The changes suffered by the motor parameters under the above mentioned conditions were also highlighted in comparison with the sinusoidal supply regime. A mathematical model has been developed allowing a simplified study of the induction machine fed by PWM inverter. We considered various rotor geometries, including those for high rectangular bars. The theoretical research conducted so far has been experimentally verified and it is based on software support, namely CALCMOT computing program, which enables the determination of the parameters from the mathematical model. All these results represent a solid starting point for the future research that aims to establish the optimal constructive-technological design criteria and measures to be followed in order to improve the parameters and the functional dimensions of the three-phase induction motors fed by PWM inverters. This under the conditions that the vast majority of the studies conducted both nationally and globally, mainly targeted the converter. The design method that I will study has to satisfy the functional criterion (making a motor with some technical features required by the customer); the safety criterion (providing a safe behavior of a machine operating under nominal and short-term overloads conditions) and the economic criteria (constructing a machine at a minimum total cost taking into account both the constructive-technological and exploitation expenses). Considering these requirements, I will continue the implementation of the study in an international project with an machine manufacturer from Slovenia. This project is in the planning stage, based on the request of the manufacturer, at feasible production cost of the final product, using these motors.

The studies in the second domain of the first area of research, (ii) *The optimal design of ferrite magnets-assisted variable reluctance synchronous machines,* will represent the further development of the study undertaken so far, summarized in Section 2.2.2. There are presented and analyzed the results for two different permanent magnet assisted synchronous reluctance motor (PMSynRM), in which the rotor is made of a row of flux-barriers 1V, respectively with two rows

of flux-barriers 2V and a variant of rotor machine with flux concentration. The latter solution was carried out practically in two constructive variants. These options are destined to fit the washing machines manufactured by the collaborating firm, intending to replace the permanent rare earth magnet assisted synchronous reluctance motor, the solution currently used and which significantly increases the production cost of the product. In the next period, we will develop practical tests of the implemented variants as driving machine in the structure of the washing machine. The behavior in time of the characteristics of ferrite magnets will be especially monitored. Future research in this sub domain will focus on optimizing the design of PMSynRM. In this future research, various key points in the rotor design of a low-cost permanent-magnet-assisted synchronous reluctance motor (PMSynRM) will be introduced and their effects will be studied. To fulfill this main aim, different rotor parameters and their relative effects on the motor performance in terms of output torque and saliency ratio will be studied. The design will be carried out using the two-dimensional FEM, using finite element software. The PMSynRM rotor structure must be designed in such a way that it is possible to achieve the maximum torque per current ratio. This ratio will become the objective function to be applied to the optimization method. For the computing software that will be developed, Hooke-Jeeves algorithm will be used as appropriate for the given application. It is known that Hooke-Jeeves method selects the search directions in a manner that adapts to the form of the function to be minimized. The calculation method used to evaluate the torque will take into account the effect of cross saturation between the *d-* and *q*-axes inductances. In this research, an FEM approach will be performed to analyze the effects of rotor design variables such as the flux-barrier width, flux-barrier location, insulation ratio, pole-span over pole-pitch ratio, and length of the radial and tangential ribs on PMSynRM performance. A systematic procedure will be applied to obtain the optimized geometry for rotor flux barriers. This research direction will be implemented in a new international project concluded with the German company Diehl at their request.

In the second area, *The optimal control of electric drives,* I will address a new research direction in the area of the sensorless control of the Switched Reluctance Motor (SRM).The motivation for introducing this theme is given by a few reasons summarized below. Switched reluctance motor (SRM) drives continue to penetrate the growing market of adjustable-speed motor drives. The SRM drives have been found to be suitable for automotive applications, household goods, electric vehicles (EVs) and hybrid electric vehicles (HEVs), compressors, etc. Rotor position detection is an integral part of SRM control because of the nature of reluctance torque production. In fact, excitations of the SRM phases need to be properly synchronized with the rotor position for effective control of speed, torque and torque ripple. A shaft position sensor is usually used to provide the rotor position. Adding discrete position sensors not only adds complexity and cost to the system, but also tends to reduce the reliability of the drive system. Also, there are certain applications, where the ambient conditions do not allow the use of external position sensors and, in these cases sensorless technique should be applied. In this future research, the team will propose new methods to estimate rotor position and speed of SRM drives. For the beginning, a flux linkage method and dual layer controller will be developed for an application with a low-voltage Switched Reluctance Motor (SRM) drive. The basic concept of this application is that of a sensorless speed closed loop with an inner current loop using flux linkage position estimation. The voltage drop on the power devices is more significant in case of low voltage then in case of the high voltage drive. This voltage drop needs to be considered the algorithm which will be also developed. To ensure a sure operation, a startup algorithm will be also included. The proposed method will be implemented and tested by using a digital signal processor 56F807EVM from Freescale Semiconductor Company and an 8/6 switched reluctance motor coupled with a brushless DC motor as load.

The research in the field of *Power factor correction converters* will continue in an international project, currently in progress. The contract was signed in early 2014 with the German company Diehl, with the theme of *Analysis and Evaluation of Current Topologies and Solutions for three phase Power Factor Correction (PFC) for 400 V mains voltage,* BCI 1/24.01.2014. I participated in this project as a manager. The research deals with the design study of actual topologies for the power range of 1.5 [kW] up to 10 [kW], selected from a state-of-the-art from literature. The following topologies should be considered: passive PFC- single diode bridge rectifier system (with smoothing inductor on the ac/dc side, passive 3-rd harmonic injection, multi-pulse rectifier system; low-frequency active PFC; hybrid systems- 3-rd harmonic injection, combination of diode rectifier and dc/dc converter system (buck type – for 350 V dc bus, boost type), electronic reactance based rectifier system; high-frequency active PFC- phase modular system, direct three-phase system (buck type for 350 V dc bus, boost type). The evaluation will be done in regards to electromagnetic compatibility (EMC) requirements. The next step will be the implementation of their hardware and control parts in Matlab/Simulink simulation environment and finally with their performances evaluation and electromagnetic interference EMI analysis using comparison. Loss analysis and efficiency evaluation will also be provided. The results must be compliant with international standards, the European EN 61000−3−2, or EN 61000-3-4 Norms.

The publication of the results to be obtained will be oriented towards internationally recognized journals, especially ISI indexed. The outcomes will be disseminated through international conferences, international events that are intended for information and best practices.

I will continue my activity as a reviewer and member of the editorial staff of the *International Journal of Electromagnetic and Applications* and the *American Journal of Electrical and Electronic Engineering*. In the near future I will respond to the invitation from the Editorial Assistant from the *Scientific & Academic Publishing* (SAP), USA to be the Editor of the Special Issue of the *Journal of Computer & Electrical Engineering*.

My future **teaching activity** will be closely related to the planned research activity. The confirmed results of my research will represent the foundation of the development of the courses I teach: *Electric drives,* respectively *Electric servomotors and the intelligent motion control.* My courses themes will be closely related to the presentation of new knowledge, with direct application in the productive activity on the international market. The research activity will result in the development of two new specialty books in the areas presented above.

The topics of the graduation and master thesis I will coordinate will be in strong connection with the research and teaching activity described so far. The results obtained will be routed to the development of scientific papers presented in prestigious scientific conferences. The funds obtained through research will provide new stands in the laboratory electric drive.

I shall contribute to the institutional development of the faculty by involving the students in the research team, respectively in the implementation of the projects, thus facilitating their participation in international conferences, a requirement for admission in doctoral studies.

My **managerial activity** will be oriented towards the cultivation of the faculty's human resources, focusing on attracting the graduates with didactic and proved research potential and towards the development of the necessary material basis for the research activity.

3. REFERNCES

3.1. Section 2.2.1

[1] Bitoleanu A, Ivanov S., Popescu M., *Convertoare statice,* Editura INFOMED, Craiova, 1997.

[2] Muşuroi S., *Maşina de inducţie alimentată prin convertoare statice de frecvenţă*, Editura Eurostampa, nr. pp. 140, ISBN 978-606-569-815-4, 2014.

[3] Mohan N., Underland M.T., Robins P.W., *Power Electronics: Converters, Applications and Design,* John Wiley & Sons, New-York, 1994.

[4] Murphy J., Turnbull F., *Power Electronic Control of AC Motors,* Pergarmen Press, British Library, London 1988.

[5] Popovici D., *Bazele convertoarelor statice,* Editura Politehnica, Timişoara, 1999.

[6] Muşuroi S., Popovici D., *Acţionări electrice cu servomotoare,* Editura Politehnica, Timişoara, 2006.

[7] Seracin E., Popovici D., *Tehnica acţionărilor electrice*, Editura Tehnică, Bucureşti, 1985.

[8] Rui Estevez Araujo, Muşuroi S., sa., *Induction motor. Modelling and control , Chapter 2. The Behavior in Stationary Regime of an Induction Motor Powered by Static Frequency Converters*, pp. 45 – 72, Editura InTech Europe, Rijeka, Croaţia, ISBN 979-953-307-716-0, 2012.

[9] Horga V., Onea A., Diaconescu M., *A Method for Parameters Estimation in Induction Motor Drives*, 6th WSEAS International Multiconference on Circuits, Systems, Communications and Computers (CSCC 2002) Rethymno, Crete, Greece, July 7-14, pp. 444-411, 2002.

[10] Marungsri B., Meeboon N., Oonsivilai A., *Dynamic Model Identification of Induction Motors using Intelligent Search Techniques with taking Core Loss into Account*, Proceedings of the 6th WSEAS International Conference on Power Systems, Lisbon, Portugal, September 22-24, pp. 108-115, 2006.

[11] Muşuroi S., Olărescu N. V., Vătău D., Şorândaru C., *Theoretical and Experimental Determination of Equivalent Parameters of Three-Phase Induction Motor Windings in Case of Power Electronic Converters Supply*, WSEAS Transactions on Systems, Volume 8, Issue 10, October, pp. 1115-1124, 2009.

[12] Muşuroi S., Şorândaru C., Olărescu N. V., Svoboda M., *Mathematical Model Associated to Three-Phase induction Servomotors in the Case of Scalar Control*, WSEAS Transactions on Systems, Volume 8, Issue 10, October, pp. 1125-1134, 2009.

[13] Muşuroi S., Olărescu N. V., *The Equivalent Factors Determination of Rotor Parameters Modification In Case of Cage Induction Motors Supplied By Static Frequency Converter*, Applied Research Review on Technology and Automation, Athens Piraeus, Greece, Vol. I, No.1, pp. 363-366, 2000.

[14] Muşuroi S., Bogoevici Gh., *Theoretical Aspects Regarding the Penetration Deepness of the Electromagnetic Field in Rotor Bars, Placed in Randomised Slots, in Case of Induction Motors, Having as Source of Supply the Static Frequency Converters*, Buletinul Institutului Politehnic Iaşi, Conferinţa Internaţională de Inginerie Electrică şi Energetică, EPE-ETH 1999, Iaşi, Tomul XLV(IL), Fasc. 5, pp. 202-205, 1999.

[15] Muşuroi S., Olărescu N. V., Vătău D., Şorândaru C., *Equivalent parameters of induction machines windings in permanent regime.Theoretical and experimental determination*, Proceedings of the 9th WSEAS International Conference on POWER SYSTEMS (PS '09), Budapest Tech, Hungary, 3-5 Septembrie, pp. 55-62, 2009.

[16] Muşuroi S., Şorândaru C., Olărescu N. V., Svoboda M., *Mathematical Model of Three-Phase Asynchronous Servomotors in Stationary Non-sinusoidal Regime*, Proceedings of the 9th

WSEAS International Conference on POWER SYSTEMS (PS '09), Budapest Tech, Hungary, 3-5 Septembrie, pp. 123-126, 2009.

[17] Muşuroi S., Vătău D., Andea P., Şurianu F., Frigură-Iliasa F., Bărbulescu C., *Analysis of the Magnetic Losses from the Induction Machines Supplied by Inverters,* Proceedings of The International Conference on Computer as a Tool, IEEE Region 8, EUROCON 2007, Warsaw, Poland, 9-12 Septembrie, pp. 1800-1809, 2007.

[18] Muşuroi S., Svoboda M., Şorândaru C., Koblara Th., Olărescu N. V., *Deep bar effects produced by PWM power supplies in induction machines: Application to rotor Parameters determination*, Conference Proceeding of International Conference on Computer as a Tool - Joint with Conftele, EUROCON 2011, Lisbon, Code 85630, 27 - 29 Aprilie, art. no. 5929282, 4 pagini, 2011.

[19] Muşuroi S., Bogoevici Gh., *The Determination of the Equivalent Modification Factors of the Rotoric Parameters whit the Cage Induction Motors are Being Supplied by Inverters*, Conference Record of the 15th International Conference on Electrical Machines ICEM 2002, Bruges, 25-28 August, Index 367, D 2002/0277/3, pp. 238 BOOK OF ABSTRACTS, 2002.

[20] Muşuroi S., Olărescu N. V., *The Mathematical Model for Three-Phase Cage Induction Motors Supplied by Static Frequency Converters*, Proceedings of the International Aegean Conference on Electrical Machines and Power Electronics, Acemp 2001, Kuşadasi, Turkey, 27-29 Iunie, pp. 260-264, 2001.

[21] Măgureanu R., Micu D., *Convertizoare de frecvenţă în acţionări cu motoare asincrone,* Editura Tehnică, Bucureşti, 1985.

[22] Cioc I., Bichir N., Cristea N., *Maşini electrice. Îndrumar de proiectare,* Vol. II*,* Editura Scrisul Românesc, Craiova, 1981.

[23] Dordea T., *Maşini electrice,* Editura didactică şi pedagogică, Bucureşti,1977.

[24] Muşuroi S., Madescu Gh., Moţ M., Greconici M., *The Analysis of the Skin Effect in the Deep Bars of the Rotors of the Induction Motors Supplied by Inverters*, Proceedings of the 8th International Conference on Applied Electromagnetics PES 2007, Nis, Serbia, 3-5 Septembrie, 6 pages, ISBN 978-86-85195-43-8, 2007.

[25] Şora C., *Bazele electrotehnicii,* Editura Didactică şi Pedagogică, Bucureşti, 1982.

[26] Chioreanu V., *Materiale electrotehnice*, I.P.T.V.T., Timişoara, 1983.

[27] Dordea T., Biriescu M., *Proiectarea maşinilor electrice*, Volumul 1-1, IPTVT, Facultatea de Electrotehnică, Timişoara, 1992.

[28] Muşuroi S., Olărescu N. V., *The Determination of Equivalent Total Factors for Rotoric Parameters Modification in the Case of Cage Asyncronous Motor Supply with Static Converter*, International Conference on Applied And Theoretical Electricity – ICATE 2000, Craiova, 25-26 Mai, pp. 378-381, ISBN 973-657-005-3, 2000.

[29] Muşuroi S., *Influenţa efectului pelicular asupra modelului matematic asociat motoarelor asincrone trifazate cu rotorul în colivie alimentate de la reţea prin intermediul convertoarelor statice de frecvenţă*, A doua Conferinţă Internaţională de Sisteme Electromecanice SIELMEN '99, Chişinău, Vol. I, 8-9 Octombrie, pp. 27-30, ISBN 9975-944-30-2, 1999.

[30] Muşuroi S., Bogoevici Gh., *Modelling and simulation of the equivalent factors for the rotor parameters' modification in three-phase asynchronous machines supplied through voltage inverters*, Buletinul institutului Politehnic Iaşi, Electrotehnică. Energetică. Electronică, IEEE Romanian Section, Tomul XLVIII(LII), Fasc. 5C, pp. 39-44, ISSN 0258-9109, 2002.

[31] Muşuroi S., Novac I., *Mathematical Model Associated to Low Power Cage Induction Motors Supplied by Static Frequency Converters*, Buletinul Ştiinţific al Universităţii „Politehnica" din Timişoara, Transaction on ELECTROTEHNICS. ELECTRONICS AND COMMUNICATIONS, Tom 42 (56), Fasc. 2, pp. 47-56, ISSN 1224 – 6034, 1997.

[32] Muşuroi S., *Consideraţii teoretice şi experimentale privind posibilităţile de îmbunătăţire a parametrilor maşinilor asincrone trifazate cu rotorul în scurtcircuit alimentate de la convertoare statice de frecvenţă*, Analele Universităţii „Eftimie Murgu" Reşiţa, Fasc. III, pp. 221-226, ISSN 1453-7394, 1996.

3.2. Section 2.2.2

[33] Muşuroi S., Şorândaru C., Greconici M., Olărescu N.V., Weinman M., *Low-cost ferrite permanent magnet assisted synchronous reluctance rotor an alternative for rare earth permanent synchronous motors*, Industrial Electronics Society, IECON 2013- 39th Annual Conference of the IEEE, 10-13 Nov. 2013, Vienna, pp. 2966-2970.

[34] Morimoto S., Sanada M., Takeda Z., Taniguchi K., *Optimum machine parameters and design of inverter driven synchronous motors for wide constant power operation*, in Conf. Rec. IEEE-IAS Annu. Meeting, 1994, pp. 177–182.

[35] Cross J., Viarouge P., *Synthesis of High Performance PM Motors with Concentrated Windings*, IEEE Transactions on Energy Conversion, vol. 17, no. 2, June 2002.

[36] Vagati A., Fratta A., Franceschini G., Rosso P.M., *A.C. motor for high performance drives: a design-based comparison*, IEEE Trans. On Industry Applications, Sept.-Oct. 1996, vol. 32, n. 4, pp. 1211-1219.

[37] Akita H., Nakahara Y, Miyake N., Oikawa T., *New Core Structure and Manufacturing Method for High Efficiency of Permanent Magnet Motors*, Rec. of 2003 IEEE Industry Applications Society Annual Meeting, vol. 1, Salt Lake City, UT, October 2003, pp. 367-372.

[38] Takeda Y., Matsui N., Oyama J., Domeki H., *Classification and technical term of reluctance motors from the viewpoint of control strategy and motor construction*, in Proc. JIASC'02, vol. 2, 2002, pp. 759–762.

[39] Lipo T.A., Vagati A., Malesani L., Fukao T., *Synchronous reluctance motors and drives-a new alternative,* IEEE-IAS Annual Meeting Tutorial, October 1992.

[40] Vagati A., Pastorelli M., Franceschini G., Petrache S.C., *Design of low-torque-ripple synchronous reluctance motors*, IEEE Trans. Ind. Appl., vol. 34, no. 4, pp. 758–765, Jul./Aug. 1998.

[41] Niazi P., Toliyat H.A., Cheong D.H., Kim J.C., *A Low-Cost and Efficient Permanent-Magnet-Assisted Synchronous Reluctance Motor Drive,* IEEE Transactions on Industry Applications, Vol.43, no2, (2007).

[42] Talebi S., Niazi P., Toliyat H.A., *Design of Permanent Magnet-Assisted Synchronous Reluctance Motors Made Easy*, Industry Applications Conference, 2007, 42nd IAS Annual Meeting. Conference Record of the 2007 IEEE, 23-27 Sept. 2007, pp. 2242 – 2248.

[43] Matsuo T., Lipo T.A., *Rotor design optimization of synchronous reluctance machine*, IEEE Trans. Energy Conversion, vol. 9, pp. 359–356, June 1994.

[44] Long S.A., Schofield N., Hawe D., Piron M., McClelland M., *Design of a switched reluctance machine for extended speed operation*, IEEE Proc. of IEMDC03, pp235-240.

[45] Armando E., Guglielmi P., Pastorelli M., Pellegrino G., Vagati A., *Accurate Magnetic Modelling and Performance Analysis of IPMPMASR Motors*, IEEE-IAS Annual Meeting, 23-27 Sept. 2007, New Orleans (USA), pp. 133 – 140.

[46] Bianchi N., *Electrical Machine Analysis Using Finite Elements*, ser. Power Electronics and Applications Series. Boca Raton, FL: CRC Press, 2005.

[47] Montalvo-Ortiz E.E., Foster S.N., Cintron-Rivera J.G., Strangas E.G., *Comparison between a spoke-type PMSM and a PMASynRM using ferrite magnets*, Electric Machines & Drives Conference IEMDC 2013, 12-15 May, 2013, Chicago IL, pp.1080-1087.

[48] Guglielmi P., Boazzo B., Armando E., Pellegrino G., Vagati A., *Permanent-Magnet Minimizationin PM-Assisted Synchronous Reluctance Motors for Wide Speed Range*, IEEE Transactions on Industry Applications, vol. 49, no. 1, pp. 31-41, January/February 2013.

[49] Muşuroi S., Popovici D., Şorândaru C., Greconici M., Svoboda M., *Contract for research-development and consultancy*, Protocol contract 9228/6.07.2010.

[50] Fratta A., Vagati A., Villata F., *Permanent magnet assisted synchronous reluctance drive for constant-power application: Drive power limit*, Proc. Intell. Motion Eur. Conf. (PCIM), Nürnberg, Germany, pp. 196–203, Apr. 1992.

[51] Bianchi N., Dai Pré M., Bolognani S., *Design of a fault-tolerant IPM motor for electric power steering,* IEEE Trans. Veh. Technol., vol. 55, no. 4, pp. 1102–1111, Jul. 2006.

[52] Welchko B.A., Jahns T.M., Soong W/L., Nagashima J.M., *IPM synchronous machine drive response to symmetrical and asymmetrical short circuit faults*, IEEE Trans. Energy Convers., vol. 18, no. 2, pp. 291– 298, Jun. 2003.

[53] Fratta A., Troglia G.P., Vagati A., Villata F., *Evaluation of torque ripple in high performance synchronous reluctance machines*, Conf. Rec. IEEE IAS Annu. Meeting, Toronto, Canada, pp. 163–170, Oct. 1993, vol. I, pp. 163–170.

[54] Bianchi N., Bolognani S., *Reducing torque ripple in Pmsynchronous motors by pole-shifting*, Proc. ICEM, Helsinki, Finland, pp. 1222–1226, Aug. 2000, pp. 1222–1226.

[55] Sanada M., Hiramoto K., Morimoto S., Takeda Y., *Torque ripple improvement for synchronous reluctance motor using asymmetric flux barrier arrangement*, Proc. IEEE Ind. Appl. Soc. Annu. Meeting, pp. 250–255, Oct. 12–16, 2003.

[56] Li T., Slemon G., *Reduction of cogging torque in permanent magnet motors*, IEEE Trans. Magn., vol. 24, no. 6, pp. 2901–2903, Nov. 1988.

[57] Bianchi N., *Analysis of the IPM motor—Part I. Analytical approach in design, analysis, and control of interior PM synchronous machines*, Conf. Rec. IEEE IAS Annu. Meeting.

[58] Boldea I., *Reluctance Synchronous Machines and Drives*, Clarendon PRESS, OXFORD, 1996.

[59] Soong W., Staton D.A., Miller T.J., *Design of a new axially-laminated interior ermanent magnet motor*, Proc. IEEE IAS Annual Meeting, pp 27-36, 1993.

[60] Vegati A., Canova A., Pastorelli M., *Design and control of high performance synchronous reluctance motor with multiple flux-barrier rotor*, IPEC 2000, Tokyo, Japan.

3.3. Section 2.3.1

[61] Năvrăpescu V., Ghiţă C., Musuroi S., *Maşini şi acţionări electrice,* Editura Academiei Oamenilor de Ştiinţă din România, ISBN 978-606-837-139-9, 2011.

[62] Atanasiu Gh., Muşuroi S., Popovici D., *Modelare dinamică prin SIMULINK. Maşini electrice. Acţionări electrice. Convertoare statice*, Editura Politehnica Timişoara, ISBN (10) 973-625-351-X, ISBN(13) 978-973-625-351-5, 2006.

[63]. Şorândaru C., Muşuroi S., Svoboda M., Olărescu N. V., Popovici D., *Field Oriented Control Drives for Naval Mechanism*, Proceedings EUROCON 2009, EUROCON '09. International Conference of IEEE, Saint Petersburg, Russia, 18-23 Mai, pp. 717-720, ISBN 978-1-4244-3861-6, 2009.

[64] Madescu Gh., Biriescu M., Greconici M., Muşuroi S., Moţ M., *Field Analysis of Induction Machine Using Two Different Models*, Proceedings International Aegean Conference on Electrical Machines and Power Electronics&Electromotion, Bodrum, Turkey, 10-12 Septembrie, pp. 616-620, ISBN 978-975-93410-2-2, 2007.

[65] Muşuroi S., Torac I., *A Simulink Model of a Direct Orientation Control Scheme for Torque Control Using a Current-Regulated PWM Inverter*, Proceedings of the 1st International

Scientific Conference on Information Technology and Quality. TEI of Piraeus, Greece, University of Paisley, U.K., Athens, 5-6 Iunie, pp. 60-63, ISBN 1-903978-19x, 2004.

[66] Ursu D., Păpuşoiu Gh., Svoboda M., Muşuroi S., *Angle transducer for the monitor of the power factor on the alternative current machines*, Proceedings of International Scientific Conference eRA-4, SynEnergy Forum(S.E.F.) – 2, TEI of Piraeus&University of Paisley, 24-26 Septembrie, 6 pages, ISBN 1791-1133, 2009.

[67] Glava M., Păpuşoiu Gh., Olărescu N. V., Muşuroi S., *Three-phase rectifier with linear dependency between rectified voltage and command voltage*, Proceedings of International Scientific Conference eRA-4, SynEnergy Forum(S.E.F.) – 2, TEI of Piraeus&University of Paisley, 24-26 Septembrie, 6 pages, ISBN 1791-1133, 2009.

[68] Şorândaru C., Sfâşie A., Muşuroi S., Olărescu N. V., *PLC Control of an industrial process using LabVIEW*, International Conference on Remote Engineering and Virtual Instrumentation – REV 2008, Duesseldorf, 23-25 Iunie, 6 pages, ISBN 978-3-89958-352-6, POS. 02.7, 2008.

[69] Şorândaru C., Muşuroi S., *Low Cost Data Acquisition Setup for Electrical Machines Laboratory*, 15 th IMEKO TC4 Symposium on Novelties in Electrical Measurements and Instrumentation, Iaşi, 18-22 Septembrie, pp. 659-664, ISBN 978-973-667-260-6, 978-973-667-260-0, 2007

[70] Muşuroi S., Gheorghiu S., Dobref V., Deliu F., Svoboda M., Şorândaru C., Cornea O., *Electric Drives with Field Orientated Control for Naval Mechanisms*, Scientific Bulletin of the Politehnica University of Timişoara, Transaction on Power Engineering, Tom 53(67), 4 pages, ISSN 1582-7194, 2008.

[71] Atanasiu Gh., Muşuroi S., *Dynamic Analysis of Induction Motors Using Simulation Technique*, Scientific Bulletin of the Politehnica University of Timişoara, Transaction on Power Engineering, Tom 53(67), pp. 19-24, ISSN 1582-7194, 2008.

[72] Svoboda M., Şorândaru C., Popovici D., Muşuroi S., *Numerical command for the drive of a rolling crane*, Scientific Bulletin of the Politehnica University of Timişoara, Transaction on Power Engineering, Tom 52(66), pp. 621-626, ISSN 1582-7194, 2007.

[73] Şorândaru C., Svoboda M., Muşuroi S., Popovici D., *Electrical drive systems with vectorial control for the induction motors implemented on naval mechanisms*, Scientific Bulletin of the Politehnica University of Timişoara, Transaction on Power Engineering, Tom 52(66), pp. 609-614, ISSN 1582-7194, 2007.

[74] Muşuroi S., Şurianu F., Şorândaru C., *Modelling and simulation of a vectorial leading system of the induction machine with speed control*, Scientific Bulletin of the Politehnica University of Timişoara, Transaction on Power Engineering, Tom 52(66), pp. 439-444, ISSN 1582-7194, 2007.

[75] Muşuroi S., Şorândaru C., Şurianu F., *The Modeling and Simulation of an Adjusting System for the Position of the Induction Machine Supplied by a PWM Inverter with the Identification of the Rotor flux*, Buletinul Institutului Politehnic Iaşi, Seria Electrotehnică, Energetică, Electronică, Tomul LII (LVI), Fasc.5A, pp. 39-44, ISSN 1223-8139, 2006.

[76] Muşuroi S., Greconici M., Moţ M., *A Direct FOC of a Inverter Fed Induction Motor*, Electronics, Yu ISSN 1450-5843, Vol. 9, No. 2, pp. 53 – 56, 2005.

[77] Boldea I., Nasar S., *Vector Control of AC Drives*, CRC Press, Inc. 2000, Florida, 1992.

[78] Şorândaru C., *Instrumentaţie virtuală în ingineria electrică*, Editura Orizonturi Universitare, Timişoara, 2003, ISBN: 973-8391-52-0.

[79] Popovici D., Muşuroi S., Şorândaru C., Svoboda M., Cornea O., Gheorghiu S., Dobref V., ş.a., *Sisteme de acţionare electrică cu control vectorial pentru motoarele de inducţie implementate la mecanismele navale*, Protocol grant, Universitatea Politehnica Timişoara şi Institutul de Marină Mircea cel Bătrân din Constanţa, GR 226, 2009.

[80] Biriescu M., Groza V., Creţu V., Liuba Gh., Toader D., Moţ M., Madescu Gh., Muşuroi S., Şorândaru C., *Some Aspects Concerning Testing of Electrical Machines in Power Engineering*, WEC Regional Energz Forum FOREN 2006, Neptun, 11-15 Iunie, code sp-117, 7 pages, ISBN 973-720-032-2, 2006.

3.4. Section 2.3.2

[81] Bianchi N., Bolognani S., *Parameters and Volt-Ampere Ratings of a Synchronous Motor Drive for Flux-Weakening Applications*, IEEE Trans. On Power Electron. vol. 12 no. 5 pp. 895–903, September, 1997.

[82] Morimoto S., Sanada M., Takeda Y., *Effects and Compensation of Magnetic Saturation in Flux-Weakening Controlled Permanent Magnet Synchronous Motor Drives*, IEEE Trans. On Ind. Appl., vol. 30, no. 6, November/December 1994.

[83] Morimoto S., Sanada M., Takeda Y., *Wide-Speed Operation of Interior Permanent Magnet Synchronous Motors with High-Performance Current Regulator*, IEEE Trans. On Ind. Appl., Vol. 30, No. 4, pp. 920-926, July/August 1994.

[84] Kim J.M., Sul S.K., *Speed Control of Interior Permanent Magnet Synchronous Motor Drive for the Flux Weakening Operation*, IEEE Trans. On Ind. Appl.,Vol. 33, No. 1, pp. 43-48, January/February,1997.

[85] Kwon T.S., Sul S.K., *Novel Antiwindup of a Current Regulator of a Surface-Mounted Permanent-Magnet Motor for Flux-Weakening Control*, IEEE Trans. On Ind. Appl., vol. 42, no. 5, pp. 1293-1300, September/October 2006.

[86] Yoon Y.D., Sul S.K., *New Flux Weakening Control for Surface Mounted Permanent Magnet Synchronous Machine Using Gradient Descent Method*, The 7th International Conference on Power Electronics, pp. 1208-1212, October 2007.

[87] Gallegos-Lopez G., Gunawan F.S., Walters J.E., *Optimum Torque Control of Permanent-Magnet AC Machines in the field-Weakened Region*, IEEE Trans. On Ind. Appl. vol. 41, no. 4 pp. 1020–1028, July/August 2005.

[88] Lenke R.U., De Doncker R.W., Kwak M.S., Sul S.K., *Field Weakening Control of Interior Permanent Magnet Machine using Improved Current Interpolation*, IEEE PESC, pp. 1-5, June 2006.

[89] Bae B.H., Patel N., Schulz S., Sul S.K., *New Field Weakening Technique for High Saliency Interior Permanent Magnet Motor*, IEEE 38th IAS Annual Meeting, vol. 2, pp. 898-905, October 2003.

[90] Choi G.Y., Kwak M.S., Kwon T.S., Sul S.K., *Novel Flux-Weakening Control of an PMSM for Quasi Six-Step Operation*, IEEE IAS Annual Meeting, pp. 1315-1321, September 2007.

[91] Nalepa R., Orlowska-Kowalska T., *Optimum Trajectory Control of the Current Vector of a Nonsalient-Pole PMSM in the Field Weakening Region*, IEEE Trans. On Ind. Electronics, vol. 59, no. 7 pp. 2867-2876, July 2012.

[92] Hava A.M., Kerkman R.J., Lipo T.A., *Carrier-Based PWM-VSI Overmodulation Strategies: Analysis, Comparison, and Design*, IEEE Trans. On Power Electronics vol. 13, no. 4 pp. 647–689, July 1998.

[93] Khambadkone M., R. and J. Holtz, *Compensated Synchronous PI Controller in Overmodulation Range and Six-Step Operation of Space-Vector-Modulation-Based Vector-Controlled Drives*, IEEE Trans. On Ind. Electronics, vol. 49, no. 3 pp. 574-580, July 2002.

[94] Olărescu N. V., Muşuroi S., Şorândaru C., Weinmann M., Zeh St., *Optimum Current Control for Wide Speed Range operation of PMSM Drive Without regenerative Unit Utilizing PWM-VSI Overmodulation*, Proceedings of 13th International Conference on Optimization of Electrical and Electronic Equipment OPTIM 2012, Braşov, 24-26 Mai, pp. 612-617, ISBN 978-1-4673-1652-1, 2012.

[95] Olărescu N. V., Weinmann M., Muşuroi S., Şorândaru C., *Novel flux-weakening control algorithm for PMSM with large DC-link variations utilizing PWM-VSI overmodulation*, Electromotion, Vol. 20, No. 1–4, pp. 53–59, ISSN 1223-057X, 2013.

[96] Matsuo T., Lipo T.A., *Current sensorless field oriented control of synchronous reluctance motor*, Conf. Rec. IEEE-IAS Annual Meeting, pp. 672–678, 1993.

[97] Ohishi K., Nakamura Y., *High Performance Current Sensor–less Speed Servo System of PM Motor Based on Current Estimation*, Trans. on Ind. Appl., vol. 37, pp. 1240–1246, September/October, 2001.

[98] Morimoto S., Sanada M., Takeda Y., *Optimum efficiency operation of synchronous reluctance motor without current sensor*, in Proc. 8th Int. Conf. Power Electronics and Variable Speed Drives, pp. 506–511, 2000.

[99] Morimoto S., Sanada M., Takeda Y., *High-Performance Current-Sensorless Drive for PMSM and SynRM with Only Low-Resolution Position Sensor*, Trans. on Ind. Appl. vol. 39, no 3, pp. 792–801, May/June 2003.

[100] Schmirgel H., Krah J.O., *Compensation of Nonlinearities in the IGBT Power Stage of Servo Amplifiers through Feed Forward Control in the Current Loop*, PCIM Europe, pp. 94–99, June 2005.

[101] Olărescu N.V., Muşuroi S., *Enhanced Simplified Control Algorithm for Surface-Mounted Permanent Magnet with Sinusoidal Excitation*, IPEMC China, vol. 2, pp. 1049–1053, August 2004.

[102] Olărescu N. V., Muşuroi S., Şorândaru C., Frigură-Iliasa F. M., *Scalar control systems with permanent magnet synchronous motors with sinusoidal current control. Calculatin of speed controller parameters*, Revue Roumaine des Sciences Techniques. Serie Electrotechnique et Energetique, Tome 57, Issue 1, pp. 70-79, ISSN 0035-4066, 2012.

[103] Olărescu N. V., Weinmann M., Zeh St., Muşuroi S., Şorândaru C., *Control of Wide Speed Range PMSM Drives with Large DC-Link Variations without Regenerative Unit utilizing PWM-VSI overmodulation,* Proceedings of 4th Annual IEEE Energy Conversion Congress&Exposition ECCE 2012, Raleigh, North Carolina, 15-20 Septembrie, pp. 831-837, ISBN 978-1-4673-0801-42012, 2012.

[104] Olărescu N. V., Weinmann M., Zeh St., Muşuroi S., Şorândaru C., *Optimum Current Reference Generation Algorithm for Four Quadrant Operation of PMSMS Drive System without Regenerative Unit*, IEEE INTERNATIONAL SYMPOSIUM ON INDUSTRIAL ELECTRONICS (ISIE 2010), Conference Proceeding, Bari, Italia, 4-7 Iulie, pp. 1408-1413, ISBN 978-1-4244-6391-6, 2010.

[105]. Olărescu N. V., Weinmann M., Zeh St., Muşuroi S., Şorândaru C., *Optimum Current Reference Generation Algorithm for PMSMS Drive System for Wide Speed Range,* MELECON 2010, THE 15TH IEEE MEDITERRANEAN ELECTROTECHNICAL CONFERENCE, Conference Proceeding, Malta, 25-28 Aprilie, pp. 1073-1077, ISBN 978-1-4244-5795-3, 2010.

[106] Olărescu N. V., Muşuroi S., Şorândaru C., Weinmann M., Zeh St., *Optimum Current Command Algorithm for Wide Speed Range and Four Quadrant Operation of PMSMS Drive without Regenerative Unit,* Proceedings of the International Conference on Optimisation of Electrical and Electronic Equipment, OPTIM 2010, 20 - 22 Mai, pp. 704-709, ISSN 18420133, ISBN 978-142447019-8, 2010.

[107] Olărescu N. V., Weinmann M., Zeh St., Muşuroi S., *Novel Flux Weakening Control Algorithm for PMSMS,* Proceedings of 2009 International Conference on power Engineering Energy and Electrical Drives, Lisbon, IEEE Ind. Elect. Soc., 18-20 Martie, pp. 123-127, ISBN 978-1-4244-4611-7, 2009.

[108] Olărescu N. V., Muşuroi S., Şorândaru C., Atanasiu Gh., *Enhanced Current-Sensorless Drive System for PMSMS Using Two Hall-Effect Sensors for Wide Speed Range*, Proceedings of the 11th International Conference on Optimization of Electrical and Electronic Equipment,

OPTIM 2008, Braşov 22-23 Mai, pp. 87-92, ISBN 978-973-131-030-5, Library of the Congress: 2007905111, 2008.

[109] Olărescu N. V., Muşuroi S., *The Simplify Control Algorithm for Permanent Synchronous Motors with Sinusoidal Current Control (BLAC),* Conference Proceedings, 16th International Conference on Electrical Machines ICEM 2004, Cracow-Poland, 5-8 Septembrie, nr, 401, 4 pagini, ISBN 12-345678-90, 2004.

[110] Holtz J., Quan J., *Drift and parameter compensated flux estimator for persistent zero stator frequency operation of sensorless controlled induction motor*, in IEEE Transaction on Industry Applications, vol. 39, No. 4, July/Aug. 2003, pp. 1052-1060.

[111] Xu X., De Doncker R., Novotny D.W., *A stator flux oriented induction machine drive*, Conf. Rec. IEEE PESC 1988, vol. 5, pp. 870-876.

[112] Xu X., De Doncker R., Novotny D.W., *Stator flux orientation control of induction machines in the field weakening region*, IEEE IAS Annual Meeting, 1988, vol. 1, pp.437-443.

[113] Xu X., Novotny D.W., *Selection of the flux reference for induction machine drive in the field weakening region*, IEEE Transactions on Industry Applications, vol. 28, no. 6, pp. 1353-1358, Nov./Dec. 1992.

[114] Kim S.H., Sul S.K., *Maximum torque control of an induction machine in the field weakening region*, IEEE Transactions on Industry Applications, vol. 31, no. 4, pp. 787-794, Jul./Aug. 1995.

[115] Shin M.H., Hyun D.S., Cho S.B., *Maximum torque control of stator-flux-oriented induction machine drive in the field-weakening region*, IEEE Transactions on Industry Applications, vol. 38, no. 1, pp. 117-121, Jan./Feb. 2002.

[116] Bojoi R., Guglielmi P., Pellegrino G., *Sensorless stator fieldoriented control for low cost induction motor drives with wide field weakening range*, IEEE IAS Annual Meeting, 2008, pp.1-7.

[117] Britz F., Diez A., Degner M.W., Lorenz R.D., *Current and flux regulation in field weakening operation of induction motors*, IEEE Transactions on Industry Applications, vol. 37, no. 1, pp. 42-50, Jan./Feb. 2001.

[118] Bunte A., Grotstollen H., Krafka P., *Field weakening of induction motors in a very wide range region with regard to parameter uncertainties*, Conf. Rec. IEEE PESC, 1996, vol. 1, pp. 944-950.

[119] Grotstollen H., Wiesing J., *Torque capability and control of a saturated induction motor over a wide range of flux weakening*, IEEE Transaction on Industrial Electronics, vol. 42, no. 4, pp. 374-380, August1995.

[120] Abu-Rub H., Schmirgel H., Holtz J., *Sensorless control of induction motors for maximum steady-state torque and fast dynamics at field weakening*, in IEEE IAS Annual Meeting, Tampa, FL, Oct. 8-12, pp. 96-103, 2006.

[121] Blasko V., *Power conditions and control of a regenerative Brake*, IEEE IAS Annual Meeting, vol. 2, pp. 1504-1510, 1998.

[122] Jiang J., Holtz J., *An efficient braking method for controlled AC drives with a diode rectifier front end*, IEEE Transactions on Industry Applications, vol. 37, no. 5, pp. 1299-1307, September/October 2001.

[123] Hinkkanen M., Luomi J., *Braking scheme for vector-controlled induction motor drives equipped with diode rectifier without braking resistor*, IEEE Transactions on Industry Applications, vol. 42, no. 5, pp. 1257-1263, September/October 2006.

[124] Wasynczuk O., Sudhoff S.D., Corzine K.A., Tichenor J.L., Krause P.C., Hansen I.G., Taylor L.M., *A maximum torque per ampere control strategy for induction motor drives*, IEEE Transaction.

[125] Olărescu N. V., Weinmann M., Zeh St., Muşuroi S., Şorândaru C., *Optimum torque control algorithm for wide speed range and four quadrant operation of stator flux oriented induction machine drive without regenerative unit* , Proceedings of 3rd Annual IEEE Energy Conversion Congress and Exposition, ECCE 2011, Conference Proceeding, Phoenix, AZ; Code 87357, 17 Septembrie, pp. 1773-1777, ISBN 978-145770542-7, 2011.

3.5. Section 2.4

[126] Grigore V., *Topological Issues in Single-Phase Power Factor Circuits*, Dissertation for the degree of Doctor of Science in Technology, Helsinki University of Technology, Institute of Intelligent Power Electronics, Otamedia Oy, Espoo, 2001, ISBN 951-22-5735-1.

[127] Mallika K.S., *Topological Issues in Single Phase Power Factor Correction*, Thesis for Master Degree, Department of Electrical Engineering, National Institute of Technology, Rourkela, 769008, 2007.

[128] Qiao C., Smedley K.M., *A Topology Survey of Single Stage Power Factor Corrector*, IEEE 2000, 0-7803-5864-3/00.

[129] Azazi H.Z., EL-Kholy E.E., Mahmoud S.A., Shokralla S.S., *Review of Passive and Active Circuits for Power Factor Correction in Single Phase, Low Power AC-DC Converters*, Proceedings of the 14th International Middle East Power Systems Conference (MEPCON'10), Cairo University, Egypt, December 19-21, 2010, Paper ID 154.

[130] Mühlethaler J., Uemura H., Kolar J.W., *Optimal Design of EMI Filters for Single-Phase Boost PFC Circuits*, Proceedings of IECON 2012, Oct. 2012, pp. 632-638.

[131] Raggl K., Nussbaumer T., Doerig G., Biela J., Kolar J.W., *Comprehensive Design and Optimization of a High-Power Density Single-Phase Boost PFC*, IEEE Trans. on Industrial Electronics, Vol. 56, No. 7, pp. 2574-2587, July 2009.

[132] Kanaan K.Y., Al-Haddad, *A Comparative Study of Single-Phase Power Factor Correctors: Modeling, Steady-State Analysis, Tracking Ability and Design Criteria*, International Symposium on Power Electronics, Electrical Drives, Automation and Motion, 2012, ISBN 978-1-4673-1301-8/12.

[133] Athab H.S., Ramar K., Lu D.D., *An Efficient Quasi-Active Power Factor Correction Scheme*, Proceedings of the 2009 Symposium on Industrial Electronics and Applications, ISIEA 2009, pp. 536-541.

[134] Athab H.S., Lu D.D, *A High-Efficiency AC/DC Converter with Quasi-Active Power Factor Correction*, IEEE Trans. on Power Electronics, Vol. 25, No. 5, pp. 1103-1109, May 2010.

[135] Savithri M., Jebasalme, *AC-DC Converter with Quasi-Active Power Factor Correction*, Proceedings of the Int. Conf. on Computing and Control Engineering, ICCCE 2012, April 2012.

[136] Shin J.W., Seo G.S., Ha J., Cho B.H., *A Low Common Mode Noise Bridgeless Boost-Buck-Boost Power Factor Corection Rectifier*, 978-1-4673-0803-8/12, IEEE 2012, pp. 2901-2907.

[137] Li Q., Andersen M.A.E., Thomsen O.C., *Conduction Losses and Common Mode EMI Analysis on Bridgeless Power Factor Correction*, PEDS 2009, pp. 1255-1260.

[138] Yazdani M.R., Farzanehfard H., Faiz J., *Classification and Comparison of EMI Mitigation Techniques in Switching Power Converters – A Review*, JPE 11-5-18, pp. 767-777, 2011.

[139] Marxgut C., Biela J., Kolar J.W., *Interleaved Triangular Current Mode (TCM) Resonant Transition, Single Phase PFC Rectifiers with High Efficiency and High Power Density*, Proceedings of the 2010 IEEE International Power Electronics Conference, pp. 1725-1732.

[140] Fariborz Musavi, Wilson Eberle, William G. Dunford, *A High-Performance Single- Phase Bridgeless Interleaved PFC Converter for Plug-in Hybrid Electric Vehicle Battery Chargers*, IEEE Trans. On Industry Applications, vol. 47, no. 4, July/August 2011.

[141] Beltrame F., Roggia L., Pinheiro J.R., *Comparative analysis of electromagnetic interference produced by high power single-phase power factor correction pre-regulators*, Proceedings of COBEP'09, Brazil, Nov. 2009, pp. 816-823.

[142] Beltrame F., Roggia L., Abaide A.R., Schuch L., Pinheiro J.R., *EMI Investigation Yield by Single-Phase PFC Pre-Regulators*, Proceedings of IECON'09, Brazil, Nov. 2009, pp. 4128-4133.

[143] Mühlethaler J., Uemura H., Kolar J.W., *Optimal Design of EMI Filters for Single-Phase Boost PFC Circuits*, Proceedings of the 38th Annual Conference of the IEEE Industrial Electronics Society (IECON 2012), Montreal, Canada, October 25-28, 2012.

[144] Vyshakh A.P., Unni M.R., *BLIL PFC Boost Converter for Plug in Hybrid Electric Vehicle Battery Charger*, International Journal of Scientific Engineering and Research (IJSER), Volume 2 Issue 1, January 2014.

[145] Jin-kwei Lee, Yung-Chung Chang, Chia-chin Chuang, *Conversion Circuit Design for High Efficiency Bridgeless Interleaved Power Factor Correction*, International Journal of Energy Engineering 2013.

[146] Nithin V., Siva Priya P., Siva Sumanth N., Seyezhai R., Vigneshwar K., *Investigation of two phase bridgeless interleaved boost converter for power factor correction*, International Journal of Recent Advances in Engineering & Technology (IJRAET), Volume-1, Issue-3, 2013.

[147] Muşuroi S., Hedeş A., Ancuţi M. C., Svoboda M., Popovici D., Muntean N., *Analysis and Evaluation of Current Topologies and Solutions for the Single Phase Power Factor Correction (PFC) for Grid Tied Inverters,* Protocol proiect, BCI 1/28.01.2013.

[148] Muşuroi S., Popovici D., Ancuţi C. M., Hedeş A., Svoboda M.arcus, Tămaş I., *Analysis and Evaluation of Current Topologies and Solutions for three phase Power Factor Correction (PFC) for 400 V mains voltage,* Protocol proiect, BCI 1/24.01.2014.

[149] Shen W., Wang F., Boroyevich D., *Conducted EMI characteristic and its implications to filter design in 3-phase diode front-end converters*, Proc. of the IAS 2004, Vol.3, 3-7 Oct. 2004, pp. 1840-1846.

[150] Shen W., Wang F., Boroyevich D., Liu Z., *Definition and acquisition of CM and DM EMI noise for general-purpose adjustable speed motor drives*, Proc. of the PESC'04, Vol.2, 20-25 June 2004, pp. 1028-1033.

[151] Nussbaumer T., Heldwein M.L., Kolar J.W., *Differential Mode Input Filter Design for a Three-Phase Buck-Type PWM Rectifier Based on Modeling of the EMC Test Receiver*, IEEE Trans. Ind. Electron., Vol.53, No.5, Oct. 2006, pp.1649-1661.

[152] Laimer G., Kolar J.W., *'Zero'-ripple EMI input filter concepts for application in a 1-U 500 kHz Si/SiC three-phase PWM rectifier*, Proc. Of the INTELEC'03, 19-23 Oct. 2003, pp. 750-756.

[153] Yifan Zhao, Yue Li, Lipo T.A., *Force commutated three level boost type rectifier*, IEEE Trans. Ind. Appl., Vol.31, No.1, Jan/Feb 1995, pp.155-161.

[154] Heldwein M.L., Kolar J.W., *Impact of EMC Filters on the Power Density of Modern Three-Phase PWM Converters*, IEEE Trans. Power Electron., Vol.24, No.6, June 2009, pp.1577-1588.

[155] Kolar J.W., Drofenik U., Minibock J., Ertl H., *A new concept for minimizing high-frequency common-mode EMI of three-phase PWM rectifier systems keeping high utilization of the output voltage*, Proc. of the APEC 2000, Vol.1, pp.519-527.

[156] Joergensen H., Guttowski S., Heumann K., *Comparison of Methods to Reduce the Common Mode Noise Emission of PWM Voltage-Fed Inverters*, Proc. of the 37th Int. Power Conf. Conf., Nuremberg, Germany, May 26-28 1998, pp. 273-280.

[157] Raggl K., Nussbaumer T., Kolar J.W., *Guideline for a Simplified Differential Mode EMI Filter Design*, IEEE Trans. Ind. Electron., 2009.

[158] Holmes D.G., *A general analytical method for determining the theoretical harmonic components of carrier based PWM strategies*, Proc. of the 33rd IAS Industry Appl. Conf., vol.2, 12-15 Oct 1998, pp.1207-1214.

[159] Deng H., Helle L., Yin Bo, Larsen K.B., *A General Solution for Theoretical Harmonic Components of Carrier Based PWM Schemes,* Proc. of the APEC 2009, 15-19 Feb. 2009, pp.1698-1703.

[160] Heldwein M.L., Kolar J.W., *Design of Minimum Volume Input Filters for an Ultra Compact Three-Phase PWM Rectifier*, Proc. of the 9th Brazilian Power Electron. Conf. (COBEP'07), 2007, Vol.1, pp.454-461.

[161] Ye H. et al., *Common mode noise modeling and analysis of dual boost PFC circuit*, Proc. of the INTELEC 2004, 19-23 Sept. 2004, pp. 575-582.

[162] Wang S., Kong P., Lee F.C., *Common Mode Noise Reduction for Boost Converters Using General Balance Technique*, IEEE Trans. Power Electron., Vol.22, No.4, July 2007.

[163] Shuo Wang S., Lee F.C., Odendaal W.G., *Improving the performance of boost PFC EMI filters*, Proc of the APEC '03, 9-13 Feb. 2003, Vol.1, pp. 368-374.

[164] Heldwein M.L., Nussbaumer T., Beck F., Kolar J.W., *Novel three-phase CM/DM conducted emissions separator*, Proc. of the APEC '05, Vol.2, 6-10 March 2005, pp.797-802.

[165] Walther P., *A new rectifier system high efficient, high dense, modular, quick to install and superior for service*, in Proc. 15th Int. Telecom.Energy Conf., Sep. 27–30, 1993, vol. 2, pp. 247–250.

[166] Pietkiewvicz A., Tollik D., *Cost/performance considerations for 1-phase input current shapers*, in Proc. 16th Int. Telecom. Energy Conf., Apr. 11–15, 1994, pp. 165–170.

[167] Paice D.A., *Power Electronics Converter Harmonics:Multipulse Methods for Clean Power,* Hoboken, NJ: Wiley, 1999.

[168] Sakkos T., Sarv V., Soojaarv, *Optimum diode-switched active filters for power factor correction of single- and three-phase diode rectifiers with capactive smoothing*, in Proc. 7th Eur. Conf. Power Electron. Appl., Sep. 8–10, 1997, pp. 870–875.

[169] Yoo H., Sul S.K., *A novel approach to reduce line harmonic current for a three-phase diode rectifier-fed electrolytic capacitor-less inverter*, in Proc. 24th IEEE Appl. Power Electron. Conf. Expo., Feb. 15–19, 2009, pp. 1897–1903.

[170] Yoo H., Sul S.K., *A new circuit design and control to reduce input harmonic current for a three-phase ac machine drive system having a very small dc-link capacitor*, in Proc. 25th IEEE Appl. Power Electron. Conf. Expo., Feb. 21–25, 2010, pp. 611–618.

[171] Takaku T., Homma G., Isober T., Igarashi S., Uchida Y., Shimada R., *Improved wind power conversion system using magnetic energy recovery switch (MERS)*, in Proc. 40th IEEE Ind. Appl. Soc. Annu. Meet., Oct. 2–6, 2005, vol. 3, pp. 2007–2012.

[172] Wiik J.A., Widjaya F.D., Isobe T., Kitahara T., Shimada R*., Series connected power flow control using magnetic energy recovery switch (MERS)*, in Proc. IEEE/IEEJ Power Convers. Conf., Apr. 2–5, 2007, pp. 983–990.

[173] Huber L., Gang L., Jovanovic M.M., *Design-oriented analysis and performance evaluation of buck PFC front-end,* in Proc. 24th IEEE Appl.Power Electron. Conf. Expo., Feb. 15–19, 2009, pp. 1170–1176.

[174] Kolar J.W., Biela J., Minibock J., *Exploring the Pareto front of multi-objective single-phase PFC rectifier design optimization—99.2% efficiency vs. 7 kW/dm3 power density*, in Proc. 6th IEEE Int. Power Electron. Motion Control Conf., May. 17–20, 2009, pp. 1–21.

[175] Chapman D., James D., Tuck C.J., *A high density 48 V200 A rectifier with power factor correction—An engineering overview*, in Proc. 15th Int. Telecom. Energy Conf., Sep. 27–30, 1993, vol. 1, pp. 118–125.

[176] *Cool MOS C3* 900 *V—First 900V High Voltage Power MOSFET Using Charge Compensation Principle*, Infineon, Neubiberg, Germany, 2008.

[177] Weis B., Braun M., Friedrichs P., *Turn-off and short circuit behaviour of 4H SiC JFETs*, in Proc. 36th IEEE Ind. Appl. Soc. Annu. Meet., Sep. 30–Oct. 4, 2001, vol. 1, pp. 365–369.

[178] Friedli T., Round S.D., Kolar J.W., *A 100 kHz SiC Sparse Matrix Converter*, in *Proc. 38th IEEE Power Electron. Spec. Conf.*, Jun. 17–21, 2007, pp. 2148–2154.

[179] Aggeler D., Biela J., Kolar J.W., *Controllable du/dt behaviour of the SiCMOSFET/JFET cascode—An alternative hard commutated switch for telecom applications*, in Proc. 25th IEEE Appl. Power Electron. Conf. Expo., Feb. 21–25, 2010, pp. 1584–1590.

[180] Hull B., Das M., Husna F., Callanan R., Agarwal A., Palmour J., *20 A, 1200 V 4H-SiC DMOSFETs for energy conversion systems*, in *Proc.* 1st IEEE Energy Convers. Congr. Expo, Sep. 20–24, 2009, pp. 112–119.

[181] Sun J., Grotstollen H., *Averaged modeling and analysis of resonant converters*, in Proc. 24th IEEE Power Electron. Spec. Conf., Jun. 20–24, 1993, pp. 707–713.

[182] Perreault D.J., Kassakian J.K., *Design and evaluation of a cellular rectifier system with distributed control*, in Proc. 29th IEEE Power Electron. Spec. Conf., May 17–22, 1998, vol. 1, pp. 790–797.

[183] Salmon J.C., *Comparative evaluation of circuit topologies for 1-phase and 3-phase boost rectifiers operated with a low current distortion*, in Proc. Canadian Conf. Electr. Comput. Eng., Sep. 25–28, 1994, pp. 30–33.

[184] Zhao Y., Li Y., Lipo T.A., *Force commutated three level boost type rectifier*, in Proc. 28th IEEE Ind. Appl. Soc. Annu. Meet., Oct. 2–8, 1993, pp. 771–777.

[185] Stoogerer F., Minibock J., Kolar J.W., *Implementation of a novel control concept for reliable operation of a VIENNA Rectifier under heavily unbalanced mains voltage conditions*, in *Proc.* 34nd IEEE Power Electron. Spec. Conf., Jun. 17–21, 2001, vol. 3, pp. 1333–1338.

[186] Krahenbuhl D., Zwyssig C., Bitterli K., Imhof M., Kolar J.W., *Evaluation of ultra-compact rectifiers for low power, high-speed, permanent magnet generators*, in Proc. 35th IEEE Ind. Electron. Soc. Conf., Nov. 3–5, 2009, pp. 448–455.

[187] Schafmeister F., *Indirekte Sparse Matrix Konverter*, Ph.D. dissertation, no. 17428, Power Electron. Sys. Lab., ETH Zurich, Zurich, Switzerland, 2007.

[188] Schweizer M., Lizama I., Friedli T., Kolar J.W., *Comparison of the chip area usage of 2-level and 3-level voltage source converter topologies*, in Proc. 36th IEEE Ind. Electron. Soc. Conf., Nov. 7–11, 2010, pp. 391–396.

[189] Schweizer M., Kolar J.W., *Shifting input filter resonances—An intelligent converter behavior for maintaining system stability*, in Proc. IEEE/IEEJ Int. Power Electron. Conf., Jun. 21–24, 2010, pp. 906–913.